Muonic Background in the Gerda $0\nu\beta\beta$ Experiment

Dissertation

der Mathematisch-Naturwissenschaftlichen Fakultät
der Eberhard Karls Universität Tübingen

zur Erlangung des Grades eines
Doktors der Naturwissenschaften
(Dr. rer. nat)

vorgelegt von

Kai Lorenz Freund

aus Winsen (Luhe)

Tübingen, 2014

Tag der mündlichen Qualifikation: 18.07.2014

Dekan:	Prof. Dr.	W. Rosenstiel
1. Berichterstatter:	Prof. Dr.	P. Grabmayr
2. Berichterstatter:	Prof. Dr.	J. Jochum

Abstract / Kurzfassung

Abstract

Muons can cause a non-negligible background in rare-event experiments like Gerda which searches for the neutrinoless double-beta decay ($0\nu\beta\beta$) in the isotope ^{76}Ge. The kinetic energy of cosmogenic muons depends on the progenitor particle, hence they can have an energy which is high enough to penetrate even the deepest underground laboratory. For this reason Gerda is equipped with a powerful muon veto system which in most parts was developed in Tübingen.

In this work, a plastic scintillator veto was added to the existing water Cherenkov veto in order to protect a weak spot. Existing hardware was maintained, frequently calibrated and faulty modules exchanged when possible. The DAQ and analysis was upgraded in order to run both veto systems simultaneously. The system was simulated with an Geant4-based Monte-Carlo simulation. Multiplicity and photon spectra of the simulations were found to be in good agreement with the experimental data and give an efficiency for the detection of energy-depositing muons of $\varepsilon_{\mu d}^{\mathrm{sim}} = (99.935 \pm 0.015)\%$. Two external effects were clearly identified in the muon veto data: additional muons originating from the Cngs-beam at Cern and an annual flux modulation due to seasonal atmospheric temperature changes. Both effects were measured with high precision and agree well with other experiments. Coincidences with the germanium detectors were studied and muon-germanium coincidences were clearly identified. By defining a muon cut, a muon rejection efficiency of the germanium detectors of $\varepsilon_{\mu r}^{\mathrm{Ge}} = (99.2^{+0.3}_{-0.4})\%$ was found. Two methods were pursued to find radioactive isotopes produced by muons through spallation or neutron activation. The result of both methods is compatible with zero, i.e. no events could be clearly identified. The overall functionality of the muon veto for Phase I of Gerda was successfully maintained and verified.

Kurzfassung

Myonen können in Experimenten, die nach extrem seltenen Ereignissen suchen, einen nichtverschwindenden Untergrund verursachen. Durch die potentiell extrem hohe kinetische Energie der Myonen, koennen diese in die tiefsten Untergrundlabore eindringen. Aus diesem Grund ist das Gerda Experiment, welches den neutrinolosen Doppelten Betazerfall ($0\nu\beta\beta$) im Isotop ^{76}Ge sucht, mit einem Myonveto ausgestattet, welches zu den größten Teilen in Tübingen entwickelt wurde.

In dieser Arbeit wurde das Wasser-Tscherenkow-Veto durch ein System von Plastik-

szintillatoren komplettiert, welches einen blinden Fleck schützen soll. Die verbauten Detektoren wurden instand gehalten, regelmässig kalibriert und fehlerhafte Module ausgetauscht, sobald sich die Möglichkeit ergab. Die Datenverarbeitung und die Analysemodule wurden erweitert um die beiden Vetosystem parallel zu betreiben und auszuwerten. Das gesamte Veto wurde mithilfe einer auf GEANT4-basierenden Monte-Carlo Simulation untersucht. Die erzeugten Photonen- und Multiplizitätsspektren der Simulation wurden mit den Daten verglichen und stimmen gut überein. Myonen, die in den Germaniumdetektoren Energie deponieren, werden in den Simulationen durch das Veto mit einer Effizienz von $\varepsilon_{\mu d}^{\text{sim}} = (99.935 \pm 0.015)\%$ verworfen. Zwei Effekte wurden untersucht, die den Myonfluss beeinflussen: zum einen zusätzliche Myonen vom CNGS am CERN, zum anderen die natürliche Modulation des Myonflusses durch die jahreszeitliche Veränderungen der atmosphärischen Temperatur. Beide Effekte wurden mit hoher Präzision vermessen und stimmen gut mit anderen Experimenten überein. Koinzidenzen zwischen Myonveto und Germaniumdetektoren konnten klar identifiziert werden und eindeutige Myontreffer in den Germaniumdetektoren können mit einer Effizienz von $\varepsilon_{\mu r}^{\text{Ge}} = (99.2^{+0.3}_{-0.4})\%$ verworfen werden. Mit zwei Methoden wurde versucht Isotope zu identifizeren, welche von Myonen duch Spallation und Neutronenaktivierung produziert werden. Diese blieben bisher erfolglos. Die Funktionalität des Vetosystems wurde gezeigt und erweitert.

CONTENTS

CHAPTER 1

INTRODUCTION

The question about the contents of the universe is as old as humanity itself. From the earliest pre-historic astronomers to modern observatories like e.g. the Planck satellite [Ade13a], mankind has displayed a fascination for what lies beyond the earth's atmosphere. After the discovery of countless galaxies, stars and even planets beyond the borders of our own solar system, the question of the content of the universe is still of the highest interest. While the recent discoveries in the field of cosmology can model the overall content of our universe with high precision it cannot tell what exact particles it is comprised of.

Similar huge advances have been made in the search for constituents of matter. Over the past century, a great number of (sub-)atomic particles have been found, some even after very precise theoretical predictions. The most recent discovery was that of a Higgs-like boson with the CMS and ATLAS detectors at the Large Hadron Collider (LHC) located at the Conseil Européen pour la Recherche Nucléaire (CERN) [Aad12, Cha12]. However, the particle properties and interaction models are unable to explain the current universe on a cosmological scale.

But there are efforts to combine these fields by searching for particles and their properties with a special interest to their relation to cosmology. Of great interest in the field of non-accelerator based astro-particle physics are for example the direct search for Dark Matter, which was long proven to exist by indirect surveys [Oor32, Zwi33]. Only recent developments in observation techniques made it possible to search for direct interaction between dark matter and matter. Neutrinos and their properties are of equal interest not only because neutrinos are next to photons the most abundant particles in the universe. They show some rather remarkable properties like for example an oscillating behaviour which allows a neutrino of any kind transform into any other. This was first seen by the Homestake experiment as a deficit in the neutrino flux from the sun [Dav68]. In addition it was hypothesised by the Italian physicist Ettore Majorana that the difference for matter and anti-matter vanishes for neutrinos [Maj37]. Should the latter property be experimentally verified, a door for new physics and the understanding of our universe would be opened since this would provide a stepping stone towards a theory regarding the matter generation in the early universe.

1.1   Muonic Background in Rare-Event Experiments

Since the middle of the last century, a number of astro-particle physics experiments have been performed which are aimed to detect effects of an extremely rare nature. Low interaction rates caused by e.g. small cross-section of neutrino or dark matter demand an increased ability to filter false-positive or "background" events. Rare events could be lost if a detector was constantly busy to record unwanted background or simply vanish in a multitude of physical "garbage". Due to the search for even rarer events the effort to keep these experiments free of background was steadily increasing up to the point where it has become the main investment for money and manpower. The reward however is the knowledge of physics, which brings us closer to the basic understanding of the cosmos.

One of these experiments is the Germanium Detector Array (Gerda), which is searching for the Neutrinoless Double-Beta Decay ($0\nu\beta\beta$) in the germanium isotope ^{76}Ge [Abt04, Ack13]. The existence of this decay would strongly suggest a Majorana nature of the neutrino, i.e. it is its own anti-particle. There are several isotopes which could undergo this decay and a number of experiments are currently operating or in preparation to test them. However, this decay mode has an exceptionally long half-life, the currently known limits for its half-life exceeds $T_{1/2} > 10^{23}$ yr depending on the isotope in question [Bar11].

Background events can be caused by a number of sources: ambient radioactivity, cosmogenic particles or even electronic artefacts. One background which is almost impossible to prevent are muons which are produced when the atmosphere is bombarded with cosmic rays. Since muons and electrons are extremely alike, any detector which is sensitive to electrons and their by-products will detect muons as well. Alternatively, they can shatter a nucleus (in a process called "spallation") and can produce radioactive nuclei and free neutrons which may in turn activate a nucleus. Due to the potentially very high initial energy of the muons, they can penetrate deeply into any laboratory or through any shielding. The rock overburden of an underground laboratory like e.g. the Laboratori Nazionali del Gran Sasso (LNGS) with about 3400 m.w.e. is able to shield the experiments from this cosmic radiation to a certain extend. However the reduction of the muon flux in comparison to sea level of the order of $\approx 10^6$ at LNGS is still not sufficient in order to reduce the background to a desirable level. For this reason, most of these experiments are equipped with an active detection system that records passing cosmic muons. Events that were caused by such an interaction can thus be ruled out or "vetoed" in a later analysis.

1.2   This thesis

This work describes the performance of the muon veto system of the Gerda experiment at the LNGS. The Gerda muon veto is a water Cherenkov veto installed in a water tank which surrounds the cryostat of Gerda in which the germanium detectors are submerged. In previous works, the veto was designed and constructed with the help of Monte-Carlo studies [Kna09] and both hard- and software of its data-acquisition and

-analysis were developed [Rit12]. Based on this, the main point of this work was to show and enhance the overall functionality of the muon veto after more than two years of operation.

In this work, the muon veto was completed by the installation of a layer of plastic scintillation panels on top of the Gerda clean room. These panels protect a weak spot in the water Cherenkov veto where muons could pass the cryostat and hence not be detected by the muon veto. The Data Acquisition system (DAQ) of the muon veto was hence changed to accommodate for the additional 36 panels.

During the duty-cycles of the muon veto, it was frequently calibrated using the calibration system implemented in previous works. Using light pulses of known intensity, the response of the Photo-Multiplier Tubes (PMTs) in the water tank was measured and the response was adjusted afterwards in order to check for electronic drifts or deteriorations. Apart from four detectors which exhibited problems, the apparatus performed reliably and three of the problematic detectors were accessible and could be exchanged. One of the main points of this work was the deconvolution of the signals recorded by the DAQ into different event classes. In order to achieve this, the Monte-Carlo simulations studies in [Kna09] were extended. Here, only muons with energy deposition were simulated and a simplified detector geometry sufficed. Studying the response of the real detector required a simulation of all muons traversing the water tank and an updated geometry. These data were compared to the recorded spectra of the muon veto. As in the previous works, the data from the Monopole, Astrophysics and Cosmic Ray Observatory (Macro) were used for the initial muon angular and spectral distribution [Ahl93]. Additional tests were performed in order to identify an unexpected enhancements in the data. This enhancement appears at low PMT multiplicities and low photo-electron counts and can be explained with a scintillation effect of the reflective foil covering the interior of the water tank.

In order to gauge the performance of the veto, time series of the muon rates were studied. These exhibited two features caused by external physical effects. First, a neutrino beam by the Cern Neutrinos to Gran Sasso (Cngs) facility at Cern was inducing secondary muons in the experimental halls of the LNGS. This causes an offset in the muon rate which could be shown to be in direct relation to the neutrino beam intensity. A data sample of the Cngs was obtained and with the aid of the timestamps of both Cngs and muon veto, these events were discarded. Due to the fact that this beam was only operated from March to November this offset appeared as a seasonal modulation. A secondary effect is a true seasonal modulation which is due to the dependence of the muon production processes in the atmosphere on its temperature. Temperature data from two independent survey systems—the European Centre for Medium-Range Weather Forecast (ECMWF) and the NASA Atmospheric Infrared Sounder (AIRS)–were procured and compared to the modulations. By applying a muon production model to the temperature data an effective temperature for muon generation was found the change of which agrees well with the observed change in the flux observed in Gerda. Both effects may cause a change in the muon rate of ≈1.5% of the entire rate and are well described and understood. These values could hence be compared to other experiments the the LNGS like Macro, Large Volume Detector (Lvd) or Borexino and show good agreement.

The most important factors of such a veto system are its rejection efficiencies, i.e. the percentage of muons which can positively identified and thus vetoed from the germa-

nium data. The efficiency of both panel and Cherenkov veto was evaluated using data from the Gerda physics runs and both are sufficiently high in order to achieve a good performance in the next Phase of the Gerda experiment. In addition, the energy deposition of the muons in the germanium crystals were studied and different classes of energy depositions were identified, prompt events in the volume and slow events on the surface. Long-lived spallation products or neutron-activated nuclei, which deposit their energy in the germanium detectors in a much larger period between muon and germanium event are of special interest, as they cannot be vetoed with the conventional set-up of Gerda. Only in a software post-processing, these can be identified. Several candidates of these products were looked for, but so far, none could be identified which is a satisfactory result for the sake of the experiment.

1.3 Outline

In this thesis the motivation for a muon veto of an experiment with a low count-rate will be given and its performance parameters explained. In Chapter 2 the underlying physics for the $0\nu\beta\beta$ will be introduced and its importance will be discussed. In Chapter 3 the utilized detectors and their predominant sources of background will be listed. A special focus will rest on muons, created either in the atmosphere by cosmogenic particles or by man-made accelerators. In Chapter 4 the Gerda experiment will be introduced and a short view on competitors—past, present and future—will be taken. Especially the recently published results by the Gerda collaboration will be reviewed. In Chapter 5 the veto system will be briefly described and the focus will rest on the changes made after the previous works [Kna09, Rit12]. After its current duty cycle, the overall performance of the veto system will be summarized in Chapter 6. This includes long-term stability of the entire apparatus, seasonal changes and observed anomalies like the additional muon flux caused by the Cngs. The interaction of the muons with the core of the experiment—the germanium detectors—will be given in Chapter 7. Coincident events will be studied and classified. Estimations for the muon rejection efficiency will be given as well as searches for delayed coincidences originating from spallation products and neutron activated nuclei caused by muons. A summary of this work and an outlook on the future of the Gerda experiment and $0\nu\beta\beta$-experiments in general will be given in Chapter 8. The appendices will cover statistical tools used throughout this work (App. A), auxiliary data on the stability of the detector systems used (App. B.1 and B.2), an additional study of coincidences between the Cngs events and the Cryogenic Rare Event Search with Superconducting Thermometers (Cresst) experiment (App. C), a list of data analysis chains developed for Gerda Layout for Input/Output (Gelatio), the Gerda analysis framework (App. D), simulation studies with different attenuation lengths of optical photons in the Gerda water tank (App. E) and tables containing a number of possible cosmogenic isotopes which can be produced in the entire Gerda set-up (App. F).

THE SEARCH FOR THE NEUTRINOLESS DOUBLE-BETA DECAY

In this chapter the motivation and experimental efforts for the search for the $0\nu\beta\beta$ decay will be discussed. For this, a brief overview over the theory of weak interaction and the implications of a $0\nu\beta\beta$ decay to cosmic scales is necessary. The basic neutrino properties will be introduced with a highlight on the neutrino's peculiar properties like e.g. its oscillating behaviour. The mechanics of the $0\nu\beta\beta$ decay and its main detection principles will be described. An overview of the different isotopes which are candidates for the $0\nu\beta\beta$ decay will be given. Unless otherwise noted, the introductory sections are based on standard textbooks like [Sch97, Bil10, Moh04, Giu07].

2.1 BEYOND THE STANDARD MODEL OF PARTICLE PHYSICS

The rather young field of astro-particle physics is the meeting point of astronomy and astrophysics on one hand and nuclear and particle physics on the other. Optical photons were for the longest part the most potent messenger of cosmic events in observational science. With the introduction of methods and detectors used in particle physics, a new range of particles like e.g. air showers or neutrinos could be observed for astronomical purposes. This has already lead to a number of discoveries and new questions like for example the origin and production mechanisms of ultra-high energy cosmic rays[†].

One of the most prominent questions in cosmology or astro-particle physics however is the question regarding the (anti-)matter asymmetry observed in the universe. Anti-matter is frequently produced in radioactive decays, cosmic ray showers or at accelerator facilities, however it is exceedingly rare in both nature and an experiment. Matter and anti-matter annihilate to γ-rays when they meet, i.e. highly energetic photons. Hence any larger abundance of one type of matter in contact with the other could easily

---

[†]A very prominent example is the 3.2×10^{20} eV / 51 J proton seen by Fly's Eye [Bir95]. Its kinetic energy is equivalent to dropping a small bucket of water on your foot. In comparison, the design goal for particle energies of the LHC is 1.4×10^{13} eV.

be detected. This characteristic signature radiation has not been detected yet neither on earth nor by astronomical means in the universe. This rules out (anti-)matter "bubbles" since the border region would show this signature. On the other hand, there is no known process that would favour the production of matter over anti-matter. It is therefore reasonable to assume that in the early universe matter and anti-matter have been produced in equal amounts.

Since our existence is a somewhat good proof that matter actually exists in the universe, the question remains how and when this (anti-)matter asymmetry came to be. With the recent high-precision observations of the cosmic microwave background by the Planck satellite [Ade13b], this asymmetry can be derived. Assuming that the primordial anti-matter has annihilated into photons, the current baryon density can be compared with the photon density obtained from the universe's temperature. From the cosmological parameters a baryon-photon asymmetry η_b can be derived:

$$\eta_b = \frac{n_b}{n_\gamma} \approx 6.1 \times 10^{-10}, \tag{2.1}$$

where $n_{b/\gamma}$ is the baryon/γ number density. Since this there is no observed anti-matter, this can also be considered the number for the $n_b - n_{\bar{b}}$, i.e. the (anti-)baryon asymmetry. This means that in the primordial nucleosythesis a minute fraction more matter than anti-matter was produced or that there is a mechanism that could turn anti-matter into matter. Since the production should be symmetrical, a process is preferred which turns one into the other.

In the following sections, the basics of neutrino physics will be introduced and how neutrinos could very well be responsible for this asymmetry and subsequently us.

2.2   NEUTRINO PROPERTIES AND WEAK INTERACTION

Neutrinos were first proposed by Wolfgang Pauli in 1930 in his famous letter to the "radioactive ladies and gentlemen" [Pau30]. Here, he proposed a solution to the momentum conservation in the radioactive β decay. The energies of the β particles or electrons show a continuous spectrum and hence another—at that time undetectable—particle was needed to carry off the excess energy which should be constant for any decay of the same isotope[†]. Due to the low cross-section i.e. reaction probability of the neutrino, it took almost 30 years until any neutrino could be detected. This was achieved by the POLTERGEIST experiment [Cow56] in 1956, almost 30 years after they were proposed. Since then, a number of properties of the neutrino have been discovered, some of which make it a very interesting particle to study.

Neutrinos are leptons, i.e. they are elementary particles which are subject to the weak interaction and gravity but not electro-magnetism like the charged leptons (electrons, muons and tauons). Similar to the three generations of charged leptons, there are three generations of uncharged neutrino of different "flavour". The leptons contained in the Standard Model of particle physics appears as the following doublets including both

---

[†]Any β^- decay follows the reaction $(A, Z) \rightarrow (A, Z+1) + e^- + \bar{\nu}_e$, $\Delta E = Q_\beta$. That means a neutron in the nucleus decays into a proton under emission of an electron and an electron anti-neutrino. Both particles have a combined kinetic energy of Q_β.

the charged and the uncharged leptons:

$$\begin{pmatrix} e^- \\ \nu_e \end{pmatrix} \qquad \begin{pmatrix} \mu^- \\ \nu_\mu \end{pmatrix} \qquad \begin{pmatrix} \tau^- \\ \nu_\tau \end{pmatrix}. \tag{2.2}$$

The same holds true for the anti-leptons e^+, $\bar{\nu}_e$ and so on. The first detected neutrino were ν_e as mentioned above, the ν_μ was discovered by the Brookhaven AGS experiment in 1962 [Dan62] and finally the ν_τ was first reported by the DONUT collaboration in 2000 [Kod01].

Shortly after the first neutrino detection, a number of other experiments and theories were published about different properties of the neutrino. In the Wu experiment[Wu57] it was shown that the parity conservation in weak interactions is violated[‡]. In this experiment the spin of a β-emitter was fixed by a mixture of an external magnetic field and a smart cooling apparatus. In a parity-conserving reaction, the emission of the particle would be the same if the experiment or in this case the nucleus was mirrored. However, it was found that the electron was always emitted in opposite direction of the spin of the nucleus even when the spin was reversed by changing the external field. The weak interaction is hence the only force that does not conserve the parity but violates it maximally.

This lead to an increased interest in the helicity $H = \sigma \frac{p}{|p|}$ of a particle, which is the normalized product of the momentum p and and the spin direction σ of a particle. The helicity of the neutrino was the main point of interest of the Goldhaber experiment [Gol58]. Here, a system was prepared where an electron-capture source emitted a γ-ray after the decay which had the same spin as the neutrino. By measuring the helicity of the γ, the helicity of the neutrino could be determined as well. It was found to be $H(\nu_e) = +1$ for neutrinos or "left-handed" and $H(\bar{\nu}_e) = -1$ for anti-neutrinos or "right-handed". The discovery of the helicity confirmed the V-A theory, which was developed at the same time [Sud58, Fey58]. Here, a theory for electroweak forces was given which leads to the point, that the weak force only acts on left-handed neutrinos and right-handed anti-neutrinos. This lead immediately to the notion that there should be right-handed neutrinos and left-handed anti-neutrinos. Thus, this model contains four types of neutrinos $\nu_{L,R}, \bar{\nu}_{L,R}$. The helicity of the particle also implies that in the weak interaction, the charge-operator C, which transfers particles into anti-particles is violated. Even further, by studying the decays of the neutral kaons, it was found that even the combination of charge and parity operators CP is violated in the weak interaction.

The weak force is mediated by elementary bosons, as all the other forces are as well. Unlike the photon in electro-magnetism or the gluon of the strong force, the weak bosons $W^\pm, Z^0$ which are quite massive with masses of 80.4 MeV/c^2 and 91.2 MeV/c^2 respectively. All three weak bosons are very short lived which means that they decay very fast, i.e. their range is very short as well. This also coined the name for the weak force as in relation to e.g. the photon the range of any weak boson is severely limited. In addition the $W^\pm$ also transfer an electric charge of ± 1, which lead to the names of Charged-Current (CC) for reactions with the charged $W^\pm$ (like e.g. the β decay) and Neutral-Current (NC) for reaction with the electrically neutral Z^0 (like electron-neutrino scattering). These three particles were predicted by Glashow, Weinberg and

---

[‡]The parity is defined as a point reflection operator on a wave-function $P\psi(x,t) = \psi(-x,t)$.

Salam in 1967 [Wei67] and the neutral currents were discovered by the Gargamelle experiment in 1973 [Fry75] and all three particles were identified by the U1A and U2A Collaborations in 1983.

Due to the extremely low likelihood of interaction or cross section of the neutrinos, direct measurement of any neutrino is still difficult. Usually large detectors are needed in order to give the neutrinos a sizeable target which makes it in most cases far easier to observe the secondary effects of the neutrinos. A pioneering expeiment was the Homestake experiment which was able to observe the ν_e-flux from the sun [Dav68]. However, despite the difficulty of the set-up and diligent theoretical calculations, only a third of the expected flux was recorded. As the deficit was confirmed by later experiments, this discovery led to the so-called "solar neutrino problem". In order to explain this, the models of the thermonuclear fusion in the sun were doubted but detailed studies of the solar structure overruled these doubts. This included measurements by e.g. the Gallex experiment [Ham99] which operated from 1992–1997. A different target nucleus for the neutrino capture pushed the threshold of the experiment to below the neutrinos from the pp-chain, i.e. the primal fusion chain in the sun. Since the same deficiency was seen for all different fusion chain and as the results were in accordance with other experiments neither the solar model nor the experimental data was doubted any more. A physical explanation for this effect was needed. This problem was finally solved in 2001, when the Sno experiment published its data on the entire solar neutrino flux [Ahm01]. As the experiment was sensitive to other neutrino flavours as well and not just ν_e, a much higher neutrino-flux was found in comparison to the Homestake or Gallex experiments. This consolidated the concept of neutrino oscillations which was already introduced previously, i.e. that a neutrino which is created in a certain flavour-eigenstate actually consists of a superposition of different mass-eigenstates. This can be written as a transformation of the mass eigenstates $|\nu_i\rangle$ to the flavour eigenstates $|\nu_f\rangle$, where $f = \{e, \mu, \tau\}$:

$$|\nu_f\rangle = \sum_i U_i |\nu_i\rangle. \tag{2.3}$$

This requires that the mass of the neutrinos is non-vanishing, which was previously thought to be zero. As the neutrino propagates, the phases given in the matrix U_i advance at different speeds, which then leads to a change in the flavour-composition over time and thus a different composition in terms of neutrino-flavours after the propagation from e.g. the sun to earth. This matrix is called the Pontecorvo-Maki-Nakagawa-Sakata matrix [Mak62]. When the three neutrino flavour eigenstates are considered, this matrix takes the following 3×3 form:

$$U_i = \begin{pmatrix} 1 & 0 & 0 \\ 0 & c_{23} & s_{23} \\ 0 & -s_{23} & c_{23} \end{pmatrix} \begin{pmatrix} c_{13} & 0 & s_{13}e^{-i\delta} \\ 0 & 1 & 0 \\ s_{13}e^{-i\delta} & 0 & c_{13} \end{pmatrix} \begin{pmatrix} c_{12} & s_{12} & 0 \\ -s_{12} & c_{12} & 0 \\ 0 & 0 & 1 \end{pmatrix} \begin{pmatrix} e^{-i\alpha_1} & 0 & 0 \\ 0 & e^{-i\alpha_2} & 0 \\ 0 & 0 & 1 \end{pmatrix}. \tag{2.4}$$

Here, $s_{ij} = \sin\theta_{ij}$ and $c_{ij} = \cos\theta_{ij}$ where θ_{ij} are the mixing angles between two eigenstates i and j. In addition to these mixing angles the matrix contains the CP-violating phases δ and the Majorana phases $\alpha_{1,2}$ which only apply if the neutrino is a Majorana-particle (see below). Only ten years after the confirmation of the neutrino oscillation, all three of the mixing angles were measured when the Daya Bay, Reno

and DOUBLECHOOZ experiments almost simultaneously published the last unknown mixing angle θ_{13} [An12]. The three angles are $\theta_{12} = (33.36^{+0.81}_{-0.78})°$, $\theta_{23} = (40.0^{+2.1}_{-1.5})°$ and $\theta_{13} = (8.66^{+0.44}_{-0.46})°$ [GG12] which means that the off-diagonal elements in the mixing matrix are very large, i.e. that almost maximal mixing occurs. As already mentioned, these oscillations are only possible if the neutrinos have a rest-mass which is so far not contained in the Standard Model of particle physics. The kinematic of these oscillations even allow to evaluate the neutrino mass-differences in the form $\Delta m_{ij} = m_i^2 - m_j^2$, i.e. a mass difference which unfortunately does not make assumptions about the absolute values of either $m_{i,j}$. The mass differences are found to be $\Delta m_{21}^2 = 7.50 \times 10^{-5}$ eV, $\Delta m_{31}^2 = +2.47 \times 10^{-3}$ eV and $\Delta m_{32}^2 = -2.43 \times 10^{-3}$ eV which leads to the the question of the neutrino hierarchy. One of these mass differences is small compared to the others, which means that the absolute mass ν_1 and ν_2 are close together while it is currently unknown if ν_3 is heavier (normal hierarchy), lighter (inverted hierarchy) or if the total masses are such that this difference is small compared to it (quasi degenerate hierarchy).

Since the neutrinos flavours are always defined as a superposition of mass-states, the neutrino derived from $\beta\beta$ experiments is usually given as an effective neutrino mass:

$$\langle m_{\beta\beta} \rangle = \left| \sum U_{ij}^2 \right| = \left| \sum |U_{ij}|^2 e^{i\alpha_j} m_j \right|. \tag{2.5}$$

However, from e.g. cosmological constraints a limit on the neutrino mass can be derived and the probing of the cosmic microwave background yielded a limit of $\sum_i m_i < 0.28$ eV/c^2 [Tho10]. With the Δm_{ij} being small, it is a further confirmation that the mass of the neutrinos is very small with the next heavier lepton being the electron with 511 keV/c^2. This was already known since the first observations of the β decay because a neutrino with a large mass would have shifted the endpoint energy of the emitted β-particle.

In general, the neutrinos exhibit a number of puzzling properties which makes them an interesting particle to study. Unfortunately, due to their low cross section, this kind of research usually requires dedicated efforts in the apperatus and measuring time.

2.3 MAJORANA AND DIRAC PARTICLES

The neutrinos, which have been introduced above, are Dirac particles. This means that there are four different neutrinos, particle and anti-particle, left- and right-handed. The Italian physicist Ettore Majorana however first considered a case, where particle and anti-particle are indeed the same [Maj37]. Since the neutrino possesses no charge like e.g. the photon, it could be indeed its own anti-particle. Unlike the photon however, the neutrino is subject to the weak interaction and is not invariant under C, P and CP operations, so that for the generation of the anti-particle the time component is added in a CPT transformation. This transformation can be seen as a Lorentz boost. Since the neutrinos have a rest-mass and thus $v_\nu < c$, the boost transforms the system in a way that the helicity flips into the other direction. This reaction would turn a ν_L into a $\bar{\nu}_L$ and for a Majorana particle these two would be the same.

In the Dirac case, the Lagrange density of a particle is given as:

$$-\mathcal{L} = \bar{\psi} \left(\gamma_a \delta_a + m_D \right) \psi, \tag{2.6}$$

where the first term is the kinetic energy and the second term the mass term. Only the mass term is of interest for the following. Since the spinors ψ can be written as a the sum of their components $\psi = \psi_L + \psi_R$, the Lagrange density can be re-written in terms of the Weyl-spinors $\psi_{L,R}$ as:

$$-\mathcal{L}_\mathcal{D} = m_D \left(\bar{\psi}_L \psi_R + \bar{\psi}_R \psi_L \right), \tag{2.7}$$

which vanishes in the Standard Model, as neutrinos are considered massless, i.e. $m_D = 0$. Since it it already known that neutrinos do possess a mass, i.e. $m_D > 0$, this is not the case. In addition, if the neutrino is a Majorana particle, the following mass-terms are added to the Lagrange density:

$$-\mathcal{L}_\mathcal{M}{}^L = -\frac{1}{2} m_L (\bar{\psi}_L \psi_R^c + \bar{\psi}^c{}_R \psi_L)$$
$$-\mathcal{L}_\mathcal{M}{}^R = -\frac{1}{2} m_R (\bar{\psi}_R \psi_L^c + \bar{\psi}^c{}_L \psi_R), \tag{2.8}$$

where c denotes the charge conjugate of the respective spinor. If combined, it leads to the Dirac-Majorana mass term:

$$-2\mathcal{L}_{\mathcal{DM}} = m_D(\bar{\psi}_L \psi_R + \bar{\psi}^c{}_L \psi_R^c) + m_R \bar{\psi}^c{}_L \psi_R + m_L \bar{\psi}_L \psi_R^c + h.c.$$
$$= \begin{pmatrix} \bar{\psi}_L & \bar{\psi}^c{}_L \end{pmatrix} \begin{pmatrix} m_L & m_D \\ m_D & m_R \end{pmatrix} \begin{pmatrix} \psi_R^c \\ \psi_R \end{pmatrix} + h.c. \tag{2.9}$$

In a pure Majorana case, the Dirac mass $m_D = 0$, which leads to just the entries in the diagonal which are the eigenvalues of this matrix as well. The eigenfunctions are $\phi_1 = \psi_L + \psi_R^c$ and $\phi_2 = \psi_R + \psi_L^c$. There is one solution with a left-handed contribution and an anti-right-handed which is the regular neutrino which interacts via the weak force. The other has an anti-left-handed and a right-handed contribution, which cannot interact via the weak force. For this reason, the second neutrino is called sterile.
In the Dirac case, the $m_{L,R}$ are zero and the eigenfunctions become $\phi_1 = \frac{1}{\sqrt{2}}(\psi + \psi^c)$ and $\phi_2 = \frac{1}{\sqrt{2}}(\psi - \psi^c)$. This is a combination of two Majorana neutrinos so four neutrinos in total. Two of these neutrinos are sterile and two of which interact via the weak force. A case in which this model becomes very simple is the See-saw model when it is assumed that the left-handed neutrino-mass is very small $m_L \approx 0$. The mass-eigenstates are reduced to $m_1 = \frac{m_D^2}{m_R}$ and $m_2 = m_R$. If it is further assumed that the m_R belongs to a heavy sterile neutrino which is capable of the lepton-number violation and that the Dirac-mass m_D has a mass of $\mathcal{O}(\text{MeV})$, the m_1 would be very small as it is observed for the effective neutrino mass and the m_2 gains a mass in the order of $\mathcal{O}(10^{15} \text{ eV})$.
The existence of a lepton number violating, sterile and very massive Majorana neutrino, would open a possible explanation for the (anti-)matter asymmetry which is observed in the universe. If there is indeed a channel which allows the production of these heavy neutrinos, they could decay in the early universe to e.g. baryons. With such a process the existence of the universe as a whole could possibly explained. In addition a sterile heavy neutrino is a viable candidate for Dark Matter, since it is heavy and weakly (but not weak) interacting.

2.4 $2\nu\beta\beta$ AND $0\nu\beta\beta$

A common tool in the search if the neutrino has a Dirac or Majorana nature are double-beta decay experiments. If neutrino are indeed Majorana particles, the following process would be possible. If an anti-neutrino $\bar{\nu}_e$ is emitted in e.g. a β decay it could be immediately be re-absorbed in a second vertex as its neutrino ν_e following the reaction $\nu_e + n \rightarrow p^+ + e^-$. Overall, the nucleus would appear to have undergone two beta decays at the same time, however with no emission of neutrinos. As already mentioned, the energy of the electron from a β decay is not fixed, as part of the energy is carried away by the neutrino. In this case however, there are two simultaneous β decays without any neutrino-emission which means that the entire energy of the decay $Q_{\beta\beta}$ is carried away by the electrons. If the electrons would now be detected, their sum energy would appear as a sharp peak. This is the $0\nu\beta\beta$ decay as it takes the form of two simultaneous β decays but without any neutrino emission, see Fig. 2.1. It has to be noted that there are other reaction which could cause the same effect. Additional theoretical assumptions include an emission of a hypothetical particle called "Majoron" or right-handed current mechanisms. The decay follows

$$(A, Z) \rightarrow (A, Z + 2) + 2e^- + 0\bar{\nu}_e \qquad \Delta L = 2. \qquad (2.10)$$

so if this decay is observed, regardless of the theory of Majorana particles, a violation of the lepton number L is observed, which is so far not explicable with the Standard Model. If the decay happens as is depicted in Fig. 2.1 i.e. via left-handed current the neutrino needs to be a Majorana particle with a rest-mass in order to change its helicity.

Unfortunately, the experimentalist who has to observe this decay is faced with many challenges. The first of these challenges is, that this decay is exceedingly rare as the neutrino cross-sections are so low. With the current experiments, limits on the half-lifes for the $0\nu\beta\beta$ decay can be given in the order of $T^{0\nu}_{1/2} > 10^{25}$ yr. If for example a material with a single β decay were observed, the spectrum would be entirely dominated by the spectrum of the normal β decay and any $0\nu\beta\beta$ contribution would be lost in the statistics. For this reason, isotopes which undergo the Two-Neutrino Double-Beta Decay ($2\nu\beta\beta$) are chosen for this research. If the single β decay is energetically forbidden, the nucleus might still undergo a simultaneous (regular) double β decay. The reaction of this process is:

$$(A, Z) \rightarrow (A, Z + 2) + 2e^- + 2\bar{\nu}_e \qquad \Delta L = 0 \qquad (2.11)$$

and this decay has been confirmed in over 10 different isotopes. A selection of these is listed in Tab. 2.1. The half-lives of this second order process are generally much higher in comparison to the single β decay, half-lives in the order of $T^{2\nu}_{1/2} \approx 10^{20}$ yr are common. If the half-life of the $0\nu\beta\beta$ is known, the effective neutrino mass can be calculated following [Smo10]:

$$\frac{1}{T_{1/2}} = G^{0\nu} |\mathcal{M}^{0\nu}|^2 \left| \frac{\langle m_{\beta\beta} \rangle}{m_e} \right|^2, \qquad (2.12)$$

where $G^{0\nu}$ is the phase space integral of the target nucleus, $\mathcal{M}^{0\nu}$ the Nuclear Matrix Elements (NME) and m_e the mass of the electron. While the phase space integral can
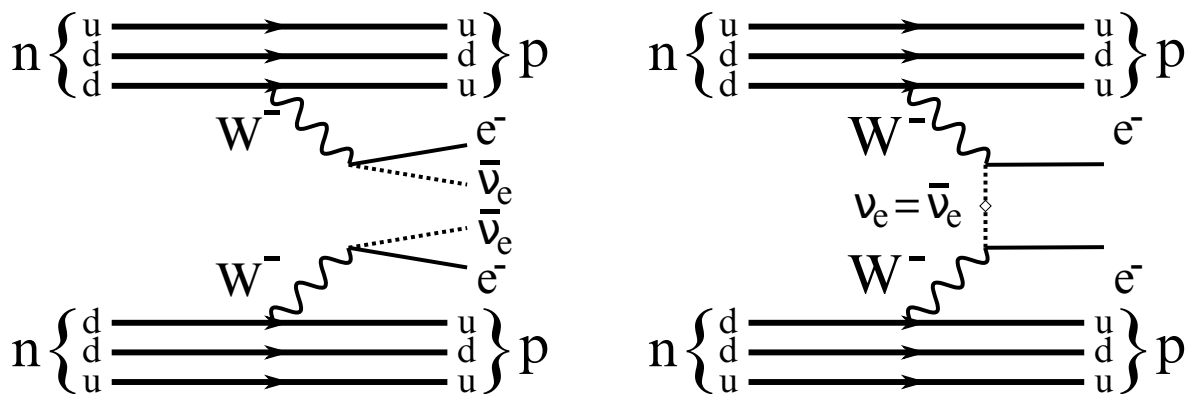
Figure 2.1: *Feynman diagrams of the $2\nu\beta\beta$ and $0\nu\beta\beta$ decays. The exchange for the $0\nu\beta\beta$ is via left-handed current.*

be calculated and the mass of the electron as well, the NME are subject of discussion as there are multiple approaches to these theoretical calculations (see e.g. [Bil10]).

The choice of the isotope however is a very important factor too as there are multiple things to consider regarding the detection mechanism when approaching a $0\nu\beta\beta$ experiment. First, the natural abundance is the amount of the respective isotope in the naturally occurring material. If the value is high (e.g. ^{130}Te), the material does not need to be artificially enriched, which is a time-consuming and expensive process. Second, the end-point energy $Q_{\beta\beta}$ of the decay is different for each isotope. As the highest naturally occurring γ-line has an energy of 2.6 MeV, every isotope with a higher $Q_{\beta\beta}$ (like ^{48}Ca) will not be prone to background related to natural radioactivity. Third, the phase space of the target nucleus factors in as well. An isotope with a higher phase space (^{150}Nd) would see more counts for a given effective neutrino mass than one with a low factor (^{76}Ge). A high half-live of the $2\nu\beta\beta$ is beneficial as well, since the contamination at the end-point of the spectrum will be smaller (^{136}Xe). In addition, some of these isotopes are more suited for the construction of detectors, like the semiconductors germanium or CdZnTe, which have both been in use in particle physics for some time nd are well studied. Liquid xenon is a scintillator, which means that energy deposition within a volume of xenon produces light which can hence be detected. For these reasons it is difficult to say that there is a $0\nu\beta\beta$ "super-isotopes", as most have their own advantages be it in their properties or in their handling.

The most notable historical $0\nu\beta\beta$ experiments were Heidelberg-Moscow (HDM) and International Germanium Experiment (IGEX), which both used germanium detectors enriched in ^{76}Ge in a low-background set-up. Both experiments reported no discovery and set good limits on the half-life. However, a sub-group of HDM published a discovery with a half-life of $T^{0\nu}_{1/2} = 1.19 \times 10^{25}$ yr [KK04]. In a later analysis, the half-life was even further reduced [KK06], but both results were controversially discussed in the community and even refuted [Sch13].

Fuelled by this claim, the search for the $0\nu\beta\beta$ is currently a very lively field of research and there are many experiments with different techniques and isotopes currently searching or in construction in order to verify or refute the claim. The bolometric experiments include GERDA and MAJORANA which use germanium detectors [Ack13, Abg14], CUORE which will use cryogenic TeO$_2$ in a calorimetric set-up [Pat13], the liquid xenon scintillation experiment EXO or KAMLAND-ZEN which uses xenon-doped liquid scin-

Table 2.1: *List of $2\nu\beta\beta$ isotopes after [Bar11, Due11, Bar13, Ago13a]. A selection of $0\nu\beta\beta$ experiments–current and coming–is listed as well.*

isotope	$Q_{\beta\beta}$ [keV]	natural [%]	$T_{1/2}^{2\nu}$ [yr]	$G^{0\nu}$ [$10^{-14}/yr$]	experiment
^{48}Ca	4271	0.187	4.4×10^{19}	6.4	Candles
^{76}Ge	2039	7.8	1.8×10^{21}	0.62	GERDA, Majorana
^{82}Se	2995	9.2	9.2×10^{19}	2.7	SuperNEMO, Lucifer
^{96}Zr	3350	2.8	2.3×10^{19}	5.6	
^{100}Mo	3034	9.6	7.1×10^{18}	4.4	MOON
^{116}Cd	2809	7.5	2.9×10^{19}	4.62	COBRA
^{128}Te	867	31.7	2.0×10^{24}		
^{130}Te	2529	34.5	6.9×10^{20}	4.1	CUORE, COBRA
^{136}Xe	2479	8.9	2.2×10^{21}	4.3	EXO, Kamland-ZEN
^{150}Nd	3367	5.6	8.2×10^{20}	19.2	SNO+

tillator [Aug12, Gan12]. The are tracking experiments like SUPER-NEMO which will use thin foils of decay material in drift chambers [Arn10] or COBRA with pixilated CdZnTe detectors [Ebe13].

Due to the powerful assumption about the nature of the neutrinos, which one can derive with a positive signal on the $0\nu\beta\beta$, this is a very interesting field of research with even cosmological implications.

Detectors and their Background

All experiments with low count-rates, as for example neutrino or Dark Matter experiments, are strongly dependent on the level of background. Background is generated either by physical events like radioactive decays, cosmic radiation and spallation products or non-physical events like electronic noise. If the level of background is too high, a contribution with only a few events may vanish in an abundance of undesired counts in the detector. Hence, background reduction techniques or set-ups which are not susceptible to certain types of background are of very high interest in this field of physics. In this chapter, first the detection techniques applied in the GERDA experiment will be introduced which are commonly used in the field of astro-particle physics. Afterwards, the potential sources of background for an experiment with a low count-rate will be discussed. Especially muons—cosmogenic and artificial in origin—and their secondary effects will be considered.

3.1 Detection Systems

Before the sources of background are introduced, the typical detection systems need to be discussed. Different systems have their own particular advantages and may also suffer from different technical shortcomings. The detection systems applied and used in this work and for the GERDA experiment in general are commonly used detection components in the field of astro and particle physics: semiconductor detectors, Cherenkov detectors, scintillators and PMTs. This section is based on standard textbooks such as [Kno00, Leo94].

3.1.1 Semiconductor Detectors

Semiconductor devices owe their success in the field of particle detectors to a number of unique properties. First, the crystal structure of commonly used semiconductors —silicon, germanium or compound semiconductors like gallium arsenide— is a durable diamond (Si and Ge) or a zinc-blende (GaAs) lattice. In the case of silicon, mono-crystalline ingots with a diameter of 30 cm can be grown and stable germanium detectors of $\approx$2.5 kg can be produced. The high density of solid-state materials permits

Table 3.1: *Properties of two select semiconductors after [Spi05].*

semiconductor	Si	Ge
atomic weight	28.06	72.61
stable isotopes	28-29-30	70-72-73-74-76
density [g/cm^3]	2.33	5.33
atoms [cm^{-3}]	5.0×10^{22}	4.4×10^{22}
min. bandgap [eV]	1.12	0.67
av. bandgap [eV]	3.63	2.96

the production of sturdy detectors, with the option of miniaturisation. In addition, semiconductors are neither hygroscopic like e.g. sodium-iodine (NaI) scintillators and do not suffer from oxidization if the surface has been passivated.

Second, the electrical properties of high-purity semiconductors can be easily altered via "doping". Materials with more or less valence electrons (electron donors, n-type or acceptors, p-type) can be brought into the tetrahedral crystal lattice of quatro-valent atoms as a form of controlled impurity. This can happen either during the growth process or later by e.g. sputtering a select area with the desired dopand. Third, the relatively small band gap of semiconductors (0.67 eV in the case of germanium at room temperature, see Tab. 3.1) permits the detection even of optical photons, giving semiconductor detectors a very broad range of applications from optical detectors to γ spectroscopy. And finally, the readout electronics can be made out of the same material as the detector itself, allowing an integrated structure on a common substrate. With this feature, even complex electronic structures can potentially be integrated into the detector itself.

Semiconductors are characterized by the electronic band-gap of the crystal. The electronic bands are continuous energy levels which the electrons are allowed to occupy. If the highest fully occupied band (the valence band) overlaps with the next highest band (the conduction band) the electrons can move freely; the material is a conductor. If the gap is greater than 3 eV, the electrons are unable to move and the material is an insulator. A material with a band-gap in-between is a semiconductor. When two differently doped semiconductors are brought into contact, the excess electrons from an n-doped side may fill the electron "holes" from a p-doped side and thus create a zone free of charge carriers like electrons or holes and generate a field across this pn-junction. By applying a reverse bias over this junction, the charge-free zone can be enlarged until the entire crystal is depleted.

Under irradiation by any sort of ionizing radiation, an deposited energy in the junction generates electron-hole pairs which are immediately separated by the field over the junction and the bias voltage. The charges generated by the radiation drift to the electrodes and are then enhanced immediately by electronic amplifiers usually in the form of field effect transistors. Afterwards the signal can be further processed by its respective DAQ.

As the ionizing radiation can take the form of a multitude of particle types and take a wide range of energies, there are several effects for the process of the energy deposition to consider. Photons in general are the most commonly radiation to be detected and

there are three main physical effects which can lead to an energy deposition. First, the photon can be fully absorbed by an electron which in turn deposits its energy rapidly and very close to its point of generation. This is the process of photo-electric absorption (or photo effect) and its cross-section $\sigma_{\text{phot.}} \propto Z^5 E_\gamma^{-3.5}$ strongly increases with nuclear weight and decreases with γ-energy. Thus, this process dominates for low energies $E_\gamma < 0.5$ MeV (this and the following energy ranges are all given for germanium). Second, the photons can scatter quasi free on the electrons. This is the Compton effect and its cross section is described by the Klein-Nischina cross section $\sigma_{\text{Comp.}} \propto \frac{1}{E_\gamma}$ which dominates in the energy range of ≈ 1 MeV. The re-emitted photons have a shifted wavelength according to $\lambda' - \lambda = \frac{h}{m_e c} \cos \theta$, where λ is the initial and λ' the final wavelength, h Planck's constant, m_e the electron mass and θ the scattering angle. The electron on which the photon has scattered is soon thermalized as in the previous case. Its maximum energy corresponds to the maximum energy transfer at $\theta = 180°$ and leaves a characteristic Compton-edge below the full-energy peak in the spectrum if the re-emitted photon leaves the crystal. For higher energies, the photon may interact with the field of the nucleus and create a $e^+ e^-$ pair in addition to any recoil energy. The kinetic energy of the photon is used to generate this matter/anti-matter pair which demands that the transferred energy is at least equal to the rest-mass of the two particles, i.e. 1.022 MeV for an electron-positron pair. This process of pair-production is proportional to $\sigma_{pp} \propto Z^2 \ln E_\gamma$, i.e. it is the dominating effect for higher energies $E_\gamma > 2$ MeV. As germanium has a much higher Z-value in comparison to silicon and the mentioned processes are mostly dependent on Z, it is much better suited for the detection of high-energy photons.

Modern germanium detectors are single diode structures with a bulk material comprised of high-purity germanium and the contacts electrodes being strongly doped. This way, the crystal lattice is mostly free of inhomogeneities introduced by the dopand. While especially germanium detectors need to be cooled down in order to operate and are quite expensive, the pay-off is an excellent energy resolution. Some scintillation crystals have a higher acceptance towards high-energy photons, but the resolution of germanium detectors is unprecedented, which makes them a popular—albeit expensive—choice in the field of particle physics.

3.1.2 CHERENKOV DETECTORS

Whenever a sufficiently fast charged particle traverses an optically transparent dielectric medium with a refractive index $n > 1$, the medium emits a characteristic light called Cherenkov radiation [Che08, Jel58]. In the regular case of a slow-moving particle, the charge causes the dipole moments of the atoms in the dielectric to align towards the charge, i.e. the medium becomes polarized. However, the polarization is unidirectional and symmetric around the charge. As the particle progresses through the medium, it polarizes it at any point on its track. As the polarizations relax, electromagnetic radiation is emitted. But as the polarizations are symmetric as already mentioned, these emission interfere destructively and hence no emission is observed. This case is different if the particle travels at a speed v_p which is $c > v_p > c_m = \frac{c_v}{n}$, i.e. slower than the speed of light in the vacuum c but faster than the phase velocity of light in the medium c_m which is divided by its refractive index n. In this case, the
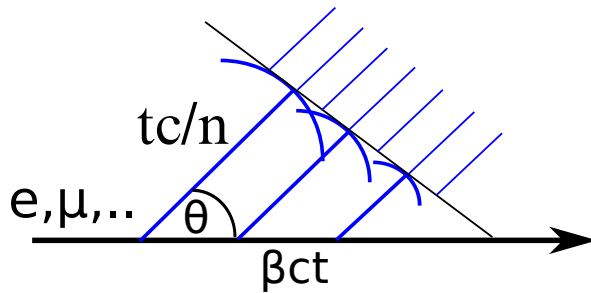
Figure 3.1: *Schematic Cherenkov effect.*

particle is not polarizing unidirectionally, as it is escaping from its own polarization effect. The medium remains dominantly polarized and its relaxations cannot interfere destructively any more. When the polarization relax, electromagnetic radiation is emitted. If it is assumed that each point on the track is polarized, the radiation now interferes constructively for an angle characterized by the speed of the particle $\beta = \frac{v_p}{c}$ and the refractive index:

$$\cos \theta = \frac{1}{\beta n}. \tag{3.1}$$

The geometry of this process is also shown in Fig. 3.1. For highly relativistic particles (i.e. $\beta \lesssim 1$) and water with a refractive index of $n = 1.33$, the Cherenkov angle is 41.2°. It emits photons in the range between λ_1 and λ_2 according to:

$$\frac{dN}{dx} = 2\pi\alpha z^2 \int_{\lambda_1}^{\lambda_2} \left(1 - \frac{1}{n^2\beta^2} \right) \frac{d\lambda}{\lambda^2}, \tag{3.2}$$

where $\alpha = \frac{1}{137}$ and z the particles charge. This means that e.g. in water, a particle with a single charge (e.g. a muon) which is highly relativistic[†] emits a total number of photons in the optical range of:

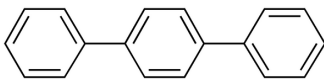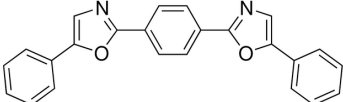$$\frac{dN}{dx}(300 - 500 \text{ nm}) = 266 \text{ photons/cm} \tag{3.3}$$

and in the ultra-violet:

$$\frac{dN}{dx}(100 - 300 \text{ nm}) = 1330 \text{ photons/cm} \tag{3.4}$$

i.e. a factor of five more compared to the optical photons. This leads to the characteristically blue light emission from the Cherenkov effect, which can even be observed with the eye in strong charge emitting environments like e.g. a nuclear reactor. In the case of single Cherenkov emissions, only a few thousand photons are produced, depending on the length of the track and hence a powerful light detector is required in order to record this light like e.g. a PMT. Due to their entrance window, PMTs are usually insensitive to ultra-violet light (see Fig. 3.2), but there is usually sufficient light emitted in the optical spectrum for the PMT to record the light. The total energy loss of a particle due to the Cherenkov effect in matter is of the order $\approx 10^{-3}$ MeV cm^2/g. Hence highly energetic particles like e.g. muons lose only a fraction of their energy due to this effect.

[†]Muons at the location of the GERDA experiment have a mean kinetic muon energy of $\langle E_\mu \rangle = 270$ GeV and a thus highly relativistic, see e.g. Sec. 5.6.

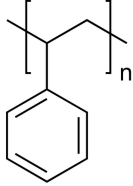***Table 3.2:*** *Properties of select organic scintillators after the online catalogue of Sigma Aldrich.*

short name	**PTP**	**POPOP**
name	para-terphenyl	1,4-Bis(5-phenyl-2-oxazolyl)benzene
diagram		
lin. formula	$C_6H_5C_6H_4C_6H_5$	$C_24H_16N_2O_2$
function	primary fluor	wave-length shifter
absorption [nm]	277	–
emission [nm]	343	410
CAS number	92-94-4	1806-34-4

3.1.3 Scintillation Detectors

Much like Cherenkov detectors, scintillators are technically not detectors but signal-enhancing media which are read out by a light-sensitive detector like e.g. a PMT. Along and in combination with the PMT, these are the most common types of detectors of the field. There are many different kinds of scintillators with different physical mechanisms and (dis-)advantages, but all share the same principle of a light emission when an ionizing particle passes through. As the material absorbs energy it can re-emit it in the form of fluorescence light on time scales ranging from pico- to micro-seconds. The de-excitation in any other form but light emission is known as quenching, in other words an emission inefficiency. Usually the light emission takes the form of an exponential decay over time with one or even more components, with decay-times ranging from nano- to microseconds depending on the scintillator and other parameters like its temperature. A scintillator is characterized by the light-yield per deposited energy or conversion efficiency (usually in the order of $\approx 10^4$ photons/MeV), transparency to its emitted light, the speed of the light output and the linearity of the light emission with respect to the deposited energy.

Organic scintillators are usually aromatic hydrocarbon compounds containing benzene rings, as sketched for two scintillators in Tab. 3.2. Much like a solid, molecules have different bands and energy levels, in which valence electrons can be excited. As in the atom, the de-excitation happens by the emission of light. The electron is mostly excited in a vibrational state of an energy level, i.e. a fine structure corresponding to the vibration modes of the molecule. By internal conversion, the electron looses the vibrational energy and then decays from the main energy state to the ground state. Hence the emitted light is lower than the absorbed energy and the material is mostly transparent to its own emission. Usually an organic scintillator consists of two to three different materials. First the scintillator itself like PTP, the "primary fluor" which is responsible for the light emission. Second, a solvent material like the solid plastic polysterene or the liquid oil tetradecane which acts as a carrier for the primary fluor (see Tab. 3.3). Both solid and liquid options have their clear advantages: a plastic can be cast into a fix shape, which it then contains. It is sufficiently light and sturdy, which

Table 3.3: *Properties of plastic solvent polysterene after the online catalogue of Sigma Aldrich.*

short name	polysterene
name	Poly(1-phenylethylene)
diagram	
lin. formula	$(C_8H_8)_n$
function	solid plastic solvent
density [g/cm^3]	0.96–1.04
melting point [°C]	240
refr. index	1.6

is ideal for the production of macroscopic detectors with any desirable geometry. An oil with a solved scintillator is more difficult to handle, however it can be easily used to fill an entire volume almost regardless of size. Much like water Cherenkov detectors, current liquid scintillator detectors range up to many kilo-tonnes in weight. Third, a wave-length shifter can be added. The light emission of the scintillator can be in the ultra-violet as e.g. PTP and PMTs are usually not very efficient in this region. A wave-length shifter like POPOP is able to converse this ultra-violet light to a more suited wave-length for the detector. However, this can introduce new decay-times to the light signal and more options for quenching.

Inorganic scintillators work in a way for which one has to return to the band model of a material. In most solids, when a valence electron is excited into the conduction band and falls back, the emitted light is immediately re-absorbed unless the event was at the surface. However there are processes which produce optical light which can be observed in a macroscopic detector. In all inorganic scintillators, it is possible to produce excitons, which are bound electron-hole pairs which occupy energy levels just below the conduction band and just above the valence band respectively. As the electron is lifted towards the conduction band, the Coulomb repulsion of the surrounding electrons and the attraction of the hole causes a bound state with slightly less energy than the band-gap. If the electron re-combines with the hole, light with less energy than the band-gap is emitted. Alternatively, the crystal can be "activated" by the addition of specific impurities. This distorts the band structure in a way, that localized energy levels below the valence-band can be occupied. The charge carriers can now drift to these activation centres and de-excite from the lowered levels into the ground state by the emission of light with an energy, which is less than the band-gap. Typical examples for inorganic scintillators are thallium-activated sodium-iodine (NaI(Tl)) or calcium-tungstate (CaWO$_4$).

Contrary to semiconductor detectors, scintillators can be efficiently operated at room temperature. In addition, due to the high Z-value which some inorganic scintillators possess, they are much more suited for the detection of γ-rays as the interaction pro-
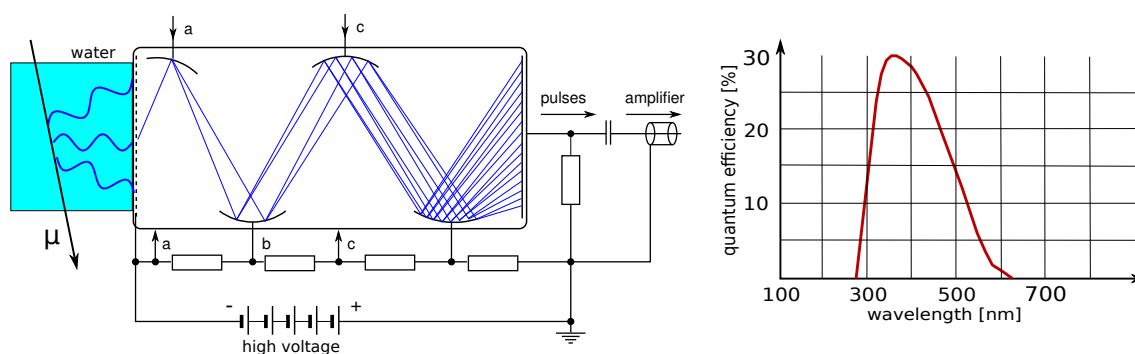
Figure 3.2: *PMT working principle and efficiency curve of a 9354KB PMT after [Ent12].*

cesses rise more than linearly with Z. However, the resolution of most scintillators is worse in comparison to e.g. germanium detectors by about a factor of ten, especially when operated at non-cryogenic temperatures. Due to the many different forms and possible applications of scintillators, they are very popular and very often used in any nuclear- and particle-physics experiments.

3.1.4 PHOTOMULTIPLIER TUBES

Many effects in particle physics produce light, which can be used to identify or else analyse the effect in question. Often, these effects can cause only faint traces of light, which have to be detected. The detector of choice in this case is the PMT. It combines several features, which are very beneficial in this type of research. First and foremost, PMTs are able to detect single photons with an efficiency which can exceed 30%, which means that even the faintest traces of optical light can be detected with reasonable efficiency. In addition, PMTs are scalable depending on the area which needs to be covered with an active detectors. Typical PMTs range fom 2" to 10" diameter and even 20" PMTs were produced for the Kamiokande experiment. Thus, the PMT can be chosen dependent on the need of the experiment.

The detection principle of PMTs is based on a primary photo-emission followed by secondary charge-multiplication. A sketch of this can be seen in Fig. 3.2. Optical photons are produced by muons emitting Cherenkov light in a water tank (see the following section). This light reaches the PMT, which is an evacuated envelope, made usually of glass. On the inside of the entrance window, the photon hits the photo-cathode of the PMT. Here, the light is absorbed and electrons are emitted via the photo effect. The liberated electron has now to leave the absorbing material and escape the cathode. Due to a high-voltage, which is applied from the cathode to the anode, the electron is now accelerated inside the evacuated tube towards a series of electron multipliers. Some PMTs also contain electron-focussing electrodes in order to assure that the primary electron is focussed on the subsequent multiplication line (not in the sketch). A series of resistors act as voltage dividers for the multipliers. Due to this acceleration voltage, the primary electron gains enough kinetic energy in order to ionize an atom via the photo effect in the first dynode "a". These secondary electrons are again accelerated from "a" to "b" and cause further photo effects. This

continues on, until the end of this multiplication chain is reached. The overall gain g is determined by the idealized gain function:

$$g = \alpha \delta^N, \tag{3.5}$$

where α is the fraction of electrons detected by the dynode structrure, δ the multiplication factor and N the number of dynodes. By choosing typical values ($\alpha \approx 1$, $\delta = 5$, $N = 10$), a gain of $\approx 10^7$ is reached. This gain is mostly linear over a wide range of operation, i.e. unless the PMT is illuminated with over several thousand photons by a "bright" light source the number of multiplied electrons is linearly proportional to the number of incident photons. This charge-cloud is hence accumulated by the anode and the pulse can be further amplified and read out by a DAQ.

The difficulty of manufacturing a PMT lies in the appropriate material for the photocathode and the coating of the multipliers. Especially the cathode needs to be optically absorbing, yet thin enough so that the emitted electron can freely pass into the tube itself. The work function for this material needs to be very low, but high enough so that thermal ionization does not become problematic. Room temperature translates to a mean kinetic particle energy of 0.025 eV, however the Maxwell-Boltzmann distribution has a high-energy tail, which can reach into the range of the ionisation-energy. This effect leads to a thermally generated rate of the detector of $10^6 - 10^8/(\text{s m}^2)$, i.e. for an 8" PMT dark rates of $10^4 - 10^5$ are not uncommon. The purity of all used compounds plays a role in the dark rate as well, as radioactive contaminations in the PMT can mimic a detected photon. The cathode material also determines the efficiency of the PMT towards different wavelengths e.g. commonly used boron-silicate windows are opaque for ultra-violet light. A typical efficiency curve for the 9354KB PMT from ET Enterprises used in this work is shown in Fig. 3.2 as well.

The quality of a PMT is usually determined by the study of the pulse height spectrum. For this, the PMT is usually illuminated with a short-pulsed Light-Emitting Diode (LED) which is dim enough to illuminate the PMT with a single photon per pulse in order to record the PMTs Single-Photon Peak (SPP). A high-quality PMT will show a SPP which is clearly distinguishable from the recorded noise events (the pedestal). The ratio of the peak in comparison to the "valley" in-between pedestal and SPP is called the "peak-to-valley" ratio and for the PMTs used in this work, this ratio is typically between $1.5 - 2.5$. Typical calibration curves for seven PMTs can be found in App. B.1.

Other types of detectors may be sensitive to single photons as well. For example semiconductors usually have a band-gap which permits the production of single electron-hole pairs, however as regular semiconductor detectors do not possess the ability of secondary multiplication of the charge carriers, single photons usually disappear in the noise of the detector. In recent years, silicon photomultipliers (SiPM) have been developed, i.e. the combination of an array of avalanche diodes on a common substrate. These modules reach the efficiencies of a PMT as well as the gain. On one hand, these modules are much less affected by external magnetic field, are small and more sturdy in comparison to an evacuated glass tube. In addition the array structure allows an imaging, much like a CCD and with similar overall dimensions. On the other hand, the size is a limiting factor as well. As already mentioned, PMTs have a much larger area for light-collection; PMTs with a diameter of 20" can be fabricated and 8" modules are very frequently used. This allows a much larger sensitive area in experiments which mostly aim to detect small traces of light in larger detectors. To cover the same

area with SiPMs, many modules including cables and read-out electronics are needed. Alternatively, light-guides could also be used. In any case, the development of SiPMs brings diversity into this field of detection and allows the construction of new types of detectors.

3.2 MUONS

As muons, their generation mechanisms and their potential danger to low count-rate experiments are the main focus of this work, they will be given special focus in this section. Other types of background sources will be briefly covered afterwards. This section is based on [Ber12, Gai90].

Muons are charged leptons with a rest mass of 105.7 MeV/c^2 and a mean life-time of 2.2 μs [Ber12]. Due to this very long life-time, a muon with even a moderately relativistic kinetic energy can traverse quite a long distance (in the order of several 10 km) before decaying. The life-time of e.g. a tauon is 2.9×10^{-13} s, i.e. it decays immediately in comparison to the muon. Due to the large mass of the muon in comparison to the electron (0.511 MeV/c^2) muons are not as easily decelerated and hence the radiative loss by e.g. Bremsstrahlung is much smaller. This means that produced muons travel even in matter much further than other charged particles and high-energy muons can even penetrate deep underground laboratories.

The energy loss of a muon in matter can be summarized in a general form:

$$\frac{dE_\mu}{dx} = a(E_\mu) + b(E_\mu)E_\mu, \tag{3.6}$$

where $a(E_\mu)$ is the fraction of energy lost to ionization processes. This is following the Bethe-equation for energy loss of charged particles and is valid for muon energies in the intermediate range, i.e. a kinetic muon energy 100 keV $\leq T_\mu \leq$ 100 GeV. If the particle has an energy with the minimum of this distribution it is in the "minimum ionization" region. Typical stopping powers in this region are ≈ 2 MeV cm^2/g almost independent on the Z of the material. The factor $b(E_\mu)$ includes radiative losses like e^+e^- pair production, Bremsstrahlung and photo-nuclear processes like spallation and is flat for high values of E_μ. Especially the last processes can be troublesome for an experiment as new radioactive isotopes or hadronic cascades including neutrons can be produced. As this factor is proportional to E it dominates the spectrum in the region 100 GeV $\leq T_\mu$. The energy at which radiative and ionizing energy-loss is in equilibrium is conventionally called the critical muon energy $E_{\mu c}$.

Muons decay via the following CC-reaction:

$$\mu^+ \rightarrow e^+ + \nu_e + \bar{\nu}_\mu \qquad\qquad (\approx 100\%). \tag{3.7}$$

and the same for their respective anti-particles. This means that all muons detected in an experiment need to be produced by a high-energy facility. This can be achieved by the collision of protons. The energy in the collision can be transformed by creating new particles, e.g. mesons like kaons ($K^{\pm,0}$) and pions ($\pi^{\pm,0}$). These mesons can in

Table 3.4: *Mesons and muons produced in the atmosphere [Ber12]. Some of these mesos are progenitor particles for muons.*

particle	composition	charge	mass $[\text{MeV/c}^2]$	$T_{1/2}$ [s]
$\mu^\pm$	$-$	± 1	105.7	2.2×10^{-6}
$\pi^\pm$	$\pi^+ : u\bar{d},\ \pi^- : d\bar{u}$	± 1	139.6	2.6×10^{-8}
π^0	$u\bar{u}, d\bar{d}$	0	135.0	8.4×10^{-17}
$K^\pm$	$K^+ : u\bar{s},\ K^- : s\bar{u}$	± 1	493.7	1.2×10^{-8}
K_L^0	$\frac{d\bar{s}-s\bar{d}}{\sqrt{2}}$	0	497.6	5.1×10^{-8}
K_S^0	$\frac{d\bar{s}+s\bar{d}}{\sqrt{2}}$	0	497.6	8.9×10^{-11}
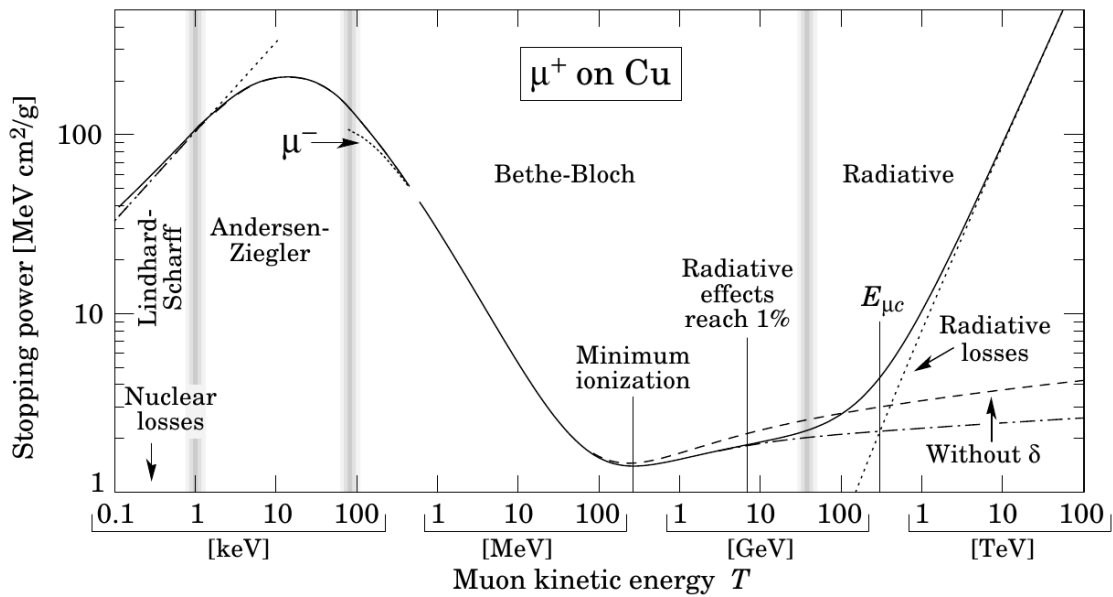
Figure 3.3: *Muon stopping power for different energies in a moderately heavy material [Ber12].*
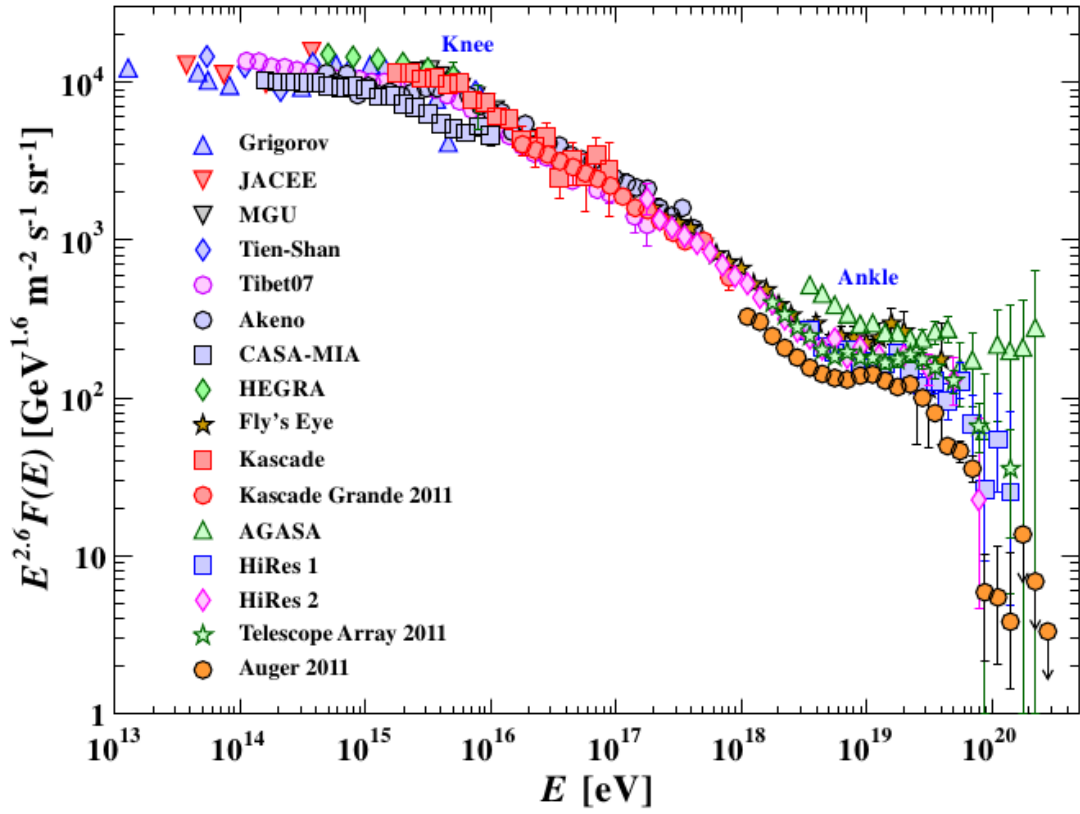
Figure 3.4: *All-particle energy spectrum of cosmic rays [Ber12].*

turn decay within $T_{1/2}^{\pi^\pm}$ following the CC reactions:

$$
\begin{aligned}
\pi^+ &\to \mu^+ + \nu_\mu & (> 99\%) \\
\pi^0 &\to 2\gamma & (99\%) \\
K^+ &\to \mu^+ + \nu_\mu & (63\%) \\
K^+ &\to \pi^0 + \mu^+ + \nu_\mu & (3\%) \\
K^+ &\to \pi^+ + \pi^0 & (21\%) \\
K^+ &\to \pi^+ + \pi^+ + \pi^- & (6\%) \\
K^+ &\to \pi^+ + \pi^0 + \pi^0 & (2\%)
\end{aligned}
\tag{3.8}
$$

and the same for their respective anti-particles. The neutral particles decay as well and with much shorter life-times, but as they either mostly decay into neutral particles (like e.g. $\pi^0 \to \gamma + \gamma$), their contribution is negligible. The charged pions have with 139.6 MeV/c² a much lower mass as the charged kaons with 493.7 MeV/c² and are much more often produced. Hence charged pions are the main contributor to the production of muons. The decay of the neutral kaons and heavier mesons may contribute to the generation of muons as well, but was here omitted for brevity and the small effect.

3.2.1 COSMOGENICALLY PRODUCED MUONS

Unless an artificial high-energy particle source like an accelerator is involved, all the muons which appear in an experiment are cosmogenic in origin. The earth's atmosphere is constantly bombarded with cosmic particles which originate from out of the solar system. This radiation consists of particles which are the content and product of stellar evolution, i.e. clearly dominated by protons ($\approx 94\%$) with small additions of helium ($\approx 4\%$), electrons ($\approx 1\%$) and heavier elements. Some elements show up in even higher abundance as expected like lithium or beryllium which are produced by spallation in the cosmic gas. However, their overall abundance is negligible.

The energy spectrum of cosmic rays (shown in Fig. 3.4) shows several notable features. The energy follows roughly a power-law, however, the spectral index changes slightly around energies of $10^{15} - 10^{16}$ eV ("knee") a dip structure at $10^{18} - 10^{19}$ eV ("ankle") and a steep cut-off at energies exceeding 10^{20} eV. It is assumed that the most energetic cosmic rays produced in our galaxy do not exceed 10^{18} eV, i.e. starting from the "knee" the galactic accelerators reach their maximum. The particles in the "ankle" region are widely regarded as extra-galactic in origin. If other (or stonger) acceleration mechanisms can be assumed like e.g. processes in Active Galactic Nuclei which govern this region, these particles start to overtake the galactic particles. At even higher energies, it is assumed that the extremely high-energetic protons start to interact with the Cosmic Microwave Background (CMB) radiation $\gamma p \rightarrow e^+ + e^-$ and are thus lost in the spectrum. This is known as the Greisen–Zatsepin–Kuzmin cut-off for particles $> 5 \times 10^{19}$ eV. Regardless of the spectral behaviour of the cosmic rays, it clearly shows that the energies that a single particle can possess are enormous. The spectrum in Fig. 3.4 starts at energies which are of the order of the strongest man-made acceleration source, i.e. the LHC which is supposed to have a collision energy of 14 TeV in 2015 after the current upgrade is finished. This means that the necessary energies for muon-generating reactions shown in Eq. 3.8 are easily reached. In the atmosphere, the high-energy cosmic rays are now able to produce a whole shower of secondary particles, consisting of the electro-magnetic component ($e^{\pm}, \gamma$), the hadronic component ($K^{\pm}, p, n$) and the muonic component ($\mu^{\pm}, \nu_{\mu}, \bar{\nu}_{\mu}$).

The energy spectrum of the muons produced is not only dependent on the energy of the incident cosmic ray. The density of the medium is relevant, because if the secondary pions and kaons have undergone scattering before they decay, their energy will be lowered. The atmosphere or any amount of matter between generation and decay will cause an energy loss to the muon and thus stop low-energetic ones. Thus, the production altitude for muons is high up in the atmosphere at $10 - 15$ km. If observed under large angles, the muon flux will be reduced in relation to the zenith, as especially low-energy muon will be able to decay and because the atmosphere will stop some of the muons as well. At sea level, the muon flux takes thus a characteristic form $\cos^2 \theta$ of the zenith angle θ. These muons show a rate of $\approx 200/(\text{s·m}^2)$ for a horizontal detector and the mean energy of the muons is $\langle E_{\mu} \rangle = 4$ GeV. Since the primary cosmic rays are for the most part positive, the generation of positive mesons and thus muons is favoured. The ratio of positive to negative muons is found to be $F_{\mu^+}/F_{\mu^-} \approx 1.3$.

The muon spectrum under a sufficiently large amount of overburden (conventionally given in meter water-equivalent m.w.e.) takes a different form. Due to the increased shielding at higher angles, the distribution becomes sharper around $\theta' = 0$. In addition,
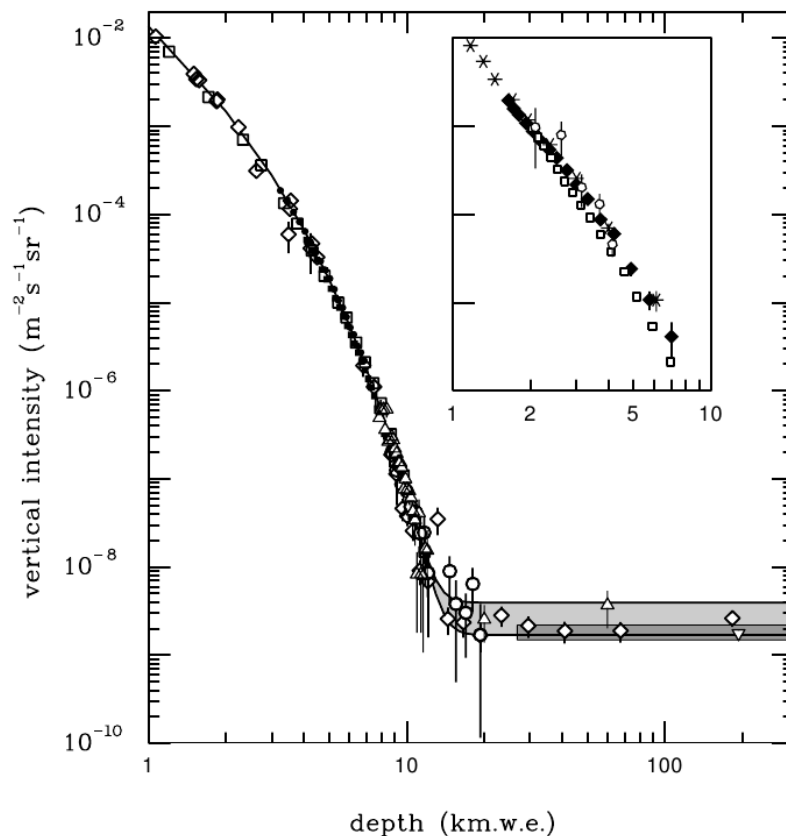
Figure 3.5: *Vertical muon intensity in relation to the the depth in km.w.e. measured by different experiments [Ber12].*

the energy losses by the processes described above will accumulate much more quickly in comparison to the atmosphere. For standard rock and 1 TeV muons, the parameters of the stopping power take the values for the ionization losses $a(E_\mu) \approx 2.68$ MeV cm^2/g and for the radiative losses $b(E_\mu) \approx 3.92 \times 10^{-6}$ cm^2/g. As the radiative losses are still multiplied by the energy (see Eq. 3.6), this is already the dominant factor and the muon has a range of 2.45 km.w.e. which is of the order of an already deep laboratory. In comparison, the halls of the LNGS have an overburden of 3.5 km.w.e. and the muon "threshold" by the overall energy losses rises to ≈ 1.8 TeV. The vertical intensity of the muon flux is shown in Fig. 3.5 which shows the effect especially of the radiative losses on the depth of the site in which the flux was measured. Since the overburden is in most cases not homogeneous, but for example a mountain range with features, this relation can only be taken as a general rule and the muon spectrum and flux should be measured independently for each site. It steeply decreases as expected, however at ≈ 14 km.w.e. the curve becomes flat which is due to neutrino-induced muons. Neutrinos can produce muons via the CC reaction $\nu_\mu + u \rightarrow d + \mu^+$ and since the earth provides little to no shielding for neutrinos, they can unidirectionally impact the experiment and hence cannot be shielded regardless of depth.

A sufficiently detailed model of the muon production processes in the atmosphere, including the various differential meson production and decay models, their attenuation lengths, slant depth and so on can be found in [Gai90, Gra08, Bug98]. Part of this
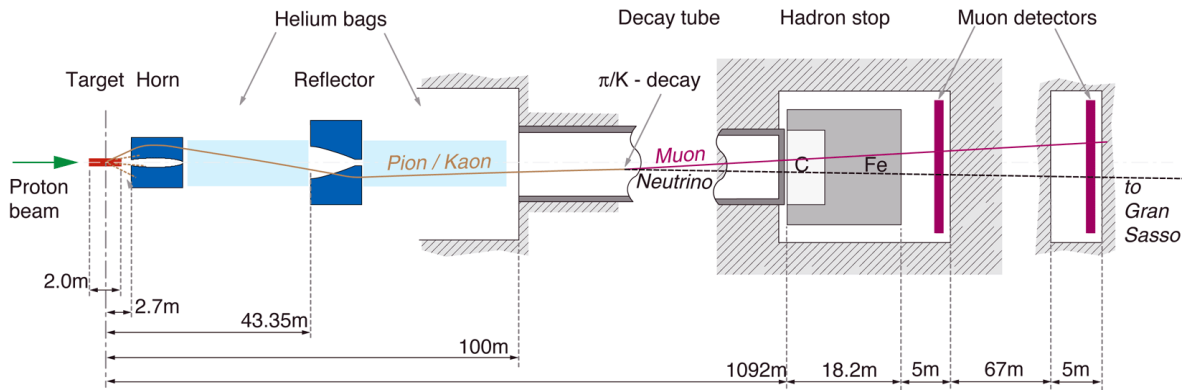
Figure 3.6: *A schematic view of the* Cngs *facility at* Cern *[Gsc13].*

model is important for a natural seasonal modulation of the muon flux and will be explored in Sec. 6.6.

3.2.2 Artificially Produced Muons

Next to the naturally occurring or cosmogenic muons, there is a non-negligible muon source at the LNGS which is man-made. There is a beam line at the Cern called Cngs [CNG13, Gsc13]. This facility aims to project a beam of muon-neutrinos (ν_μ) to the LNGS in order to observe oscillations to tau-neutrinos (ν_τ). At the LNGS, several detectors mainly Icarus and Oscillation Project with Emulsion-tRacking Apparatus (Opera) aim to see the neutrinos and their oscillations by characteristic signatures of the secondary particles produced in these reactions. So far the Opera-experiment has published the appearance of two of these events [Aga13a] and reported a third event on their website [OPE13]. The same experiment measured the Time-of-Flight (TOF) of the neutrino candidates and reported a faster-than-light anomaly in the speed of neutrinos. This anomaly was later corrected as several smaller errors were found in the experimental set-up which led to a distorted measurement [Ada12]. Unfortunately, the first report was blown out of proportion in the media, despite the fact that the authors "deliberately do not attempt any theoretical or phenomenological interpretation of the results" [Ada11]. Many newspaper reported prematurely about faster-than-light particles and completely ignored the entirety of Opera's physics goals despite the already published ν_τ-appearance.

The general set-up of the Cngs experiment is shown in Fig. 3.6. A proton beam with an energy of 400 GeV/c^2 is extracted from the Super Proton Synchrotron (SPS), which serves currently as the final pre-accelerator for the LHC. After extraction, the proton beam is sent along a slanted pipe with a slope of $\approx 3.5°$ in order to accommodate for the earth's curvature between the two facilities. The protons collide with a graphite target producing pions and kaons, similarly to the effects in the atmosphere (see section 3.2). Two energy-selecting and focussing lenses (called "horn" and "reflector") guide the positively charged mesons to an ≈ 1 km long decay tube pointing towards the LNGS. Here, both mesons decay to μ^+ and ν_μ. At the end of the decay line, a hadron stop absorbs any particles that have not decayed yet. Two systems of ionisation chambers serve as detectors for the produced muons and thus as an indication of the neutrino

beam intensity. In addition a detector system in the extraction line measures the proton beam intensity. While the earth's crust serves as a beam stop for the muons, the neutrinos may pass almost unhindered to the LNGS. The produced muons are beamed in forward direction, however the distance to the LNGS of ≈ 732 km causes the beam to open up to a diameter of about 1 km.

The CNGS facility has been in operation from 2006 to 2012, with a maximum beam intensity in 2011 which is measured in Protons-On-Target (POT). At the moment the LHC is shut down and being upgraded, afterwards the CNGS will not restart. During its operation it delivered $\approx 4 \times 10^{19}$POT/ yr in beam intensity. Each extraction from the SPS consists of two proton bunches which are 10.5 µs wide and 50 ms apart. These bunches delivered 1.8×10^{13}POT on average. The extraction time and beam structure was occasionally varied in order to provide the experiments at the LNGS with a clearer time structure. All detectors at the CNGS are equipped with Global Positioning System (GPS) timing systems in order to provide precise time information.

There are about one order of magnitude more pions produced than kaons, which leads to a neutrino spectrum consisting of a large low energy component from the pions and a smaller high-energy component from the kaons. The two reflectors accommodate this feature and achieve a ν_μ-beam with a mean energy of $\langle E_{\nu_\mu} \rangle = 30$ GeV [Els98].

However, the produced ν_μ may also react in the rock close to the halls of the LNGS. Here, the neutrinos may scatter mostly off nuclei and produce particles such as muons according to the CC-reaction:

$$\nu_\mu + u \rightarrow \mu^+ + d. \tag{3.9}$$
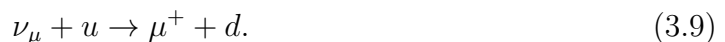
Thus, the neutrino beam creates an additional flux of muons in all halls of the LNGS. The properties of this muon beam has been simulated (see e.g. [Bal01]) and measured by the LVD experiment in the same experimental hall where the GERDA experiment is located [Agl04]. The largest contribution of muons are originating from the "upstream" rock as opposed to interactions happening inside the detector. The CC-reaction probability of the ν_μ as shown in Eq. 3.9 is given as 5.85×10^{-17}CC events/(POT·kt) i.e. depending on the number of pp-collisions at the CNGS and the amount of material in which the reactions are supposed to happen in kilo-tonnes. This leads to a muon flux from upstream rock of ≈ 1.2 muons/(d·m^2) with a mean energy of $\langle E_\mu(\text{CNGS}) \rangle = 17$ GeV. In addition, for a large-volume experiment like LVD the number of events caused by a CC-reaction in the detector volume itself ("internal events") is already a considerable amount of the total CNGS-induced flux. LVD reports ≈ 120 muons/day from external reactions and an additional ≈ 30 muons/day from internal reactions for an experiment of ≈ 2 kt and a surface of 13×11 m^2 [Agl04].

3.3 OTHER BACKGROUND SOURCES

Apart from muons, there are are many other different sources which may interfere with a measurement. As already mentioned, some of these sources are more likely to affect a certain measurement or detector type and are sometimes even entwined.

3.3.1 Spallation Products and Neutrons

A source of background which is closely related to muons is the are spallation products and the generation of free neutrons. Since the muons inherit a large portion of the energy of their cosmic parents, their energy can be sufficiently high (> 100 MeV) in order to shatter a nucleus in a process called "spallation" [Krá10]. This process consists of two steps. First, the projectile (in this case the muon) interacts directly with individual nucleons and shares its kinetic energy via elastic collisions. The excited nucleons can in turn collide with other nucleons of the same nucleus. This is the intra-nuclear cascade, a process which is very fast ($\approx 10^{-22}$ s). With higher energies of the projectile, even other hadronic particles like e.g. pions can be produced. After the interaction with the nucleus comes the de-excitation phase which is much slower ($\approx 10^{-16}$ s). Here, the nucleus loses the accumulated energy by the isotropic evaporation of neutrons or light charged particles like α-particles, deuterium or tritium. What remains is an excited nucleus, which usually emits de-excitation γ-rays and decays via β-decay until a stable state is reached.

This process poses a threat to any low count-rate experiments for two reasons. First, radioactive isotopes are created by un-shieldable radiation. As muons can even penetrate the deepest laboratories which can only be "vetoed" in analysis and not truly discarded, they will create radioactive isotopes, regardless of the radio-cleanliness of the experiment. The β-decays of the spallation products can have high end-point energies Q_β and thus cast a background over an analysis-region which lies below. The same is true for the Compton-spectrum of γ-rays. Second, especially the free neutrons can activate a nucleus via the reaction $(A, Z) + n \rightarrow (A + 1, Z)^*$, i.e. it creates an excited nucleus which is in most cases unstable and will undergo further decay. Depending on the experiment, the neutron component can be even more dangerous than the first, as neutrons are difficult to shield and can easily penetrate even lead and copper shieldings. Neutrons can only be efficiently shielded either by low-mass nuclei like hydrogen which allow a maximum transfer of momentum in collisions or by elements which have a high cross-section towards the caption of neutrons like e.g. boron or cadmium.

As this work is mostly concerned with muons and their background, a further look into the production of cosmogenic isotopes will be given in Sec. 7.3.

3.3.2 Ambient Radioactivity

The predominant background for any spectrometry is the ambient radioactivity that is found naturally in any material. Every material–be it anorganic, organic or living–contains traces of different radioactive isotopes. Living tissue for example contains the isotopes ^{14}C and ^{40}K, which are produced in the atmosphere by nuclear reaction of the cosmic radiation. In addition, nuclear waste from e.g. atomic explosions can contaminate the atmosphere and hence precipitate on the ground. One of the most common background stems however from nuclear decay chains of heavy elements.

Apart from faint traces of light elements like e.g. lithium, all elements are produced during the stellar evolution. During the regular fusion-cycles of a star, only elements up to iron can be produced by the regular stellar fusion processes. Heavier elements are only able to form either in environments of high neutron fluxes, e.g. in the core of intermediately heavy stars or during catastrophic events like supernovae. In these

events, nuclei can be produced which are even beyond the heaviest stable element ^{208}Pb. Most of these elements have half-lives which are small in comparison to cosmic scales, however there are isotopes which decay much slower. Amongst these few isotopes are ^{238}U ($T_{1/2} = 4.47 \times 10^{10}$ yr) and ^{232}Th ($T_{1/2} = 1.40 \times 10^{10}$ yr) [NND14]. Due to the long half-lives, these isotopes are still present in the universe and abundant in e.g. the earth's crust. As they are much heavier than ^{208}Pb, they have to decay via multiple α- and β-decays before they reach a stable isotope. Since some of the daughter-nuclei do not decay immediately as well, any material containing an abundance of mother nuclei will also contain all daughter nuclei in various relative abundances. These decay chains can be found in almost any material originating from the earth's crust especially metals and rock. Some of these contaminants can be removed during production processes as e.g. during the smelting of a metal, however faint traces will be found in most materials.

In addition, the daughter element radon is a noble gas and gaseous at room temperature. It can emanate from any material into the atmosphere and hence contaminate it with α- or β-emitting isotopes depending on the decay chain. As a precaution, experiments are frequently flushed with a gas like nitrogen which displaces the radon-containing air.

The more sensitive an experiment gets, the less studied the potential background sources become. This was the case as well for the GERDA experiment, as a previously unknown amount of radioactive ^{42}Ar was found in the argon used for the shielding [GSTR12-04]. In concentrations much higher than the measured it would have posed a problem, but it shows that the most sensitive detectors can face entirely unexpected issues.

3.3.3 DETECTOR RESOLUTION

Each detector has a resolution, i.e. the ability to discern between events of different energies. As already mentioned, the resolution of germanium detectors is in the range of few permil Full Width at Half-Maximum (FWHM) while the resolution of e.g. scintillators may rise to values of 10% FWHM depending on the material, temperature and energy. The resolution can now introduce a background if there are multiple peaks in the observed region. Due to a poor resolution, events from two close peaks may more easily overlap, so that the treatment of one peak is affected by the statistical error of both peaks. In the case of a low count-rate experiment this effect can prove fatal. In order to circumvent this, it has to be assured that either the detector has a very good resolution or that the desired effect has no adjacent spectral lines. This makes scintillators still a viable option for the $0\nu\beta\beta$ experiments as there are many potential $0\nu\beta\beta$ isotopes with a $Q_{\beta\beta}$ value above the highest naturally occuring γ-line. If the $Q_{\beta\beta}$ value is below this, a good resolution is necessary so that no peak is accidentally identified as the signal peak of the $0\nu\beta\beta$ decay.

<div align="right">

CHAPTER 4

</div>

THE GERDA EXPERIMENT

In this chapter, the GERDA experiment at the LNGS will be introduced, especially the utilized High-Purity Germanium detectors (HPGes) and Broad-Energy Germanium detectors (BEGes). The measuring principle, hardware components and data analysis tools will be explained. Of special interest to this work is the observed Background Index (BI) which is conventionally given in cts/(keV·kg·yr), i.e. the number of background events per mass of target material, time and size of the Region of Interest (ROI) in the energy spectrum. The background model applied to the data will be introduced here but its muonic component will be covered in great detail in the following chapters. GERDA was proposed in 2004 [Abt04], funded and after nearly 7 years of preparation and measurement has recently published its first results [Ack13, Ago13a, Ago13b, Ago13c, Ago14]. This ended the Phase I of operation for GERDA. Phase II is planned to start in the middle of 2014 with additional detector material and upgraded hardware. The major upgrade here is not only the additional detector mass, but also the holder structure, cabling etc. needed for accommodating more than twice the amount of detectors. Phase III is a long-term project to perform a joint-venture experiment with the MAJORANA collaboration with an overall detector mass of ≈1 ton. This chapter will summarize experiment and results based on the aforementioned literature.

4.1 THE GERMANIUM DETECTOR ARRAY

Many experiments with low rates in astro- and particle physics use a by now almost standardized method of shielding. The shielding effect of materials versus γ-radiation is the sum of several different effects. Photo-electric absorption rules the low-energy (<0.5 MeV), Compton scattering the mid-energy (≈1 MeV) and pair-production the high-energy regime (>2 MeV). Both photo-effect and pair production depend on the atomic (or proton) number Z of a material and thus a material with high Z shields more efficiently. Lead has a rather high Z-value and thus, γ-rays, i.e. the predominant background radiation, have a small radiation length. In addition, lead is easily available and affordable. On the other hand, due to its high Z value it is a good target for cosmogenically produced neutrons which can activate a nucleus, i.e. turn it into a radioactive isotope. Copper is available and affordable as well but has a lower Z,
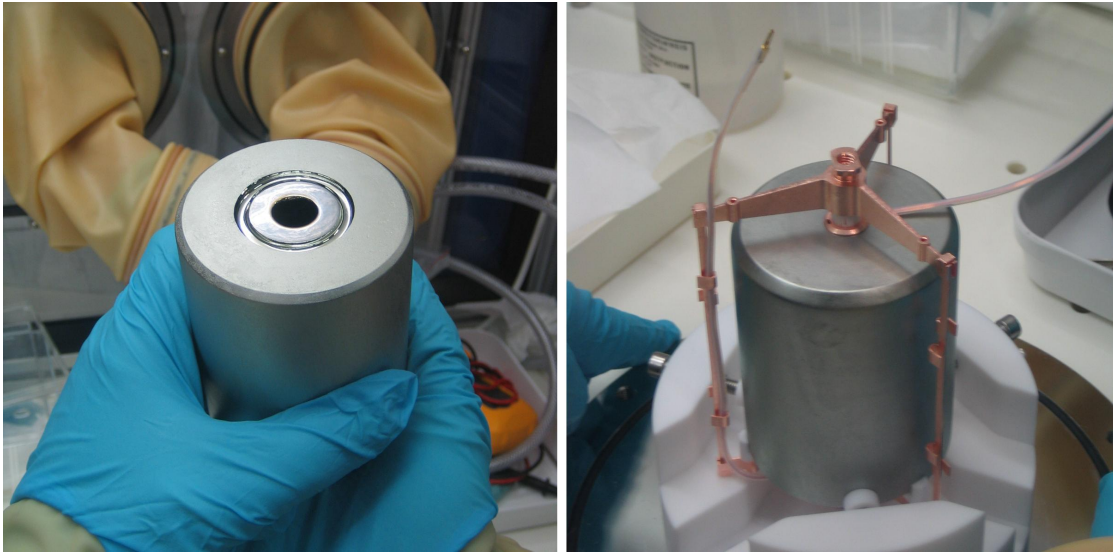
Figure 4.1: *Pictures of a HPGe detector. Left: the bare detector after refurbishing. Right: the same detector mounted upside-down in a low-mass holder.*

making it a worse shielding option. However, copper can be produced electrolytically, which means that it is extremely clean and thus void of potentially radioactive contaminants. A "standard" shielding consists of layers of copper and lead in different degrees of (radio-)purity, as thick and as pure as one is willing to afford or able to obtain. In addition, sheets of plastic like polyethylene can be inserted into the shielding as well. Plastic consists mostly of atomic hydrogen and is thus a good target in order to moderate neutrons. The neutrons are of the same mass as the atomic hydrogen and thus the transferred energy in a collision is maximal. Exemplary experiments using such a kind of shielding are Cresst [Ang09] or HdM [KK04].

The Gerda experiment pursues a different approach to its shielding. It follows the the idea of using low-Z materials for shielding like water and a cryo-liquid like Liquid Nitrogen (LN2) or Liquid Argon (LAr) in which the detectors are submerged [Heu95]. Even the germanium detectors, which are usually encased in aluminium housings are operated "naked" in the cryogenic liquid. The Genius test facility was the first to follow this idea, but with LN2 instead of LAr as in Gerda [Hel97]. The LAr serves not only as a shield but also as a cooling medium for the detectors as its boiling point is at 87.15 K. The Z-value of these materials is much lower than that of lead and copper and thus lowers the potential to be cosmogenically activated. The water is a good shield against neutrons and the LAr provides protection against γ-rays by sheer volume.

Apart from this innovative shielding design, Gerda tries to measure the $0\nu\beta\beta$ in the isotope ^{76}Ge which can potentially undergo the $0\nu\beta\beta$ decay. Germanium detectors are extremely suited to measure the two electrons emitted from any kind of $\beta\beta$ decay due to their excellent resolution and high efficiency. The candidate $0\nu\beta\beta$-isotope in germanium has a natural abundance of $f_{76} = 7.8\%$. By enriching germanium in the potential $0\nu\beta\beta$-isotope (abundances of $f_{76} = 86\%$ and even higher are possible) and manufacturing germanium diodes out of the enriched material, a method of measuring the $\beta\beta$ decay is obtained. As already introduced in Ch. 2, germanium is a reliable choice for this search. The endpoint energy of the $2\nu\beta\beta$ at $Q_{\beta\beta} = 2039$ keV is lower

than a lot of naturally occuring γ-lines and due to a maximum size of the diodes this technique does not scale as well as e.g. experiments which are using liquids. However, the operation and crystal growing of germanium is well-studied and the $0\nu\beta\beta$ search with ^{76}Ge has a very successful history with the HdM [KK04] and Igex experiments [Aal99]. In addition, germanium detectors have an excellent energy resolution of a few permil, depending on the energy range, which allows very precise energy and thus peak identification. In addition, germanium detectors allow the use of powerful Pulse-Shape Discrimination (PSD) methods. These can be used to further reduce the background by studying the trace of each event in search of mutiple energy depositions which are caused by other processes than a $0\nu\beta\beta$ decay. These properties make germanium detectors a very valid choice for this kind of research. The name of Gerda stands for **Ger**manium **D**etector **A**rray, since a multitude of these detectors is operated simultaneously.

4.2 Germanium Detectors

All HPGe germanium detectors that were used in Phase I of Gerda were refurbished detectors from the HdM and the Igex experiments. These detectors are standard coaxial HPGe. Characteristically, this type of detector is a single diode with a bore-hole over almost the entire length of the detector. The two electrodes are the n$^+$ lithium doped mantle of the detector and the p$^+$ boron doped bore-hole. The electrodes are separated by a groove close to the bore-hole. The detector is read out on the p$^+$ electrode via a charge amplifier and the diode is biased with up to +4600 V on the n$^+$ electrode.

Germanium detectors are usually operated encapsulated in an aluminium casing with optional entrance windows. The detectors in Gerda however are operated "bare" within LAr, a cryogenic liquid. This warranted extensive tests prior to submersing the detectors in Gerda . It was e.g. found, that γ-rays can ionize the argon, which in return caused the ions to stick to the electrodes of the detector. This caused an undesired leakage current between the electrodes. This was increasing in time, as the ions accumulated. By removing a layer of passivation on the detector, this leakage current could be almost entirely suppressed. The long-term stability of this mode of operation was successfully demonstrated.

The detectors used were ANG 1-5 from HdM and RG 1-3 from Igex. A picture of two of these detectors can be seen in Fig. 4.1. These detectors have a diameter of 60-80 mm, a height of 70-110 mm and weigh 0.6-3 kg with an enrichment of $f_{76} = 85.5 - 88.3\%$. The mass of all detectors sums up to 17.7 kg. In order to keep the amount of cosmogenically activated iotopes as low as possible, the detectors were always stored in underground facilities where the muon flux is severely dimished. Even during the refurbishment procedure, the detectors were stored in an underground facility close to the manufacturer.

Due to the rigid demands in regards to radioactive contaminations and thus the background, the holder structure of the detectors needs to be sturdy but as light as possible. In addition, each detector has to be electrically well isolated. The support structure itself consists for e.g. detector RG 3 of select radio-pure copper (80 g), PTFE (10 g) and silicon (1 g). The holder structure causes a BI of $\leq 10^{-3}$ cts/(keV·kg·yr).

For Phase II of Gerda 37.5 kg of ^{enr}Ge was procured by Electrochemical Plant (ECP) in Zhelengorsk, Russia. The enrichment material was produced from GeF_4 gas with the standard method of centrifugal separation. After testing the enriched and depleted raw material, it was transported to PPM Pure Metal GmbH, Germany. Here, the germanium in form of GeO_2 was processed to metallic germanium and purified to a purity of 6N[†]. From Germany, the remaining enriched material was shipped to Canberra, United States of America where the material was purified to 11N and where the crystals were pulled. 30 crystal slices were produced and shipped again to Canberra, Belgium, where the slices were manufactured into BEGe.

After the production, all detectors have been thoroughly tested. Their ability to operate bare in LAr was shown in Ref. [Bar10]. A sketch of the different detector geometries can be seen in Fig. 4.2. As can be seen, the BEGe detectors are much smaller and possess only a very small read-out electrode in comparison to the coaxial HPGe detector which means that in order to have the same mass, more detectors and hence cables and read-out channels are necessary.

Figure 4.2: *Schematic drawing of HPGe (top) and BEGe (bottom) detectors*

sary. On the other hand, the BEGe detector show an excellent energy resolution of 1.7 keV FWHM@1.3 MeV even in the first tests. In addition this type of detector allows an mode powerful event-discrimination based on the shape of the pulse in comparison to the HPGe. This will be discussed in Sec. 4.5.

4.3 Hardware

Due to the lower shielding effect of water and LAr in comparison to lead and copper, an increase in the overall dimensions is needed in comparison to its predecessors. A sketch of the Gerda experiment can be seen in Fig. 4.3 which shows the main hardware features. The germanium detectors (see the following section) are submersed in a cryostat which contains 64 m^3 of LAr. The cryostat consists of two coaxial vessels of 4 m in height and width which rests on a metal "skirt". A system of cylindrical pipes, bellows and plastic fabrics open the cryostat to the top and allow for thermal shrinkage of the inner vessel when it is filled with LAr. The gap between the vessels is evacuated for a thermal decoupling of the interior of the cryostat and the outside. A heat exchanger prevents the LAr from boiling. This could cause microphonic noise and a loss of argon from the tank. However, due to this and a number of other safety precautions, no LAr had to be replenished since the cryostat was first filled.

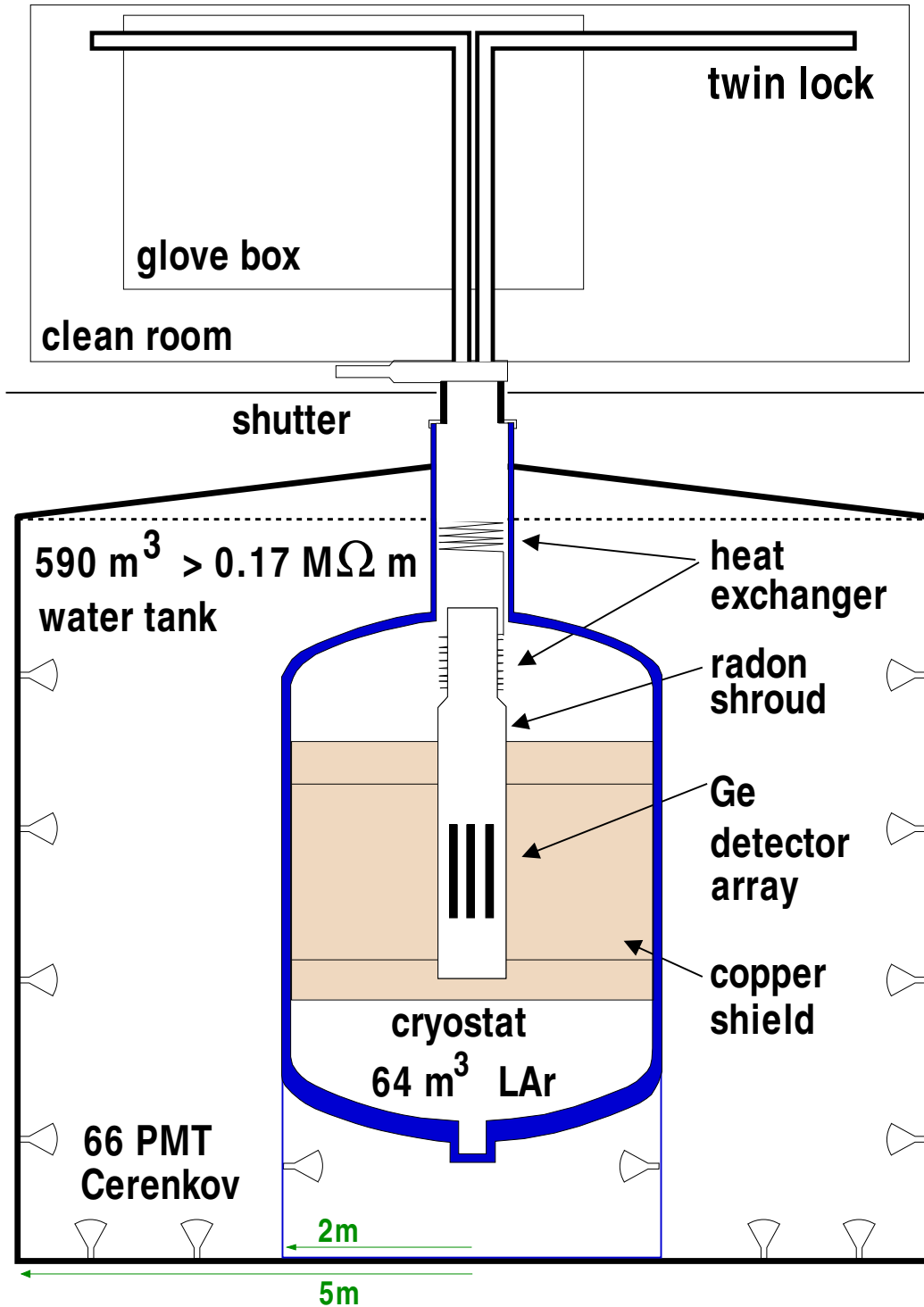[†]A purity of xN means that there is one impurity in 10^x atoms

Figure 4.3: *The main hardware components of the* GERDA *experiment.*

The cryostat is made of stainless steel. At first, a copper version was proposed as copper can be manufactured extremely pure. However, it was not clear if a cryostat as large would have been able to fulfil the security benchmarks or be affordable. Thus, a steel with a low activity was procured for the cryostat. As a compromise to the copper cryostat and to shield from the radioactivity from the steel the cryostat is lined with radio-pure copper sheets at the respective height of the germanium detectors. However radioactive radon may still emanate from the steel walls and be transported close to the germanium detectors. In order to prevent this, a 30 μm thick copper cylinder with a height of 3 m and a diameter of 0.75 m was installed around the central volume of the cryostat. It is called radon shroud and should prevent the transportation of radon to the detectors via thermal convection. After iterated cleaning of the cryostat the final BI contribution of the cryostat was estimated to be $\approx 7\times 10^{-4}$ cts/(keV·kg·yr).

The cryostat has a "neck" on top which connects it to the clean room on top of the set-up. The neck is the only access to the cryostat and all items including detectors and cables are fed through it. The neck can be separated from the clean room with a shutter. Inside the clean room, there is a lock system which provides the ability to lower two different sets of strings with detectors into the cryostat. The lock system is surrounded by a glove box inside the clean room. Here the detector strings can be assembled and connected to the pulley system inside the lock and afterwards lowered into the cryostat.

As an additional means of shielding the cryostat is surrounded by a solid steel cylinder of 5 m diameter and a height of 8.3 m. The conical roof extends to 8.9 m. This cylinder is filled with 590 t of ultra-pure water from the Borexino plant, which is able to produce water with close to 0.18 MΩ m. This water tank serves a number of purposes. Water is a neutron absorber which can shield the experiment from neutrons produced outside of the experiment. Despite its low Z value such an amount of water can even attenuate γ-rays rather well. In addition, traversing muons will emit Cherenkov light inside the water. For this reason the water tank is instrumented with 66 PMT in order to record this light as an active muon veto. The performance of this muon veto is the central point of this work.

At ground level the water tank can be accessed by a 1400×800 mm^2 manhole. On the conical top there is a central hole for the neck of the cryostat and two flanges on top for additional access and the cables of the muon veto. Apart from that, the water tank has a number of smaller flanges for water drainage, purification, temperature gauges, security pressure valves etc. The water is constantly circulated by a water plant, which removes pollutants such as radioactive particles like uranium and its decay products or organic carbon, which could deteriorate the optical properties of the water.

The water tank is surrounded by a super-structure, which supports two necessary buildings of Gerda . There are three stories between Gerda and the Lvd experiment next to it. These rooms contain the water plant, radon monitors, control rooms for both Gerda and Lvd, cryogenic infrastructure for the cryostat, the safety valves and the electronics for the muon veto. The building on top of the experiment is the above mentioned clean room. In addition to the lock, pulley and glove-box systems needed to submerge the germanium detectors, the clean room also houses the calibration system. By means of other pulley systems, three ^{228}Th sources can be lowered into the vicinity of the germanium detectors inside the cryostat. By recording the radioactive emissions of three well-known sources, the detector performance can be frequently checked.

Electronic drifts or detector degradations can be easily identified and corrected. The detectors are calibrated (bi-)weekly.

4.4 Monte-Carlo Studies

Prior to the construction of the main parts of the experiment, the apparatus of Gerda was simulated with the Geometry and Tracking Toolkit (Geant4) [Ago03]. This is a `C++`-based simulation package using Monte-Carlo algorithms. Here, randomized numbers are used to simulate the steps a particle and its produced secondaries take in an user-defined experimental geometry. The incident particles originate from a parametrizable `particleGun`. For the physical interactions, a number of pre-defined libraries called `physicsList` is used to determine the interactions and processes the particle is allowed to undergo. These lists can be expanded and or shortened, depending if a more complicated physical model is needed or if computing power is scarce. Geant4 is widely used in nuclear and particle physics; a great number of experiment uses this package as a simulation tool, the most prominent being the LHC.
For the Gerda and Majorana experiments, the Geant4-based Majorana and Gerda Simulation Framework (MaGe) was developed [Bau06]. In this framework, a number of standardized `physicsLists`, geometries, `particleGuns` etc. are available. Multiple set-ups for the germanium detectors are available, as well as the instrumented water tank and a muon generator which provides muons according to the measured muon angular distribution and energy. These provided settings can be used, modified and expanded upon. Geant4 was chosen as this toolkit provides not only a wide range of physics processes such as muon spallation, scintillation, isotope production or Cherenkov radiation. It also provides standard outputs of data and visualisation. MaGe was successfully used to simulate the experiment from pulse-shape details in the germanium detectors up to the cosmogenic background [Pan07], which is of particular interest to this thesis.

4.5 Data Stream and Analysis

The germanium detectors in Gerda are read out with custom made charge sensitive pre-amplifiers. These contain—amongst others—an input transistor for amplification and an operational amplifier, both of which enhance the signal of the detector. The entire pre-amplifier is operated close to the detectors submerged in LAr, which puts limits on the radioactivity of the components as well as on the functionality under cryogenic temperatures. The signal and high-voltage cables are fed through custom feed-troughs and the signals are recorded by 14 bit, 100 Msample/s Flash Analog-to-Digital Converters (FADCs). For each event and detector, a trace of 160 μs is recorded. The signal usually consists of a rise in the order of 1 μs depending on the detector and the signal followed by an exponentially decaying tail. The energy of the event is reconstructed off-line.
The main reason for utilizing the aforementioned BEGe detectors is the enhanced ability to discriminate different types of physical interaction in the detectors according to the shape of the signal. The $0\nu\beta\beta$ will emit two electrons which thermalize immedi-
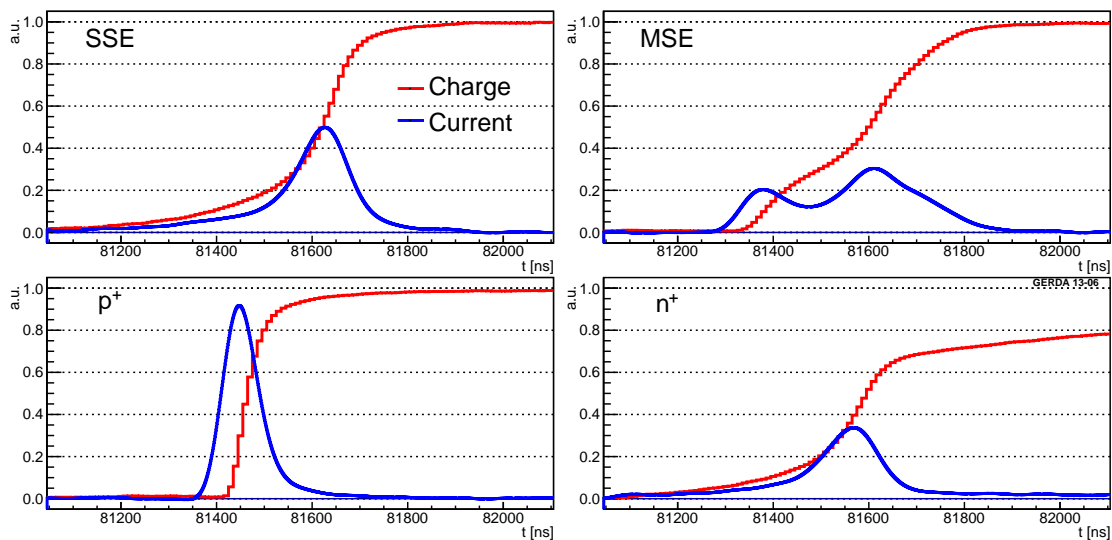
Figure 4.4: *Basic principle of pulse shape discrimination. Different types of event leave a characteristic signature in the charge signal (red) compared with its derivative, the current signal (blue).*

ately inside the detector. This is commonly called a Single-Site Event (SSE), since the entire energy is deposited within a very small volume. A γ-ray can for example deposit energy multiple times in the detector via Compton scattering. Muons at the LNGS have very high energies and can deposit energy along their path multiple time, too. These events are called Multi-Site Event (MSE). By studying the shapes of the signals, SSE and MSE can be told apart. This method is called Pulse-Shape Discrimination (PSD).

The signal recorded by the DAQ is the recorded charge (E) deposited in the detector. Its derivative is the current (A). The maximum of the charge signal (the total charge) can now be compared to the maximum of the current signal in form of the quotient A/E. While the collected charge of a SSE and a MSE can be similar, the current signal can be very different in MSEs. The reason for this is that drift velocities are proportional to the field in the detector. When multiple energy depositions happen in volumes of different fields, the different charge carrier clouds will have different drift times, i.e. they arrive at different times. This is schematically shown in Fig. 4.4. The MSE has two depositions at the same time, which are recorded due to drift times with a time difference of about 300 ns. In comparison to the large contact coaxial germanium detectors, the BEGe detectors have a point-like contact on one side. This makes the field gradient inside the detector much more inhomogeneous. Thus, MSEs can be discriminated much better as in the coaxial case where the field is more homogeneous. The efficiency of this cut can be determined when calibrating with a ^{228}Th source. The survival probability for the full-energy peak–a MSE–is only 0.22 while the double-escape peak[†]–a SSE– has a surviving fraction of 0.93.

Not only MSE and SSE can be told apart using this method. Particles depositing their energy close to the surface the p^+ readout electrode rise very sharply. Since the grove of the BEGe detectors is not covered and this type of detector is not passivated, e.g.

[†]A high-energy γ-ray which causes pair production and both annihilation photons of the positron leave the detector.

α-particles emanating from the ambient cryo-liquid can directly deposit their energy here. On the other hand, events that deposit energy in the dead layer between the n$^+$ surface electrode can still drift charge carriers into the detector. This type of signal is caused by e.g. β-particles penetrating the surface electrode. The signal is hence a lot slower and produces a lower A/E ratio.

The data analysis is performed with a custom made software called Gelatio (see Refs. [Ago11, Ago12]). It is based on `C++` and incorporates a number of libraries including CLHEP‡ and FFTW§ for scientific computing. The concept of this tool is to allow a multi-tier data structure with modular signal processing and analysis depending on the data stream and the aim of the analysis. Different input streams from e.g. germanium, PMT or simulation data can be converted into a common format on which customizable modules can be run. The same data analysis tools are available for the entire collaboration independent of the focus in order to assure comparable results.

The first step in the analysis chain is a decoder, which translates the data in a format based on Root and encapsulated in custom data containers called Majorana-Gerda Data Objects (MGDO). The raw data and the "rootified" data are commonly known as Tier 0 and Tier 1 of the analysis chain. The next Tiers of data can be obtained by running modular algorithms for e.g. baseline restoration, trigger identification, rise time calculation or energy reconstruction. In case of the germanium detectors the energy is reconstructed by using a moving differentiation filter on the trace and subsequently integrating the pulse until a Gaussian shape is reached the height of which corresponds to an uncalibrated energy. The next Tier for germanium data would contain the reconstructed energies using calibration runs where the detectors were irradiated with known sources. Afterwards, quality cut parameters can be introduced like e.g. given by the PSD method above. This way, un-physical events can later be discarded in the analysis. Additionally, a neural network based on TMVA¶ were applied to perform a cut on the shape of the trace, similar to the PSD method. By providing well-known SSE and MSE traces from calibration data, a network could be trained which can distinguish both types of events. This method yields similar results as the PSD a SSE survival rate of $0.90^{+0.05}_{-0.09}$ and a rejection of 45% of all other events. This was applied to the coaxial data.

In Phase I of Gerda the germanium data were blinded. By using an energy estimate of the DAQ system, an automated system generated Tier 1 files which did not contain the energy region of (2039 ± 20) keV. The raw data is kept on disk and on backup at the LNGS and in Heidelberg. The blinded data could now be used to define the treatment of the background prior to unblinding. This means that for example pulse-shape cuts for valid events were determined before the entire spectrum containing $Q_{\beta\beta}$, i.e. the ROI were made public. This method aims to keep experimental bias as low as possible. The values and spectra obtained from the last analysis modules can now be used to study the contribution by all possible background sources. This includes also possible shifts and drifts in the electronic configuration. Due to long measuring times, electric potentials may shift over times for various reasons which can be seen in the data as well. The background in the experiment will be introduced in the next section. The data analysis tool for the muon veto will be discussed in Sec. 5.4.

---

‡Project homepage: http://proj-clhep.web.cern.ch/proj-clhep/
§Project homepage: http://www.fftw.org/
¶Toolkit for Multi Variate Analysis, project homepage: http://tmva.sourceforge.net/

4.6   Background Data

The most important factor of an experiment measuring a rare event is its ability to discriminate against background events. As already mentioned in previous chapters, this can either be done by choosing a method which is not susceptible to certain types of background or by reducing the background as low as possible. An example for the first method would be to chose a $0\nu\beta\beta$ isotope with a $Q_{\beta\beta}$-value above 2.61 MeV like e.g. ^{115}Nd (see Tab. 2.1), as this energy corresponds to the γ-line of ^{208}Tl which is the highest naturally occurring one. A clean environment is achieved by using carefully selected materials for the construction of the experiment which have been screened for radioactive contaminants (see e.g. [Man08]), the use of a clean room for detector handling or flushing of the experiment with nitrogen to prevent the collection of radon gas.

As the experiment is searching for a mono-energetic line at 2.039 MeV, all other physical signals can be considered background. Un-physical signals are e.g. test-pulses or muons which deposit enough energy for an overflow. The blinded spectrum, i.e. without a ± 20 keV window around $Q_{\beta\beta}$ was used to determine the background sources and compare it to the expected background from screening results. This model is hence used to extrapolate the background in the blinded ROI. The background and the model can be seen in Fig. 4.5 for a spectrum from 600 keV up to 3.6 MeV. The data set used for this background is the "golden-coax" set. This is data taken with the coaxial germanium detectors with an exception of 30 days after the first BEGe detectors were deployed. This caused a spike in the background, which took about 30 days to reach the previous level of background. The strongest contribution is the $2\nu\beta\beta$ decay of ^{76}Ge which is of course to be expected and it is a magnitude higher than all other background sources combined. The $2\nu\beta\beta$ contribution in the HdM experiment was of the same magnitude as all other backgrounds in this energy range [KK01], which speaks for the enhanced purity obtained in Gerda. The background include other well-known sources of background like nuclei from the thorium decay chain (i.e. ^{228}Ac, ^{228}Th), radium decay chain (^{214}Po, ^{214}Bi) and ^{60}Co. An unexpectedly high background was the contribution by the argon isotope ^{42}Ar. While this isotope undergoes β decay with a low Q_β value of 599 keV, its daughter nuclei ^{42}K and ^{42}Ca show a γ-line at 1.525 MeV and a β with $Q_\beta = 3.53$ MeV. In order to reduce this background contribution, the germanium detectors are deployed inside thin, miniature shrouds made of ultra-pure copper. These mini-shrouds prevent convection around the detectors and an electric field between the detectors and the mini-shroud drifts the ^{42}K ions away from the detectors. In addition, there are small contaminations of the isotopes ^{226}Ra, ^{222}Rn and ^{210}Po which are α-sources, which contribute mainly in the higher energy regions around 5 MeV. Due to their low specific range, the α-spectra take the form of a reverse exponential with a tail towards lower energies, which is the main background above 3 MeV. The overall model was fit to the data and the model fits within reasonable statistical fluctuations to the data.

The spectrum around the ROI was analysed in a similar way using a much higher resolution of the energy spectrum. In the region from 1.93-2.19 MeV, the contributions of the model were fit to the data and then extrapolated to the blinded region. This yielded the expected amount of background for the data on $0\nu\beta\beta$. The interpolated BI is $(1.1 \pm 0.2)\times 10^{-2}$ cts/(keV·kg·yr) for the coaxial and $(0.5^{+0.4}_{-0.3})\times 10^{-2}$ cts/(keV·kg·yr)
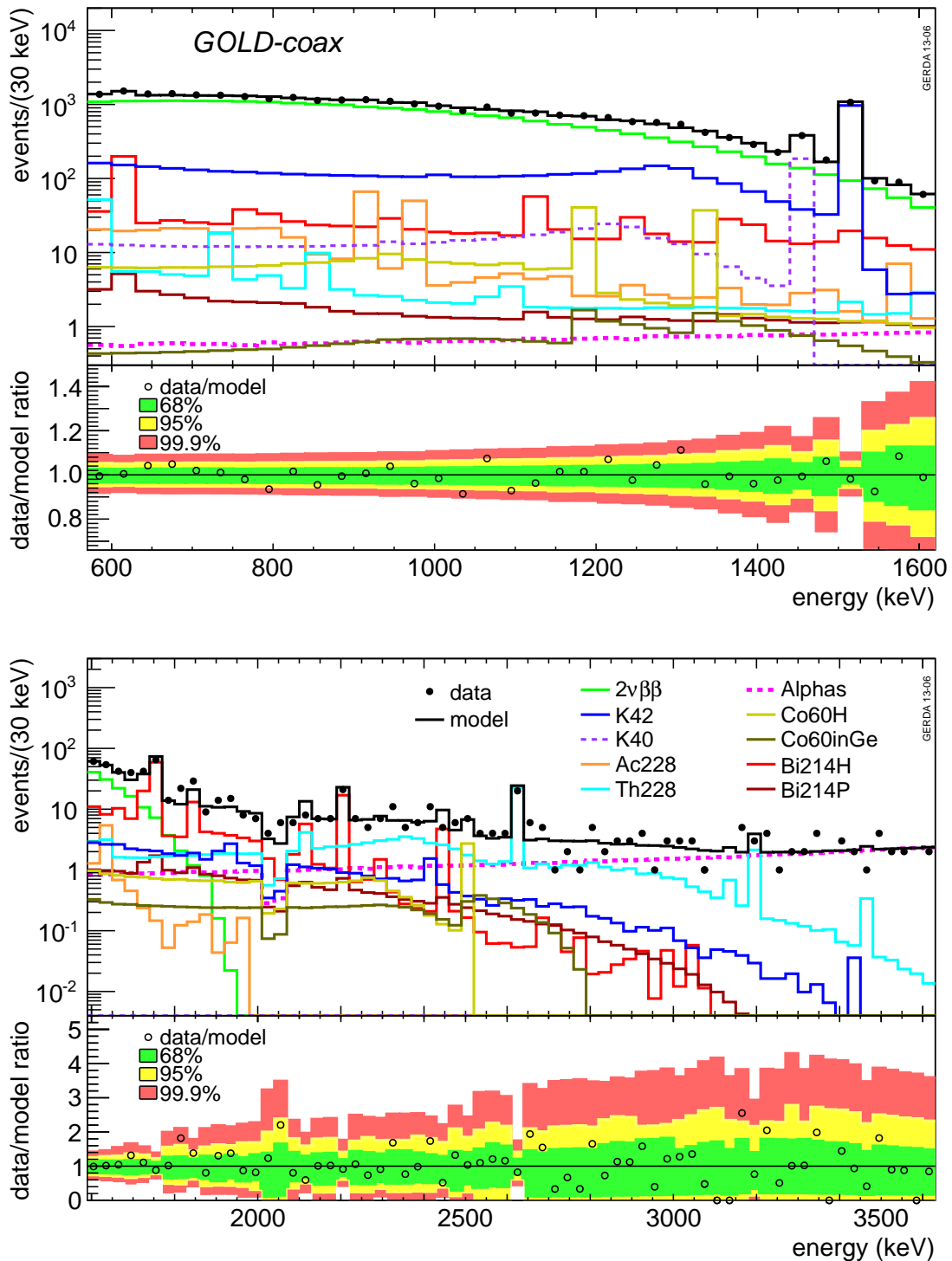
Figure 4.5: *Background composition fit to the GERDA golden-coax data set. On the top, the different background contributions are shown. On the bottom, the deviation of the data from the model is shown.*

for the BEGe detectors after PSD. The resolution of the germanium detectors was found to be 4.8 keV FWHM for the HPGe and 3.2 keV FWHM for the BEGe in the ROI. The half-life of the $2\nu\beta\beta$ decay was derived with great accuracy and a value of $T_{1/2}^{2\nu}(^{76}\text{Ge}) = (1.84_{-0.08}^{+0.09}) \times 10^{21}$ yr.

4.7 Data on $0\nu\beta\beta$

With the constraints given by the background model, the efficiencies of the pulse-shape cuts and the inherent efficiencies of the germanium detectors well known, the data was unblinded and the data analysed. The half-life of the $0\nu\beta\beta$ was calculated using:

$$T_{1/2}^{0\nu} = \frac{(\ln 2) N_A}{m_{\text{enr}} N^{0\nu}} \mathcal{E} \varepsilon$$
$$\varepsilon = f_{76} f_{av} \epsilon_{\text{FEP}} \epsilon_{\text{PSD}}$$

(4.1)

where N_A is Avogadro's Number, $\mathcal{E}$ the total exposure, $m_{\text{enr}} = 75.6$ g the molar mass of the enriched material and finally $N^{0\nu}$ the signal strength or an upper limit. The factor ε is an overall efficiency factor containing the fraction of ^{76}Ge atoms in the material f_{76}, the fraction of active volume f_{av}, the acceptance factor by the PSD methods ϵ_{PSD} and the survival probability of a full-energy peak ϵ_{FEP}. Mechanisms that lead to peak with not the full energy include Bremsstrahlung or X-rays escaping the germanium detector. These effect were simulated and a factor of $\epsilon_{\text{FEP}} = 0.92(0.90)$ was found for the coaxial (BEGe) detectors.

After the unblinding, seven events in total were found in the signal region, i.e. (2039 ± 5) keV with an expectation of a background of 5 ± 0.5 counts. Six of these events were found in the coaxial data, one in the BEGe data. Of the six coaxial events, three were classified as SSE and hence accepted. The only event in the BEGe data was rejected by the PSD cut. The remaining data was fit using a binned maximum likelihood approach to determine the signal strength or an upper limit. The best fit for the data was with a value of $N^{0\nu} = 0$, i.e. a flat background with no excess $0\nu\beta\beta$ events. The fit gives a limit of the half-life of

$$T_{1/2}^{0\nu} > 2.1 \times 10^{25} \text{ yr } (90\% \text{ C.L.})$$

(4.2)

which includes systematic uncertainties. Thus, the data show no indication of a peak at $Q_{\beta\beta}$ and the claim for a $0\nu\beta\beta$ decay is not supported. The model of the claim (H_1) can now statistically be compared with the three experimental events none of which are within $\pm 1\sigma$ of the fit i.e. a background-only model (H_0). The Bayes factor gives the ratio of the probabilities of the two models in this case $P(H_1)/P(H_0) = 0.024$. If the Gerda data are combined with the Igex and HdM data (the limits of which are fully consistent with this Gerda result), the Bayes factor drops to 2×10^{-4}, i.e. the claim is even stronger disfavoured. In Fig. 4.6, the combined spectrum of all $^{\text{enr}}\text{Ge}$ detectors are shown. The derived limit and the claim are shown in blue and red respectively. A larger fraction of the spectrum shows no unexpected peaks in the analysis window used for background interpolation.

As there are a number of other experiments searching for $0\nu\beta\beta$, the results can be compared. However, any non ^{76}Ge-experiment can only be compared to this result when
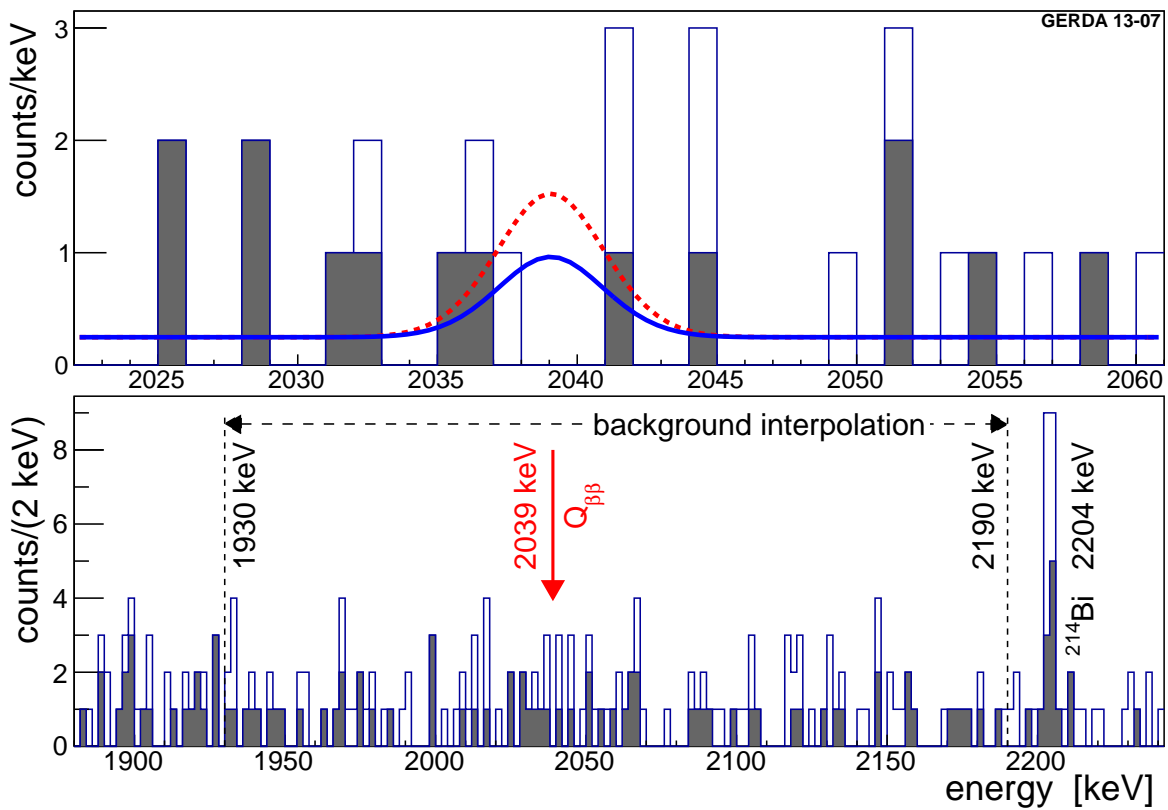
Figure 4.6: *The combined energy spectrum of all ^{enr}Ge detectors is shown without (all) and with (grey) PSD. On the top, the region of interest around $Q_{\beta\beta}$ is shown with the 90% upper limit derived from the data (blue line) and the central value from [KK04] (red dashes). On the bottom, the region for background interpolation is shown.*

it is assumed that the $0\nu\beta\beta$ works via exchange of light Majorana neutrinos. Even in this case, the different nuclei demand a comparison of the calculated NME for the respective nuclei. As the ^{136}Xe experiments (KamLAND-Zen [Gan13] and EXO-200 [Aug12]) are currently the most advanced in terms of data taking their data can be compared to the germanium data given that the same $0\nu\beta\beta$ process is taking place in both isotopes. Both experiment do not show any hint of the $0\nu\beta\beta$ so far and have given limits. When the most conservative NME is picked for comparison of the two isotopes, the combined model excludes the claim with a Bayes factor of 0.0022. This means that so far the claim is strongly disfavoured.

4.8 THE FUTURE OF GERDA

GERDA is currently preparing for its second phase, in which the already unprecedented background is aimed to be lowered by another order of magnitude. The LAr will be instrumented with a hybrid PMT/SiPM veto, which will further enhance the vetoing capabilities especially from reaction in the LAr or around the germanium array. Several rare radioactive decays may cause a background in the detector, which originate from the LAr. With the LAr instrumentation, events like these can be tagged and identified. In addition, with the combined power of muon- and LAr-veto, cosmogenically produced isotopes can be identified.

The PSD methods will be refined and the detector response will be studied in much greater detail. Especially the handling of the relatively new BEGe detectors can be refined and perfected. In order to accomodate the large number of new detectors, a new lock system is currently in development. This will be deployed on site in the coming months.

The Cherenkov and scintillator muon veto however is complete and working exceedingly well. Its function and performance will be discussed in the following chapters.

CHAPTER 5

THE GERDA MUON VETO SYSTEM

In this chapter, the general layout and the hardware of the GERDA muon veto will be discussed. As this work is mostly based on [Kna09] and [Rit12], the main focus will be on the changes in both detector and DAQ. Nevertheless, a short introduction into the veto system and its components will be given as well as a description of the current set-up which has been used for Phase I of GERDA.

The muon veto consists of two parts. The water tank of GERDA is instrumented with PMTs to detect the Cherenkov light emitted by muons passing the water. This water Cherenkov veto is complemented by a layer of plastic scintillator panels which cover the neck of the cryostat. The muons which pass the water tank through or around the neck may traverse the sensitive volume of the water tank only a very short distance if at all which reduces the efficiency of the muon veto. By placing scintillator panels on top of the clean room, the efficiency of the muon veto at this angle is regained.

This chapter will mostly cover the hardware and acceptance test, data from the physics runs of Phase I will be shown in the following chapters.

5.1   THE CHERENKOV WATER VETO

There are 66 PMTs operated under water in the GERDA water tank. The detectors are 8" PMTs type 9350KB/9354KB from ET Enterprises [Ent12]. Each PMT is housed in a stainless steel encapsulation, which is sketched in Fig. 5.1(a). The capsule is low radioactivity steel by Raff und Grund GmbH, closed with a custom made polyethylene cap and is filled with spectroscopy oil 161403 by Sigma-Aldrich [SA14]. The oil keeps the optical transition of a Cherenkov photon on the way to the photo cathode of the PMT as smooth as possible. Thus, efficiency losses by total internal reflections are minimized. The bottom of the base of the PMT is encased in polyurethane UR5041 by Electrolube and sealed with silicon gel SilGel 612 by Wacker. The lower part of the PMT, i.e. the dynode structure is protected from magnetic fields by a cone of μ-metal by ET Enterprises. An underwater high-voltage cable RG213/U by JoWo Systemtechnik (with a custom polyurethane cladding) connects the PMT to the data acquisition on one side and a CAEN SY1527LC High-Voltage supply (HV) module via a signal splitter which is located outside of the tank. Due to the distance to the
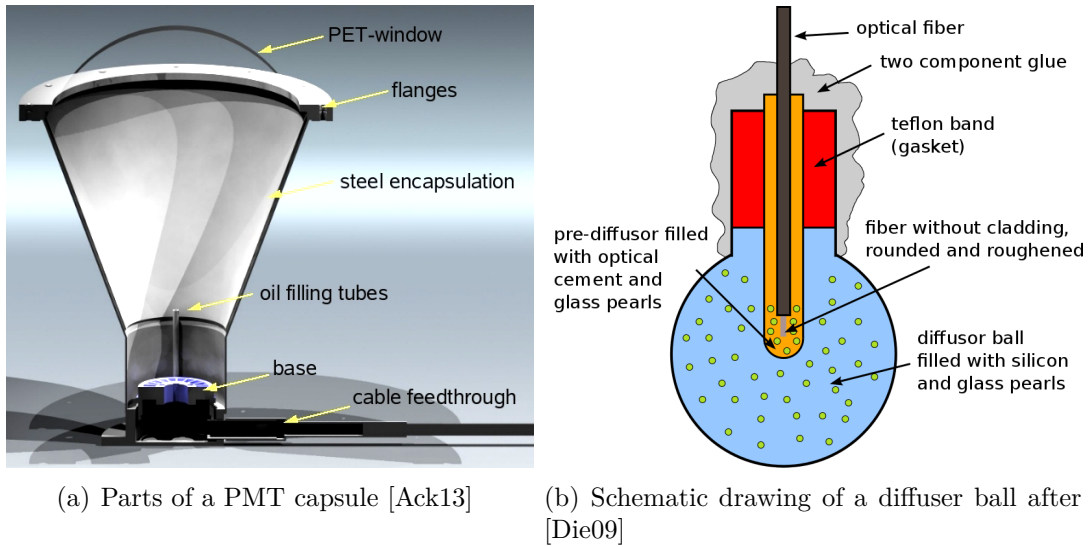
(a) Parts of a PMT capsule [Ack13]

(b) Schematic drawing of a diffuser ball after [Die09]

Figure 5.1: *Hardware components of the water Cherenkov veto.*

Figure 5.2: *A view inside the Cherenkov water veto. The inner walls of the water tank, the outer walls of the cryostat, the pillbox and the floor plate are covered with reflective foil. Several mounted PMTs can be seen.*
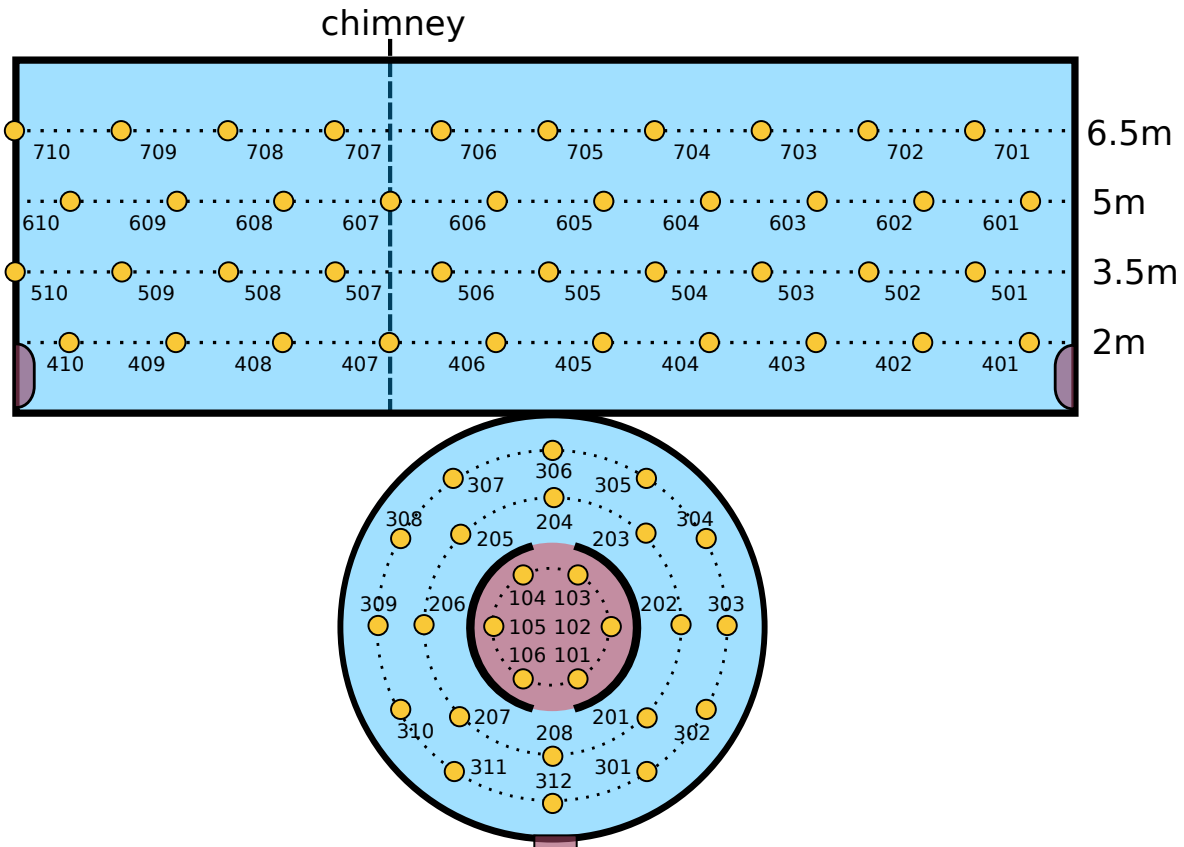
Figure 5.3: *Distribution and naming scheme of the PMTs.*

germanium detectors and the low overall mass, the radioactivity of the parts of the veto is unproblematic [Kna09]. A schematic view of the encapsulation can be seen in Fig. 5.1(a).

The PMTs are arranged in seven rings in the water tank. Two rings of eight and 12 PMTs respectively are placed on the bottom of the water tank looking upwards into the main water tank and four rings of 10 PMTs are placed on the wall, pointing towards the cryostat. The last ring of six PMTs is pointing inside the separate volume under the cryostat which is commonly known as the "pillbox"[†]. Distribution and naming scheme of the PMTs is shown in Fig. 5.3. The number of PMTs and their placement was chosen after an extensive Monte-Carlo study [Kna09]. In addition the tank is clad with the reflective foil Daylighting Film DF2000MA by 3M[‡] [3M07] which is better known by the name "VM2000". This reflective foil does not only increase the light yield of each muon due to its reflectivity, but it shifts the predominantly ultra-violet Cherenkov photons to around 400 nm where the PMTs are most efficient.

The reflective foil has a twofold fixation to the surfaces. First, the sheets of foil have a side which is covered with an adhesive. This glue adheres exceptionally well to the stainless steel. In addition, a number of metal ears are placed on the inside of the water tank and a steel wire is drawn through these in order to keep the foil in place should a

---

[†]Its diameter is 2 m as the cryostat and the curved bottom of the cryostat reduces the minimum height to 1.35 m.

[‡]The foil is discontinued by the manufacturer 3M, the data sheet however is still available on the 3M Multimedia Server, as of March, 2014.

larger area rip off. The outside of the cryostat is covered with the insulating material Jackodur by Jackon. Since this material is rather porous, the foil does not adhere as well as on the stainless steel. For this reason, a nylon rope was tightly wound around the cryostat to prevent the foil from coming off as no ears for a wire were available on the outside of the cryostat. The HV cables and optical fibres on each PMT are secured on multiple points with clamps and cable binders. All cables are lead to a chimney flange on top of the roof of the water tank which contains sufficient light-tight feed-throughs for all cables. On the outside a number of cable trays connect the chimney flange with a control room on the second floor of the GERDA building where the DAQ and other electronics are housed in a custom muon-veto rack.

Due to the almost full coverage with the reflective foil the interior of the muon veto is a spectacular sight to behold. A picture of the veto can be seen in Fig. 5.2. This picture has become one of the iconic images for the entire experiment.

5.2   THE SCINTILLATOR PANEL VETO

Muons passing through the neck of the cryostat may traverse a too short distance either in the "pillbox" or in the water tank. Thus, they may not produce enough Cherenkov photons to be detected. In order to retain the muon rejection efficiency, a veto of plastic scintillator panels was conceived and installed [GSTR11-05, GSTR11-10, GSTR11-11]. Each scintillator panel contains a $200 \times 50 \times 4$ cm^3 sheet of plastic scintillator UPS-923A by Kharkov Crystal Institut based on polystyrol with an addition of PTP (2%) and POPOP (0.03%). In addition the panel contain optical fibres S-Type Y11(250)M by Kuraray on the narrow sides as light-guides, an electronics board with a trigger and shaper and a PMT. From overall 36 installed panels 17 are equipped with H6780-2 PMTs by Hamamatsu Photonics K.K[†] and 19 with PMT-085 by Kvadrotech[‡]. The PMT-085 are powered by the same HV supply as the Cherenkov veto PMTs. The H6780-2 PMTs and the internal electronics of all panels are powered by a custom made power source. Each panel contains a signal shaper and a discriminator logic with two outputs, one with a high and one with a low threshold. Both thresholds are unique to each panel depending on the response of the respective PMT.

The first underground tests of the panels were already taken in 2008 [GSTR08-16]. Due to the success of these initial measurements the other panels were manufactured and installed in 2011. In the following section, additional tests and calculations will be shown which were for the most part made in this work. This lead to the arrangement of three layers covering an area of 4×3 m^2 centred over the neck of the cryostat.

5.2.1   INITIAL SET-UP AND IN-SITU TESTS

The originally planned layout for the scintillator veto was a double layer of 7×2 panels covering a solid angle of $50° \times 40°$ from the neck of the cryostat. The geometry of the roof of the clean-room where the scintillator veto should be located allowed for the installation of only 28 panels with a double-layer approach. The roof of the clean room

---

[†]This PMT seems discontinued by the manufacturer, and the data-sheet is available on extertnal websites like http://www.alldatasheet.com, as of March, 2014.

[‡]No further information available

Table 5.1: *Expected coincident rates and random coincidences for different panel set-ups. Each value is given for a single stack of panels. The first two values are taken from [GSTR11-05]. The random rates are calculated values using the respective rates and the given coincidence windows. The values for "layer" are calculated assuming that all panels of a layer are added up for single-channel read-out with a summed dark-rate.*

panel coincidence set-ups	rates $[1/\mathrm{s}]$
single panel	250
double panel (NIM)	0.2-15
double panel (FADC)	2×10^{-2}
triple panel (-6/-7/-6 mV)	3.7×10^{-4}
triple panel (-7/-7/-7 mV)	2.8×10^{-4}
quadruple panel	2.5×10^{-4}
expected µ-rate per m^2	2.5×10^{-4}
random double panel (60 ns)	3.75×10^{-3}
random triple panel (60 ns)	5.6×10^{-8}
random triple "layer" (40 ns)	4.3×10^{-5}
random triple "layer" (60 ns)	9.7×10^{-5}
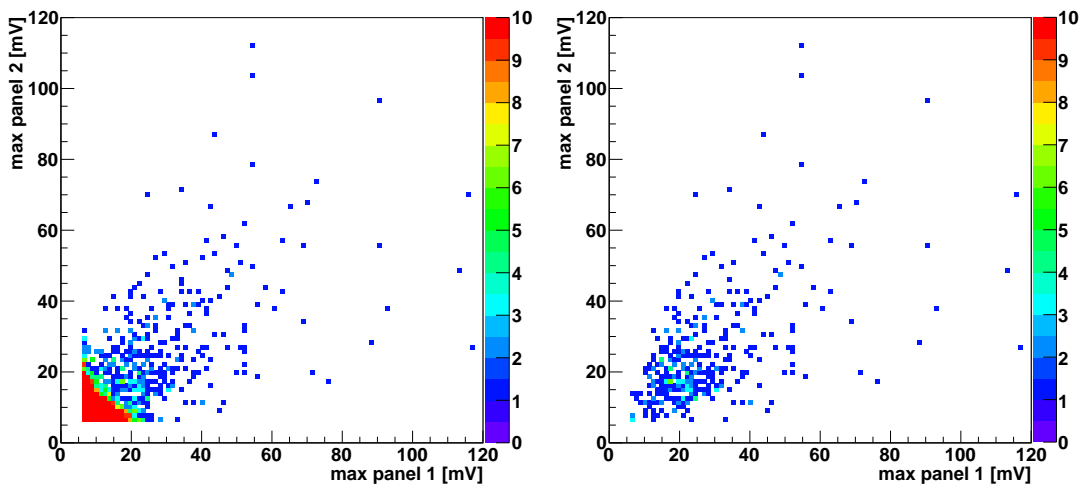
(a) Double panel trigger, rate 2.0×10^{-2} /s   (b) Triple panel trigger, rate 2.9×10^{-4} /s

Figure 5.4: *Comparison of double and triple panel set-up. A double stack of panels was measured with a third panel on top. The pulse height distribution shows a much lower contribution of low-energy events (i.e. random coincidences and $\gamma\gamma$ coincidences) when the third panel is used in triple coincidence.*

is not flat but there is a part of the clean-room which is elevated by about 40 cm to the main part of the roof. This elevated part is directly above the neck of the cryostat and only 3.5 m wide. Since a panel is 50 cm wide, no more than 7 panels can be placed next to each other. A panel is 2.2 m in length, thus two panels in a line would mean an overlap of 25 cm on each side of the elevated part. This is undesirable for anyone who has to work on the clean-room roof as this would pose a danger for tripping. It would also partially cover the safety cord which runs around the elevated roof and is used for personal safety harnesses.

A number of initial measurements were taken with different set-ups of panels, which can be seen in Tab. 5.1. The measurements with single panels using the built-in discriminator threshold yields a rate of 250 /s (see [GSTR11-05] and [GSTR11-11]) which differs by several orders of magnitude from the expected value. This is due to regular backgrounds such as γs from radioactive decays, which are not cut away with the discriminator threshold. The "NIM" data were acquired using an external Nuclear Instrumentation Module (NIM) coincidence logic. Here, a coincidence was demanded between the logic signals of the discriminator built into each panel. The "FADC" data were acquired by using the muon veto DAQ system with FADCs, triggering on a threshold of -6 mV and demanding a coincidence within 60 ns. The different rate between "NIM" and "FADC" data is due to the trigger threshold, which is much lower for the "NIM" data. The measured "FADC" rates are still much higher than the expected random coincident rate. A candidate for these excess events are γs, which deposit energy in more than one panel.

Additional data were taken with a triple and a quadruple stack of panels in order to test the muon detection efficiency in dependence of a higher coincidence. Two scatter plots of the maximum PMT pulse height of two panels can be seen in Fig. 5.4. For the case of a double coincidence, most of the events are very close to the trigger threshold of 40 FADC channels (-6 mV as mentioned above). For the triple coincidence condition, the scatter plot closely resembles a two-dimensional Landau peak, i.e. the characteristic energy deposition of a minimal-ionizing charged particle, which punches through matter and it is not stopped. By increasing the threshold to -7 mV for all panels, the coincident rate almost exactly represents the expected muon rate (see Tab. 5.1). Were only few FADC channels available, all 12 panels in a layer could be summed for single-channel read-out. In this worst-case scenario, the dark rate of all panels is added up and the random coincidences were calculated for 40 ns and 60 ns windows. Both values are a factor of ≈3 and ≈6 lower than the expected rate which makes this still a viable option as the overall rates are so low. This would be accompanied by the obvious loss in detection resolution.

The corresponding rates for a triple and quadruple coincidence are much more in accordance with the expected muon rate. A triple layer solution was therefore proposed, especially since the expected rate of random coincidences for two panels already exceeds the expected muon rate by an order of magnitude. The rate for random coincidences of a triple panel however is negligible in comparison. Even if an entire layer of 12 panels was treated as a single detector (i.e. the summed dark-rate of all panels), the random rate would still be 3-10 times lower than the signal rate, depending on the coincidence window.

5.2.2 Final Panel Layout and Installation

For the final layout, several different options were considered. The constraints for these options were the number of available panels (40), their dimension ($2200 \times 500 \times 40\,\text{mm}$) and the maximum load allowed on the roof of the clean-room ($150\,\text{kg/m}^2$). The following three options were considered.

- **Double layer**: $7 \times 2 \times 2$ panels, $\approx 70\,\text{kg/m}^2$. $50° \times 40°$ coverage. Many unused panels, random rate very high.

- **Double layer with absorber**: e.g. $5\,\text{mm}$ lead attenuates only in the hard X-ray regime, adds $\approx 55\,\text{kg/m}^2$

- **Triple layer**: $6 \times 2 \times 3$ panels, $\approx 100\,\text{kg/m}^2$. $50° \times 36°$ coverage. 4 spare panels, low random rate.

Due to the high background rejection that a triple coincidence offers, the third option was chosen for the final installation. In addition, with three layers of panels a pixelization is possible, offering a more precise handle where a muon passes through the panel layers. The last $200\,\text{mm}$ in length of a panel contain the PMT, the front-end electronics and the cable plugs. Therefore, in order to pixelate the panels (i.e. turn a layer by $90°$), space has to be made for the electronic parts and cables to fit. This was be achieved by placing a $40\,\text{mm}$ spacer frame on top of the middle panels and placing part of the top layer on this spacer frame. A sketch of this layout can be seen in Fig. 5.5.

This layout scheme was realised at the LNGS in June/July 2011. A photo of the panels on the roof of the clean-room can be seen in Fig. 5.6. A cable duct leads to the control room, 3rd floor, where the HV power supply and data acquisition are located. In addition to the HV supply the panels need power for the front-end electronics and the PMT. All working panels with a PMT-085 (19 panels) were installed, since their PMT shows a better resolution. The necessary high-voltage for this type of panel is supplied by the Cherenkov veto HV-crate. Only six slots were still available, so the panels have to be daisy-chained in groups of three and four panels. Due to their low power consumption (50 µA at 820 V), this is unproblematic for the HV supply. The HV crate uses the Safe High-Voltage (SHV) standard, the panels use "ШР" male/female plugs[§]. The other 17 panels generate the supply voltage for the PMT internally and thus need a higher supply power for the electronics. The power demands of the panels are listed in Tab. 5.2.

At first, the power for the front-end electronics and low-voltage PMTs was supplied by a single $+12/\pm 6\,\text{V}$ power supply NIM module, which is also located in the control room. All panels have a 9-pol DSUB connector and were in a single daisy-chain. As this power module was insufficient to power all panels, it has been replaced by a custom power source in Nov. 2012 which is located in the muon veto rack. Prior to that, some of the panel signals were suppressed in their height and some baselines were shifted due to the low power. These features disappeared with the new power source. The power source has an extension module with four outlets which allows four independent daisy-chains. This reduces the risk of a total failure of the entire scintillator veto in

---

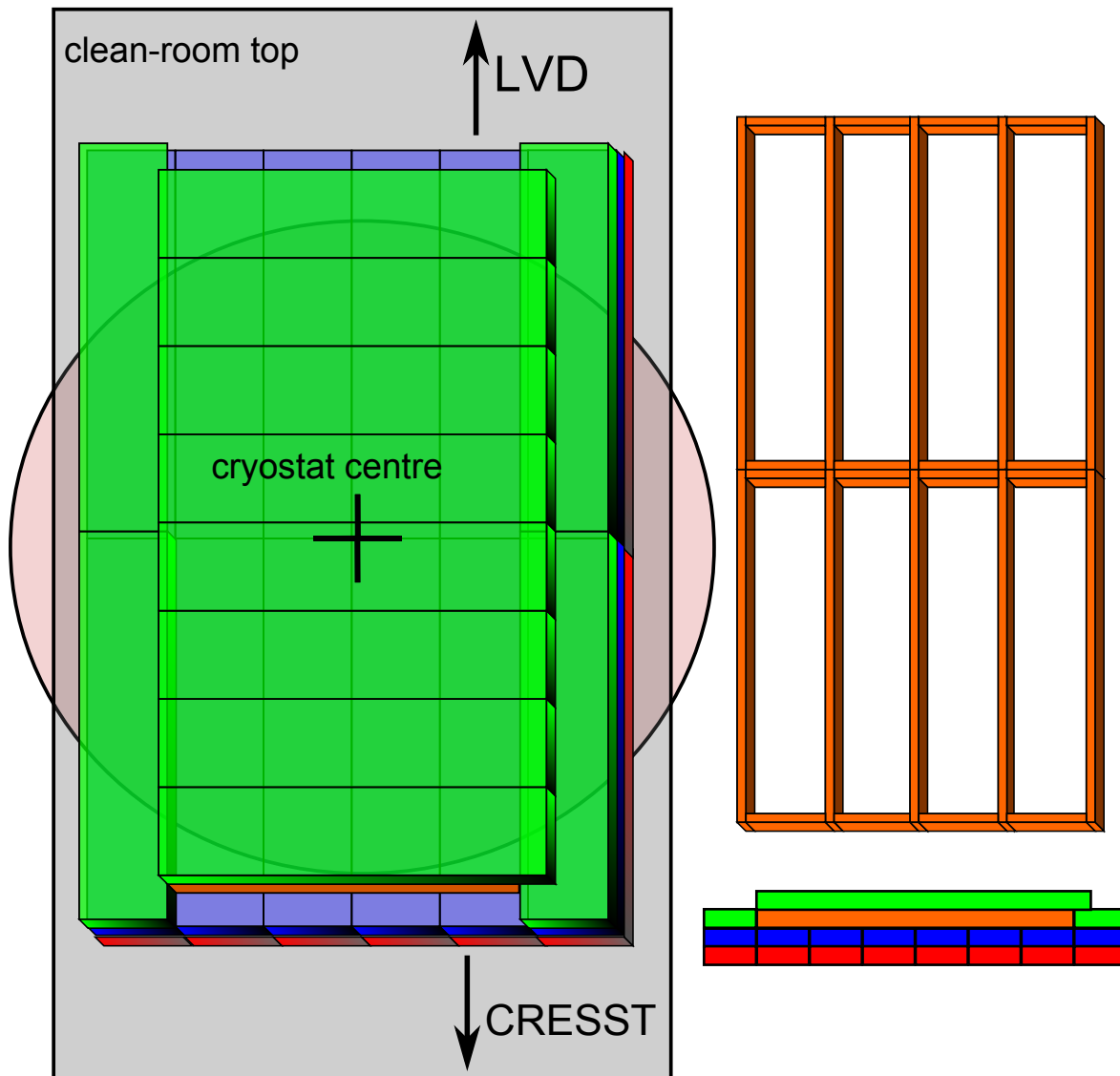[§]See http://www.eandc.ru/techinfo/sr.pdf for technical details

Figure 5.5: *The set-up of the scintillator panels. The spacer frame between second and third layer is drawn in orange next to the stacked panels. A cross section of the panel stack is drawn beneath the spacer frame. The part of the "green" panels overlapping the stack on the side on the right hand side of the sketch contains the panel PMT and front-end electronics.*

Table 5.2: *Power consumption for the scintillator panels. All value are given for a single panel of the respective type.*

panel / PMT type	+6 V	-6 V	+12 V	-820 V
H6780-2	25 mA	90 mA	30 mA	–
PMT-085	25 mA	25 mA	–	50 µA

Figure 5.6: *An image of the scintillator panel veto on top of the* Gerda *clean room.*

case that one panel suffers a break-down of the electronics.

In order to secure the panels against sliding to either side, a metal fence was constructed around the panels. Currently, this fence is held in place by four steel wires, which can hold 400-500 kg each. These steel wires are fed through a metal ring, which is welded into the steel superstructure directly left and right of the panel stack. Additionally the fence can be screwed into the roof, but due to the already high weight and the strong steel wires, this was refrained from at present. A fifth steel wire protects the panels in the upmost layer from jumping up in case of an earthquake.

5.3 Data Acquisition (DAQ)

Prior to the installation at the LNGS in 2010, the muon DAQ Versa Module Eurocard (VME) crate was prepared in Heidelberg[†]. It consists of 14 SIS 3301 ADC FADC with 8 channels and a resolution of 14 bit. In addition it contains a clock, a controller and a VME-PC. In Tübingen a Precision Analog Systems Digital-to-Analog Converter (DAC) was added as a power supply for the calibration system [Rit12], [GSTR10-03]. This calibration system consists of six pulser boxes (and one spare) with ultra-fast, bright LEDs. Five of these LEDs are connected to one of five diffuser-balls. The sixth drives the optic fibres that are connected to every single PMT via a homogeneously illuminated bunch of fibres which is still to be installed.

The pulser boxes as well as the 66 PMT signal splitter boxes (and four spares) are installed in a custom made 19" crate. The splitter consist of two simple RC filter, a low-pass which allows the HV to pass and a high-pass for the signal. This crate is placed on a rack directly under the cable trays of the HV cables and optical fibres from the chimney flange on top of Gerda. The rack also contains a SY1527LC HV crate by CAEN with six 12-channel A1733 HV cards. The six spare card slots in the HV crate allow the operation of the muon scintillation panels on top of the clean-room. A sketch of this set-up can be seen in Fig. 5.7. The controller PC for the FADCs

---

[†]T.Kihm & B.Schwingenheuer, *priv. comm.*, 2010
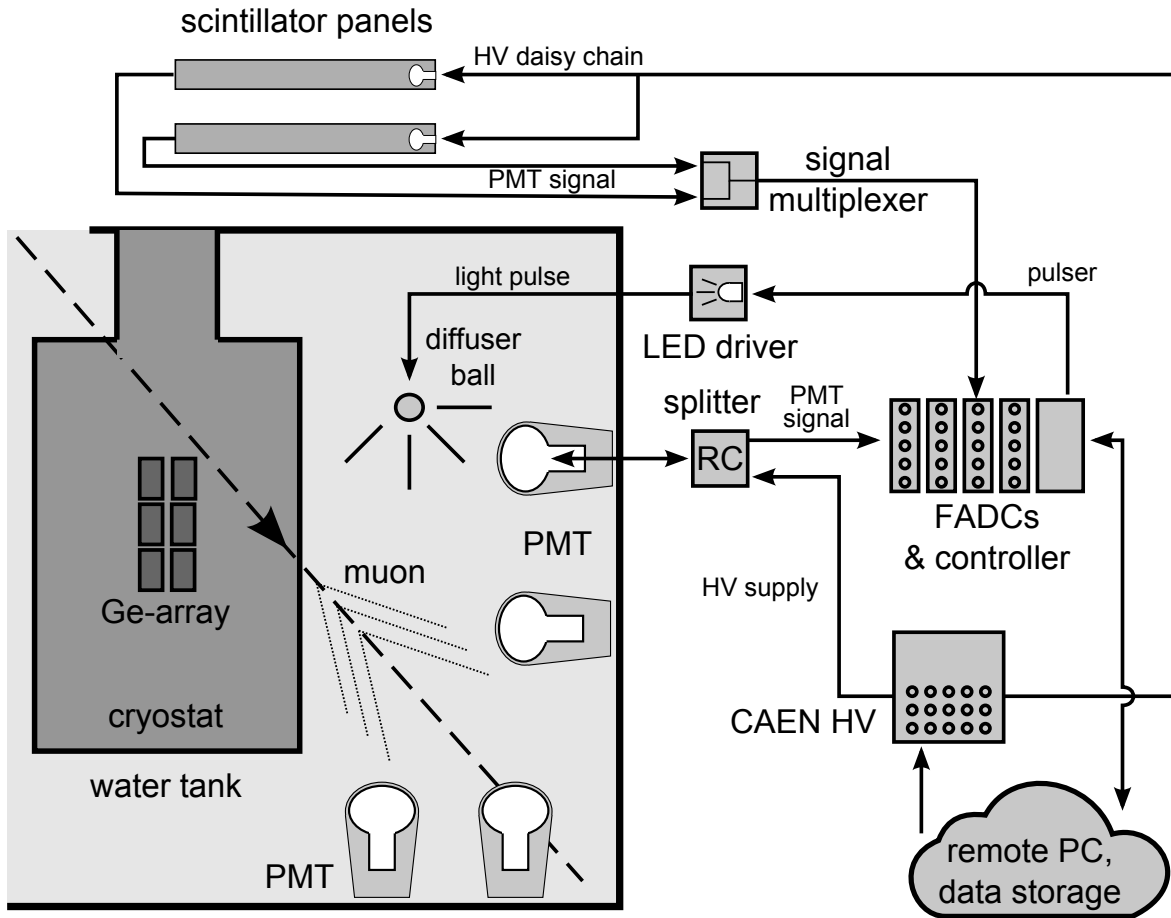
Figure 5.7: *Schematic DAQ chain of the* Gerda *muon veto.*

has a 2 TB storage which was more than sufficient for Phase I of Gerda as only ≈0.5 TB was used. It runs a DAQ data taking programme which records binary data tag-files, the DAQ tags are given in [GSTR14-02]. The data files contain e.g. precise timestamp information, run information (calibration run, test run, trigger thresholds, trigger multiplicities) as well as storage containers for germanium, positive and negative PMT data. The PC can also be used to power the LEDs for a calibration of the PMTs via the DAC. The data is automatically copied to an above-ground storage and a back-up is kept in Heidelberg and Tübingen. As the muon data contains no information about the germanium data, the blinding is not violated and the data is available freely. The entire set-up can be controlled and operated remotely. The external GPS clock from Borexino is used to synchronize the internal clocks of the muon and germanium DAQs with the GPS signal every second.

The current version of the DAQ programme allows separate trigger conditions for the Cherenkov veto and the scintillator veto. A trigger is generated when a certain number of FADCs (containing up to 8 detectors) have recorded a trace above a trigger threshold within a certain time window. The trigger signals of each FADC are fed into a special "MPIC"-module and in turn read out by the DAQ PC. The muon DAQ contains 14 Struck FADCs with the following assignment and trigger conditions:

FADC 1: MPIC channel: E3, `ge_adc`, "utility" FADC, only used for calibration, trigger on the MPIC pulser in channel 1

Table 5.3: *FADC channel assignment. The channel marked with ∅ in FADC 2 is broken.*

ch.	FADC 1	FADC 2	FADC 3	FADC 4	FADC 5	FADC 6	FADC 7
8	—	—	—	—	—	—	—
7	—	11/12	—	—	706	705	704
6	—	9/10	23/24	35/35	604	603	602
5	—	∅	21/22	33/34	501	510	509
4	—	7/8	19/20	31/32	409	408	407
3	—	5/6	17/18	29/30	301	310	303
2	—	3/4	15/16	27/28	307	304	207
1	pulser	1/2	13/14	25/26	101	106	105

ch.	FADC 8	FADC 9	FADC 10	FADC 11	FADC 12	FADC 13	FADC 14
8	—	—	—	—	—	—	—
7	703	702	701	710	709	708	707
6	601	610	609	608	607	606	605
5	508	507	506	505	504	503	502
4	406	405	404	403	402	401	410
3	302	312	311	309	308	306	305
2	206	205	204	203	202	201	208
1	104	103	102	—	—	—	—

FADC 2-4: MPIC channels B1-B3, `pospm_adc`, FADCs for the panels, multiplicity: 3, threshold: -20 channels (-2.5 mV), trigger length/gap 40/50 clk tics, trigger window: 60 ns

FADC 5-14: MPIC channels: B4-E1, `pm_adc`, Cherenkov PMT FADCs, multiplicity: 5, threshold: -50 channels (-6 mv), trigger length/gap: 2/3 clk tics, trigger window: 60 ns

Each PMT has its own FADC channel, there are 6-7 PMTs on each FADC. In order to keep the trigger efficiency as high as possible, it was assured that no neighbouring PMTs were set on the same FADC. This assures that if for example events with a spatially small light distribution still are able to trigger the veto [Kna09]. The trigger threshold of each PMT is kept at 50 FADC channels. The naming scheme and the distribution inside the water tank was already shown in Fig. 5.3 and the distribution of all detectors on the FADC channels is summarized in Tab. 5.3.

Since there are only 24 FADC channels available for the 36 panels, the signals of two different panels are multiplexed on a single output by means of a $16.5\,\Omega$ resistor cross. This allows a reflection-free connection at the cost of -6 dB in signal height, i.e. an attenuation of 1/2. Each layer is kept on a separate FADC. In order to better identify triple coincidences in each half of the stack, the 18 panels towards LVD are connected with an additional 30 m cable which gives an offset of ≈150 ns. THis means that all panel stacks in the same half will show the same offset, while coincidences between the two halves of the stack are fruhter excluded. The multiplexing layout can be seen in

4/8					
3/6					
2/4					
1/2					
5/10					6/12
9/18	8/16	7/14	12/24	11/22	10/20
15/30	16/32	17/34	18/36	13/26	14/28

5 9 15 35	4 27 / 8 16	4 19 / 7 17	4 11 / 12 18	4 3 / 11 13	6 10 14
	3 28 / 8 16	3 20 / 7 17	3 12 / 12 18	3 4 / 11 13	1
	2 29 / 8 16	2 21 / 7 17	2 13 / 12 18	2 5 / 11 13	
	1 30 / 8 16	1 22 / 7 17	1 14 / 12 18	1 6 / 11 13	

4/7					
3/5					
2/3					
1/1					
5/9					6/11
12/23	11/21	10/19	9/17	8/15	7/13
13/25	14/27	15/29	16/31	17/33	18/35

5 12 13 36	4 31 / 11 14	4 23 / 10 15	4 15 / 9 16	4 7 / 8 17	6 7 18
	3 32 / 11 14	3 24 / 10 15	3 16 / 9 16	3 8 / 8 17	2
	2 33 / 11 14	2 25 / 10 15	2 17 / 9 16	2 9 / 8 17	
	1 34 / 11 14	1 26 / 10 15	1 18 / 9 16	1 10 / 8 17	

Figure 5.8: *The top side points towards LVD, the bottom side towards Cresst. The left sketch shows the FADC channels / cable number, where the even cable numbers are 150 ns delayed with respect to the odd ones. The right sketch shows which FADC channels are needed for a coincidence of the respective pixel. Each pixel was given a number, shown in red.*

Fig. 5.8. The right sketch shows, that each pixel needs a unique combination of panels. Since not all panel combinations are possible, certain random events can be discarded in the analysis. This can potentially reduce the number of random events by a factor of 6, since only 36 out of 216 possible combinations are valid.

The threshold for each panel is currently set to the same value (-20 FADC channels / 2.5 mV). In the current DAQ version it is possible to give each FADC channel its own threshold. However, since two panels are read out with one FADC channel but have different gains, a compromise between the two panels has to be made. Additional tests showed that especially since the internal thresholds of the panels are quite different, a common low threshold for the FADC trigger generation in triple panel coincidences shows good results. Otherwise, the trigger system for the panels is working the same way as for the Cherenkov PMTs.

There are two main modes in which the veto DAQ is operated. In the regular run mode, there are two trigger groups, the `pospm_adc`, i.e. the panels and the `pm_adc` for the Cherenkov PMTs. As soon as the trigger condition is fulfilled for either trigger group, the entire veto is read out, i.e. 400 data points for each detector with a time resolution of 10 ns, i.e. 4 μs in total. Each trigger is generated using a moving-window average. This means that two sampling windows with a certain length and a certain gap in-between run constantly on each detector trace. As soon as the difference of the integral of the two windows surpass the trigger threshold, a trigger signal is generated. The respective multiplicities are for entire FADCs, i.e. at least one detector on an FADC has to have surpassed the trigger threshold and if a certain number of FADCs show a trigger signal, the event is recorded. In this case 3 out of 3 panel FADC or 5 out of 10 Cherenkov FADC need to have surpassed the threshold in order to record

Table 5.4: *Forward voltages for the diffuser ball LEDs. The location of the four diffuser balls in the water tank is given as an angle counter-clockwise from the manhole. They are roughly at the same height as the second highest PMT ring, i.e. 5 m.*

LED	forward volt. @ SPP [V]	location
1	10.3	main tank, 225°
2	9.8	main tank, 135°
3	10.8	main tank, 45°
4	10.2	main tank, 315°
5	9.3	pillbox

the 400 data-point traces from an internal buffer. The FADC possess two ring buffers for temporary data storage. Once an overall veto-trigger is generated, the data from one buffer is written to disk, while the other buffer starts recording. This reduces dead time in the recording and allows trigger rates of ≈ 100 Hz with this set-up with only few percent dead-time. The real rate is four orders of magnitude lower, hence dead-time of the detector is negligible. Events that trigger while one buffer is still read out will leave the read-out incomplete and shortly after the original event a small number of artificial and nonsensical events (usually four to five) will be introduced, which have to be discarded. This happens randomly by two events coming in very short order. A very high rate favours this effect, but it is still a measurable effect despite the low rate of the muon DAQ. These events can however be easily tagged by checking for standard values in some of the data containers and hence discarded.

The second main run-mode is the calibration. Here, pulser signals are generated by a pulser in the MPIC-module and multiplied via a CAEN V976 fan-in / fan-out module. The multiple pulser signals are now used to power the LED drivers illuminating the diffuser balls. A custom programme on the DAQ-PC allows the operation of the DAC, i.e. the forward voltages of the calibration LEDs. One pulser signal is fed into the `ge_adc` which serves as a trigger for the whole veto. As in the normal mode, 4 µs of data are recorded for each detector.

5.3.1   Calibration Method

The PMTs are calibrated regularly with a set of five custom made diffuser balls [Die09]. These balls are filled with a mixture of silicon gel by Wacker and tiny glass pearls S32 by 3M. An optical fibre is glued into a small vial inside the ball with a higher content of glass pearls. The cladding of the end of the fibre is removed and the fibre is roughened in order to obtain a unidirectional light emission. A schematic of these can be seen in Fig. 5.1(b). Ultra-fast LEDs outside of the water tank can be pulsed to illuminate the five diffuser balls [Rit10]. Four of these balls are distributed in the main water tank and a fifth is placed inside the "pillbox". With an appropriate setting of the forward voltage of the LEDs it is possible to illuminate all PMTs simultaneously with single photons and thus gain information of the position of the SPP of every PMT at the

same time. The values for the forward voltages and the distribution inside the tank can be seen in Tab. 5.4. With this setting a ratio of one Photo-Electron (PE) in 10 pulser events can be achieved for each PMT. Due to the proximity of some PMT to the diffuser balls, this value is subject to change, but the excess light that some PMTs see during calibration is not high enough that it would warrant a separate measurement. Thus, with this settings, the entire veto can be conveniently illuminated at once.

This system is usually used in pauses of the germanium data taking. In a first step, SPPs of each PMT are recorded. In a second step, the HV supply voltage of each PMT can be adjusted. This way, the response of each PMT to single-photon illumination can be homogenized. In additional steps, the HV supply voltages can be re-adjusted until the desired response is reached. The SPP position of each PMT is usually adjusted to 100 FADC channels and the trigger threshold of the Cherenkov veto is set to 50 FADC channels for each channel. As the gains of the PMTs drift only very little over time (see e.g. App. B.1), only very few PMTs need to be adjusted each calibration. This makes the calibration a very convenient process. The SPP of only two PMTs deviate from the aspired value of 100 FADC channels. PMT 502 is operated at maximum voltage (2100 V) which shows a lower SPP and PMT 603 shows a flat SPP.

5.4   Muon Data Analysis Tools

In this work, two different data analysis tools have been used, which will be introduced in the following. As the DAQ of the muon veto was operational before the respective system for the germanium detectors, a data analysis tool was developed in Tübingen specifically tailored for the demands of the muon veto which is called `Tag2Root` [Rit12]. This macro is based on the `root` analysis framework [†] and translates the binary data file from the DAQ into the `root` format using the tags given in [GSTR14-02]. Basic analysis operations are run on the data like information regarding the trigger point, maximum and integral of each detector trace. Separate data containers for pillbox PMT, PMT in the water tank and the scintillator panels are kept. Each event has information about the timestamp in Unix-time[‡] with a resolution of 10 ns. In addition, for every event the DAQ settings and pulse height histograms of all PMTs are stored. This analysis tool is predominantly used in this work.

The Gerda collaboration started to develop an own independent data analysis tool called Gelatio (see Sec. 4.5 and [Ago11]). In this work, the first muon veto modules for this framework were developed. The entire analysis chain starts with a decoder, which translates the raw data into the Root -based MGDO format. The DAQ systems of both germanium and muon veto are essentially the same and the same data-taking programme is used on both. However, a different converter was necessary, as the germanium converter treats any other channels but germanium FADC-channels (see Sec. 5.3) as auxiliary channels. In addition, the previous converters and analysis modules did not support as many FADC-channels as needed by the muon veto, i.e. 112 channels for the entire veto. The standard graphical user interface of Gelatio supports this number of channels as can be seen in Fig. 5.9. Each line of traces represents all eight channels of an FADC and each trace represents the full 400 data points / 4 μs of each

---

[†]Project homepage: http://root.cern.ch/drupal/

[‡]Also known as POSIX-time, a method of time-keeping, recorded in seconds from 1st Jan. 1970.
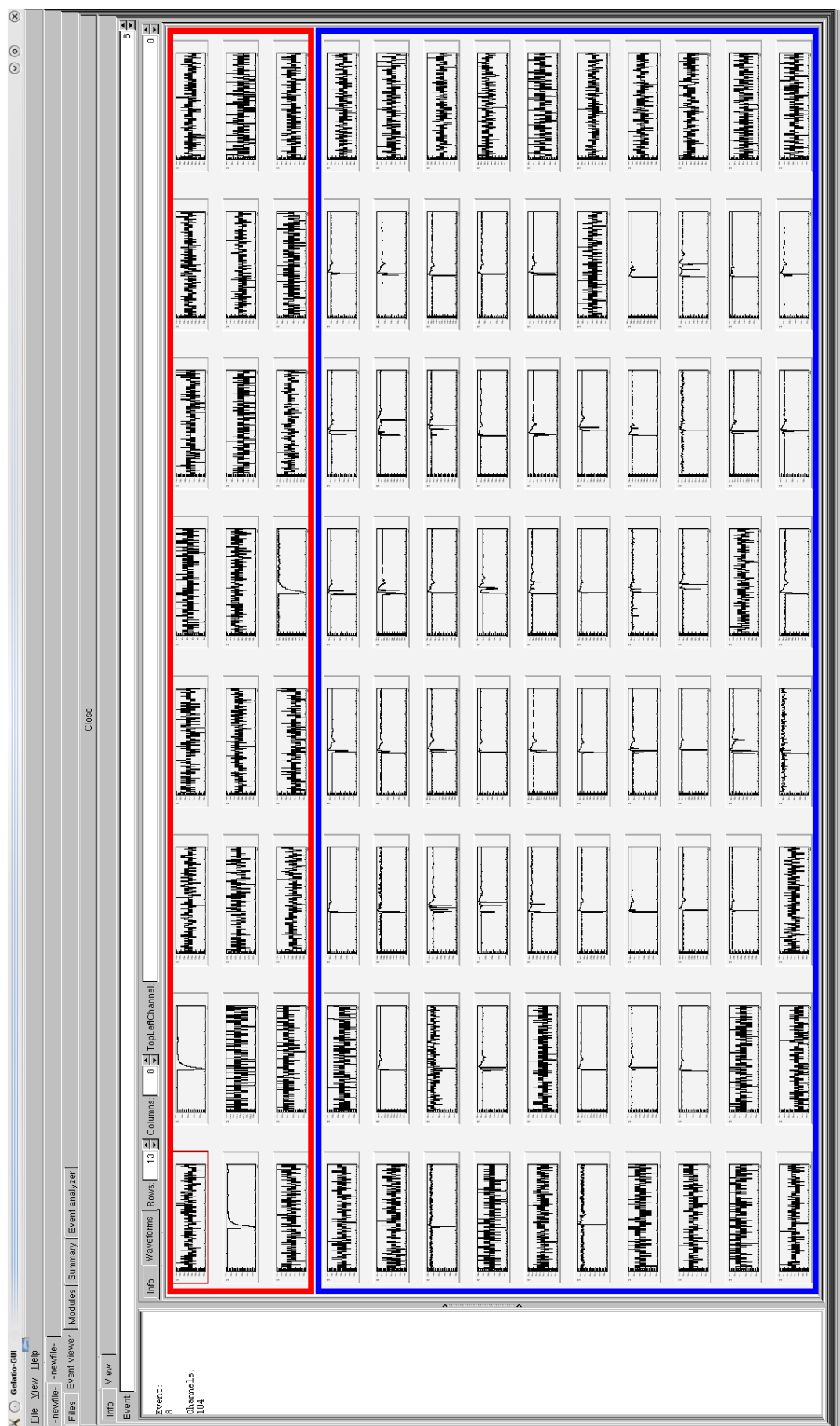
Figure 5.9: *One event shown in the GELATIO GUI where eight horizontal traces represent one FADC. The three FADCs of the panels are highlighted in red, the ten Cherenkov veto in blue. Most of the channels which belong to the panels show the baseline but each FADC has recorded a single trace, while only a few Cherenkov channels show the baseline and most show a trace. The distribution of detectors to the channels is listed in Tab. 5.3.*

channel. As can be seen, each panel FADC has fired once and most PMTs recorded a signal as well.

For the analysis chain with Gelatio a different approach was chosen in comparison to the more common analysis in `Tag2Root`, which is based on standard pulse height and integral analysis. In the Gelatio analysis, the calibrations are used to generate standard "template" pulses for each PMT. These template pulses are generated from the calibration files, which contain almost exclusively either one-PE pulses or a baseline. Once the template pulses are generated, PMT pulses from background runs can be deconvoluted with this template. They are transformed into Fourier-space, divided by the template pulse and transformed back[§]. This yields a trace with a single peak for each PMT pulse. The height of this pulse is now equal to the total amount of PE in the original pulse, an example of such a trace is shown in Fig. D.1.

While this system is more complex as the common pulse height / integral analysis it offers a number of advantages. The accuracy of both pulse height and integral of a trace are susceptible to certain types of detector behaviours. When there are multiple peaks close to the trigger point, a normal pulse height method will only record one of these different peaks. The integral of a trace can be close to zero if the detector shows large negative after-pulses. This deconvolution method suffers neither of these problems. In addition, the analysis becomes less dependent on the exact gain of the PMT since the SPP can be of any height as long as there is a recent calibration which recorded this specific gain. It is still advisable to keep the SPP pulse heights at the same level if possible, as each PMT is still recorded with a set hardware trigger. The Gelatio analysis chain for the muon veto data is listed in App. D.

5.5   Muon Angular Spectrum and Effective Detector Area

The muon flux at the earth's surface takes a $1/\cos\theta$ form where θ is the zenith angle, i.e. the majority of muons come from straight above, while only very few arrive from higher slant depths e.g. just above the horizon. Contrary, the muon flux at the LNGS is not as even in terms of its direction. The massif over the LNGS is not a perfect half-sphere and hence it does not shield the laboratory equally well from all directions. As it is a geological formation with peaks, valleys, sedimentary structures etc. the muon spectrum takes not the common distribution in relation to the zenith. The source spectrum is shifted by the differences in overburden in such a way, that the median of the arriving muons in the experimental halls come from $\approx 34°$ off the zenith.

The angular and spectral distribution for the muon flux were measured by the Macro experiment with great accuracy and are hence well known (see [Ahl93] for details or [Kna09] for a Gerda-related usage). The muon flux measured by Macro is available as a data file covering 40 values of the zenith angle $\cos\theta$, 90 values for the azimuth angle ϕ and a relative muon flux from that specific angle which is shown in Fig. 5.10. Due to this, the muon flux at the experiments in the LNGS is conventionally given in relation to the muon flux as an "effective area". The surface of the detector or its active area for muon detection is projected onto every angle of the muon spectrum and

---

[§]C. Schmitt, *priv. comm.*, 2013
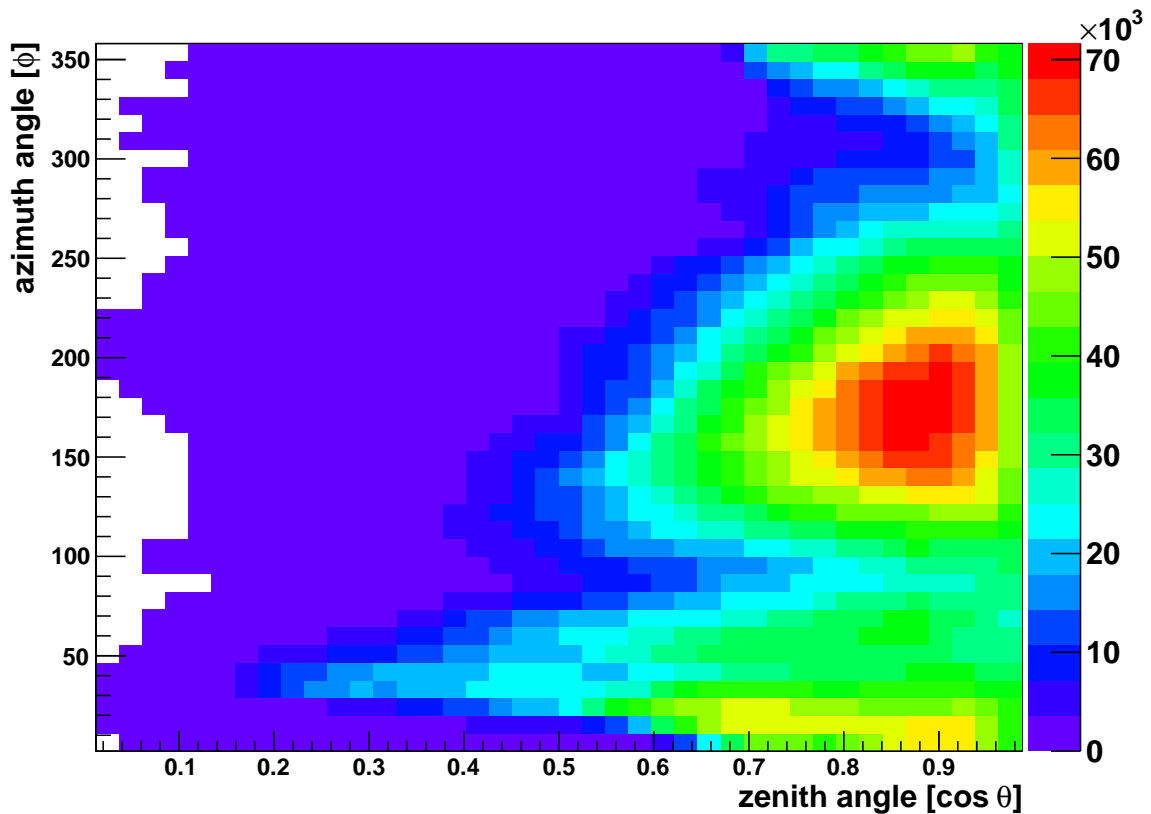
Figure 5.10: *Angular distribution for cosmogenic muons at the LNGS following the* Macro *data [Ahl93].*

weighted it with the relative specific muon flux for each zenith/azimuth combination. The result is an effective area of the experiment for the muon flux which is used to normalize the measured muon rate. The result is a muon rate that is independent of the respective detector geometry and thus comparable with other experiments. This rate is given in [muons/(s m^2)]. For an experiment like Borexino the effective area is rather easy to obtain as the central part of the detector is a perfect sphere of 13.7 m diameter. Contrary, Lvd has a much more complicated geometry with 840 individual tanks of 1.5 m^3 and ample spaces in-between.

For this purpose, the Gerda experiment was approximated to be a perfect cylinder of 8.5 m height and 5 m radius. The original geometry differs only slightly from this idealized form, see Fig. 4.3 in Sec. 4.3. This cylinder is now projected on a plane using the Macro data and an effective area of (103.5±2.0) m^2 is found. The error arises, when an uncertainty of 5 cm is assumed as a result of both physical measurement of the water tank as well as detection efficiency inside the water. However, this error can be considered mostly negative. Short tracks at the border of the water tank might not be detectable, i.e. a "dead layer" can be assumed which will however act only as an error which reduced the effective area. Unless otherwise noted, all muon rates in the following chapters will be given normalized by this value if they are given in [muons/(s·m^2)].

In a similar way the effective area for the panel veto was determined. If the panels are

assumed to take the shape of a flat stack of 12 m^2, the effective area towards the muon flux is (8.9±0.4) m^2.

5.6 Simulation Studies

A number of simulation studies regarding the muon veto were presented in [Kna09]. In this work, the main focus of the simulation was to simulate the muons with an energy deposition in the germanium crystals in order to guide the construction of the muon veto. By simulating only these very few muons, the process of simulation was accelerated as the muons at the LNGS have a mean energy of $\langle E_\mu(\text{LNGS})\rangle = 270$ GeV and produce $\approx$270 photons/cm in water via the Cherenkov effect (see Eq. 3.3). As the average track length for both muons and the produced photons is in the vicinity of 8-9 m and since every photon is stored and sequentially treated, this puts a strain on simulations which are not run on a larger cluster. For this reason regular muons which just pass the water tank were discarded in the cited work. However in the real experiment these "regular" muons are most of what is recorded. A set of simulation data has now been produced which covers a period of approximately one year of regular experimental data. In addition, a second set with muons from the Cngs beam was produced. At the same time, several crucial updates to the simulated geometry of the muon veto were made, which enhanced the simulated data.

For these studies, 10^6 cosmogenic muons and 2×10^5 Cngs muons have been simulated. In addition, 57000 muons with energy deposition in the germanium crystals were simulated as well. As mentioned above, these are very rare events. They are generated by first simulating cosmogenically generated muons which do not emit optical light. Those muons which deposit energy in the crystals were now extracted and their primary generation parameters re-used in another simulation, but this time with optical light enabled. As only a fraction of muons deposit energy, this two-fold simulation process speeds up the generation of muons with energy deposition considerably. The used programmes are Geant4 version `geant4.9.4.p04` and MaGe.

5.6.1 Muon Input Spectra

The standard muon generators already contained in MaGe allows two different settings for placement, spectrum and kinetic energy distribution. The first generates cosmogenic muons with an angular and energy distribution which was measured in great detail by the Macro experiment [Ahl93] as already mentioned in Sec. 5.5. Due to the rock overburden and its shielding power, the muon spectrum is shifted to a mean muon energy of 270 GeV, i.e. all muons that survive the shielding of the rock are of very high energy. In comparison, the mean muon energy on the ground is in the order of $\langle E_\mu(\text{surf.})\rangle =$ 4 GeV [Ber12]. The input spectra are shown in Fig. 5.11, the angular distribution of cosmogenic muons was already shown in Fig. 5.10.

The muons are generated automatically, their primary vertex is set to a disk with $\varnothing$ 20 m which is located 810 mm above the centre of the experiment, i.e. the centre of the detector array. This is already above the lock and the clean room and very slightly above the real physical placement of the scintillator panels. This disk cannot be set much higher, as the primary vertex for muon generation could hence extend
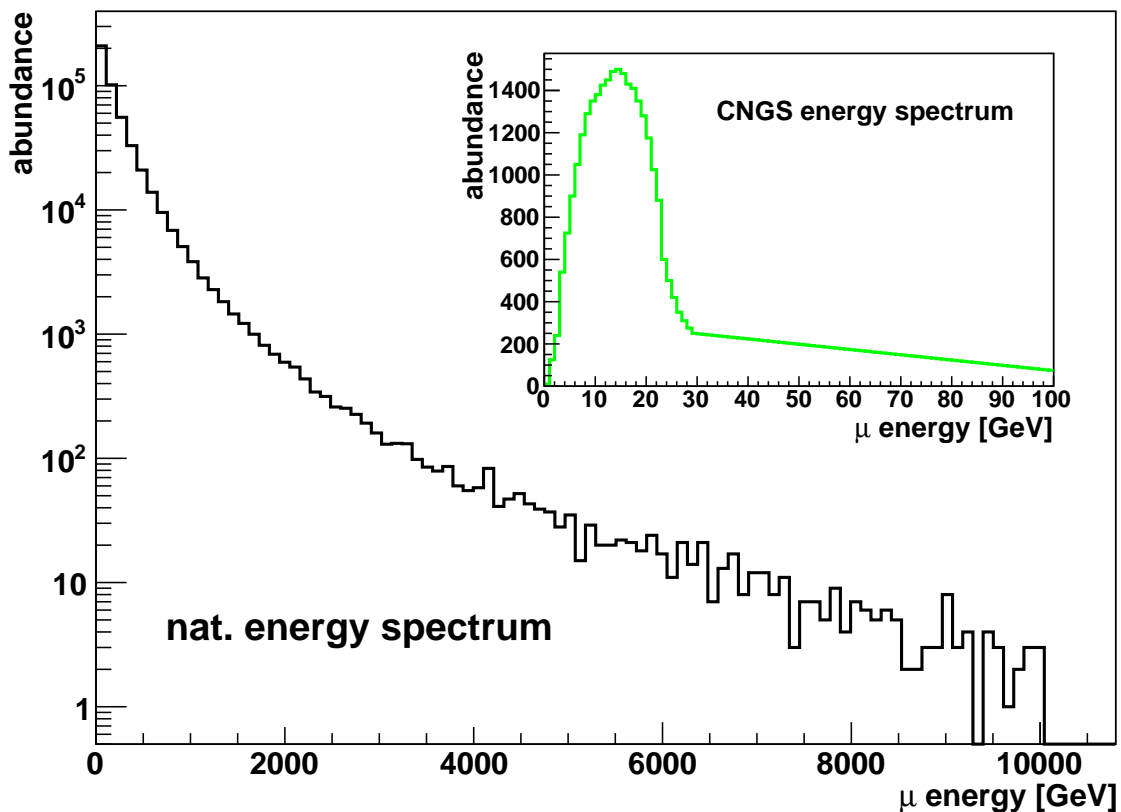
Figure 5.11: *Monte-Carlo input distributions for natural and artificial muons at the LNGS following the* Macro *data [Ahl93] and studies by the* Cngs *[Bal01]. The origin of the* Cngs *muons is a flat disk of ∅ 20 m which is 8 m upstream from* Gerda. *The muons are generated with a momentum slightly elevated (3.5%) to the horizontal.*

into the rock overburden surrounding the experimental hall. This would lead to additional interaction between the muons and the rock and thus distort the realistic input spectrum. As this disk is finite in diameter, muons with a higher initial angle will not be able to hit the experiment. With this set-up, the highest initial angle above the horizon is ≈11°. In the angular distribution of the cosmogenic muons, the abundance of events below this critical angle of ≈11° (or 0.02 in the given graphic) is zero.

For the simulation of the Cngs muons, a different primary generator had to be developed. These muons arrive at an angle ≈3.5° below the horizon and are approximately laminar, i.e. each muon has a different placement, but the same initial momentum. The input spectrum was set to a simulated input spectrum by the Cngs [Bal01]. It has to be noted that the mean muon energy of the Cngs is with $\langle E_\mu(\text{CNGS})\rangle = 17$ GeV much lower in comparison to the cosmogenic spectrum.

The third option is to supply a list of muons in form of a data-file containing the primary vertex, initial momentum and initial kinetic energy. This is especially useful in the case of studying muons with an energy deposition in the germanium crystals. The simulation of muon events is a lengthy process as the muons generate ≈270 phot./cm. All these secondary particles are stored in the memory until the primary track has

ended or left the simulated "world". Afterwards, each secondary particle is pursued until every secondary, tertiary etc. is gone. Thus, the muon energy deposition in the germanium crystals can be evaluated first, without the Cherenkov effect, i.e. no optical photons in the tank. Afterwards the muons with energy deposition may be stored in a data file and now re-used as an input data-file for a simulation with an active Cherenkov effect as already mentioned above. This step is necessary as only a minute fraction of muons at the LNGS—either real or simulated—actually deposit energy in the germanium crystal which makes it difficult to accumulate statistics without the aid of a larger cluster.

5.6.2 Geometries

In the previous model of the geometry of the water tank there were two major inconsistencies with the real experiment. First, only the floor and the wall of the water tank were covered with the reflective foil. The cryostat and the interior of the pillbox was left uncovered. The stainless steel was assigned a reflectivity of 40%, i.e. it was still a decent reflector, however, it did not have any wave-length shifting ability and only a diffuse reflection.

The second inconsistency is the lack of the man-holes of the pillbox. As the metal "skirt" of the cryostat has two 800×650 mm^2 entrances, the volume inside is optically not decoupled from the rest of the water tank. Light which is produced in the main part of the water tank may enter the pillbox and trigger a PMT and vice versa. While these changes appear to be small and are hardly recognizable in the geometry, their effect is all but negligible. The results of this change will be shown in the following.

5.6.3 Photon Spectra

For each event, the primary vertex of the muons, its initial momentum and kinetic energy are stored. In addition multiple values of different detectors in the Gerda set-up are stored. These include energy deposition in the germanium crystals, detection point and PMT of each generated PE, total number of PE, interaction time in relation to the first detected secondary in an event and many more. These values can now be used to compare the simulation with the real data which will be shown in later chapters. At this point it is not possible to give an independent efficiency for the muon veto, as there is no means to calibrate it using either an external muon tagging system or a known source as one would do with a germanium detector. However, if the simulations agree well with the data in terms of spectral shape, amount of detected light and others, efficiencies obtained from the simulations become credible values.

The method of choice for the comparison of simulation and experiment in this case are multiplicity and photon spectra, i.e. the amount of fired detectors or detected PE for a certain class of events. Event-by-event analyses are difficult in this case, due to the poor spacial resolution of the veto. The large volume of the water tank means that the mean photon tracks can be even longer than the attenuation length of photons in water (≈ 10 m), the timing of the DAQ is 100 MHz or 10 ns, in which a photon
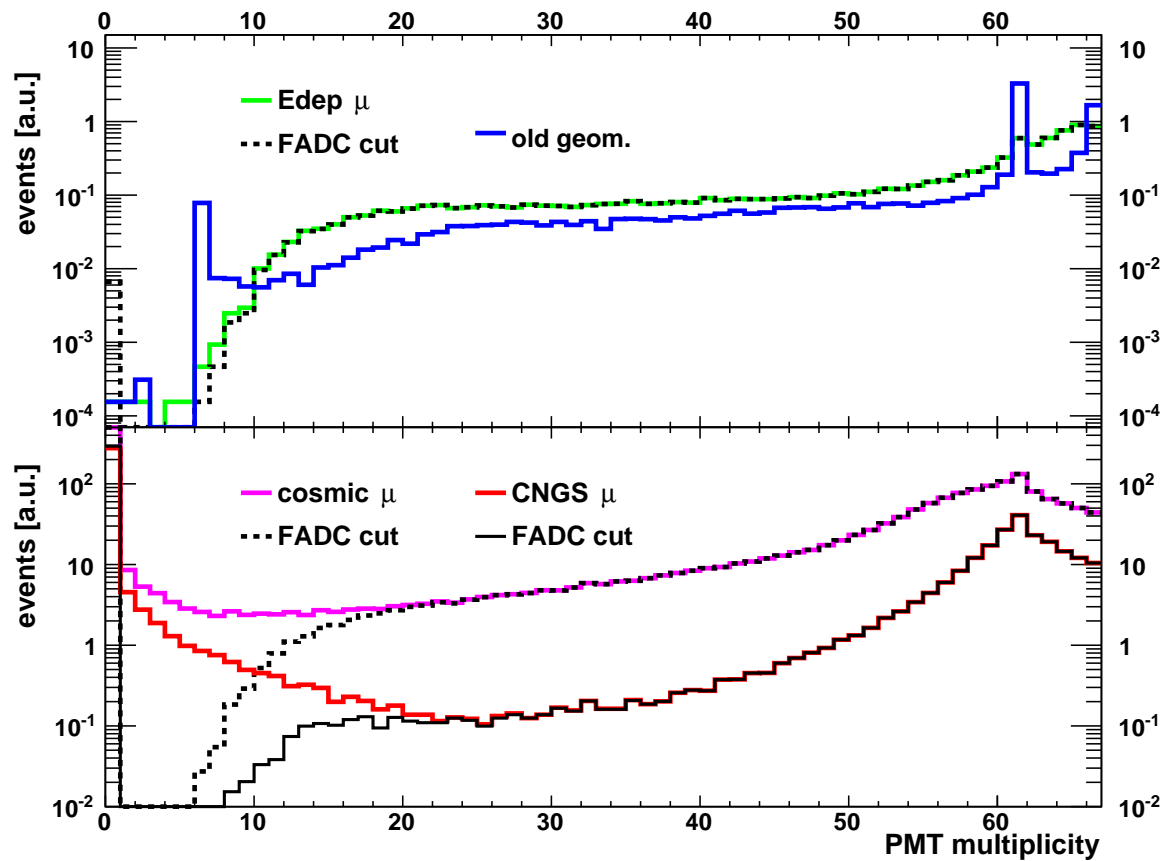
Figure 5.12: *PMT multiplicity spectra of both the simulated cosmogenic and* CNGS *muons. On the top: muons with energy deposition in the germanium crystals and the effect of the updated geometry. On the bottom: comparison of cosmogenic and* CNGS *muons. The effect of the FADC hardware-cuts (5 PMT on different FADCs within 60 ns) are shown in black for each respective spectrum.*

may traverse ≈ 3 m of distance. In addition, the high reflectivity inhibits directional analysis as it cannot be determined if a photon originates from a reflection or directly from the muon track. Hence, different classes of muons are only treated statistically until (or if) these factors can be overcome.

In Fig. 5.12 multiplicity spectra of the three different muon classes are shown. The top panel shows the muons with energy deposition and clearly shows the effect of the updated geometry. Without the openings in the pillbox and the additional reflective surfaces, the multiplicity spectrum shows sharp peaks at six and 60 PMT. This is due to the fact that light produced in the pillbox cannot be detected in the water tank and vice versa. Only events that traverse both volumes can also cause detectable light in each respective volume. With the new geometry this feature disappears and the spectrum is shifted towards higher multiplicities. These muons are direct hits of water tank and cryostat in comparison to the cosmogenic "potshots". Even if a muon traverses only the pillbox on its way through the experiment it will generate many photons, so that sufficient light can escape through the manholes and trigger PMTs in the main tank. The dashed line indicates the effects of a cut which has to be introduced in order to accommodate for the slightly limiting factor of the FADC trigger. Each FADC gives

only one trigger signal which means that if all PMTs on one, two, even three or four FADC have fired, the veto will not trigger, as five FADCs are the trigger condition. As no neighbouring PMTs are connected to the same FADC, this is a very unlikely scenario. It has only an effect on events with a very low multiplicity: only very few events at the low end of the spectrum are cut off. The described FADC-cut will be used in the following Sec. 5.6.4 to determine the detection efficiency of the simulated veto.

In comparison to the muons which deposit energy in the germanium crystals, the cosmogenic and Cngs muons show a defined peak at 60 PMT, a steeper decline towards lower multiplicities but an incline towards multiplicities below six. As these muons hit the tank anywhere and not directly as the energy-depositing class, the produced and detected light can be very low which is represented by the larger numbers of low-multiplicity events. Here, the FADC cut removes the entire low-end tail of both spectra. The peak at 60 PMTs is due to the same effect: as most events do not hit the centre of the experiment, it is more likely to produce light which does not enter the pillbox by chance. The drop from the peak to the low-end tail is approximately two orders of magnitude, the spectrum for the cosmogenic muons is slightly shallower, the Cngs spectrum steeper.

The photon spectra in Fig. 5.13 show several notable features. In each panel, the photon spectrum for all PMTs and just for the pillbox are shown for all three classes of muons. The main peak for the pillbox spectrum shifts notably for the Cngs spectrum in comparison to the other two. This results from the mean length of the path of the muons take water tank. The pillbox is a cylinder with a diameter of 4 m and a height of 1.35 m. In all cases, the main peak determines the average amount of light deposited for the most likely track-length for the respective muon class. The average incident angle for the cosmogenic muons is 34° off the zenith and if a mean maximum height of 1.5 m is assumed, a track length of 1.6 m is found. The Cngs muons however arrive straight from the side, i.e. the maximum track length is 4 m. The respective peaks in the simulation data are at (186 ± 65) and at (494 ± 111) detected PE. The ratio of both the distances and the detected PE is 2.6, which leads to the assumption of a correlation between deposited light and track length. In a similar vein, the average traversed length in the water tank is 9 m for cosmogenic muons and 6 m for Cngs muons and the peaks shift accordingly. The longest possible track for both classes would be 13 m and 10 m respectively, however the cryostat with a diameter ⌀4 m lowers the mean track-lengths considerably. The double structure between 200–400 PE in the spectrum of energy-depositing muons stems from the necessary track the muons have to take in order to pass the detector array and given the most common incident angle. As the muons have to pass the cryostat, they can produce light either before or after passing the cryostat and the germanium detectors. Under the most common angle, the tracks in the main water tank can be assumed to be ≈ 2.5 m, which represents the lower peak. As these muons are very likely to hit the pillbox with the aforementioned 1.5 m effective track length, the higher peak represents a sum peak of both volumes. The two peaks are of almost the same height, which confirms this. The same is true for the highest peak in the Cngs spectrum. The feature at low PE number is so far not understood, especially since it is not observed in the data. The comparison to the experiment will be made in detail in Sec. 6.7. It will be seen that data and simulations agree well which makes the following step—i.e. an efficiency determination based on the simulations—a valid
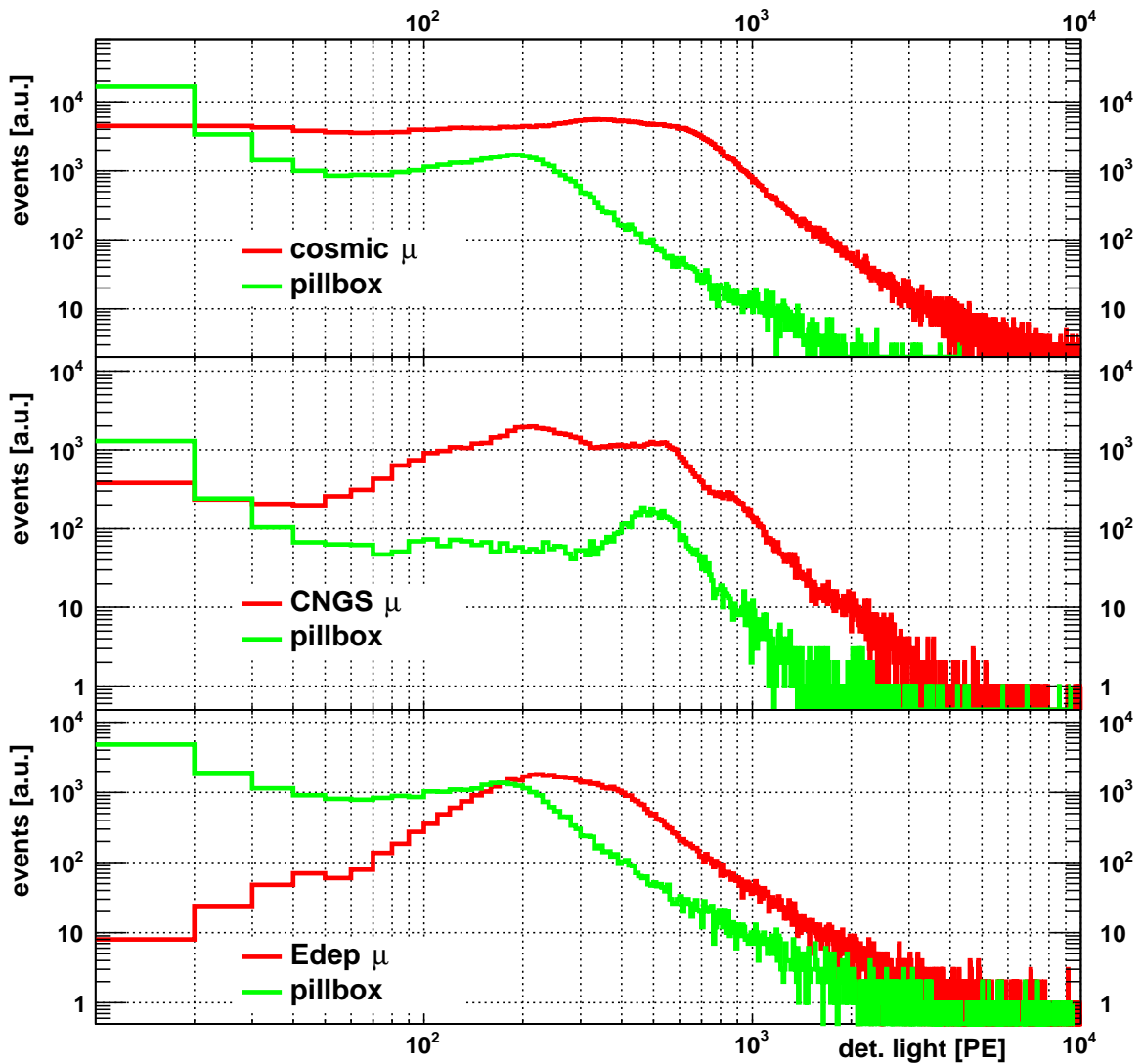
Figure 5.13: *Photon spectra of the simulated muons for light in the pillbox (green) and the entire water tank (red). The top panel shows the spectra for cosmogenic muons, the middle for* Cngs *muons and the bottom panel shows muons with energy deposition.*

Table 5.5: *Updated efficiencies of the simulated veto. The common trigger condition is that five FADC have fired within 60 ns. A "-" notes removed detectors or FADC and "−"−" indicates the same as above.*

set-up	efficiency [%]	set-up	efficiency [%]
full veto	(99.935 ± 0.015)	-FADC 1	(99.905 ± 0.015)
four FADC trig.	$(99.955^{+0.015}_{-0.005})$	-(FADC 1,2)	$(99.525^{+0.025}_{-0.035})$
-106	(99.925 ± 0.015)	-(FADC 1–3)	(96.055 ± 0.085)
-(105,106)	$(99.835^{+0.025}_{-0.015})$	-(207,208,311,312)	(99.915 ± 0.015)
-(104–106)	$(99.175^{+0.045}_{-0.035})$	−"− -(409,410)	(99.895 ± 0.015)
-(103–106)	(97.855 ± 0.065)	−"− -(206,309,310,408)	$(99.865^{+0.015}_{-0.025})$
-(207,305,401,604)	(99.925 ± 0.015)	−"− -(508–510)	$(99.845^{+0.015}_{-0.025})$

option.

5.6.4 Efficiency Updates

A PMT usually is a sturdy detector, which can function well over many years. However, every detector can suffer an early end and break down. Due to flaws during manufacture (especially concerning the glass of the entrance window), the PMT may break either literally or in terms of electronics. The same is true for the electronics involved. As the efficiency of the veto is critically dependent on working detectors, a number of additional efficiency calculations were performed with the updated geometrical model. All of these values are listed in Tab. 5.5.

For the efficiency calculations, only the simulated muons with energy deposition (short: "edep") were considered as these are the crucial events that need to be tagged. The events from cosmogenic muons or from the Cngs beam may be only glancing hits of the water tank and cause not even enough light to be detected. However, since almost none of these events interact with the germanium crystals a high efficiency is welcome, but not strictly necessary.

The method of obtaining an efficiency is to apply a cut on the hardware constraints on the data. As the trigger logic described previously may prevent an event from being detected, this FADC-cut has to be applied to the data. The muons can thus not be detected because they either produce insufficient light in general or because the combination of triggered PMTs prevents a hardware trigger. The ratio of detected muons to all energy-depositing muons gives a Muon Detection Efficiency (MDE).

Several different set-ups for the MDE-determination of the simulated events are considered. First and most importantly, the MDE for the completely intact Cherenkov veto system with the current trigger condition described in Sec. 5.3 including the placement of the PMTs on the FADCs. With the updated geometry an MDE of

$$\varepsilon_{\mu d}^{\text{sim}} = (99.935 \pm 0.015)\% \tag{5.1}$$

is found. This is higher in comparison to the value of $(99.56 \pm 0.42)\%$ cited in [Kna09] despite the fact that for this value a trigger on four FADCs was demanded instead

of five as in this work. The increase in detection efficiency can be credited to the enhanced geometry, i.e. the higher reflectivity of the walls due to the reflective foil and the openings in the pillbox. When a four-FADC trigger condition is assumed the efficiency rises to even higher values.

In the next steps, several scenarios for detector malfunction were considered. Starting with the PMTs in the pillbox, a number of PMTs are removed and the efficiency drops accordingly. However, only when three or more out of the six pillbox PMTs are removed, the efficiency drops below the previously cited efficiency. Even with four pillbox-PMTs discounted the efficiency is still at $(97.855 \pm 0.065)\%$.

Over the course of the first phase of GERDA four PMTs (i.e. PMTs 207, 305, 401 and 604) broke or were malfunctioning (see Sec. 6.1.1 in the following chapter). This can be seen as a test of four randomly distributed PMTs breaking down and the efficiency is still above $\varepsilon > 99.9\%$ which is an assuring result for this real experimental scenario for Phase I. In the following, more unlikely scenarios were tested, first the break-down of one or more FADC. For one or even two entire FADC the efficiency is still above 99% only when a third FADC breaks down the efficiency drops to 96%. In the last step, a growing cluster of PMTs is removed from the analysis. At first, only four PMTs on the floor (i.e. PMTs 207, 208, 311 and 312) are removed. This cluster is increased until 13 PMTs i.e. almost 20% are not working anymore. However, even with all 13 PMTs removed, the efficiency is still a lot higher in comparison to the loss of two pillbox PMTs.

From these calculations, it can be concluded that the loss of multiple PMTs in the water tank undesirable, but not crucial. Even if one or two entire FADCs are removed, the efficiency is still over 99% albeit this scenario is very unlikely. However, if only very few pillbox-PMTs are removed, the efficiency drops much more steeply as the loss of many more PMTs in the main water tank. This means that the loss of more than one PMT in the pillbox should be considered as a reason for an exchange of the detectors at the next possible opportunity.

MUON VETO DATA AND PERFORMANCE

In this chapter the overall performance of the muon veto will be reported. First, the hardware status in between the first two phases of GERDA will be given. Of particular interest is the reliability of the encapsulated PMTs and all of the components. Afterwards, the recorded data will be shown. The data will be de-convoluted into the contributions by cosmogenically and artificially produced muons and naturally occurring changes in the muon rate will be shown. An estimation for non-muonic components seen by the muon veto will be given. These findings will be compared to Monte-Carlo studies based on earlier works but with updated parameters.

6.1 PMT PERFORMANCE

The GERDA muon veto was installed in several sessions in 2009. Originally, a single installation period was planned but the earthquake which devastated the Abruzzo region on the 6th April 2009 interrupted the work and it had to be resumed later in the year once the region stabilized and it was responsible enough to resume the work. The PMTs were immediately tested after installation with a portable HV-supply and a scope. The the DAQ was installed in March 2010 and shortly after the water tank was test-wise filled for the first time. A drainage test followed afterwards and allowed access to the water tank for the last time before the system was prepared for continuous operation. The DAQ of the muon veto has since been running continuously with very few exceptions starting in November 2010. The duty cycle of the muon veto can be seen in Fig. 6.1. The major interruptions of data acquisition in Summer and November 2011 are due to first tests of the panels and the final installation of the entire plastic scintillator veto. The main germanium background-runs of Phase I are highlighted in red and green. Other, smaller interruptions in the data taking are either calibrations of the veto or other short maintenance works. These happen only in dedicated pauses in the germanium data acquisition, either during germanium calibrations or during work on the germanium-related hardware when the germanium DAQ is off-line. There was no artificially induced dead-time in the germanium data due to an unforeseen
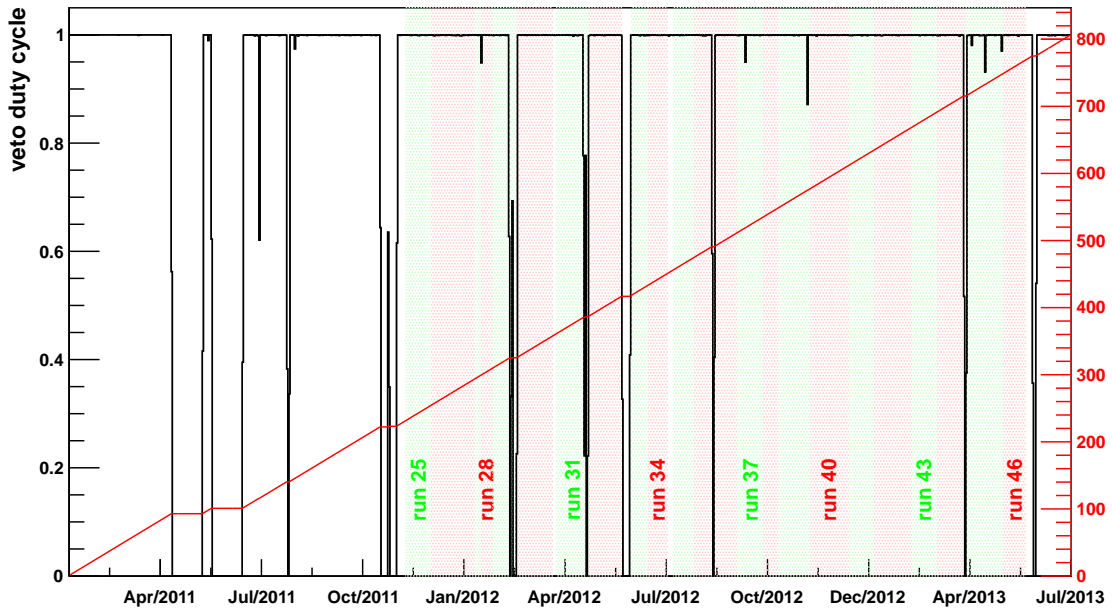
Figure 6.1: *Duty cycle of the muon veto. The main physics runs of* Gerda *Phase I are highlighted. In the shown period, 805.6 live days of muon data was recorded.*

malfunction of the veto.

The PMTs were encapsulated in 2008 and the performance of the PMTs over time is of crucial interest to the function of the veto. A PMT is a very dependable detector, which can be active for years without any significant deterioration in performance. The design of the capsules is sturdy as well. An overall dependable detector is needed as in the case of Gerda, the water tank cannot be simply drained and refilled once a single PMT is broken and needs to be exchanged. The rates of all PMTs was recorded over the duty-cycle shown in Fig. 6.1. These individual PMT duty-cycles are collected in App. B.1. The PMTs show little to no change in their respective rates, there are a few exceptions which will be examined in the following section. Overall, there is very little change in the individual rate, i.e. in the performance of each PMT.

6.1.1 Cherenkov Hardware Performance

During the first test-wise filling of the water tank in 2010, the submerged PMTs could be tested in situ for the first time. Here, it was found that there were two problematic PMTs, one of which could be immediately exchanged. In August 2013, the Gerda water tank was drained again after the end of Phase I and the veto could be accessed [GSTR13-19]. It remained unopened for three years which warranted an inspection of the surfaces for signs of rust in the solid steel of the water tank and especially the cryostat. The VM2000 foil covering the cryostat was largely unaffected but was found ripped open over a length of ≈1.5 m. This was most likely due to a pocket of water which accumulated between the foil and the insulating layer of Jackodur. As this piece of foil did not rip off, it was still held in place by the nylon rope, which was wound
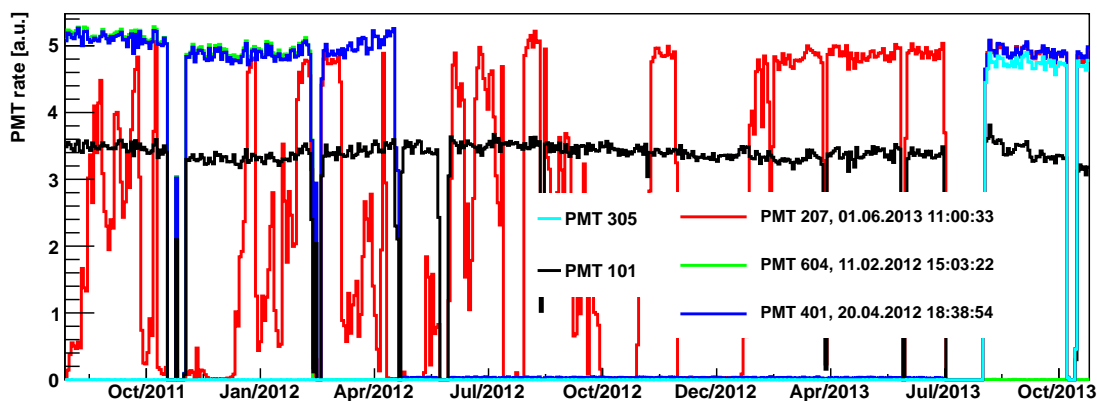
Figure 6.2: *Duty cycle of the malfunctioning PMTs. The date when PMTs 604 and 401 stopped working is more than 2 months apart. PMT 207 shows erratic behaviour but is stable especially towards the end of data taking. Pillbox-PMT 101 is included for comparison.*

around the cryostat. This opening was used to examine the solid steel on the cryostat and another small piece of foil was removed from a weld in the water tank to check for possible corrosion underneath, but none was found under the foil. Both holes were closed afterwards.

During this work the PMTs could be inspected and maintained as well which was taken as an opportunity exchange problematic detectors. In addition to the remaining PMT which was broken from the start, three more were mal-performing or outright broken. The duty cycle of these PMTs is highlighted in Fig. 6.2. All five mal-performing PMTs are listed in the following:

PMT 203: No signal from the start. The capsule was exchanged after the first filling of the water tank and is working since the beginning of continuous data-taking and hence not listed in Fig. 6.2.

PMT 305: Lost very soon after the first test-wise filling of the water tank. It was found that the underwater HV cable was punctured in a way that a discharge between signal fibre and shield was possible. The PMT was removed and the cable sealed with polyurethane before the start of Phase I.

PMT 604: Last signal: 11.02.2012, 15:03:22. Due to the very high current (i.e. > 1 mA), its HV channel switched itself off as a precaution ("I-tripping").

PMT 401: Last signal: 20.04.2012, 18:38:54. I-tripping after an $\approx 30\,\text{s}$ long burst of light.

PMT 207: As can be seen in Fig. 6.2, this PMT only works sporadically. The traces of this PMT are however satisfactory. Especially during the last months of data taking, this PMT was stable.

After opening the water tank in 2013 it was found that both PMTs 401 and 604 had imploded. The Polyethylene (PET) cap of both PMTs ruptured and spilled glass and

Table 6.1: *The properties of the two spare PMTs*

cap.	PMT	∅ bubble	gain: 2×10^7	DCTS (given/lab)	note
7	401	25 mm	1615 V	9850/11790	oily, bubble 6 cm
18	305	41 mm	1620 V	3800/19680	

oil into the tank. The floor directly underneath the PMTs had a small pool of glass shards and all the surfaces inside water tank showed traces of the spectroscopy oil used in the PMTs. Each PMT contains about 1-2 l of oil. Since the oil of the imploded PMTs was drained, it could pose a possible health hazard. According the manufacturer the used spectroscopy oil is neither a hazardous nor a dangerous material under EU regulations [SA14]. Overall, there was a maximum of 4 l of mineral oil in a total volume of 590.000 l of water. While the oil will be detectable in the drained water, the amount of oil in the water is minimal. The residual traces of oil in the water tank will be further reduced as the water is in constant circulation and cleaned by the Gerda water plant.

No other PMT capsule in the water tank seemed to be damaged in any sort of way. However, the plastic based parts of most PMTs had a strongly visible milky tint to them, i.e. the PET caps of the PMTs and the additional epoxy sealing in order to stop oil leaks. In this case, the PET cap is of course the much more critical part. However, no deterioration of the PMTs performance was visible over time as already mentioned. One PET cap was of particular interest during the maintenance. After a longer exposition to a bright light source, the cap of this PMT got very milky but only on the illuminated side. It cleared up after the flood light was adjusted again. The other milky caps cleared up over time, as well.

In addition, the air bubbles which are usually found in every capsule between PE cap and PMT had vanished over time. Usually, these air bubbles can vary from 2-50 mm in diameter in upright position, depending on how well the capsule could have been filled with oil. Over time, these bubbles disappeared. However, the caps of almost all PMTs were still found to be soft and under no tension. Only PMT 408 had a very tight fitting cap.

Prior to the exchange, the four spare PMTs were tested underground. The two best PMTs were chosen to be the replacement. Unfortunately, one spare PMT did not work at all and the second had an operating voltage of 2100 V which is close to the limit for the PMT. Thus, it was decided to exchange only two of the four PMT: 401 & 305. The values for the remaining two PMTs are shown in Tab. 6.1, see [Rit12] for the full PMT list. The air bubble of capsule 7 had grown in size due to a loss of oil. Since the PMT did not get oily after the last cleaning and since the air bubble is not overly large, it was still usable. Due to the bubble the PMT was placed on the wall. Especially the operating voltages of the PMTs were due to change, after first being operated in water. After the exchange, an immediate in-situ test with the existing calibration system was performed. For this, all the opened flanges for the water drainage had to be closed, i.e. the chimney flange, the flange for the ventilation and most importantly the manhole flange. Since the manhole flange could not easily be closed it had to be covered with several sheets of thick black cloth in order to assure basic light tightness. Due to the
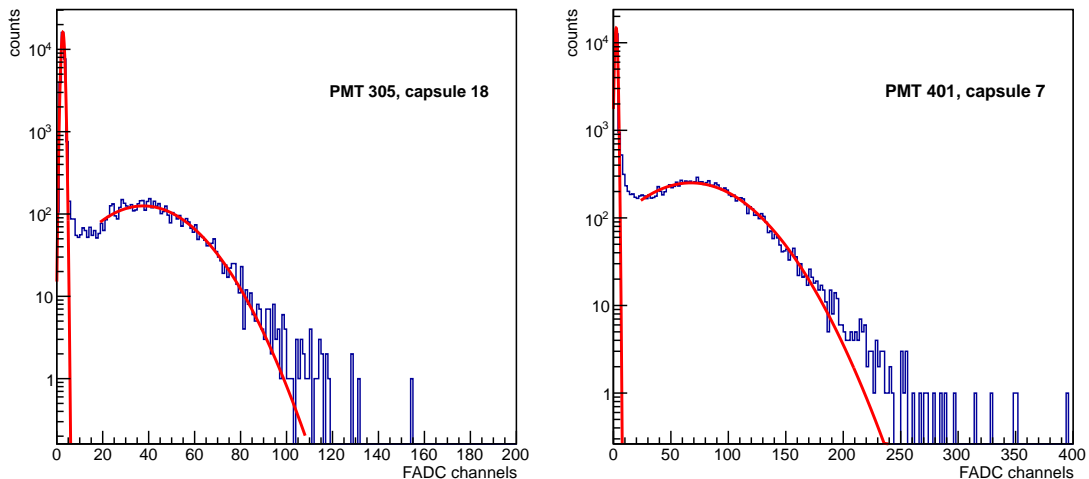
Figure 6.3: *"First light" of the exchanged PMTs. The single photon peak and the pedestal for both exchanged PMTs is shown with a gaussian fit to each (red lines). This measurement was taken inside the water tank with the veto calibration system. The mean of the SPP for PMT 305 is found at 35 channels over the pedestal, for PMT 401 at 65 channels.*

fear of a light leak, the PMTs were not operated at full voltage, but at 1500 V instead. Both PMTs successfully responded to the calibration light pulses and the spectra could be recorded. The SPP for both PMTs can be seen in Fig. 6.3. The SPP for PMT 305 is only 35 channels over the pedestal with the aim being 100 channels. This is rather low in comparison to the aim, but had been adjusted after the water tank was re-filled with water. However, the overall functional efficiency of these PMTs could be demonstrated.

6.2   "First Light" of the Panel Veto

The panels are arranged in three layers covering an area of 4×3 m^2 centred over the neck of the cryostat. It was aimed to keep both trigger rate and thus data volume of the veto as low as possible without compromising the muon detection efficiency. Therefore the triple layer was realised since it offers a high discrimination against non-muonic background events such as $\gamma\gamma$-coincidences. Bottom and middle layer are placed on top of each other, whereas eight panels of the top layer are turned by 90° to achieve a pixelation.

The panel data was available for the entire period of Phase I data taking as the installation of the panels happened just before the start of the physics runs. The rates of each separate pixel can be found in Tab. B.1 in App. B.2. It has to be noted that pixel 15-18 and 27-30 show a significant lower rate that the other pixel. All eight pixel share FADC channel #16. However, the traces recorded by this channel do not show irregularities or other indications that either the pixel mapping or the hardware is malfunctioning. Further investigations are necessary, but for now the eight pixel in question only contribute negligibly to the overall rate.

The recorded rates for different selections can be found in Tab. 6.2. Given that the
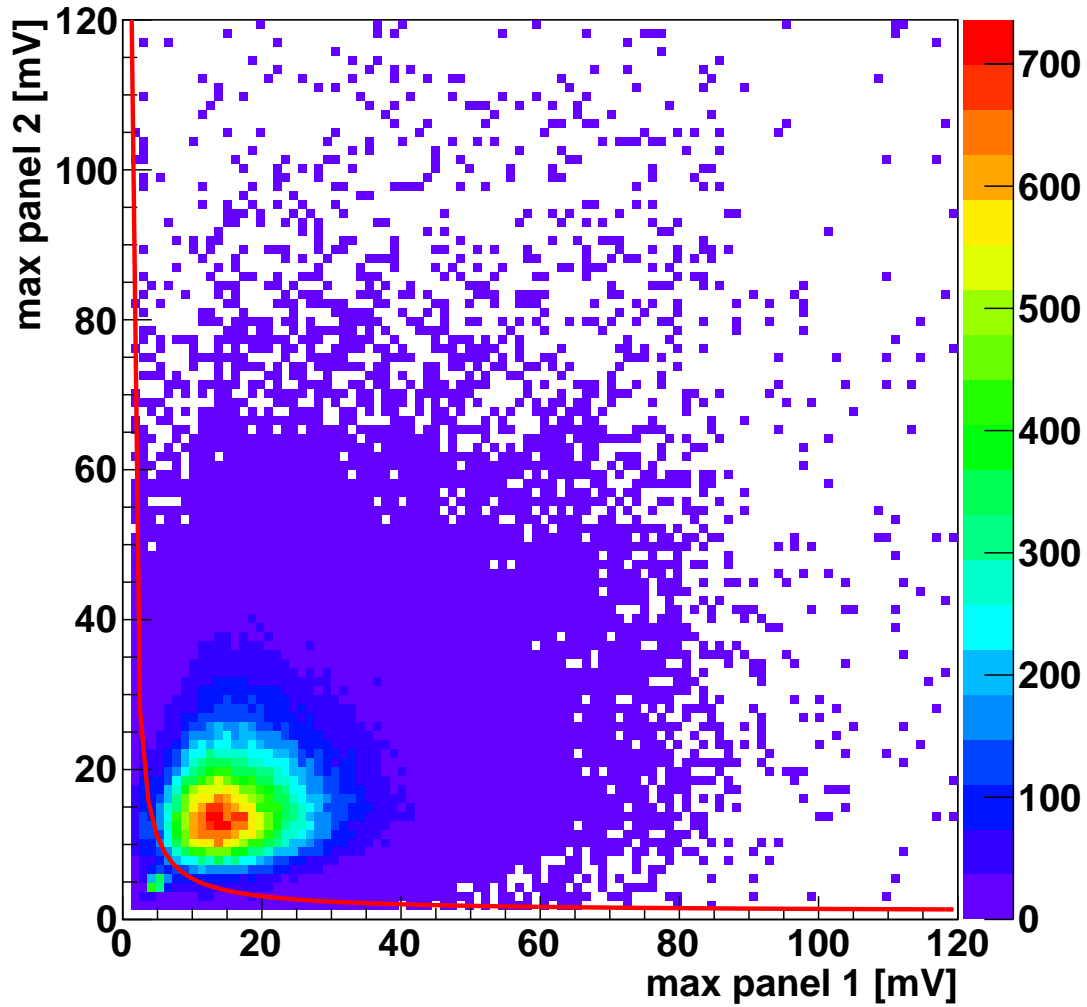
Figure 6.4: *Scatter plot of the maximum PMT pulse height of two panels in a triple stack using the finalized panel stack. This plot contains all recorded events of all valid pixel. The red curve is a $1/x^2$ cut.*

Table 6.2: *Measured rates for the pixelated panel stack. The random rate for the panels in coincidence with one PMT is calculated within 600 ns, which is the window set by the used conversion software to find coincident events even outside the trigger window.*

set-up	rates [1/s]
entire veto	4.08×10^{-2}
Cherenkov veto	3.61×10^{-2}
panel veto [$8.9\,\mathrm{m}^2$]	2.90×10^{-3}
single pixel trigger [$8.9\,\mathrm{m}^2$]	2.10×10^{-3}
panel trigger, no Cherenkov PMT	5.91×10^{-4}
panel trigger, 1-5 Cherenkov PMT	7.63×10^{-4}
random rate, all panels + 1 PMT	8.28×10^{-6}
rate of non-valid pixels	1.26×10^{-4}

effective area of the panel stack is only 8.9 m^2, the rate for the panel trigger is in agreement with the value for the muon flux given in Tab. 5.1. Most events are recorded by the Cherenkov veto, the panels record only $\approx 7\,\%$ of the total rate. While the overall panel rate fits the expectation, the rate of events where only a single pixel has fired is significantly lower. These events dismiss smaller showers however, i.e. events which have produced secondaries which are able to trigger other panels, too. Approximately 45 % of the panel events cause little to no light in the Cherenkov veto. This is due to the predominant angle of $\approx 60°$ in which the muons hit the experiment. As the scintillator veto is ≈ 4 m over the water tank there is already considerable lateral displacement in relation to the middle of the tank when an average muon passes the panels. The expected random rate of the entire scintillator veto with only a single PMT is $8.28 \times 10^{-6}/$ s and hence more than two orders of magnitude below the overall trigger rate of the scintillator veto of 2.90×10^{-3}/s (see Tab. 6.2). It is so low, that any Cherenkov response to a valid scintillator event has to be considered directly caused by a muon. The rate of events, which show an overall invalid FADC combination, i.e. an invalid pixel is 0.43 % of the rate of total scintillator events. From these rates alone, it can be said that the scintillator veto is performing well. The measured rates are within expectation and the random coincidences are low.

However, there is a small background of γ-coincidences remaining in the scintillator panels (see Sec. 5.2). This effect becomes visible when e.g. the pulse height of two panels in a stack are studied as already shown Fig. 5.4. In Fig. 6.4, this is shown for the entire muon data. The main structure is a Landau-peak, one from each panel. While in Fig. 5.4 this structure was barely discernible, here it emerges very clearly but the centre of the Landau-peaks is visible in both plots. However, there are a number of γ-coincidences at low pulse heights. These events can be discarded with an x^2-cut that takes the form:

$$(x_1 - 2)(x_2 - 2) < 200, \tag{6.1}$$

where $x_{1,2}$ is the minimum pulse height of the two panels, all values are in [mV]. In Fig. 6.4 this cut is indicated with a red line. The effect of this cut can also be studied
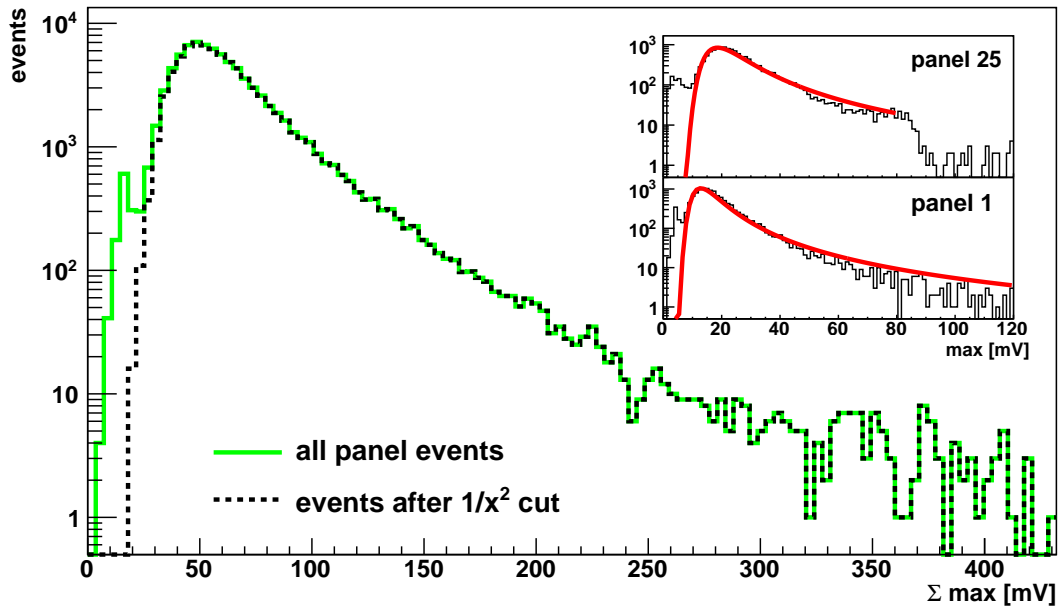
Figure 6.5: *The summed pulse height of all panels in an event triggered by the plastic veto. When an $1/x^2$ cut is applied to the overall spectrum (green line), the low energy contribution caused by γ-coincidences disappears (dashed line). The two inlays show individual pulse height spectra of two select panels with a Landau fit (red line).*

when looking at the summed pulse height of all panels in a pixel, which can be seen in Fig. 6.5. The Landau-like green spectrum exhibits a tail towards small pulse-sums. When the x^2-cut is applied, the dashed spectrum remains, which discards this tail almost entirely. The overall shape of this spectrum should be a Landau-peak as well. However, it was already mentioned in Sec. 5.2 that for a significant time during the measurement, the power supply was insufficient for the front-end electronics. The effect can be seen in the two insets. Here, two panel pulse height spectra are shown with a Landau-curve in red fit to the data. While one panel shows a decent agreement, the pulse heights of the other are shifted below a certain maximum but still well above the trigger threshold. After the installation of a new power source the front-end electronics was working properly in all the panels and hence this issue has been resolved for the next Phase of Gerda.

The overall performance of the scintillator veto could be demonstrated. The rates and spectra fit, with small background contribution and electronic irregularities well with the expectations.

6.3   Plastic Veto Detection Efficiency

In order to evaluate the efficiency of the panels, data from the four un-pixelated stacks were used since the triple coincidence is much easier to obtain in terms of the data-analysis. In addition, the efficiency of the pixelated stacks is expected to be slightly lower. The insensitive region at the edges of and between the panels extends less than 5 mm. Thus the un-pixelated panels lose 0.25% and the pixilated 0.1% in addition.

In order to obtain a reliable efficiency, a data sample of clearly identified muons had to be selected. For the panel events a simple cut on the pulse height is insufficient due to the γ-coincidences at low pulse heights. In addition to the pulse height cut, the x^2-cut mentioned above was applied. As the scintillator veto may still be subject to non-muonic background, a trigger in the Cherenkov veto was demanded as well. This way it could also be assured the events were caused by a muon. For the Cherenkov events a strong cut on the multiplicity was chosen. The detection efficiency of one panel can now be given as the ratio of events, in which the top and bottom panel of a stack have fired in comparison to the events where all three panels in a stack have fired. The specific cut conditions are:

- > 19 PMTs in the Cherenkov veto have fired

- threshold of 20 FADC channels ($\approx 2.44\,\mathrm{mV}$) for top and bottom panel in a stack

- only one panel per layer has fired

- soft pulse height product cut

The data set contained events since the beginning of the muon data taking with the panels in August 2011. Since then, $29\,951$ out of $30\,044$ of the events which triggered the top and bottom panel were found which triggered the sandwiched panel as well as the top and bottom ones. This leads to an average muon detection efficiency for the four middle panels with 68% confidence intervals of:

$$\varepsilon_{\mu d}^{\mathrm{P}} = 99.70^{+0.03}_{-0.05}\% \tag{6.2}$$

Since this value is an average over four different panels, it can be seen as an approximation for a general panel efficiency. The efficiency of a triple stack of panels is hence the product of three single efficiencies, i.e. $\varepsilon_{\mu d}^{\mathrm{P},3} = 99.10^{+0.09}_{-0.15}\%$. This efficiency is very promising towards an overall muon rejection power of the muon veto.

6.4   Veto Stability

In order to make assumptions about the stability of a detector observing a physical effect, the stability of the effect itself has to be evaluated first. The angular and spectral distribution of the naturally occurring muon flux are well known as is the average muon rate. Both of these have been measured with e.g. the Macro experiment with great precision and were confirmed by the subsequent experiments at the LNGS [Ahl93]. However, the real muon flux is more complicated. As already mentioned in Sec. 3.2, there is an additional artificial component in the muon flux from March to November caused by the Cngs beam. In addition there is a natural modulation of the muon flux caused by temperature changes in the earth's atmosphere (see Sec. 6.6). The overall muon rate can thus be approximated with a function of the form:

$$I_{\mu}(t) = I_{\mu}^0 + \Delta I_{\mu}^{\mathrm{art.}}\cdot\Theta(t - t_1)\Theta(t_2 - t) + \Delta I_{\mu}^{\mathrm{nat.}}\cdot\cos\left(\frac{2\pi}{T}(t - t_0)\right), \tag{6.3}$$

where $I_{\mu}(t)$ is the overall and I_{μ}^0 the mean muon flux. The artificial influence $\Delta I_{\mu}^{\mathrm{art.}}$ caused by the Cngs beam is indicated by two heavy-side functions for $0 < t < 1\,\mathrm{yr}$
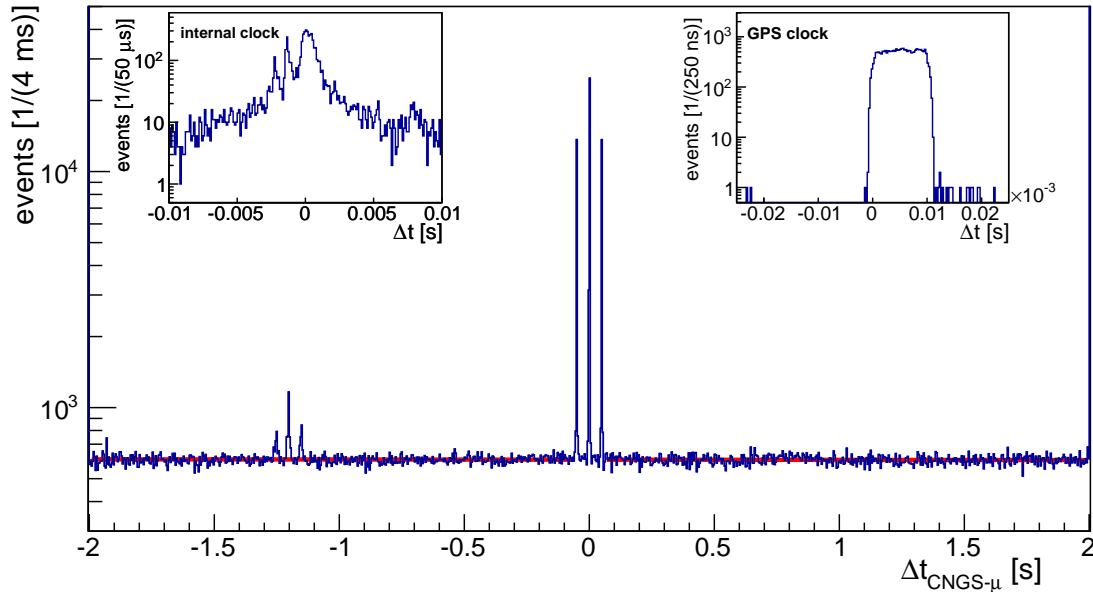
Figure 6.6: *Time difference between* Cngs *beam (at t=0) and the* Gerda *muon veto. The left inset shows the main peak structure measured with an internal clock prior to the start of the* Gerda *physics runs. The right inlay shows the same triggered with a GPS clock and represents the width of a* Cngs *bunch of 10.5* μ*s.*

depending on the duty-cycle of the accelerator between t_1 and t_2. The effect of the natural modulation $\Delta I_\mu^{\mathrm{art.}}$ can be described in first order approximation with a sine-like function. In the following sections, these two components and their effect on the overall muon flux will be introduced, calculated and shown in the taken muon data. First the influence of the Cngs beam will be studied and subtracted from the data as this is not an intrinsic property of the "normal" muon flux. Afterwards, a simplified version of Eq. 6.3 can be fit to the muon data.

6.5   Cngs-induced Muon Flux

In order to gauge the influence of the Cngs beam on the measured muon rate, a data sample from the Cngs was acquired. The data spans from November 2010 until December 2012, when the LHC was shut down for maintenance and upgrades. The Cngs subsequently ceased beam production as well and it will not resume duty once the upgrade is finished. Thus, none of the following effects that the Cngs has on Gerda will be of any importance in further Phases of Gerda.

The data of the Cngs contained timestamps and measured charges for each beam extractions. Since the scintillator veto is placed almost perpendicular to the beam, it was not taken into account for the following analysis. The events from both DAQ systems were compared by studying the amount of muon events which fall into a certain time around each Cngs event, as can be seen in Fig. 6.6. The timestamp of the Cngs events have been shifted by 2.4 μs in order to correct for the TOF of the neutrinos in the 732 km between Cern and LNGS. A trident-like structure around $t = 0$ dominates
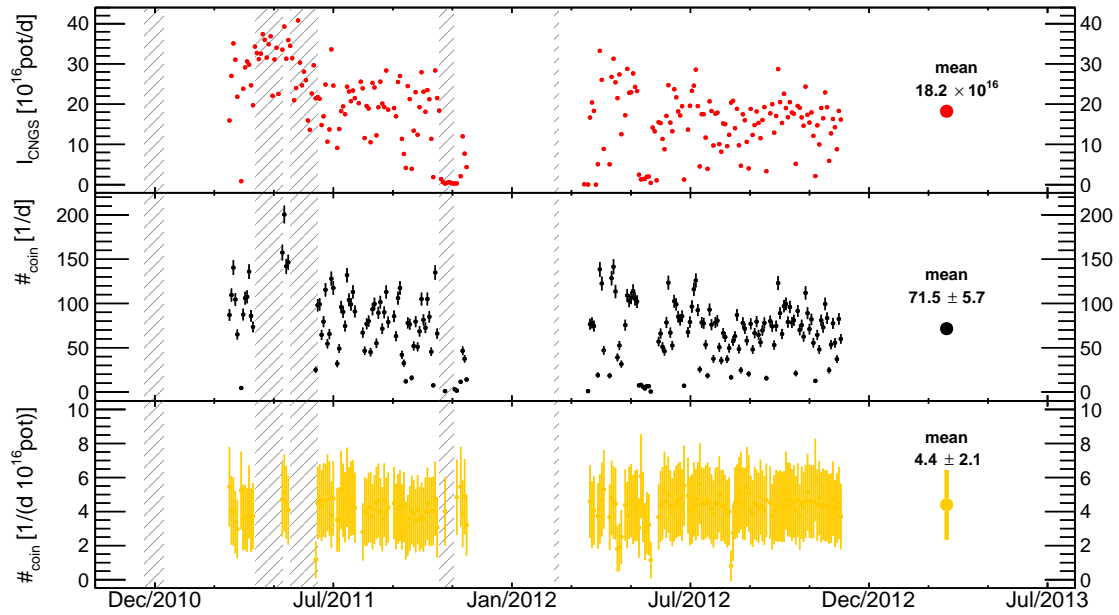
Figure 6.7: Cngs *beam intensities and coincident events over time. The top panel shows the beam intensity measured at CERN. The middle panel shows the coincident events as defined by the main peak structure in Fig. 6.6. The bottom panel shows the ratio, which indicates that the number of coincident events is proportional to the beam intensity. The grey hatched areas mark pauses in the muon data-taking.*
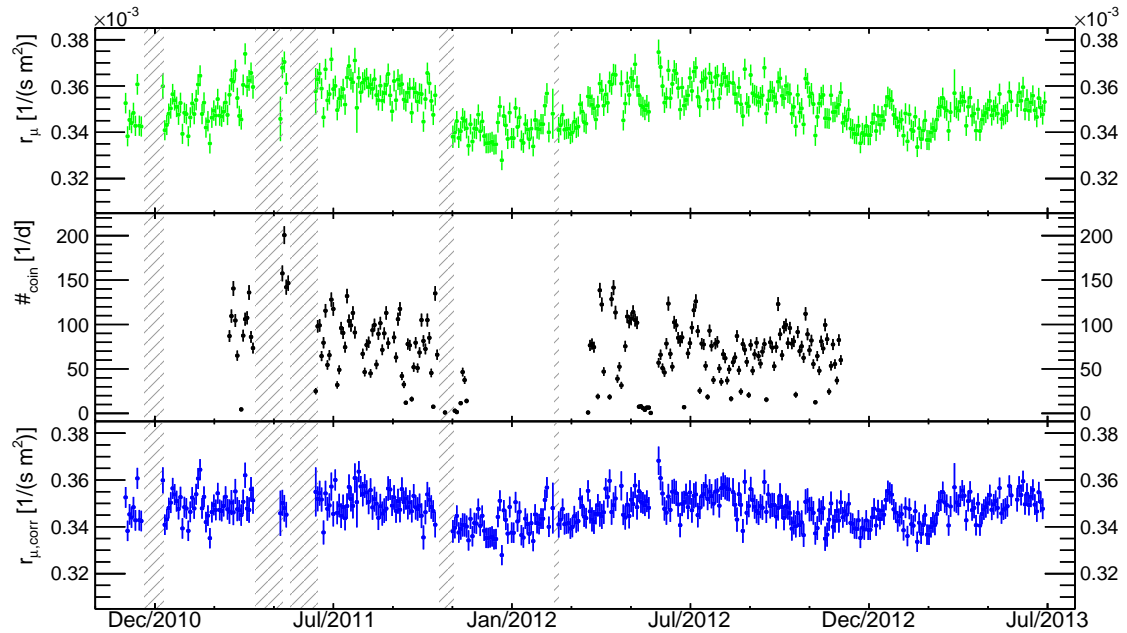
Figure 6.8: Gerda *muon rate corrected by the coincident* Cngs *events. The top panel shows the uncorrected muon rate, the middle panel the coincident events (see Figs. 6.6,6.7) and the bottom panel displays the corrected muon rates over time.*

the spectrum, the "tines" of the trident are 50 ms apart. With each extraction from the SPS the Cngs sends two bunches of neutrinos to the LNGS which are 50 ms apart with a regular repetition time of 6 s. Each bunch has either another bunch immediately following or preceding it. Since all of these cases are counted, the smaller tines represent the next or previous bunch. Since some extractions only consist of one bunch, the two smaller tines are a bit less than half of the middle tine. If a bunch does not produce a muon, but the other one does, it is still counted.

The width of the middle tine of this structure can be seen with higher resolution in the two insets. Prior to the start of the physics runs of Gerda in November 2011, the clock systems of both the muon and the germanium DAQ systems of Gerda was upgraded. Before the upgrade, both systems had used internal clock systems, i.e. standard on-board oscillators in the DAQ-PCs. The stability of these oscillators is usually sufficiently high for all application for either the PC or an experiment. However, long-term drifts in the range of seconds per year are not uncommon which is the time-frame of this measurement. Since the upgrade, both systems are continuously synchronized with the GPS clock primarily used by the Opera experiment. The two inlays of Fig. 6.6 represent the time resolution for both clock systems. While the internal clock shows a rather wide time distribution of 5-10 ms, the distribution with the GPS clock is little over 10 μs wide, which corresponds to the width of each proton bunch extracted from the SPS into the Cngs. This means that with the GPS clock, the Gerda muon veto is able to almost fully reproduce the exact beam structure at the Cngs.

With this accuracy the next step would be to study the exact time difference between the two experiments. However, these TOF measurements concerning the speed of particles on these distances are rather difficult. All concerning parameters have to be known exceedingly well, like exact distance, time resolutions, interaction speed of the secondaries and many more. Since there are other experiments which are better suited for such a task and as there were already ambiguous results from other experiments (see [Ada11, Ada12]) this shall not be attempted for these data.

The second trident-like structure at -1.2 s is caused by sudden shifts in the data sets without GPS clock. As the clock was not synchronized every second, sudden "hiccups" like this or drifts of the clocks cannot be ruled out. This feature entirely disappears with the better clock.

Apart from these features, the random coincidences are distributed flatly. A red fit function in Fig. 6.6 indicates the level of the random coincidences at 602 events per 4 ms bin. The data contained 3.98×10^6 valid Cngs events over a time of 404 days, i.e. an overall rate of $(0.114 \pm 0.006)/\text{s}$. Compared with the overall rate of the muon veto of $\approx 0.036/\text{s}$, this reproduces the measured level of background quite well.

Since the data provided the amount of POT at Cngs as well as the timestamps, the relation between beam intensity and amount of coincident events could be studied. In Fig. 6.7 time series of the events can be seen. The top panel shows the beam intensity for the operational period of the muon veto from Dec.2010-Jul.2013. The grey areas note pauses in the muon veto DAQ for upgrades or maintenance. The middle panel shows the amount of coincident events which is equal to 2.2% of the entire muon rate which is equal to the artificial muon flux $\Delta I_\mu^{\text{art.}}$ from Eq. 6.3. Heaviside functions can obviously only serve as a rough approximation of this part of the muon flux, but still describe the overall behaviour well. The target area of Gerda for particles from the
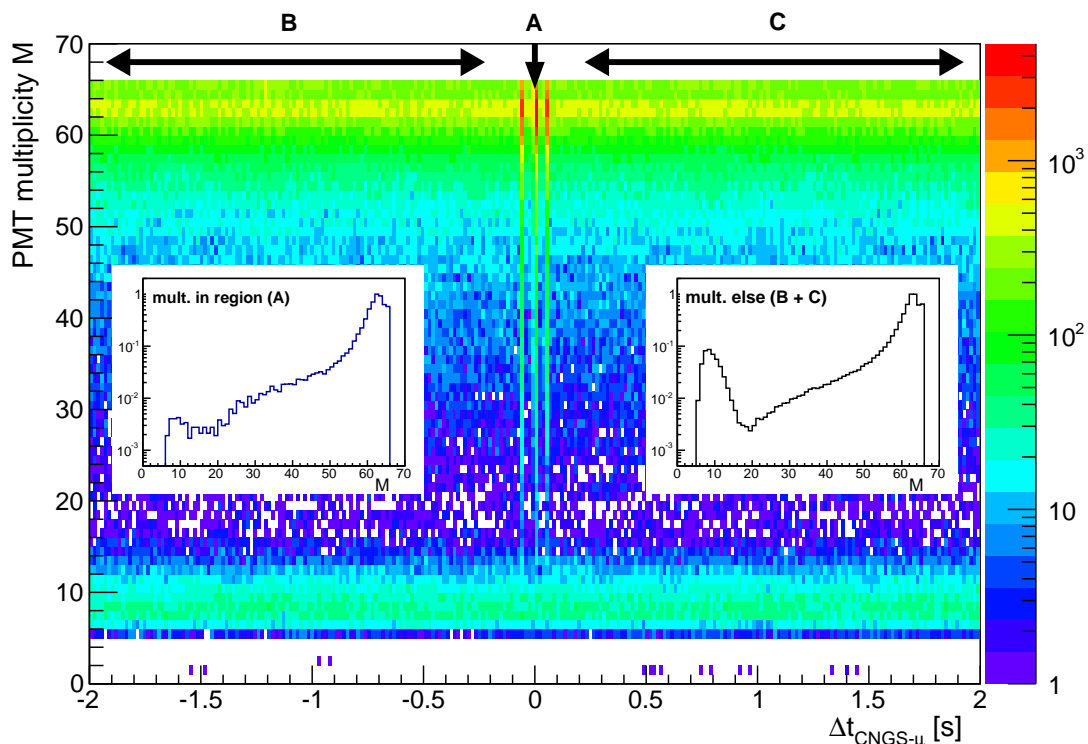
Figure 6.9: *PMT multiplicity spectrum in relation to the offset Δ_t between CNGS and muon veto events. The two insets show the multiplicity in the middle region (A) and elsewhere (B+C). Both histograms are normalized to its respective maximum.*

side is $\approx 8.5 \times 10$ m^2. This leads to a rate of 0.84 muons/(d m^2) which is lower than the rate of 1.2 muons/(d m^2) quoted by Lvd [Agl04]. Since the "effective" or active area in a cylindrical volume as GERDA is difficult to compare with an experiment as Lvd, this can be interpreted as a decent match. The bottom panel show the ratio of the CNGS events and coincident events, i.e. the amount of coincident events per POT and day. The flat distribution shows that the beam intensity is correlated with the amount of coincident events.

These events can now be used to correct the muon data. Fig. 6.8 shows the time series for the muon data. The measured muon flux is usually given normalized on the mean muon flux at the LNGS, see Sec. 5.5). The top panel shows the normalized rate for the Cherenkov veto. The middle panel shows the number of coincident events. The bottom panel is now the muon rate corrected for the number of CNGS events which shows a rate of 3.6×10^{-2}/s or 3.4×10^{-4}/(s m^2). Both the full and the corrected rates show a sine-like behaviour the origin of which shall be explored in Sec. 6.6.

Finally, since the CNGS events can be identified so well, the effect of these muons on the veto system can be studied in more detail. In Fig. 6.9 the PMT multiplicity in comparison to the time offset between the CNGS and the muon veto event can be seen. The coincidence window is the same as in Fig. 6.6. The multiplicity in the middle peak (denoted with "A") and the multiplicity in outside of the peak region ("B+C") is shown in the two insets. While the multiplicity in the other regions exhibits an enhancement in the region of 5-20 PMTs, the other does not. The CNGS events can
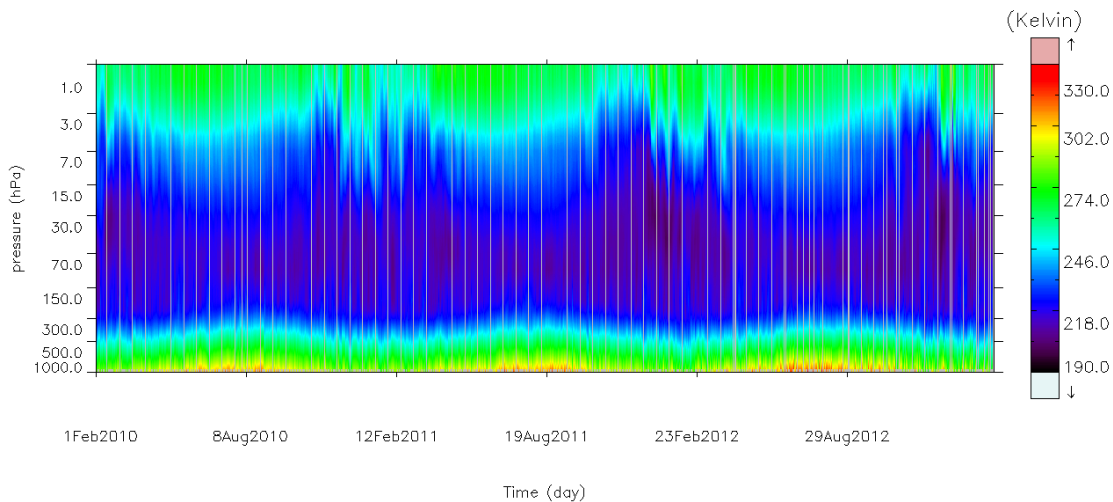
Figure 6.10: *Atmospheric temperature profile recorded by AIRS and retrieved via the online software Giovanni (see text). The data show the temperature for each level of atmospheric depth expressed in terms of the level's pressure at at 1.a.m., i.e. for the ascending path of the satellite. The data was interpolated for the location of the LNGS (42.47° N, 13.56° E) in the period from 01.Feb.2010-28.Feb.2013. The grey bars are missing data.*

be seen as a beam of pure muons. Hence the multiplicity spectrum is uncontaminated by non-muonic components. This effect will be discussed in more detail in Sec. 6.8. However, thanks to the precise GPS clock used for both DAQ systems, the Cngs contribution to the muon flux could be tagged and corrected with very high precision. The observed rate agrees with previous measurements and good correlation between Cngs beam intensity and number of induced muon events was found.

Not only the Gerda experiment is subject to this additional muon flux, but all other experiments at the LNGS as well including the Cresst experiment which is Gerda's neighbour in the Sala A. A data sample of the Cresst muon veto system has been acquired[†] and a similar analysis has been performed though in less detail. The results are presented in App. C.

6.6 Seasonal Change of the Muon Flux

The annual modulation of the muon flux caused by temperature changes in the earth's atmosphere is a well-studied phenomenon [Gra08, Bel12, Amb97]. Due to the shielding effect of atmosphere and rock overburden, only cosmogenically produced muons with an energy above a certain threshold E_{thr} will be able to penetrate an experiment located in a certain depth. As already mentioned, muons are the decay product of π- and K-mesons. Depending of the mean free path Λ_M of these mesons, energy of a produced muon will be lowered depending of how often the meson has undergone scattering in its lifetime. The mean free path depends on the density ρ of the medium. Given that the

---

[†]K.Rottler, *priv.com.*, 2014
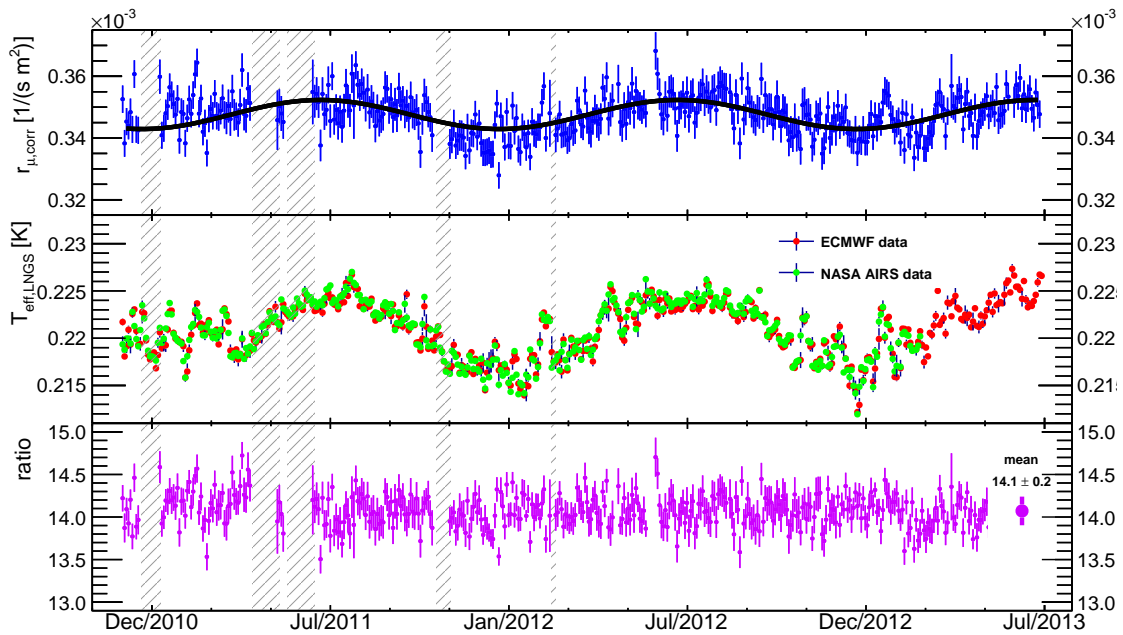
Figure 6.11: *Top: the annual modulation of the rate of the muon flux. Middle: effective atmospheric temperature T_{eff} for the muon production. The data set of the ECMWF [ECM13] is shown in red, the set of the AIRS module on-board the NASA Aqua satellite [Par03] is shown in green. Bottom: ratio of the two.*

gas in the atmosphere can be treated as an ideal gas, the ideal gas equation applies:

$$pV = nRT, \tag{6.4}$$

where p is the pressure, V the volume, n the number of particles, T the temperature and R the Boltzmann constant (8.314 J/(K mol)). Thus, if the temperature of a fixed volume at a fixed pressure is raised, it becomes less dense. The mean free path increases and hence the mean muon energy is higher. Conversely, this means that on the earth's surface this effect is only very small as the muon spectrum is shifted but not the overall flux. In this section, a model for the quantitative treatment developed in [Gra08] will be briefly introduced and applied to the data.

There are two sets of atmospheric temperature data available for the studied period between Nov. 2010-June 2013. The ECMWF [ECM13] offers climate data taken by many different observational methods such as weather stations, aircrafts, balloons and satellites to interpolate the climate at any given location. For each location, temperature data for 37 atmospheric pressure levels from 0-1000 hPa are listed four times a day. The second data set is provided by the AIRS instrument on-board the NASA Aqua satellite [Par03] and retrieved with the online software Giovanni[†]. The satellite is in a synchronous orbit with the sun and thus passes each position of the earth twice per day. The ascending overflight over the Gran Sasso is at about 01:00 a.m. and the descending overpass at 01:00 p.m. AIRS is an infra-red sounder and can therefore be disturbed by clouds. Similar to ECMWF it provides temperature data in

---

[†]The analyses regarding the AIRS data and the visualization Fig. 6.10 were produced with data retrieved with the Giovanni online data system, developed and maintained by the NASA GES DISC.

24 different pressure levels at any given point. A temperature profile over time recorded by AIRS for the area of the Gran Sasso (i.e. 42.47° N, 13.56° E) is shown in Fig. 6.10. This was taken for the ascending path of AIRS, i.e. at 01:00 in the morning. The most obvious feature is the inversion layer of the atmosphere at a pressure level of 30 hPa. In addition, the seasonal change of the temperature even in the higher layers of the atmosphere is apparent. This includes short-term jumps of the temperature. Usually, the temperature is given at certain pressure levels, not atmospheric height, however for illustrative purposes it serves sometimes to give an atmospheric height as well. The relation between an atmospheric pressure level in [hPa] and the height in [km] follows the barometric formula for a standardized atmosphere:

$$p = p_0 \left(1 - \frac{L\,h}{T_0}\right)^{\frac{g}{R}\frac{M}{L}} \tag{6.5}$$

$$\approx p_0 \exp\left(-\frac{g\,M\,h}{R\,T_0}\right) \tag{6.6}$$

where p_0 is the standard pressure at sea level (1013 hPa), L the temperature lapse rate (0.0065 K/m), T_0 the standard temperature at sea level (288.15 K), g the standard gravity (9.81 m/s²), M the molar mass of air (0.0290 kg/mol) and R the gas constant (8.31 J/(mol K)). This formula is only valid for static atmospheres and can thus only be used as a general guideline and is used in plots like Fig. 6.12 for reference.

The temperature change is seasonal which means that the choice for a sine-like function for the temperature change in Eq. 6.3 is justified. Since the artificial component has been eliminated in the previous section, the equation for the muon flux takes the simpler form:

$$I_\mu(t) = I_\mu^0 + \Delta I_\mu \cos\left(\frac{2\pi}{T}(t - t_0)\right), \tag{6.7}$$

where $I_\mu(t)$ is the overall and I_μ^0 the mean muon flux. For the GERDA experiment, a fit of the data (see Fig. 6.11) yields a muon flux of $I_\mu^0 = (3.477 \pm 0.002_{\text{stat}} \pm 0.06_{\text{sys}}) \times 10^{-4}/(\text{s·m}^2)$, a modulation of $\Delta I_\mu = (4.72 \pm 0.33) \times 10^{-6}/\text{s}$ or $(1.4 \pm 0.1_{\text{stat}})\%$ and a phase t_0 which shifts the maximum to the 10$^{\text{th}}$ of July (± 4 days). The period was set to one year for two reasons. First, the exposure of the GERDA muon veto is short in comparison to other experiments (see Tab. 6.4) and in addition the winter of 2010 was irregularly warm, which puts a strain on statistics and systematics regarding the period.

The deviation $\Delta I_\mu(t)$ from the detected average muon flux depends on the change in temperature $\Delta T(P, t)$ in a given layer of the atmosphere dP. The overall change of the muon flux can then be written as an integral over all layers:

$$\Delta I_\mu(t) = \int_0^\infty dP W(P) \Delta T(P, t) \tag{6.8}$$

The $W(P)$ is a weight function which approximates the contribution of the mesons $M = \{\pi, K\}$ to the overall muon intensity. It is a sum of two parts for the two contributing mesons $W(P) = W^\pi + W^K$. Each part has the form:

$$W^M(P) \simeq \frac{(1 - P/\Lambda_M')^2 \exp(-P/\Lambda_M) A_M^1}{\gamma + (\gamma + 1) B_M^1 K(P)(\langle E_{\text{thr.}} \cos\theta \rangle / \epsilon_M^0)^2} \tag{6.9}$$

Table 6.3: *Input parameters for the W(P) function.*

parameter	value
A_π^1	1 [Gra08]
A_K^1	$0.38 \cdot r_{K/\pi}$ [Gra08]
$r_{K/\pi}$	(0.149 ± 0.06) [Gai90]
B_π^1	(1.460 ± 0.007) [Gra08]
B_K^1	(1.740 ± 0.028) [Gra08]
Λ_N	120 g/cm^2 [Gai90]
Λ_π	180 g/cm^2 [Gai90]
Λ_K	160 g/cm^2 [Gai90]
$\langle E_{\text{thr}} \cos\theta \rangle$	1.833 [Gra10]
γ	(1.78 ± 0.04) [Amb95]
ϵ_π	(0.114 ± 0.0003) TeV [Gra08]
ϵ_K	(0.851 ± 0.0014) TeV [Gra08]

and

$$K^M(P) = \frac{(1 - P/\Lambda'_M)^2}{(1 - \exp(-P/\Lambda'_M))\Lambda'_M/P} \tag{6.10}$$

where P is the atmospheric pressure level and γ the muon spectral index. $\Lambda_{N,\pi,K}$ denotes the attenuation lengths for primaries, pions and kaons. The values for A_M^1 includes both the amount of mesons produced in forward direction as well as the branching ratios; values are $A_\pi^1 = 1$ and $A_K^1 = 0.38 \cdot r_{K/\pi}$ where $r_{K/\pi}$ is the kaon to pion ratio. The parameters B_M^1 note the relative atmospheric attenuation for mesons. The parameter ϵ_M^0 is the critical meson energy where decay and and interaction processes are in equilibrium for an isothermal atmosphere, i.e. $T(P) = T_{\text{eff}}$. For the values of the threshold energy for a certain depth and the zenith angle the median value for the LNGS is used $\langle E_{\text{thr.}} \cos\theta \rangle = 1.833$ TeV. All input parameters, their values and sources are summarized in Tab. 6.3. The mean atmospheric temperature for both data sets with the respective weight function can be seen in Fig. 6.12. As in Fig. 6.10 the inversion layer of the atmosphere is clearly visible. The weight function is highest in the upmost layers of the atmosphere. Since the atmosphere gets denser rapidly, the amount of scattering the first mesons undergo gets higher as well. Thus, in lower part of the atmosphere only few muons can be produced that have an energy that is high enough to penetrate a certain depth.

The mentioned effective temperature T_{eff} is a weighted average of the temperature over all N layers of the atmosphere, given that the atmosphere is considered to be an isothermal body and can be approximated as follows:

$$T_{\text{eff}} = \frac{\int_0^\infty \Delta P T(P) W(P)}{\int_0^\infty \Delta P W(P)} \tag{6.11}$$

With the weight function defined in Eq. 6.9, the effective temperature can be calculated for both temperature data sets. The corrected muon rate for Gerda and the effective temperature T_{eff} for the LNGS is shown in Fig. 6.11. Both muon rate and T_{eff} follow
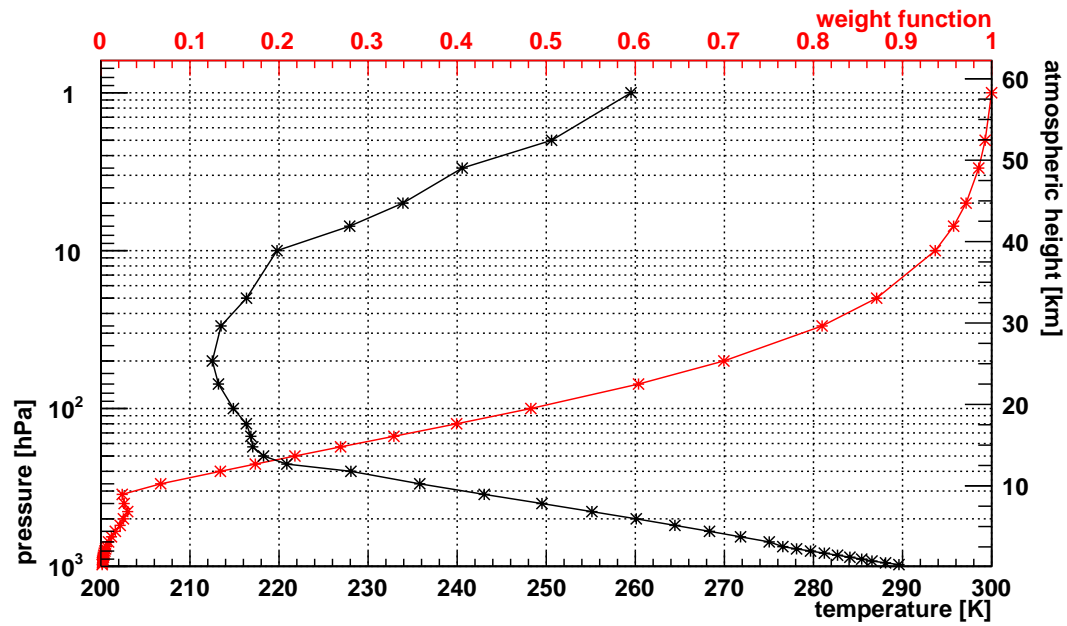
(a) ECMWF data
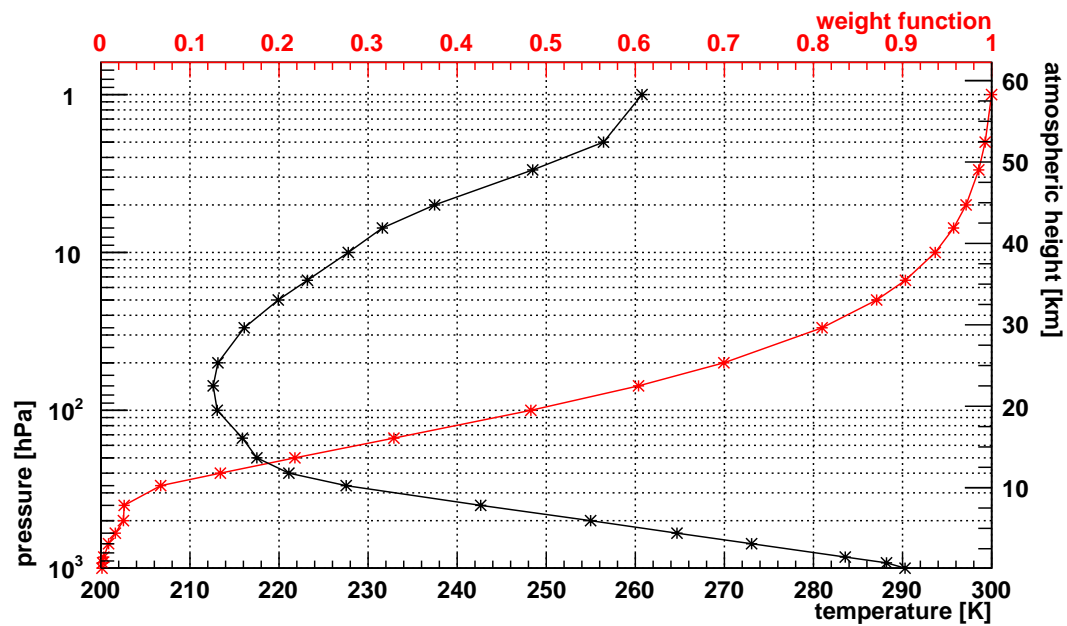
(b) AIRS data

Figure 6.12: *Atmospheric temperature (black) and effective temperature weight function (red) for the data provided by the ECMWF [ECM13] and by NASA AIRS [NAS13].*
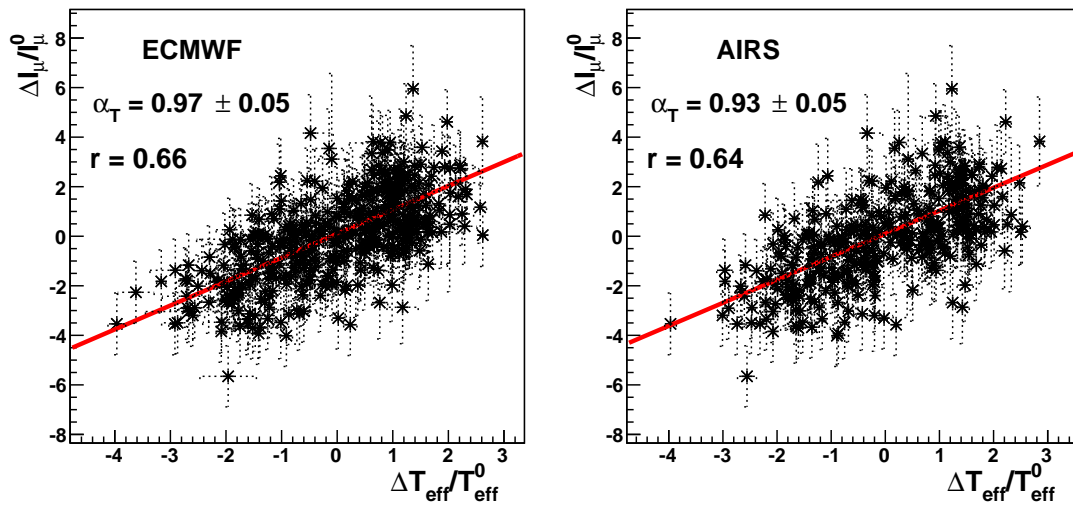
Figure 6.13: *Dependence of the change in muon rate and the change in effective temperature, for both sets of temperature data.*

a seasonal change with about the similar phase and amplitude. Sudden warm spells as for example in spring 2013 are reproduced nicely in the veto. The ratio of the two curves shows a flat distribution over time, which already indicates a good correlation. In order to quantify the correlation between the temperature and muon flux the correlation coefficient R (see App. A for details) of $\Delta I_\mu / I_\mu^0$ and $\Delta T_{\mathrm{eff}} / \Delta T_{\mathrm{eff}}^0$ was calculated. A graphical representation can be seen in Fig. 6.13, the R coefficient of both data sets is above 0.6 and thus a positive linear dependency can be assumed. Therefore the change in temperature and muon flux can be written as

$$\frac{\Delta I_\mu}{I_\mu^0} = \alpha_T \frac{\Delta T_{\mathrm{eff}}}{T_{\mathrm{eff}}^0}, \tag{6.12}$$

where α_T is an "effective temperature coefficient". With Eq. 6.8, this coefficient becomes

$$\alpha_T = \frac{T_{\mathrm{eff}}^0}{I_\mu^0} \int_0^\infty dP W(P). \tag{6.13}$$

Thus, the linear dependency between the change in temperature and muon flux gives a value for α_T, which contains like $W(P)$ the threshold energy of the respective depth. The derived $\alpha_{T,ecmwf} = (0.97 \pm 0.05)$ and $\alpha_{T,airs} = (0.93 \pm 0.05)$ is in agreement with the values derived from Borexino $\alpha_{T,bor} = (0.93 \pm 0.04)$ [Bel12] or Macro $\alpha_{T,mac} = (0.91 \pm 0.07)$ [Amb03]. These and other parameters are listed for comparison in Tab. 6.4. The temperature data from the Aeronautica Militare Italiana used for Lvd and Macro is taken at a military base ≈ 130 km from the LNGS. Both ECMWF and AIRS are superior in accuracy and coverage [Bel12]. It has to be noted, that the muon rate increases from the earliest noted experiment in Tab. 6.4 (i.e. Macro) to the latest (i.e. Gerda) over time. For the most part, the values are within the error bars of the next experiment, but an overall 7% increase between Macro and Gerda can be observed. This would be equal to an increase in the effective atmospheric temperature of ≈ 15 K, a feature which is not reproduced e.g. in the AIRS data starting from (31st Aug. 2002). Since the statistical error on these measurements especially with a long

Table 6.4: *List of parameters for the annual modulation of the muon rate after [Bel12].*

experiment	Lvd	Macro	Borexino	Gerda
site	LNGS-A	LNGS-B	LNGS-C	LNGS-A
duty cycle [y]	8	7	4	2.5
active years	2001-08	1991-97	2007-11	2010-13
E_{thr} [TeV] / [km.w.e.]	1.833 / 3.4	1.833 / 3.4	1.833 / 3.4	1.833 / 3.4
rate [1/(s·m^2)]	(3.31 ± 0.03)	(3.22 ± 0.08)	(3.41 ± 0.01)	(3.47 ± 0.06)
period [d]	(367 ± 15)	–	(366 ± 3)	–
phase [d]	(185 ± 15)	–	(179 ± 6)	(191 ± 4)
temp. data	Aer.Mil.	Aer.Mil.	ECMWF	ECMWF/AIRS
T_{eff} model	π	π	π+K	π+K
correlation	0.53	0.91	0.62	0.62/0.65
α_T	–	(0.91 ± 0.07)	(0.93 ± 0.04)	(0.97 ± 0.05)
$(\alpha_{T,\text{LNGS}} = 0.92)$				(0.93 ± 0.05)

exposure tends to be low, a systematical errors like e.g. uncertainties in the precise active surface can be considered. Therefore, this effect has to be noted and further investigated, as the warming of the atmosphere cannot be responsible for this. But as the systematic uncertainties tend to be rather large and thus the errors not negligible, the values are not inconsistent.

As already mentioned, the parameter α_T depends on the slant depth of the laboratory, where the muon flux was measured. As is apparent from Tab. 6.4, the values for different experiments at the LNGS are in good agreement, despite the fact that the atmospheric models used for Macro and Lvd omitted the kaonic component for simplicity reasons since it is small. However, in order to compare this value with different experiments at other locations, first the theoretical values for the different slant depths have to be calculated. The energy spectrum of the muons, i.e. the starting point of this calculation is given by [Gai90]:

$$\frac{dI_\mu}{dE_\mu} = \int_0^\infty \mathcal{P}_\mu(E, P) dP \tag{6.14}$$

$$\simeq A \times E^{-(\gamma+1)} \left(\frac{1}{1 + 1.1 E_\mu \cos\theta/\epsilon_\pi} + \frac{0.38 \cdot r_{K/\pi}}{1 + 1.1 E_\mu \cos\theta/\epsilon_K} \right). \tag{6.15}$$

This can be re-written as [Bar52]:

$$\alpha_T = -\frac{E_{\text{thr}}}{I_\mu^0} \frac{\partial I_\mu}{\partial E_{\text{thr}}} - \gamma \tag{6.16}$$

With Eq. 6.8 and Eq. 6.13 this becomes:

$$\alpha_T = \frac{1}{D_\pi} \frac{1/\epsilon_K + A_K^1 (D_\pi/D_K)^2/\epsilon_\pi}{1/\epsilon_K + A_K^1 (D_\pi/D_K)/\epsilon_\pi} \tag{6.17}$$
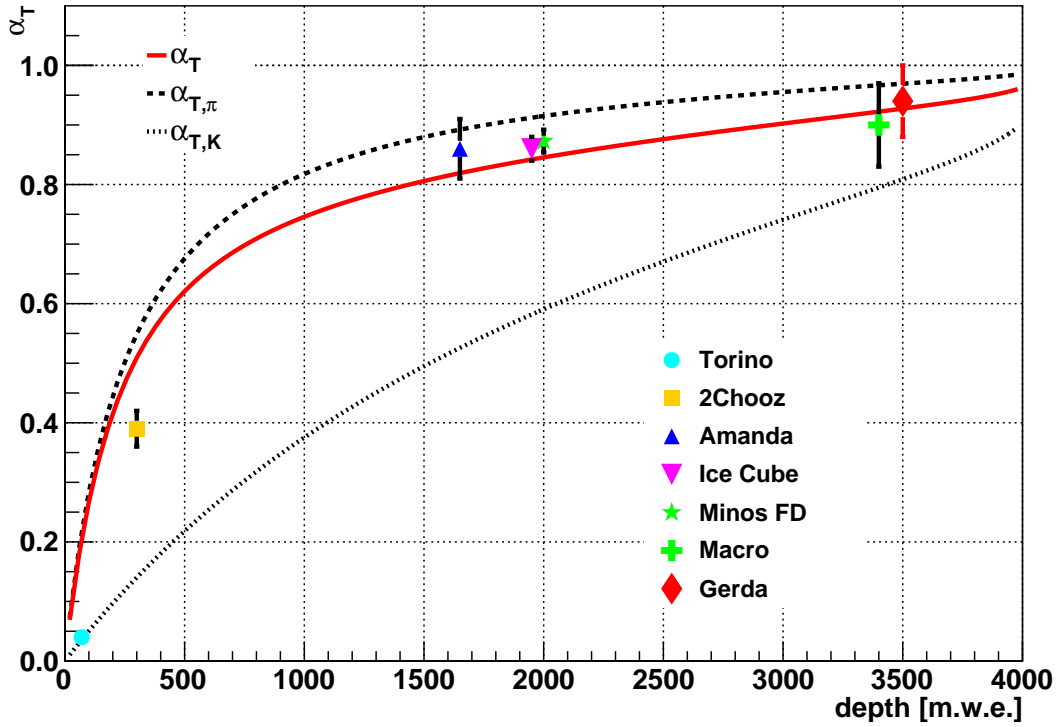
Figure 6.14: *Correlation coefficient α_T as a function of depth. Experiments are listed with different m.w.e. of rock overburden, such as Torino [Cas67], Dou-ble Chooz [Die13], Amanda [Bou99], IceCube [Des11], Minos far detector [Ada10], Macro [Amb03] and Gerda (this work). Gerda and Macro are lo-cated at the same depth but are drawn slightly apart for optical reasons. The dashed curves show muon generation models based on either purely pionic or only kaonic processes. The red line notes the literature value for the atmospheric kaon/pion ratio [Gai90, Bar06].*

where

$$D_M = \frac{\gamma}{\gamma + 1} \frac{\epsilon_M}{1.1 \langle E_{\mathrm{thr}} \cos \theta \rangle} + 1. \tag{6.18}$$

If the contribution of either kaons or pions is omitted from the overall formula, the respective coefficients become $\alpha_{T,M} = 1/D_M$, where $M = \{\pi, K\}$ is the meson as above. With these values fixed, a selection of experiments can be compared which have measured this effect. In Fig. 6.14 different experiments are listed with their value for α_T. The red curve shows the dependence of α_T on the slant depth with the literature values from Tab. 6.3. All seven experiments agree well with the theoretical prediction. It has to be noted, that both Macro and Gerda share the same rock overburden, but were drawn apart for visual reasons. The value for the parameter α_T for the LNGS from formula Eq. 6.17 is $\alpha_{T,\mathrm{lngs}} = 0.92$. All values from the experiments at the LNGS including Gerda agree well with this value (see Tab. 6.4).

Were the errors of this measurement smaller, an estimate for the literature value for $r_{K/\pi}$—i.e. the ratio in which kaons and pions are produced by primary cosmic rays—could be given. So far this was mostly measured with accelerators at certain energies. This ratio is of particular interest as it is not only contained in the theoretical model in
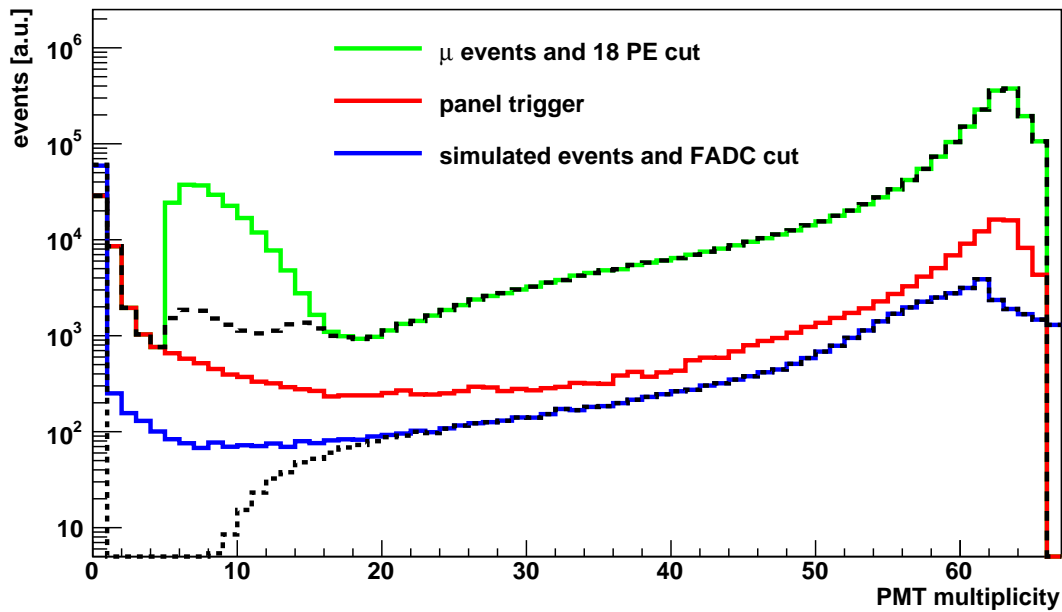
Figure 6.15: *PMT multiplicity spectra for different settings and data sets. The full experimental data set for the entire veto is shown (green) with an 18 PE cut applied (overlying dashed line). The spectrum for all events with a panel trigger is shown in red and the simulated cosmogenic muons are shown (blue) with an FADC-cut applied to it (dashed line). Unlike the experimental spectra, the simulated spectrum is arbitrarily normalized.*

Eq. 6.17 but in the weight function to determine the experimental value of α_T shown in Eq. 6.9. So far the data agrees well with the given ratio, but as the statistical errors of this measurement exceed the limit given by a purely pionic decay process, a value with this error would give non-physical results. With higher statistics and smaller errors, a value for this factor could be given in the future.

In conclusion, after the Cngs induced muons were removed from the data set, the seasonal modulation of the muon rate is verified with the Gerda muon veto. The muon data shows this $\approx 1.5\%$ effect very clearly and a high level of correlation between effective temperature and mean muon rate was found. The used atmospheric model for the muon production agrees well with other experiments at the LNGS and by expanding the model to different depths also to other experimental sites.

6.7   Comparison with the Simulations

With the constant offset caused by the Cngs muons subtracted and the annual modulation clearly identified, the muon data can now be analysed in-depth. The data from the fully operational muon veto will be used, i.e. starting in July 2011. With this set of data a similar analysis as for the simulation data (see Sec. 5.6) can now be performed. The multiplicity spectra are shown in Fig. 6.15. All three spectra show their peak at high multiplicities and a steady decline towards low multiplicities over about two orders of magnitude. The two spectra from experimental data agree in principal well with the simulation, however there are a number of notable differences. First, the main muon

spectrum shows a large enhancement at low multiplicities. These are events, which do not only show a low number of PMTs, but also an unusual low number of PE. Pillbox events can for example be of a multiplicity below ten, but the detected light is usually much higher and most events in this enhancement are for the most part single photon events in each PMT. This enhancement disappears when e.g. the events with a panel trigger are considered. Due to the additional external tagging capability that the scintillator veto offers, "true" muon events can be selected. These show an enhancement towards low multiplicities, but which is in accordance with the simulation. Multiplicity spectra of the CNGS beam were already shown in Fig. 6.9. This is a similar case where by external tagging, true muons can be select and here, the spectrum towards lower multiplicities agrees with the simulated spectrum with the FADC cut applied. These events are hence no true muon events but a source of additional background in the Cherenkov veto. The source of this is most likely scintillation light of β-particles in the reflective foil and will be explored in Sec. 6.8.

Apart from this feature, the multiplicity spectra agree well with each other albeit with a few small inconsistencies. The peak in the simulated spectrum is at the same position, but it appears to be a lot broader in comparison to the experimental spectra. However, in the real experiment a number of PMTs were malfunctioning or outright broken. In the high-multiplicity end of the simulated spectrum, this causes the same number of events to be distributed over a higher range of multiplicity, which loweres the peak. In addition, the panel spectrum shows a higher rise towards the lowest multiplicities beyond the trigger capabilities of the Cherenkov veto in comparison to the simulation. This can be explained with random coincidences with the PMTs. A single PMT has a dark-rate in the vicinity of 5-10 kHz, which causes a non-negligible rate at the lowest multiplicities. Since the Cherenkov veto has a trigger condition of five or more detectors, this random rate does not affect it but this will still show up in events recorded by the scintillator veto. These listed differences are explicable and can be considered small. Furthermore, a slightly inaccurate treatment of reflectivity or wave-length shifting in the simulations could easily cause equally small effects but this is well beyond the "interesting" muons.

In the photon spectra shown in Fig. 6.16 the same features appear as already seen in Fig. 5.13. The spectra show characteristic peaks, which are related to the respective track-length of the muon class. In the case of cosmogenic events, pillbox and water tank events show a peak at 170 and 650 PE respectively and the peak-height is approximately the same factor of three apart. Cosmogenic muons which pass the scintillator panels even further confirm the relation between track-length and deposited PE. As these muons come from straight above, the mean track-length for pillbox-events is slightly reduced, while in the water tank it is the same. Both is represented in the data. The CNGS spectra show the effect of muons coming straight from the side. The track length in the pillbox grows to a maximum of 4 m and in the water tank it is reduced to 6 m. Even the germanium events show the predicted double-peak structure of a small track in the water tank and a sum-peak of water tank and pillbox. This spectrum is shown at this point in anticipation of the coincident muon-germanium analysis in the following chapter.

Overall the simulations agree well with the experimental data, which establishes the efficiencies derived from the simulations, i.e. makes these values credible. In addition, the relation between muon class (or mean track length) and the detected number of PE
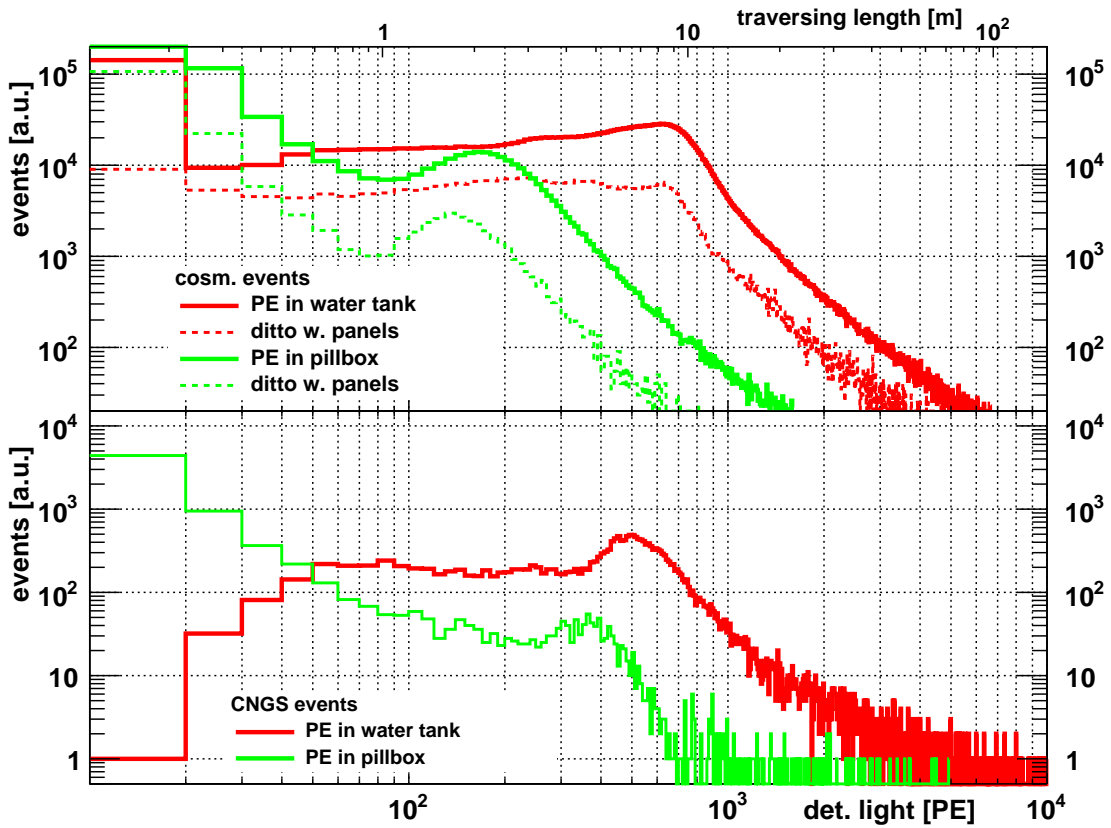
(a) Muon classes: cosmogenic and Cngs events
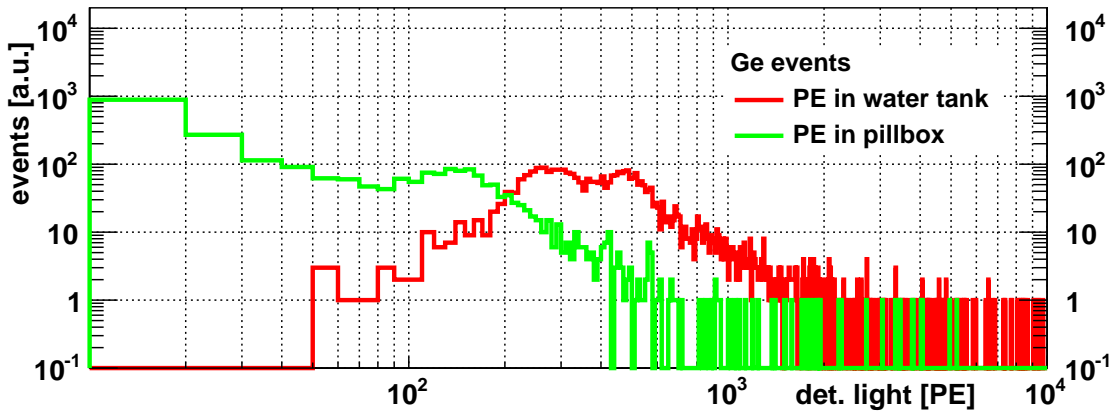
(b) Muon class: germanium events

Figure 6.16: *Photo-electron spectra from experimental data. The colours indicate PE detected in the pillbox (green) and in the entire veto (water tank and pillbox) (red). The dashed spectra show the same class of events but with an accompanying panel trigger. The germanium events are extracted using the same cut condition which will be shown in Sec. 7.1.3. See the text for the interpretation of the different peaks.*

Table 6.5: *Active volumes for ionizing radiation into the reflective foil. For the solid steel (SS) the volume for 5 MeV α-particle is assumed to originate from an active layer of 9.7 µm, the volume for 0.35 MeV β-particles is from an active layer of 0.19 mm. In the case of water, the range for α-particles is assumed to be 32 µm.*

part	$\varnothing$ [m]	height [m]	vol.$_{SS}^{\alpha}$ [cm^3]	vol.$_{SS}^{\beta}$ [cm^3]	vol.$_{H_2O}^{\alpha}$ [cm^3]
outer wall	10	8.3	2530	50400	8340
floor	10	–	760	15200	2510
cryostat	4.2	7.2	920	18400	3040
pillbox	4	1.35	170	3300	540
sum			4380	87300	14430

agrees as well with the exception of an additional structure in the CNGS simulations. As this feature is not reproduced by the data, it has to be seen as an artefact. An additional study regarding the relation of these peaks with the attenuation length of the water can be found in App. E.

6.8 LOW-MULTIPLICITY ENHANCEMENT

A thus far unknown background in the muon veto which has been of interest in previous works is the enhancement in muon rate at low multiplicities which can be seen e.g. in Fig. 6.15 or Fig. 6.9. If an 18 PE cut is applied to the pure Cherenkov data, i.e. only events in the water tank are considered, this enhancement amounts to 8.7% of the total events of a rate of 3.1×10^{-3}/s in comparison to the overall rate of 3.6×10^{-2}/s. This abundance cannot be explained with the simulated muon spectra shown in Fig. 6.15. This structure equally vanishes when external muon tagging is possible such as the muons caused by the CNGS or the coincident muons between scintillator and Cherenkov veto. For these reasons it can be ruled out, that these events are caused by muons and are thus an undesirable background in the muon veto. One of the possible explanations for this effect was already briefly introduced in [Rit12]: scintillation light from the VM2000 foil when illuminated with α-particles from the solid steel of the tank. As it covers most of the inner walls of the water tank any light production should be visible by the PMTs.

The optical scintillation properties of the VM2000 foil are well known (see e.g. [Kna09]). It shifts ultra-violet light into the optical regime at 400-450 nm which is particularly useful for the Cherenkov veto, as Cherenkov light is mostly ultra-violet (see Sec. 3.2). However, the scintillation properties under the irradiation with ionizing particles are less studied.

GERDA is not the only experiment to utilize the VM2000 foil. The CRESST experiment for example uses it to maximize the light-yield of its scintillating calcium-tungstate crystals by covering the interior of the crystal housings with this foil [Ang09]. In their data, a class of events emerges which is caused by surface contaminations with

radioactive polonium:

$$^{210}\text{Po} \rightarrow ^{206}\text{Pb} + \alpha \ (5.3 \text{ MeV}). \tag{6.19}$$
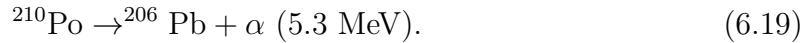
While the lead atom causes a recoil of $E_R = 103$ keV, the α-particle can either be absorbed by the clamps holding the crystal or hit the scintillating foil. In the first case, the α is absorbed and there is little to no light to be seen, which puts these events by chance close to the desired ROI and causes thus a non-negligible background. In the second case, the α-particles hit the reflective foil outside of the crystal and light is produced by scintillation. These events are quenched in comparison to γ-rays by a factor of $f_Q = 0.7$ [Ang12]. The quenching factor is given in units of deposited light per deposited recoil energy in the crystal, i.e. 103 keV deposited by the ^{206}Pb nucleus. This treats the event as if the scintillation had happened in the calcium-tungstate and not in the foil which has so far unknown scintillation properties.

However, the scintillation of the calcium-tungstate is well known and can be used to deduce the light yield produced in the foil. The light yield of the crystals at room temperature is given as $\text{Ly(CaWO}_4)_{RT} = 15800$ ph/MeV [Mos05]. But the crystals are normally operated at low temperatures, i.e. in the milli-Kelvin regime, which increases the light yield. When the crystal is cooled down from room temperature to 6 K an increase in light-yield of $f_{mK} = 1.85$ is found [Kra10], which will be used as an approximation for the operation in the milli-Kelvin regime. The light-yield of the foil can thus be calculated by the following formula:

$$\text{Ly(VM)} = f_Q \cdot f_{mK} \cdot \text{Ly(CaWO}_4)_{RT} \cdot E_R/E_\alpha \tag{6.20}$$

Given the observed recoil of a nucleus emitting a 5.3 MeV α-particle, the light-yield of the VM2000 is $\text{Ly(VM)} = 404$ [ph/MeV]. Thus, for an α-particle of 5 MeV about 2000 photons are produced in the foil. This can be seen as a very good indicator that this is indeed an effect to be considered given that the activity and the target mass are large enough to be of effect.

The solid-steel of both water tank as well as cryostat of GERDA are of low-radioactivity steel. The different radioactive isotopes and their respective activities of the steel has been studied to great extent [Man08]. The α-emitters ^{228}Th (5.4 MeV), ^{226}Ra (4.7 MeV) and ^{235}U (4.3 MeV) are listed with about the same activity. The main β-emitter is ^{60}Co (0.35 MeV), the contribution of other isotopes are either small (e.g. ^{40}K, ^{48}V or ^{137}Cs) or of extremely low endpoint energy (e.g. ^{228}Ra (0.04 MeV) or ^{234m}Pa (0.08 MeV)). The mean upper limit for the α-activity is <5 mBq/kg and the mean ^{60}Co-activity is 19 mBq/kg. This is very low, but on the other hand the size of the water tank and the cryostat is not negligible. The specific range for 5 MeV α particles in iron is 7.6×10^{-3} g/cm^2 [NIS14], which corresponds to 9.7 μm assuming a mean solid-steel density of 7.9 g/cm^3. This means that a layer of 9.7 μm can be considered an active volume for α-emission from the solid steel. For 0.35 MeV β-particles the range in iron is about 20 times larger, i.e. 1.53×10^{-1} g/cm^2 [NIS14], which is equal to a mean free path of 0.19 mm. It has to be stressed, that these values are upper limits for the active volume, as these are the half-value layers and in addition that the particles will have lost energy on their way. The respective active volumes for the different parts of the water tank are given in Tab. 6.5. Here the active volume was considered the amount of steel that is within one mean free path of the respective particle. For the α-particles, a total of 4380 cm^3 is considered active, which is equivalent to 34.6 kg. The β-particles
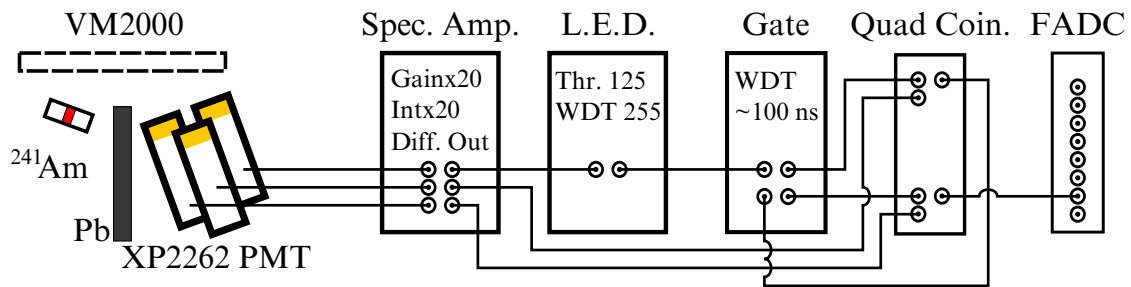
Figure 6.17: *Hardware set-up for the VM2000 scintillation test.*

have a much higher range and thus an active volume of 87300 cm³ i.e. 690 kg. With the activities given above, a maximum activity of 85 mBq for α-particles and 6.55 Bq for β-particles is expected when the half-value is considered.

However, any ionizing radiation from the solid steel would mean a back-side illumination of the foil. This means that the α- and β-particles have to pass not only adhesive glue on the back-side but also have to penetrate the foil to such an extend that the scintillation light can leave on the other side. According to the manufacturer, the reflective film itself has a thickness of 66 µm and the adhesive on the back-side a thickness of 38 µm. If the glue is assumed to be a plastic compound a mean free path of ≈30 µm for 5 MeV α-particles is expected. Hence, these particles are unlikely to even reach the foil through the adhesive side. The adhesive is translucent, however the reflective foil would reflect any energy deposition in form of light back to the adhesive side. In the case of the β-particles, the overall thickness of adhesive and foil represents about half of the mean free path.

Not only the solid steel of the water tank and the cryostat exhibit radioactivity, but the water itself, too. The water is procured from the Borexino water plant which consists of advanced filters, de-ionizer and an osmosis unit, which provides very clean water of > 0.17 MΩ m. These filters purify the water of the radioactive contaminants, however some small residues still remain solved. Namely these are the α sources ^{238}U (4.2 MeV), ^{226}Ra (4.8 MeV), ^{222}Rn (5.5 MeV) and ^{232}Th (4.0 MeV) with a total activity of ≈ 1 µBq. Measurements of the isotope composition of the water before and after the Gerda water purification plant confirm this low level even in the experiment[†]. For a 4.5 MeV α, the specific range in water is 3.2×10^{-3} g/cm² [NIS14], which is equivalent to a mean free path of 32 µm. The active volume for water is given in Tab. 6.5 as 14430 cm³, i.e. 14.4 kg with an expected activity of 7.2 µBq, which is too low to explain the enhancement.

A first proof-of-principle measurement of the scintillation properties was carried out with an α-source. The set-up can be seen in Fig. 6.17. Three XP2262 PMT in a triangular rack are pointed directly on a frame covered with VM2000. From the other side of a small lead sheet, an ^{241}Am α-source with $E_\alpha = 5.5$ MeV, (100%) and $E_\gamma = 59.5$ keV (35%) illuminates the screen from a short distance (≈ 2 cm). The PMT are further away and cover ≈5% of the solid angle. The PMT signal is amplified and set in triple coincidence as indicated in Fig. 6.17. The readout is via an SIS3301 FADC. A measurement with this set-up can be seen in Fig. 6.18. At first, the PMT were calibrated using

---

[†]M. Balata, *priv. comm.*, 2014
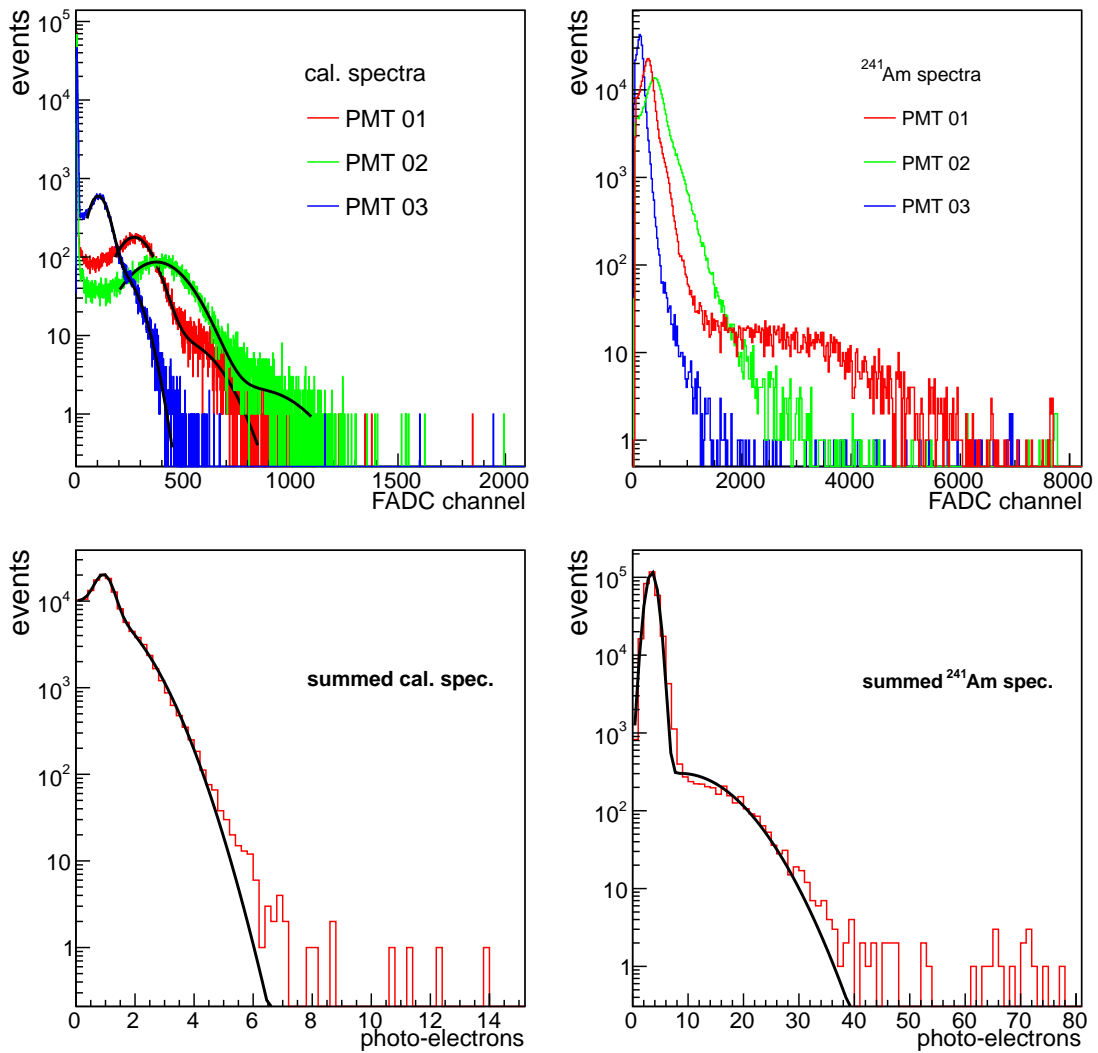
Figure 6.18: *Scintillation of the VM2000 reflective foil under α irradiation. Top left: PMT calibration spectra, bottom left: summed spectrum of all calibrated PMT, top right: spectrum with ²⁴¹Am source illuminating the foil, bottom right: summed ²⁴¹Am spectrum.*
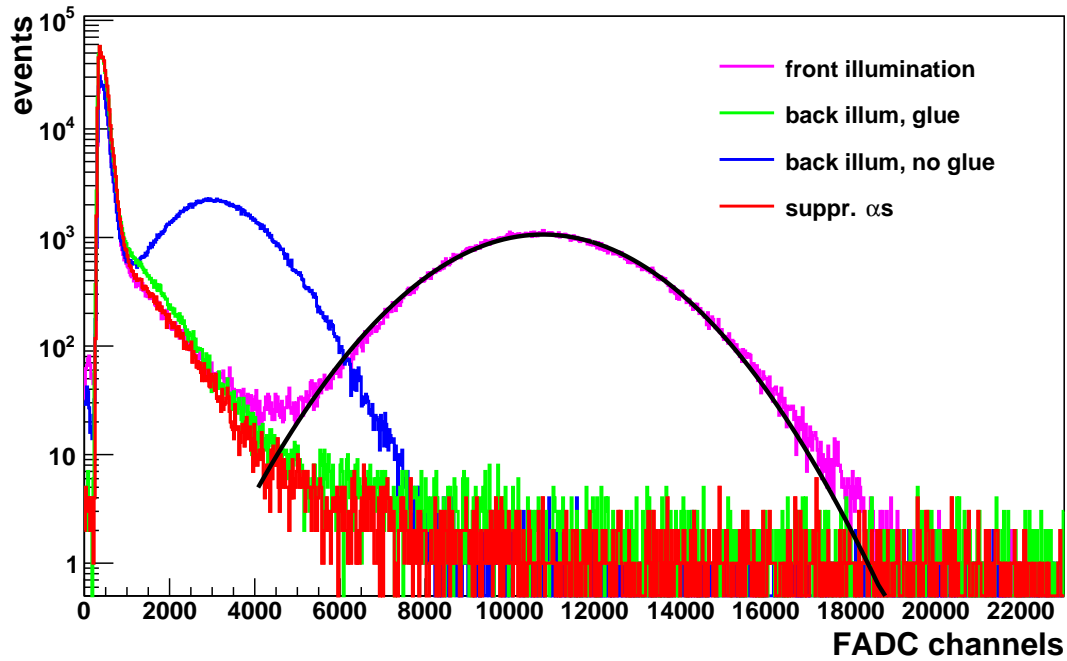
Figure 6.19: *Front and back illumination of the VM2000 reflective foil with* ^{241}Am.
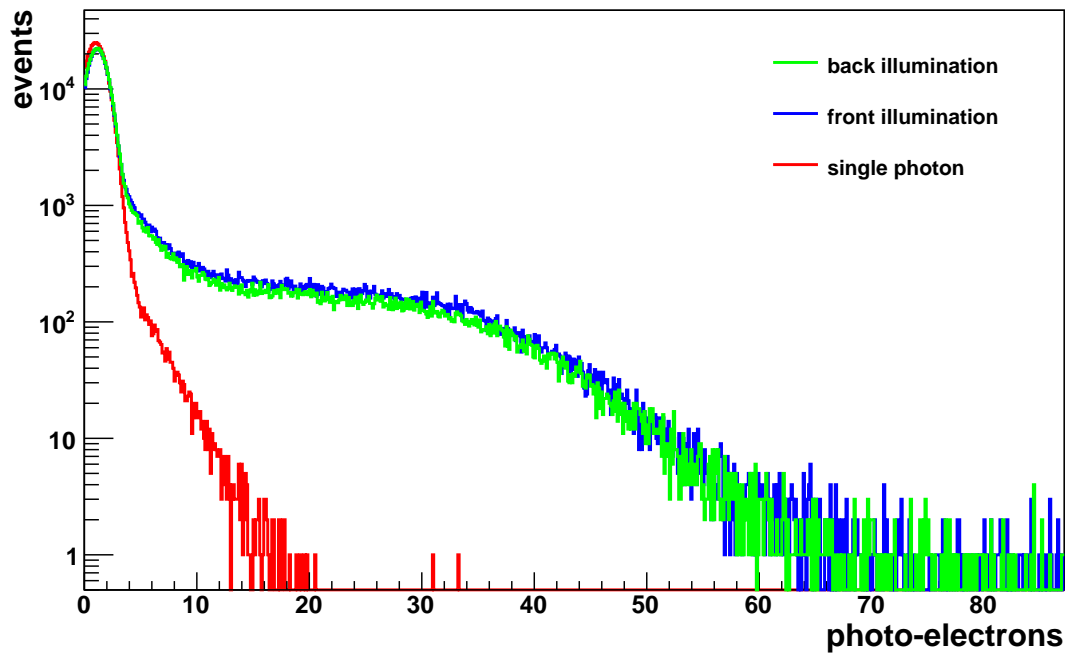
Figure 6.20: *Front and back illumination of the VM2000 reflective foil with* ^{60}Co.

an ultra-fast low intensity light source. The SPP of each PMT emerge clearly with only small contaminations from the two-photon peak. The summed calibration spectrum shows the maximum at three PEs with a small shoulder caused by two-photon events. Upon illumination with the ^{241}Am, much more light is recorded, especially in PMT01 due to its geometrical placement. The sum spectrum shows the contribution of the low-energy γ-rays at 3 PE and the contribution of the α-particles at 9 PE with a maximum at 40 PE. The overall efficiency of the PMT can be estimated as 0.2, which is partly due to the quantum efficiency of the PMT (0.25) and refractive losses due to internal scattering in the glass, the total light yield is 900 in the maximum and 4000 for the most luminous events. This can be considered in agreement with the light-yield calculation from the Cresst data in Eq. 6.20.

In this measurement the source was placed on the same side as the PMTs, i.e. the foil was illuminated from its front-side. To test the assumption, that α-particles from the solid-steel in the Gerda water tank (i.e. the foil's back-side) are not able to pass the glue in the foil, a slightly different set-up was chosen with only a single PMT[‡]. In a first set of measurements, a plastic scintillator and afterwards the VM2000 were illuminated from the front side. A comparison of the α-rates of both materials yields an efficiency for the VM2000 if it can be assumed that the efficiency for the scintillator is unity. The plastic scintillator yields a rate of 345/s and the VM2000 a rate of 315/s. The efficiency for the VM2000 foil for α-particles is in comparison:

$$\varepsilon_\alpha^{\text{VM2000}} = 91.3^{+1.4}_{-1.6}\% \tag{6.21}$$

For the front- and back-illumination a small tube of VM2000 was placed on the end of a PMT. For the front-side illumination the ^{241}Am source was placed inside the tube. First, the source was used unaltered and afterwards it was covered with tape to absorb the α-particles and to only allow the 59.5 keV γ-rays of the ^{241}Am to pass. In a second set of measurements, the source illuminated the tube from the outside, i.e. a back-side illumination of the foil. In two different measurements, foils with either glue still on its backside or with the glue removed were illuminated. In all measurements care was taken as not to illuminate the PMT with the source. The results can be seen in Fig. 6.19. While the unaltered source in front illumination shows a very clear scintillation signal, it vanishes as soon as the α-particles are suppressed by the absorber. In the case of back illumination, with glue, the same spectrum as with suppressed α-particles emerges. The α-particles are absorbed in the glue and no light passes to the other side of the foil. In the case of the removed glue, a strongly suppressed scintillation peak can be seen. Due to the thickness of the foil itself, the α-particles lose already part of their energy before they deposit their energy in the foil that it may emerge as light. With this measurement, the α-sources in the solid-steel of the water tank can most likely be discarded as a possible cause of the low-multiplicity enhancement despite its good efficiency.

As the predominant β-source in the solid steel is ^{60}Co, similar data were taken. The efficiency measurements are in this case a bit more difficult, as the $Q_\beta = 0.35$ MeV is very low and collides with the SPP of the PMT. If a cut is defined right after the SPP, the scintillator shows a rate of $\approx$1000/s and for the VM2000 $\approx$120/s. This gives

---

[‡]M. Uffinger, *priv. com.*, 2014

a much lower efficiency in comparison to the α-particles of:

$$\varepsilon_\beta^{\text{VM2000}} = 12.0_{-1.0}^{+1.1}\% \tag{6.22}$$

Despite the lower efficiency, the illumination of the foil from front and back yields almost the same number of PE, which can be seen in Fig. 6.20. This spectrum is already normalized by the number of PE. This was taken with a single PMT which was placed very close to the foil and thus covering a solid angle of 8.5%. If similar number for the efficiency are taken as above and a range of 20-60 PE is assumed to show most of the spectrum, this would mean a total amount of light of 1160-3480 photons.

As a result of these measurements can be said that the scintillation effect of the VM2000 foil has been studied and that there are the following conclusions to be drawn:

1. α-particles from the solid steel are unable to cause scintillation in the foil

2. contaminations in the water can be excluded as they are three orders or magnitudes below the sought rate

3. β-particles from the solid steel are able to penetrate the foil and cause sufficient light on the other side

4. α-particles from the front may cause sufficient light as well

At this point is it quite clear that the scintillation events are still a valid candidate for the low multiplicity enhancement. The scintillation of β-particles appears to be the most promising mechanism, as the mean rate of β-sources in the solid steel is higher as the observed rate of low-multiplicity events. Given the low efficiency of this effect and if only the most luminous β-particles of the spectrum in Fig. 6.20 can indeed be seen by the veto, the observed rate could be explained with the β-activity of the steel. On the other hand, it is also possible that the heavy nuclei from the uranium decay chain precipitate on the surface of the foil, i.e. that the water volume might be very radio-pure but the radioactive materials collect on the surface. Especially the radon isotopes from the various decay chains are dangerous in this respect. As they are gaseous they tend to enrich any surface they are exposed to with their decay-products. As these isotopes are often α-emitters, this cannot be ruled out as well. Further investigations are necessary in order to explore these possibilities. However the rate of this effect is too low to cause any random coincidences with the germanium data taking.

CHAPTER 7

MUON BACKGROUND IN THE GERMANIUM DETECTORS

The previous chapters introduced muons, their production mechanism, their sources, the GERDA muon veto and different studied external effects to the muon generation. In this chapter now follows the interaction of the muons with the core of the GERDA experiment: the germanium detector array. Muons can interact with the detectors in multiple ways. They can pass directly through a detector and deposit energy directly in a diode as muons are in principle just heavier electrons. Alternatively, the muons may spallate nuclei in the surrounding, which can lead to radioactive isotopes close to the detectors or free neutrons which can in turn activate any material they encounter and thus produce a new potentially radioactive nucleus.

As this chapter is mostly about muon-germanium coincidences, the method to generate the coincidence (i.e. how the data are connected) will be discussed first. Afterwards, different classes of events will be studied and a rejection efficiency will be given including values for the BI caused by the muons. Last, the additional sources of background like the muons from the CNGS will be shown and the data will be analysed to find the effects of spallation: characteristic radioactive isotopes or neutron activation. The coincident analysis is based on the entire muon data and the germanium runs 25-46 (apart from run 33 which was very unstable) with a total exposure of $\mathcal{E}=(21.61_{enr}+6.192_{nat})$ kg·yr.

7.1 COINCIDENT MUON-GERMANIUM EVENTS

The main goal in this chapter is to investigate the effects of a correlation between events in the muon veto and the germanium detectors. In order to study these events, two different approaches to correlate events from M-DAQ or Ge-DAQ were pursued.

The first option is to take the muon *veto bit* in the germanium data files. This bit is set when the M-DAQ has fired. A logical signal is generated by the M-DAQ, which is being read out by the Ge-DAQ and hence stored in the data file. This signal arrives usually 20 μs after the germanium trigger due to fixed delays caused by the electric cables. The germanium data stream provides two different veto bits, depending on when the muon signal arrived within the germanium trace. If it arrives within a ±10 μs window

around the trigger point, the signal is defined as `isVetointime` and `isVeto` otherwise. However, this only records muon events if they fall into the germanium trace (160 μs long, trigger point is fixed at 80 μs).

The second option is a direct comparison of the trigger timestamps of M-DAQ and Ge-DAQ. Both DAQs are synchronized every second with the Borexino GPS signal and are hence in good agreement. This was already introduced in in Sec. 6.5 where the muon timestamps were compared with an external signal which showed an excellent time resolution. By defining an acceptance window around the germanium event, coincident events may be studied without the limitation of the length of the germanium trace. This can be used to search for delayed coincidences caused e.g. by a muon spallation product.

These two methods deliver almost the same results. Only pathological events like a false-positive muon bit in the Ge-DAQ caused by an internal overflow or similar events will additionally appear in the germanium data. However, when the germanium quality cuts are applied, for the data set which was defined above, both methods show the same 3463 coincident events. The quality cuts are additional parameters in the data stream, which discard e.g. overflows in the germanium pre-amplifiers or traces outside the physically allowed range.

7.1.1   Rates of Muon-Coincident Events

Events from uncorrelated and constant physical effects at low rates should have a flat distribution over time. Therefore, the time Δt between two subsequent events of the same type should follow an exponential and the rate can be directly taken from its slope. It is important to assure that any such rate (germanium, muon or coincident rate) are purely governed by statistics and hence show a pure exponential. Any deviation from an exponential would indicate additional effects taking place.

These curves can be seen in Fig. 7.1. The germanium events have to fulfil the cut conditions of having at least one active detector which shows an event that passes the quality cuts. All test pulses, noise events etc. were therefore discarded. Any muon veto event was considered, where the total amount of light detected was > 30 PE or that the plastic veto had fired in each layer. The coincident rate was determined with the timestamp method and a window representing the length of the germanium trace of 160 μs. All curves show a good agreement with the exponential fit function. However, the coincident rate is three orders of magnitude lower and thus suffers in statistics.

As introduced in Sec. 5.5, the rate of the muon detectors at the LNGS is usually normalized with the effective area of the respective detector. The normalized effective surface of the Gerda water tank was determined to be (103.5 ± 2.0) m^2. With this value a mean muon flux of $I_\mu^0 = (3.49 \pm 0.07) \times 10^{-4}/(\text{s·m}^2)$ can be derived from the muon rate given in Fig. 7.1(b). Using this exponential method, the annual modulation of the muon rate is not accounted for, as the changes over the seasons should disappear the mean. The muon data over time and the respective sine-like fit to the data can be seen in Fig. 6.11. Here, a mean muon flux of $I_\mu^0 = (3.47 \pm 0.06) \times 10^{-4}/(\text{s·m}^2)$ was found which agrees well with the value above.

The main point of interest however is the coincident data. Germanium, muon and hence coincident events should be distributed evenly over time. Any spikes in either rate would need a special examination, as the two systems are physically and

(a) $r_{\text{Ge}} = (2.868 \pm 0.006) \times 10^{-2}/\text{s}$

(b) $r_{\mu} = (3.610 \pm 0.005) \times 10^{-2}/\text{s}$

(c) $r_{\text{coin}} = (9.39 \pm 0.40) \times 10^{-5}/\text{s}$
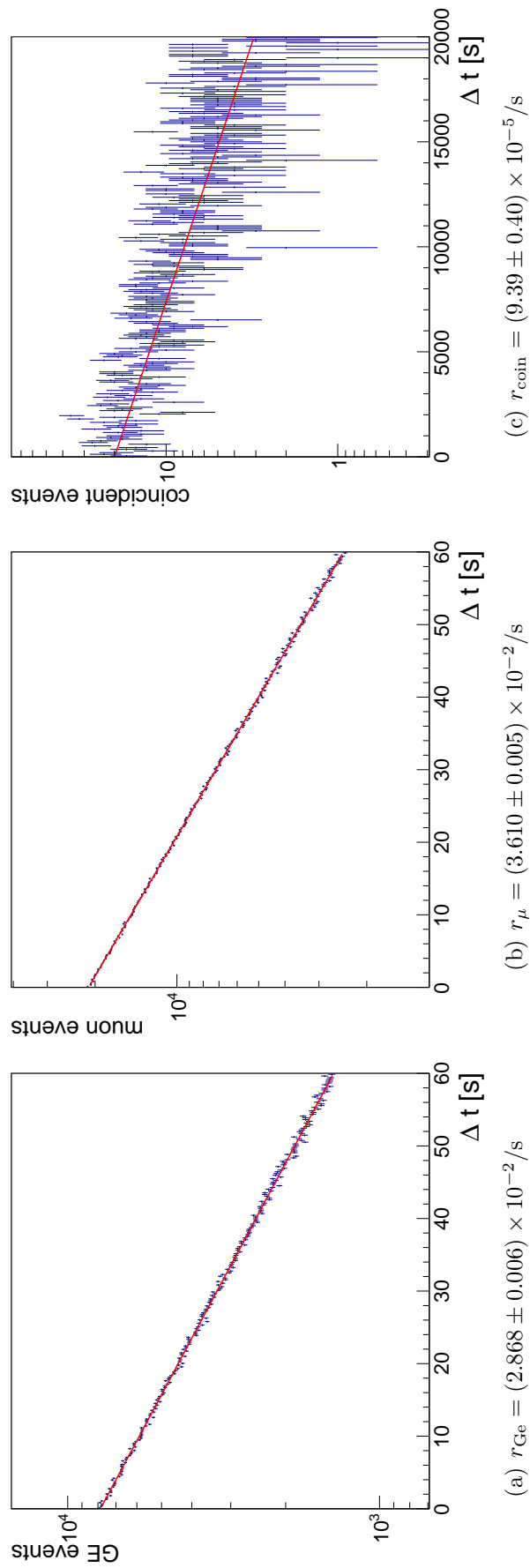
Figure 7.1: *Histograms of the time between two subsequent germanium (a), muon (b) and coincident events (c). The slope of the curves determines the respective rates* r_{Ge}, r_{μ} *and* r_{coin}. *The timestamp method was used to obtain the coincident rate.*
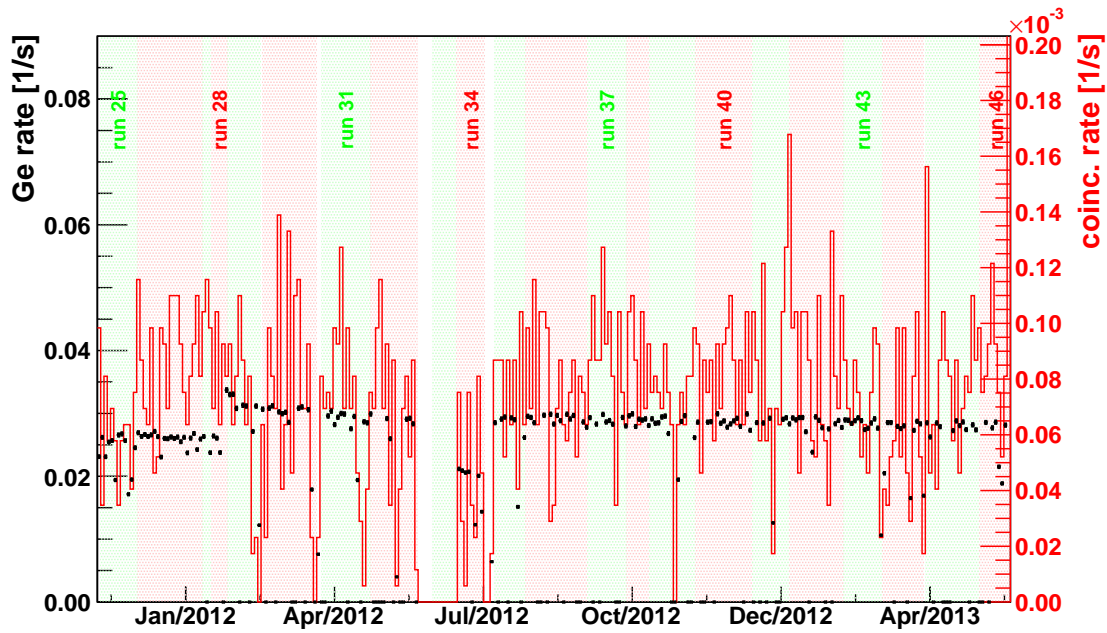
Figure 7.2: *Time series of the coincident rates of the Ge-DAQ (black crosses) and the coincident germanium-muon rate (red histogram). The coincident rate was obtained using the vetobit in the germanium data.*

electronically very stable. The rate for random coincidences between germanium and muon veto can be estimated by using the rates of the detectors and the time window of the muon trace, i.e. $\Delta t = 4\ \mu$s. The random coincident rate is found to be $r_{\text{rand}} = r_{\text{Ge}}\cdot\Delta t\cdot r_\mu = 4.1\times10^{-9}$/s, i.e. the coincident rate of $r_{\text{coin}} = (9.39\pm0.40)\times10^{-5}$/s is dominated entirely by physical events and not accidental random coincidences.

The stability of the muon veto was already shown in previous sections. For the germanium and the coincident, the stability is shown in Fig. 7.2. Both the germanium rate in black and the coincident rate in red show no major deviation. However, the germanium rate shifts sometimes from the mean. This is usually due to changes in the experimental set-up like the removal or addition of detectors. Since a new germanium runs always starts when the experimental set-up is changed, the runs are highlighted in the picture. For example during run 34, the entire string S1 was removed which leads to a much lower rate. Other changes in the rate stem from short interruptions due to calibrations during the runs or installation sessions between the runs.

7.1.2 Muon Rejection Efficiency

The most important feature of a muon veto in such an experiment is its ability to suppress the background caused by muons. For the plastic veto, a muon detection efficiency (MDE) was given in Sec. 6.3. This is a value which is the result of a "positive" measurement, i.e. the detector is brought into a certain configuration which allows a self-measurement. In contrast to this MDE, a Muon Rejection Efficiency (MRE) can be obtained by defining a cut for clearly identified muon hits in the germanium data and afterwards testing the muon veto for a signal. The rejection efficiency $\varepsilon_{\mu r}$

Table 7.1: *List of clearly identified muon events, which are not vetoed.*

Timestamp	tot. E [keV]	detectors	note
1324568784	4005.56	ANG 2, RG 2, RG 3	
1327114796	8229.38	GTF 45, GTF 32	failed QC?
1329194876	4778.73	ANG 1, ANG 2	
1337163401	5027.72	GTF 112, RG 1	
1347876553	4988.12	RG 1, ANG 4	overflow in RG 3
1350750057	5228.24	all BEGes	modulated pulses in all BEGe's
1353190193	10078.00	GD32D, GD35C	
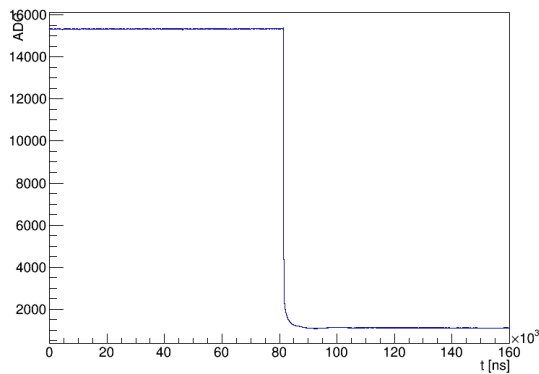
(a) GTF 32
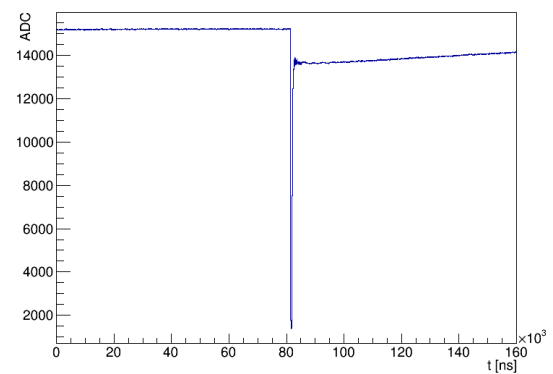
(b) GTF 45

Figure 7.3: *Germanium event at timestamp 1327114796. Energies for both traces are reconstructed despite their obviously faulty form.*

can now be given as the ratio of these events which are vetoed in comparison to the entire set. This analysis is a continuation of Ref. [GSTR11-02], where this analysis was performed for runs 1-6, runs 10-11 and run 12. The following cuts were applied to the germanium events of runs 25-46 (minus run 33) with a total exposure of $\mathcal{E}=(21.61_{enr}+6.192_{nat})$ kg·yr to identify certain muons:

- $\sum_{m=1} E_{Ge,m} > 8.5\,\mathrm{MeV}$

- $\sum_{m>1} E_{Ge,m} > 4\,\mathrm{MeV}$

In addition, a cut on the goodness of the events was performed, which weeds out test-pulser, overflows or otherwise un-physical events. This was not available in the analysis performed in [GSTR11-02] as the available analysis software was further developed since then. With these additional cuts, 841 out of 848 sure muon events were found to have the veto-bit. The non-vetoed events are listed in Tab. 7.1 for later study. This leads to a MRE with 68% credibility levels of:

$$\varepsilon_{\mu r} = (99.2^{+0.3}_{-0.4})\%\tag{7.1}$$

However, two of these seven events appear not to be standard germanium events and shall be examined. The event at 1327114796 has a multiplicity of two. When looking at the trace of the fired detectors (GTF 45 and GTF 32, see Fig. 7.3), one trace is just a spike and the other one has no decaying tail. However, for both events the energy is reconstructed. The event at 1350750057 (see Fig. 7.4) shows traces in all four active BEGes. The trace of GD32B has a flat tail and here, the energy is correctly not reconstructed. All other traces show a modulation and only two of the three remaining traces have a reconstructed energy. Obviously, these are events which should not survive the respective cuts. However, since the quality cuts are tested for a very different range of energy and as none of these events would survive a multiplicity cut, this is unproblematic for the overall germanium data analysis. The only reason why this deserves a mention is because the MRE would be even higher if these false-positive events were removed. It can be considered in agreement with the value derived from the simulations in Sec. 5.6.

7.1.3   Muonic Background Index

In order to estimate the improvement of the background index due to the muon veto, a ± 100 keV window was chosen around $Q_{\beta\beta}$. Due to the blinding window of ± 20 keV, the ROI of this study is 160 keV wide. Out of a total exposure of $\mathcal{E}=27.802$ kg·yr of germanium data, 14 vetoed events were found in this ROI that survive the germanium multiplicity cut. Were these 14 events not vetoed, they would have led to the following background (corrected by the Cherenkov efficiency):

$$\mathrm{BI}_{\mu}(\mathrm{data}) = (3.16 \pm 0.85) \times 10^{-3} \mathrm{\ cts/(keV \cdot kg \cdot yr)}.\tag{7.2}$$

A simulated value for the muonic background in the Phase I array operating in LAr and surviving anti-coincidence cuts is $\mathrm{BI}_{\mu}(\mathrm{MC}) = (1.6 \pm 0.1) \times 10^{-3}$ cts/(keV·kg·yr) given in Ref. [Pan07]. Due to the low statistics (14 events in total) and the subsequent

(a) GD35B

(b) GD32B
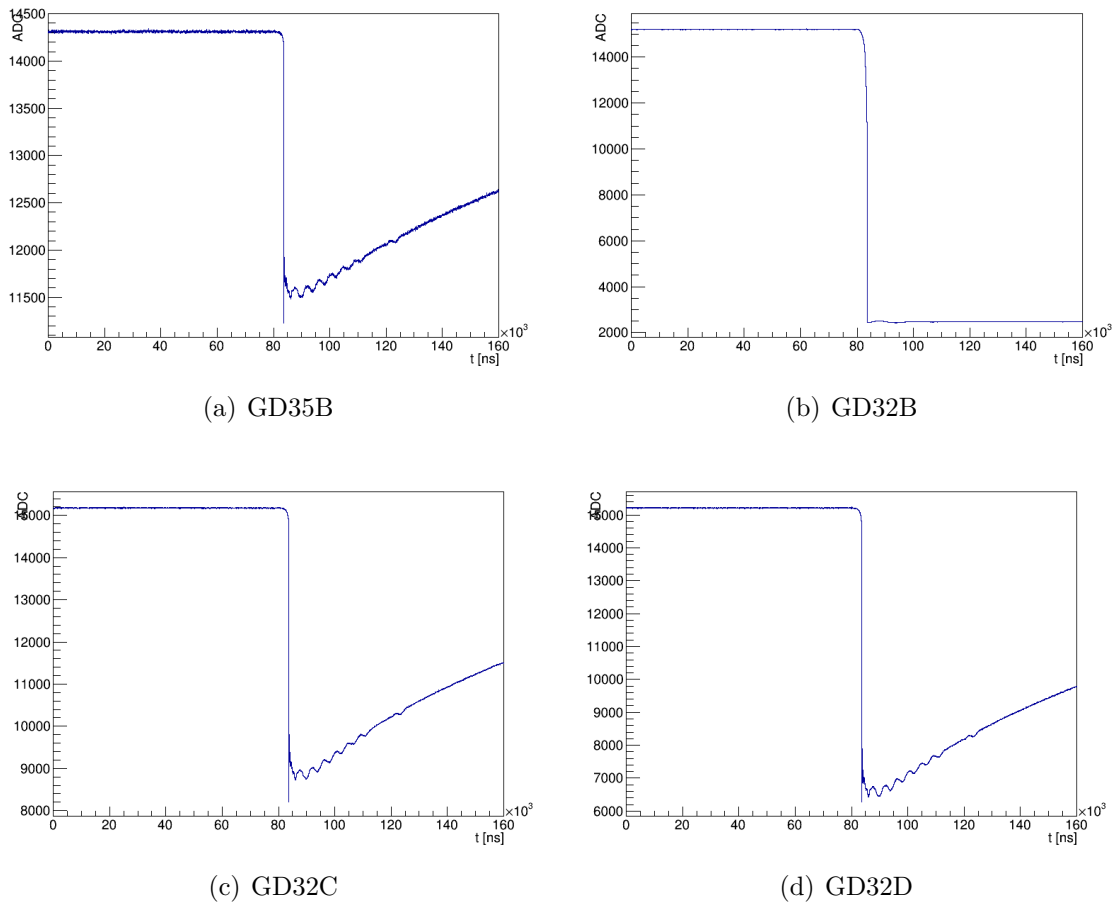
(c) GD32C

(d) GD32D

Figure 7.4: *Germanium event at timestamp 1350750057. No energies are reconstructed for GD32B (flat tail) and GD32C. All other traces show a modulation.*

large errors, this result is still considered in agreement with the simulations, especially since these values were simulated for a slightly different geometrical set-up.

With this background and the previously derived MRE, an estimation of the non-vetoed background can be given assuming that the MRE is constant over the entire energy range of the germanium detectors. The given vetoed background is equivalent to the amount of successfully vetoed muons, i.e. 99.2%. An amount of non-vetoed muons can be found:

$$\mathrm{BI}_{\mu,\mathrm{unvet.}}(\mathrm{data}) = (2.87 \pm 0.77) \times 10^{-5} \ \mathrm{cts}/(\mathrm{keV \cdot kg \cdot yr}). \qquad (7.3)$$

Phase II of GERDA demands a total BI of 10^{-3} cts/(keV·kg·yr). Thus, with the current settings, the deficiency of the muon veto would contribute 1/40 of the BI "allowance". For runs 25-46, this is equivalent to 0.16 events in a 200 keV window.

(a) 160 μs window

(b) 15 μs window
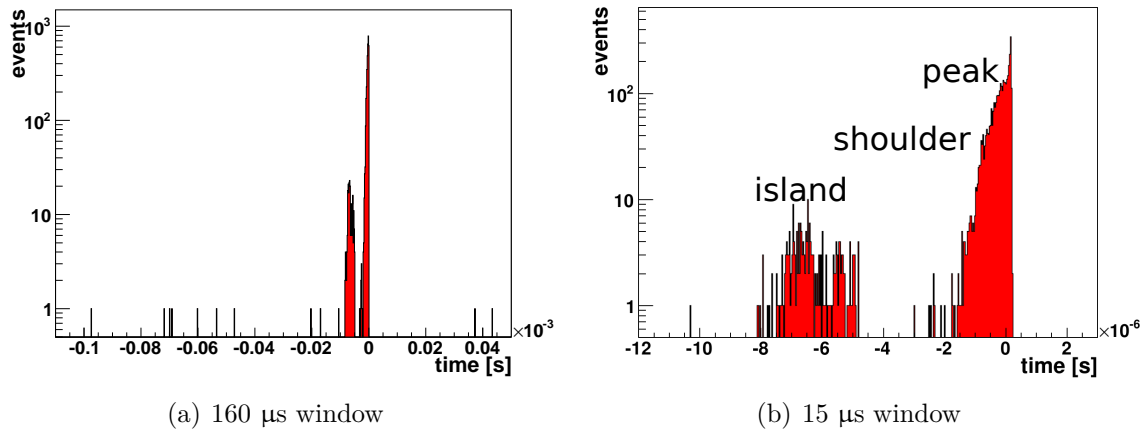
Figure 7.5: *Time difference between the germanium event (at t=0) and muon events. Two main structures are visible close to t=0 s and very few random events are scattered in the longer window. The two structures can be divided into three different types of events, which will be referred to as "island", "shoulder" and "peak". The large window is equivalent to the germanium trace. Muon events in this time frame fulfil the condition* **isVeto**. *The small window is loosely equivalent to the condition* **isVetointime**.

7.1.4   Random Coincidences and Event Classification

For the following analysis the coincidence was derived using the time difference between the muon and the germanium trigger. By defining the germanium trigger as $t = 0$ s and searching for muon events in a given window, time spectra like in Fig. 7.5 can be obtained. No quality cuts were applied to the germanium data in order to search for all muon-germanium interaction, even with "bad" traces. Muons can have–and thus deposit–very high energies. Events which can be classified non-physical for regular germanium events can therefore be potential muon candidates and have to be considered in this analysis.

Fig. 7.5(a) is comparable to the length of the germanium trace. Two major structures become apparent within 10 μs of the germanium event. Fig. 7.5(b) is a zoom-in to this double-structure and here it can be seen that the main structure is sub-divided . These three structures are from now on referred to as "island", "shoulder" and "peak" as in Fig. 7.5(b). All three event classes are accompanied by a muon with a Cherenkov multiplicity of 30 or more and are hence true muon events. These structures will be studied in the next sections.

There are 13 events in the 160 μs time spectrum, which do not appear in the smaller window. These can be considered random coincidences. The number of expected random coincidences is the product of the individual rates and the time window (in this case $\Delta t = 160$ μs). With the germanium rate $r_{\mathrm{Ge}} \approx 0.03$/s from Sec. 7.1.1 and a muon rate of $r_{\mu} \approx 0.04$/s the number of coincident events in the data during the data

(a) ANG 1   (b) RG 1
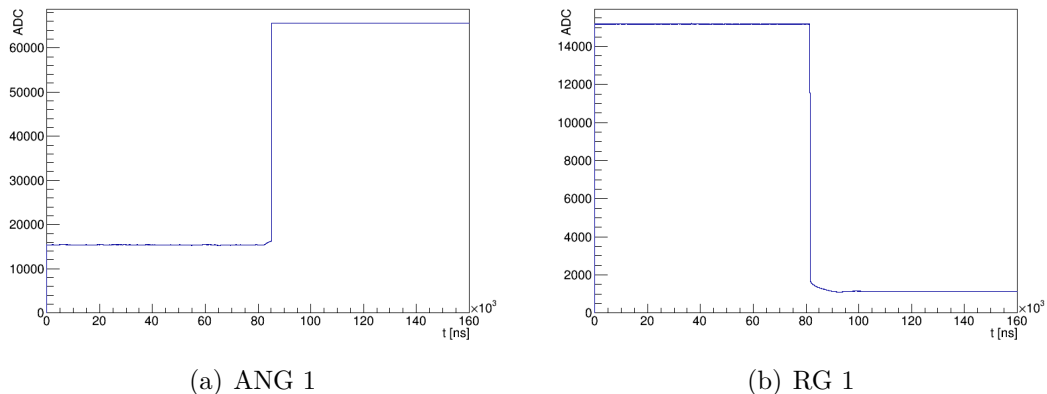
Figure 7.6: *Exemplary "island" event at timestamp 1359896997. One trace is clearly in overflow, the other trace has a non-decaying tail.*

taking period $T = 491$ d:

$$\begin{aligned}
n_r &= r_\mu \times \Delta t \times r_{\text{Ge}} \times T \\
&= 0.04 \ s^{-1} \times 160 \ \text{μs} \times 0.03 \ s^{-1} \times 491 \ d \\
&= (9.4 \pm 3.1_{\text{stat.}})
\end{aligned} \tag{7.4}$$

Thus, the number of random coincidences is in agreement with the expectation.

"Island" Events

There are about 200 events in the "island" region. On closer examination however, every event exhibits traces as shown in Fig. 7.6. One trace is in overflow and at least one other trace has a non-decaying tail, i.e. a trace which remains constant after the rise. Apart from pathological events, these events are identified as having a non-physical trace by the quality cuts and their energy is set to zero.

The shape of these non-decaying events stems from a feature of a part of the pre-amplifier of the germanium detectors, the Genius shaper[†]. In these events the shaper of the detector hit by the muon is brought into overflow, which results in an output which is still within the dynamic range of the FADC but the energy information is invalid. Since the energy information is unusable and they can be very clearly identified as both valid muon and invalid germanium trace, these events will not be studied further. Since these events do not survive the germanium quality cuts, they are unimportant for the germanium data analysis and only appear here since the the quality cuts were deliberately not considered here.

"Shoulder" and "Peak" Events

The main feature in Fig. 7.5(b) contains about 3000 events, which are distributed to about 1/3 to the "peak", the other 2/3 into the "shoulder". These events can be classi-

---

[†]D. Budjáš, *priv. comm.*, 2013
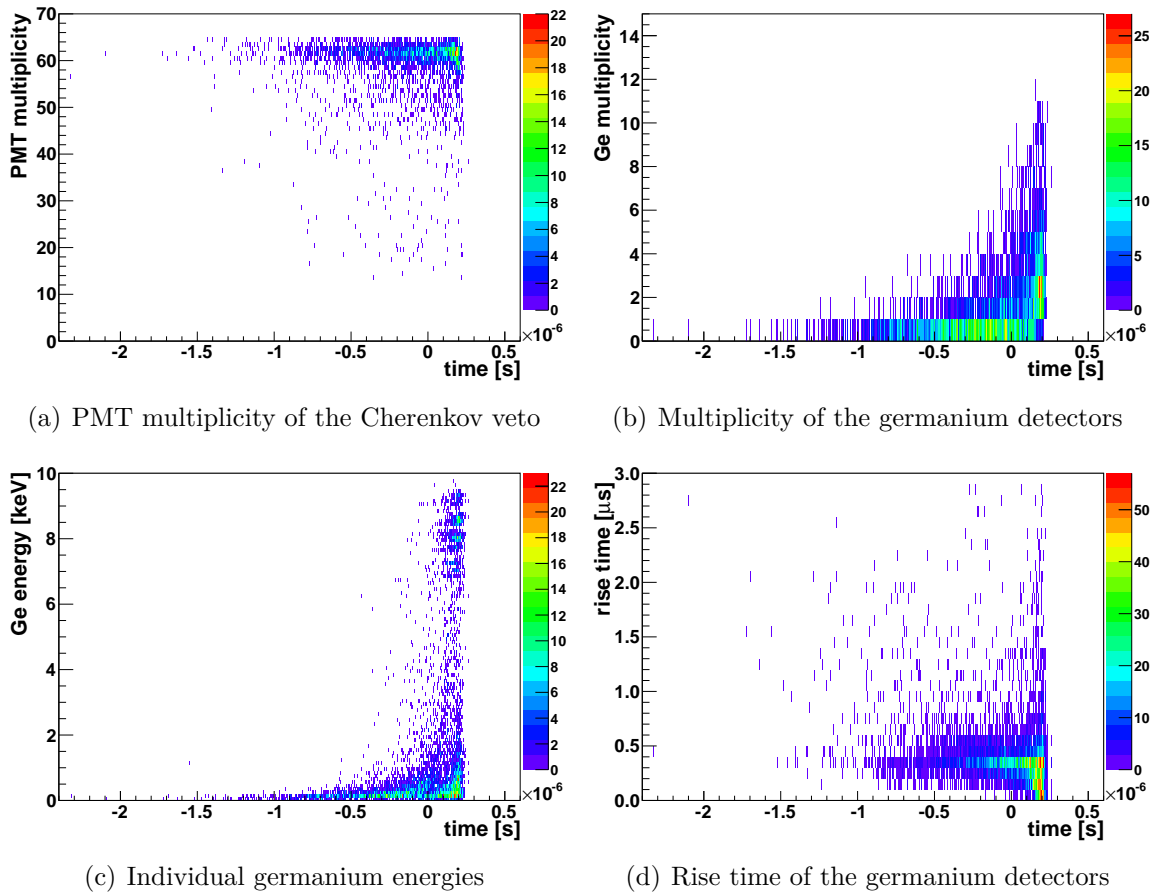
(a) PMT multiplicity of the Cherenkov veto

(b) Multiplicity of the germanium detectors
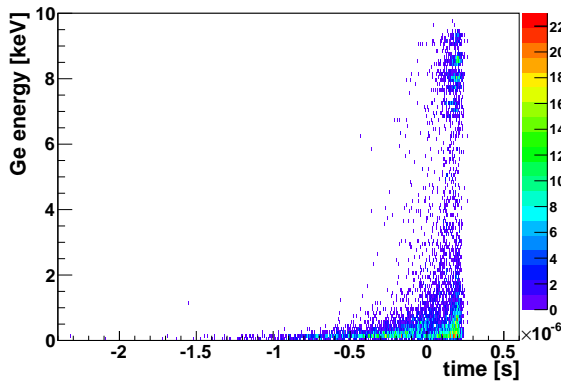
(c) Individual germanium energies
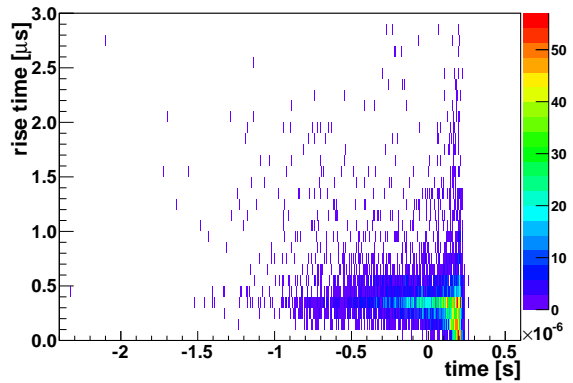
(d) Rise time of the germanium detectors

Figure 7.7: *Correlations of different observables with the time difference $\Delta t_{Ge,\mu}$. The time window is 3 μs and hence only covers the main feature in Fig. 7.5(b).*

fied by studying the event properties as it is done in Fig. 7.7. All these events have in common, that the Cherenkov muon veto showed a high multiplicity. Most events have a PMT multiplicity of around 60 and few below 30 PMTs. Hence, these events can be generally considered as true muon events.

The difference of "peak" and "shoulder" becomes apparent when looking at the germanium side of the event. The "shoulder" events (between -1.5 and 0 μs) show a Ge-multiplicity of one, an energy under 1000 keV and a rise time of the germanium detector in the region of 0.3 μs while "peak" events (at +150 ns) show a multiplicity larger than 2, energies up to the limit of the range of the FADC and events with much faster rise times. The "peak" events with low rise times however are non-standard events like in Fig. 7.6(b) or spike-like events. These events do not seem to be discriminated by the quality cuts.

It can be assumed that the "peak" events are direct energy deposition by muons. An energy deposition of 8-10 MeV is in accordance with the literature value for energy loss by muons in germanium crystals of 4.3 MeV/(g cm^2) given in Ref. [Loh85]. The "shoulder" events however are most likely indirect muon events. Due to their delay and low energy it is unlikely that a direct energy deposition has occurred. Instead, a different mechanisms for the generation can be assumed. Secondary particles from
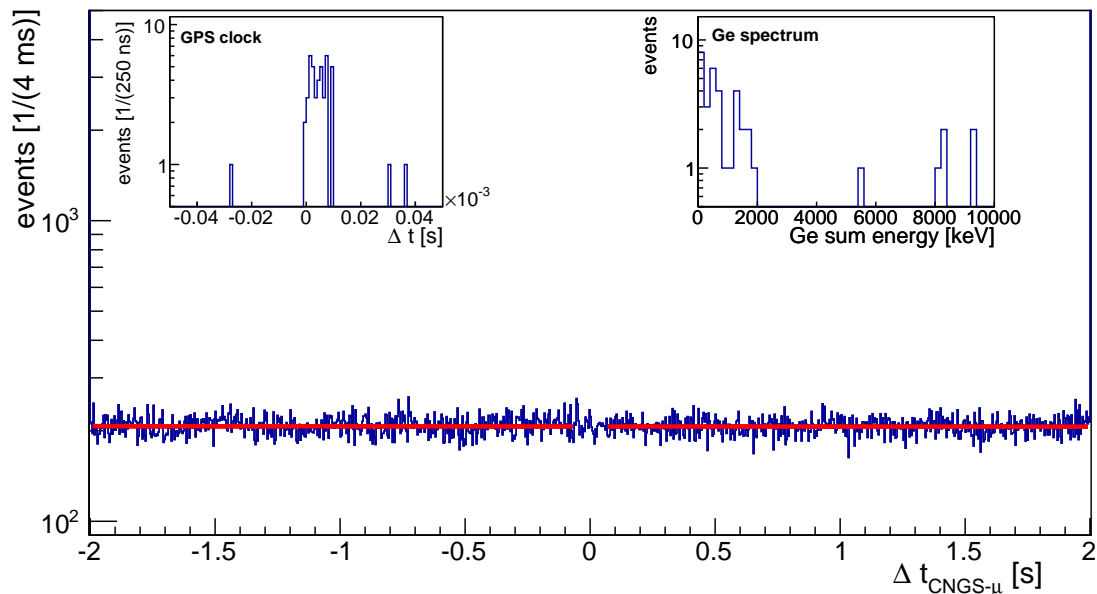
Figure 7.8: *Time difference between* Cngs *beam (at t=0) and the* Gerda *germanium events. Unlike in the muon case in Fig. 6.6, there is no clear enhancement at t=0. The red fit shows a random number of coincidences of 233 per bin. The two insets show a zoom-in at $t = 0$ and the small amount of coincident events (right) and the respective sum germanium sum spectrum (left).*

outside of the detector can deposit energy within the detectors. As the particles enter the detectors from the LAr, multiple germanium detectors can be affected.

7.2   Cngs Events in the Germanium Data

The additional muon background caused by the Cngs has been introduced in Sec. 3.2.2 and the coincidences with the muon veto were very clearly identified in Sec. 6.5. With the GPS clock used in Phase I of Gerda it is possible to reproduce the structure of the Cngs beam with a high accuracy. With this knowledge it is now possible to scan the germanium data in a similar way as the muon data in order to identify the background caused by these additional muons.

In Fig. 7.8 a similar time diagram as in Fig. 6.6 displays the amount of Cngs coincidences recorded by the germanium detectors. For the most part, the diagram is completely dominated by a flat structure caused by random coincidences. The red fit shows a flat distribution of random coincidences of (203 ± 1)/bin for 242 days of coincident data. The expected random rate can be obtained with the rate of the germanium detectors (see Fig. 7.1) of $r_{ge} = 2.87 \times 10^{-2}$/s and the rate of the Cngs of $r_{cngs} = 8.11 \times 10^{-2}$/s in this period, which leads to a number of random coincidences of (194 ± 12)/bin, which agrees well with the fit.

The two inlay show a zoom-in into the region around $t = 0$ where the coincidences should be located and the corresponding spectrum of the summed energy of the ger-

manium detectors. The same sharp structure as in Fig. 6.6 emerges, but with only 45 counts in the entire range and 42 counts in the peak. From the 45 total events, there are 6 without a muon veto including the three events outside of the peak. This fits well with the expected number of random coincidences because in this 100 μs window one would expect (4.9 ± 2.2) random coincidences from the rates given above.

The sum spectrum shows the total energy deposited in the germanium detectors. Mostly, energies below 2 MeV are deposited with varying numbers of detectors firing. There is a single event which deposits 1943 keV in a single detector. However, this particular event is accompanied by a muon veto flag and hence it is of no issue to the background interpolation shown in Sec. 4.7. All other events are either of higher multiplicity, have a muon veto flag or are much further apart from the ROI of the germanium measurements.

As there was a single event in the region for background interpolation, it can be considered as a BI of 1.78×10^{-4} cts/(keV·kg·yr). However, since this particular event was vetoed and as the Cngs beam is de-commissioned this background has had no impact on Phase I of Gerda and will have none for any future measurement.

7.3 Cosmogenic Background: Delayed Coincidences

Of very high interest in any low-countrate experiment is the amount of cosmogenically produced isotopes found in the experiment. The direct interaction of muons was shown to be within a few micro-seconds even if the two different detection systems of germanium and muon veto DAQ have to be compared. The cosmogenically produced isotopes however pose a different threat. The muons at the LNGS have a mean energy of $\langle E_\mu \rangle = 270$ GeV and thus a sufficiently high energy in order to shatter a nucleus via spallation and produce free neutrons which in turn can activate another nucleus. As the spallation product or neutron-activated isotope has a characteristic half-life, it might not decay in the coincidence window for a clear veto flag. If the half-lives are large, it thus becomes difficult in order to achieve any correlation between the delayed decay and its responsible muon. Since these events could pose a threat for the Gerda experiment as well, some work was invested in the simulation and possible listing of these events [GSTR06-02, GSTR06-10, GSTR06-16].

For these reasons this topic of research has recently gained increased attention. Experiments frequently publish their observed neutron fluxes and spallation products [Abe10, Bel13] which are hence used in order to obtain a reliable method of determining a production-yield, independent of material and site of the experiment, i.e. mean muon energy [Kud03]. By extrapolating the measured neutron production rates at different depths and for different materials, a general relation between material, mean muon energy and neutron yield was found [Aga13b]:

$$Y_n(A, E_\mu) = cA^\beta \langle E_\mu \rangle^\alpha, \qquad (7.5)$$

where Y_n is the neutron yield in n/μ/(g/cm^2), $\langle E_\mu \rangle$ the mean muon energy, A the atomic weight of the material and the constants $c = 4.4 \times 10^{-7}$, $\alpha = 0.78$ and $\beta = 0.95$. With the neutron yield it is possible to determine the overall neutron production rate

Table 7.2: *Muon-induced neutron yield in the various components in* Gerda. *The muon rate for the argon is an estimate based on the rate of the water tank.*

material	water	argon	germanium
at. weight [A]	1, 16	40	76
amount [t]	590	80	27.8 kg·yr
density [g/cm^3]	1	1.4	5.3
Y_n [n/μ/(g/cm^2)]	5.18×10^{-4}	1.15×10^{-3}	2.12×10^{-3}
muon rate [1/s]	3.61×10^{-2}	4.89×10^{-3}	9.39×10^{-5}
track length [cm]	800	600	10
N_n [n/d]	1290	410	16.1/(kg·yr)

per second via spallation:

$$N_n = Y_n R_\mu \rho L_\mu, \tag{7.6}$$

where R_μ is the muon rate in 1/s, ρ the density of the material in g/cm^3 and L_μ the mean muon track length in cm. Values for the various materials used in Gerda are listed in Tab. 7.2. From these values it is clear that the neutron production rate in the germanium detectors itself and its adjacent argon is non-negligible but small. However, in order to activate a nucleus, the neutron has to first interact with it by radiative capture. In this case only the simplest neutron activation, i.e. a single radiative neutron capture process (n, γ), will be considered as this process gives a very clear signal in form of prompt γ-lines and subsequent decays. In a first order approximation, a generic neutron spectrum can be used and the (n, γ) activation of the material can be calculated via:

$$P_{\mathrm{nc}} = \sigma \Phi N_i, \tag{7.7}$$

where σ is the cross section of the reaction, Φ the neutron flux in the material and N the number-density in the neutron-irradiated material. The (n, γ) cross-section of both germanium and argon is shown in Fig. 7.9. The energy of cosmogenically produced neutrons is approximated in the range of $10^{-1} - 10$ MeV [Kud03]. As the cross-section is in the region of $\approx 10^{-3}$ barn, a production rate of ≈ 0.1/d for the entire germanium array is found. This is however a very large oversimplification. First, the precise neutron spectrum is not known at this point. Second, the neutrons produced in the germanium detector are transported out of the volume and the vice versa. As the production rate is proportional to the A of the material (see Eq. 7.5), there will be a net effect between germanium and argon. Third, the neutrons will be moderated due to scattering, which necessitates a complete treatment involving all the elastic and inelastic processes a neutron can undergo. Once the exact and overall neutron spectrum is known, it can be convoluted with the cross-section in order to get absolute values. As this is beyond the scope of this work, a different approach will be chosen in order to give limits on the cosmogenic activation. Both the properties of neutron-activated germanium (see Tab. F.1, Tab. F.2 and Tab. F.3) and of the cosmogenic isotopes created
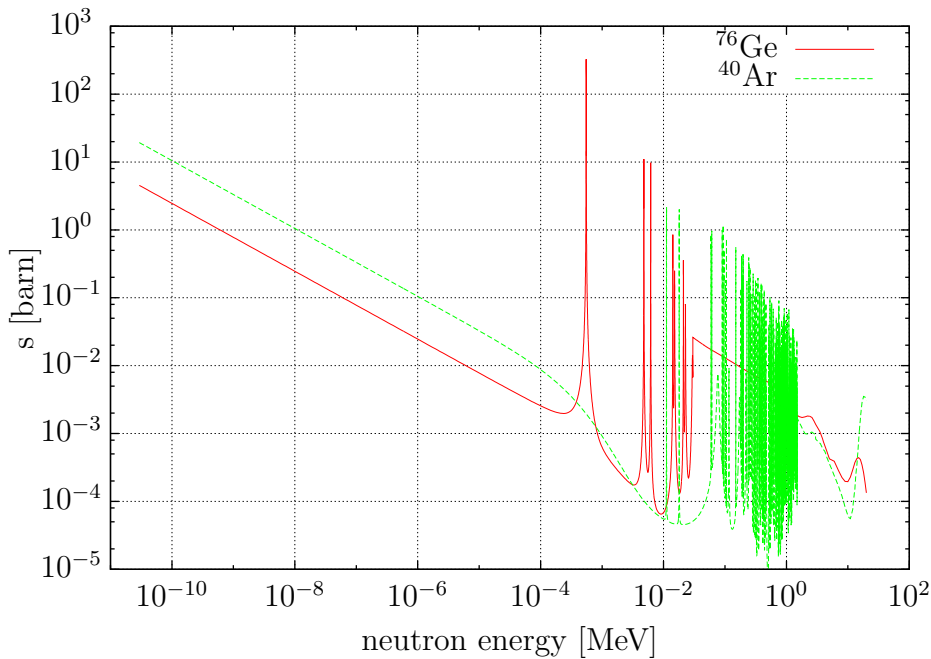
Figure 7.9: *Radiative neutron capture cross-section on* ^{76}*Ge [NND14].*

by spallation (see Tab. F.4 and Tab. F.5) are well known. By looking these characteristic isotopes in the data, limits for the production can be given.

In a first approach, the germanium data was analysed in order to find potential characteristic γ-lines. There are a number of these lines and several constraints are given for the analysis. The line has to be as strong as possible and not interfere with another line from a different isotope. For these reasons, one prompt ^{76}Ge(n, γ)-line, two isomeric transitions in ^{77}As after the β-decay of ^{77}Ge and one line from ^{39}Cl (a spallation product of argon) were chosen. In addition, the 1525 keV peak of ^{42}K was added for overall comparison. The analysed data was the Phase I data without muon or multiplicity cuts and a Gaussian with a locally linear background was fit to the various energy ranges with a 1 keV binning using a profile likelihood fit with a fixed centroid and detector resolution (5 keV FWHM). The results are shown in Fig. 7.10. As can be seen, none of the cosmogenic peaks clearly appear and all the peaks of the cosmogenic isotopes are compatible with zero. The peak for the decay of the ^{42}Ar daughter-nucleus ^{42}K was added for comparison and to test of the model. The likelihood fit yields the limit within 95% confidence level for the number of signal counts as well, which can be used to calculate an upper limit for the production yield considering the detector efficiency and exposure. The typical resolution for germanium detectors in the region around 1 MeV is ≈ 1‰[Mei10], however this case only treats a very specified geometry where a point-like calibration source is irradiating the detector from a distance. When the detector is irradiated by its immediate surrounding or from the detector within, the efficiencies rise drastically which was confirmed by a Monte-Carlo simulation[†]. The efficiency of the full-energy peak detection for e.g. the 861 keV prompt line after ^{76}Ge(n, γ) is found to be 0.168. With this efficiency, the intensities given

---

[†]A.-K. Schütz, *priv. comm.*, 2014

(a) 264 keV IT in ^{77}As, $N_{\text{sig}} < 215.8$

(b) 1085 keV IT in ^{77}As, $N_{\text{sig}} < 33.6$

(c) 861 keV prompt γ in ^{77}Ge, $N_{\text{sig}} < 25.1$

(d) 1267 keV IT in ^{39}Cl, $N_{\text{sig}} < 26.5$

(e) 1525 keV IT in ^{42}K, $N_{\text{sig}} = 1807 \pm 44$
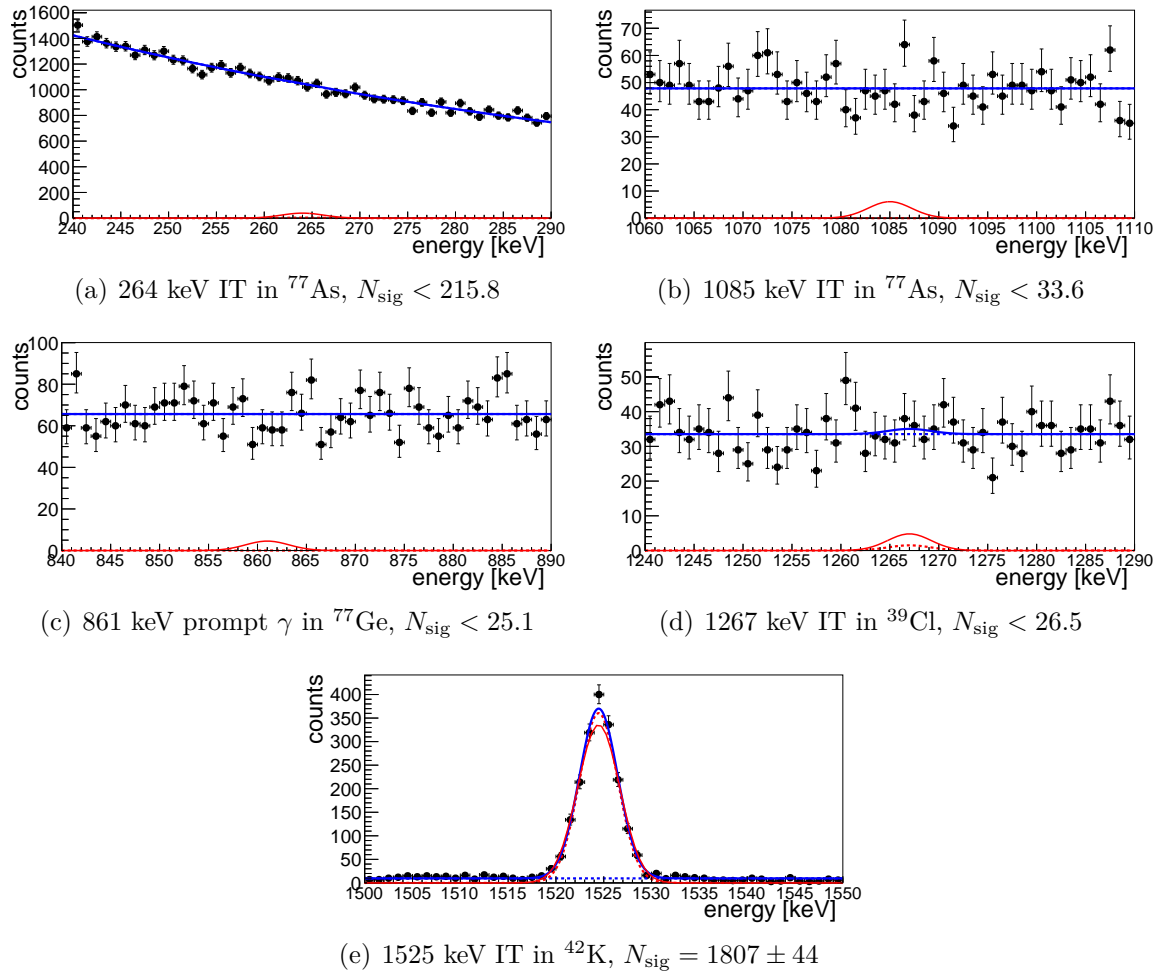
Figure 7.10: *Potential γ-emission lines from cosmogenic isotopes. The overall model fit to the data (solid blue line) consists of a polynomial background (dashed blue line), a gaussian signal (dashed red line) and an upper limit within 95 % confidence level derived with a profile likelihood fit (solid red). The limit of counts in the signal N_{sig} is given for every fit. The line of ^{42}K was added for comparison.*

in Tab. F.2 and Tab. F.3 and a total exposure of $\mathcal{E}$=21.6 kg·yr the production yields can be calculated. A value of $Y(^{76}\text{Ge}(n,\gamma)) < 52.8$ /(kg·yr) is found which is reassuringly low and this limit is fully compatible with the amount of neutrons produced in Tab. 7.2. This is interesting for the experiment as there are lines of germanium isotopes in the region of interest (see Tab. F.3). The line at 2035.5 keV is about 50 times lower in comparison to the 861 keV line, thus if the same limit applies, there would be <1.1 cts/(kg·yr) from this decay alone which would result in a limit to the BI of $^{76}\text{Ge}(n,\gamma)$) of $< 4.7 \times 10^{-3}$ cts/(keV· kg·yr) if a 230 keV window for the background interpolation is assumed. A contribution of this magnitude would be indeed possible in the spectra for the ROI, but it has to be stressed that the limits for the cosmogenic production are entirely dominated by their own respective backgrounds and not uncertainties in the line itself. This means that the methods for deriving the yields is far from perfect and needs to be refined. This could be done by e.g. chosing a potential

(a) Full energy range

(b) Energy range of 671 ± 5 keV
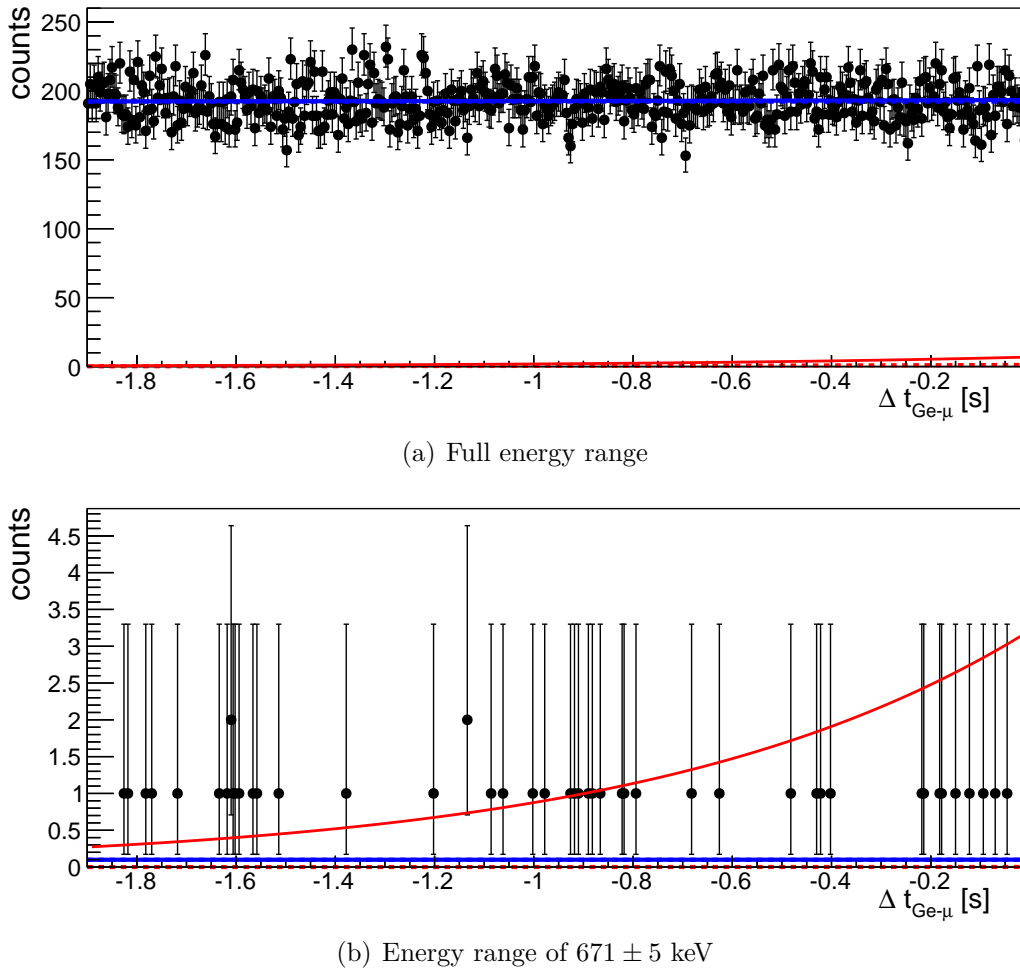
Figure 7.11: *Time-difference window for the decay ^{38}Cl with the germanium event set to zero. The prompt coincidence region (i.e. ± 10 µs around zero) has been omitted. The upper plot shows the full germanium energy range and the lower just data from the peak region. A profile likelihood fit of the model consisting of a polynomial background and an exponential with a fixed constant gives in a 95% confidence level a limit to the number of signal counts of $N_{sig} < 994$ for the entire and $N_{sig} < 24$ for the reduced data set.*

cosmogenic γ-line at a higher energy since the background would drop, but so would the efficiency of the full-energy peak. Nevertheless, some additional constraints are necessary in order to make a refined assumption of the strength of this effect.

A different approach of obtaining an upper limit is to compare the offset between germanium and muon events and search for decay structures. If a muon produces a radioactive isotope, it will decay following its half-life $N(t) = N(0)e^{-\ln 2 \cdot t/t_{1/2}}$ and by chance deposit energy in the germanium detectors. This feature is expected to appear like an exponential decay-structure when comparing the timestamps of the two DAQs. Contrary to the previous approach, much more of the germanium spectrum is observed here, since not only the full-energy peak but also the Compton region is considered. In this case, there are again some constraints regarding the half-life of the

isotope. If it is too small ($<3\,\mu$s) it will interfere with the prompt coincidences shown e.g. in Fig. 7.5. On the other hand, if the half-life is too long, any feature will be with hidden if the random coincidences are too high. The decay of ^{77m}Ge has for example a half-life of 52.9 s and the muon veto fires with a rate of 3.6×10^{-2}/s. This means that if an analysis window of 4 half-lives is chosen, there would be 8 coincidences for each germanium events by random processes alone. A candidate for this type of analysis is the isomeric transition in ^{38}Cl with a half-life of 715 ms and an energy of 671 keV (see Tab. F.4). This spallation process has the highest cross-section of those shown in the table [Bro70]. A time-difference spectrum for this decay can be seen in Fig. 7.11. Similar to e.g. Fig. 7.5, the germanium events is at $t = 0$ and all the muon events are plotted in the given window. The prompt coincidences at $t = 0$ are omitted for better visibility and the spectrum is otherwise dominated by a background. This random background is found to be (192 ± 14) counts per bin which agrees well with the expected random rate. A flat background with an exponential with a fixed half-life of $T_{1/2} = 715$ ms was fit to the data with a profile likelihood and again, the signal strength of the fit is compatible with zero and the error of the background dominates the fit. Despite this large error, a limit for $N_{\text{sig}} < 994$ cts for the decay is found for the entire data-set. The efficiency for any energy deposition of a 671 keV γ-emission from within the germanium crystal was derived again with a Monte-Carlo simulation. If an energy cut of 100 keV is assumed, the efficiency for all energy depositions, i.e. full-energy peak plus Compton spectrum, is found to be 0.343. With an intensity of 100%, a yield of this contamination in the germanium detectors is $Y(^{38}\text{Cl}) < 134.2$ /(kg·yr), which is equally low as above. But again, the limit is dominated by the background error. A clearer sample would be very beneficial too, but as there is no clear full-energy peak for this decay as well, and as the Compton spectrum coincides with all other spectra at low energies, it seems difficult to reach below this limit. Even by reducing the data-set by fitting just the peak region of 671 ± 5 keV (and thus omitting the entire Compton spectrum), no exponential was found with a lower limit of $N_{\text{sig}} < 24$ cts.

There are a more approaches, like e.g. fitting the β-decay of ^{77m}Ge to the existing background model. Here, the efficiency can be considered unity, but since the spectrum of this decay will overlap with all other spectra and since the random coincidences are already too high for the 0.715 s decay of ^{38}Cl shown above, this is an unpromising approach.

In Phase II of GERDA however, the LAr will be instrumented with a hybrid veto system. It is comprised of wave-length shifting fibres which are read out with SiPMs and several regular PMTs. If the scintillation light intensity and the resolution of the apparatus allows basic spectroscopy, it would allow a much better detection mechanism for the cosmogenic isotopes at least in the LAr. Especially the production of spallation nuclei in the LAr could be monitored easily. In addition, a full Monte-Carlo treatment of the neutron transportation, moderation and capture processes would be invaluable for anything other but the very coarse estimates given in this work. However, it is reassuring, that so far none of the most obvious peaks appear in a measurable quantity and that the limits on the decays are quite low.

SUMMARY AND OUTLOOK

8.1 MUONIC BACKGROUND IN GERDA

In this work, the cosmogenic components of the background in the GERDA experiment was systematically identified, analysed and compared to Monte-Carlo simulations. In addition, the hardware of the veto was maintained, extended and both simulation and analysis tools further developed.

A scintillator veto was added to the already existing water Cherenkov veto in order to cover an insensitive spot in the Cherenkov veto. The DAQ was updated in order to accommodate the additional detectors which now reads out all 66 PMTs and 36 panels simultaneous with virtually no dead-time. The hardware threshold were chosen in a way, that by design a very pure muon sample is recorded with only a few percent contamination by random coincidences or other sources of background. With this powerful muon veto over two years of data have been recorded including the 491 coincident days with the germanium detectors. In these data, two effects with an overall influence on the muon flux of 3% could be identified: the additional muon flux caused by the CNGS neutrino beam and the seasonal change in the muon rate caused by temperature variation in the atmosphere which influences the muon production mechanisms. A data sample of the CNGS was obtained and compared to the muon data. Due to the very precise GPS clock which GERDA uses for its DAQs the data sets could easily be correlated. As expected, a clear relation between beam intensity and amount of correlated events was found. These coincident events could then be subtracted from further analysis. The seasonal modulation was introduced and a model for the muon generation over the entire depth of the atmosphere was applied to the data. This model contains both pions and kaons in the muon production mechanism. Two sets of climate data were used to generate an effective temperature, which was found to be in direct relation and in good correlation with the recorded muon flux variation. The results were compared with other experiments and found to be in good agreement as well. A mean muon rate of $I_\mu^0 = (3.477 \pm 0.002_{\text{stat}} \pm 0.06_{\text{sys}}) \times 10^{-4}/(\text{s·m}^{-2})$ was found and the strength of the modulation was found to be $\alpha_{T,ecmwf} = (0.97 \pm 0.05)$ and $\alpha_{T,airs} = (0.93 \pm 0.05)$ for the two data sets of atmospheric data with $\alpha_T = 0.92$ being the literature value for the LNGS.

The Monte-Carlo simulation of earlier works were extended to accommodate for a more

realistic set-up of the muon veto. PMT multiplicity and PE spectra were found in good agreement with the data and the light deposition of cosmogenic muons, Cngs muons and energy-depositing muons could be related to their different track-lengths in the water tank. With the updated geometry, a new value for the efficiency of the muon veto regarding the energy-depositing muons could be obtained. This value rose from $99.56 \pm 0.42\%$ of the previous work to $\varepsilon_{\mu d}^{\text{sim}} = (99.935 \pm 0.015)\%$. This steep increase is in most parts due to the introduction of two man-holes into the volume of the "pillbox" which was optically completely decoupled in the previous simulation.

The muon events in the germanium detectors were studied in detail. Two classes of muon events were found: direct or prompt energy deposition and slightly delayed events caused by secondary particle from the surrounding. A cut to the germanium detectors was defined which identifies sure muon hits. By examining if the veto has fired as well a MRE was found of $\varepsilon_{\mu r} = (99.2^{+0.3}_{-0.4})\%$ which is equivalent to a background index of $\text{BI}_\mu(\text{data}) = (3.16 \pm 0.85) \times 10^{-3}$ cts/(keV·kg·yr). There were several events caused by the Cngs in the germanium data as well. However, most events were accompanied by a veto-flag and those that were not are in accord with the random coincident rate of the two detector systems. Last, the data was searched for isotopes generated by muon spallation or subsequent neutron activation. No characteristic peaks or time signatures of the expected decays were found and a limit for the production yield of neutron capture on ^{76}Ge could be calculated which is $Y(^{76}\text{Ge}(n,\gamma)) < 52.8$ /(kg·yr). This translates into a limit on the background of $\text{BI}(^{76}\text{Ge}(n,\gamma)) < 4.7 \times 10^{-3}$ cts/(keV·kg·yr). Since these values are entirely dominated by the errors of the background, more data or best, a LAr instrumentation has to be considered before any concise values for the production of cosmogenic isotopes can be given.

Despite the fact that several PMTs were showing malfunctioning or outright broke since the construction of the muon veto, the veto is working exceedingly well. Some of these PMTs could be exchanged in-between, but the overall functionality and efficiency could be shown.

8.2   Outlook

The muon veto of the Gerda experiment is in good shape and has served well during Phase I of the experiment. In order to maintain the efficiency of the veto for the next phase, it is mostly crucial to assure that most of the pillbox-PMTs are working properly, as the simulated efficiency is mostly affected by the lack of these PMTs. Unfortunately, the break-down of a PMT is not in the hands of the operator but the ability to quickly and efficiently exchange a detector, should the opportunity present itself is very much so.

As usual, there are several loose ends which could not be treated in full detail. These include another check of the simulations shown in Sec. 5.6. Especially the spectra of the Cngs muons showed some unexpected peaks, which deserve extra study. In addition, it would be helpful to explain smaller inconsistencies with the data but this is of lower priority.

The first muon veto modules for the Gelatio software were implemented during this work. However, the functionality offered by Gelatio is only a fraction in comparison to what was already produced for the local data-analysis chain. A complete transition

to GELATIO would bring the overall status of the software closer to completion and would facilitate the muon data analysis for more people who are not already involved in the hardware.

A big step towards the identification of cosmogenic isotopes in the germanium data would be a full Monte-Carlo simulation of all spallation processes and subsequent neutron-capture reactions. Especially the neutron transportation, scattering and different absorption processes could greatly aid the knowledge of the yield of the respective isotopes. The possible isotopes especially of germanium and their transitions are for the most part very well known. What currently lacks is a full treatment of the entire possible reactions. On the experimental side, the instrumentation of the LAr would help the identification of the cosmogenics as well. If a muon causes any spallation reaction in the LAr, the muon would be visible in the Cherenkov veto and the resulting radiation from the spallation product would be visible in the LAr which would facilitate the identification of these isotopes.

Two smaller effects which could be observable are muon showers and "bottom-up" neutrinos. About 6% of the muons arrive not as a single muon, but in the form of a shower with a muon multiplicity which can exceed 20 and a lateral distribution which can exceed 10 m. These showers are the product of a single particle which produced a number of secondaries in the upstream rock or even in the tmosphere. By utilizing either the panels or data from neighbouring experiments, these showers should be observable, given that a good time correlation bewteen the experiments can be achieved. Finally, the neutrino background on the earth causes an irreducable number of produced muons independent of the depth of the laboratoy. Since most of these muons are coming from below, a detailed study of the time delay between Cherenkov and scintillator veto could perhaps give a handle on these "bottom-up" neutrinos.

8.3 THE FUTURE OF $0\nu\beta\beta$ EXPERIMENTS

The hunt for $0\nu\beta\beta$ is currently a lively field of research. Next to GERDA, there are a number of experiments which are currently taking date, in preparation or being planned. The other germanium experiment MAJORANA is currently in the process of constructing its demonstrator module [Phi12] which is expected to deliver the first data within the next year. The MAJORANA experiment is of special interest to the GERDA experiment, as there is an expressed wish to collaborate in the future for a next-generation germanium experiment. As of now, germanium know-how, simulation and analysis codes are shared in a common effort to further the research.

The two most notable experiment which are currently running are two ^{136}Xe experiments EXO and KAMLAND-ZEN [Aug12, Gan12]. EXO uses a liquid xenon time projection chamber and KAMLAND-ZEN a balloon of liquid scintillator submerged in the KAMLAND tank. Neither experiment was so far able to observe the $0\nu\beta\beta$, but were able to give limits on the decay and hence limits on the effective neutrino mass. The CUORE experiment at the LNGS is using TeO$_2$ bolometer enriched in ^{130}Te and operated in a mili-Kelvin cryostat [Pat13]. The first tower of detectors was successfully tested and the experiment is expected to start data taking by 2015. More than ten experiments differing in isotope, detection technique and projected exposure are currently operating or being planned.

Next to the currently operating experiments and those that will start in the near future, there are already long-term projects which aim to utilize material on a tonne-scale. The Gerda-Majorana experiment is one of these and the xenon based follow-up on the Exo experiment (called nExo) another.

This illustrates the overall research interest that is currently and in the future invested into the question whether or not the neutrino is a Majorana particle. Due to the possible implications on a cosmic scale that such a question has, this interest is more than justified. Whether or not the currently running experiments can verify or further exclude the claim remains to be seen.

For the currently planned $0\nu\beta\beta$ experiments a water-Cherenkov veto as used in this work can be recommended. Despite the fact that a large water tank is necessary, water is a comparably non-dangerous material. The research in this work has proven that such a detection system performs stable and reliable with a moderate investment of 66 PMTs and a DAQ system. Despite its simple and low-maintenance set-up, a number of muon-related effects can be studied with good statistics.

STATISTICAL TOOLS

Here, a short overview over the statistical tools used in this thesis will be given. Unless otherwise noted, these can be found in standard textbooks like [Bar89, Kno00].

BINOMIAL DISTRIBUTION

One of the most general statistical models is the binomial distribution. It is a discrete probability distribution for integer numbers of repetitions n and trial outcomes x, like a coin-toss or the throw of a die. The probability that for n repetitions with a given probability p exactly x times the desired outcome is recorded is given by:

$$B(n|p,x) = \binom{n}{x} p^x \ (1-p)^{n-x} = \frac{n!}{(n-x)! \ x!} \ p^x \ (1-p)^{n-x} \qquad (A.1)$$

An application for the binomial distribution is to calculate the rate of detectors which have fired coincidentally within a given time:

$$D_C(F|N,\Delta t) = \binom{F}{N} D^N \ (\Delta t)^{N-1} = \frac{F!}{(F-N)! \ N!} \ D^N \ (\Delta t)^{N-1} \qquad (A.2)$$

where F is the overall number of detectors, N the number of detectors firing within the time window (Δt) and D is the rate of the detector, e.g. a dark rate. For two detector systems, this simplifies into the product of time window and the two rates. The GERDA set-up shall serve here as examples. Since the 66 PMTs are distributed to 10 FADC, each FADC is considered a detector with a summed rate of 7 PMTs with 2500 Hz dark rate per PMT. The FADCs have to fire within 60 ns to trigger. The resulting rate of random coincidences is $D_C(10|5, 60 \ ns) = 5.4 \times 10^{-6}$/s, which is four orders of magnitude under the real rate as seen e.g. in Fig. 7.1. If just one less FADC is required, the random rate rises to $D_C(10|4, 60 \ ns) = 4.3 \times 10^{-3}$/s, which is already 10% of the overall muon rate. The random rate of both muon veto and germanium DAQ can be calculated within the 160µs long germanium trace. With rates of $r_\mu = 3.6 \times 10^{-2}$/s and $r_{Ge} = 2.9 \times 10^{-2}$/s a random rate of $D_C(160 \ \mu s) = 1.7 \times 10^{-7}$/s is found, i.e. twice per year. Even with these rough estimates it becomes clear that the random coincidences are negligible for the current setup.

CLOPPER-PEARSON INTERVALS

Once a statistically determined value of e.g. a binomial distribution is found, a means for giving the reliability of the value within given boundaries is necessary. This is a confidence interval with a certain probability, i.e. the true value will be within the boundaries with said percentage. Given the binomial distribution and an interval of 95 %, this is the case for the upper and lower boundaries $P(X \leq k) = \sum_{i=0}^{\lceil k \rceil} B(i|p,n) = 0.025$ and $P_l(X \geq k) = \sum_{i=\lfloor k \rfloor}^{n} B(i|p,n) = 0.025$ for k successes out of a total of n. This means that P_u is the highest value of p where it can be assumed that there are k successes.

In practice the two boundaries can be calculated with the help of the beta function, as binomial and beta-function are connected via:

$$\sum_{i=0}^{k} B(i|p,n) = \text{Beta}(1-p; n-k; k+1). \tag{A.3}$$

With this function, the upper and lower limits for a statistical value can be easily calculated. This method is called the Clopper-Pearson intervals [Clo34]. The values for the MRE introduced in Sec. 7.1.2 are 841 positive outcomes out of 848 total events. This results in a mean value with 68% confidence intervals of:

$$\varepsilon_{\mu r} = 99.2^{+0.3}_{-0.4}\% \tag{A.4}$$

BAYESIAN STATISTICS

When considering real life examples, especially of unknown effects, the respective probabilities for the "success" of a probabilistic trial may not be known, e.g. the efficiency of a detector to observe a particle. However, a measurement can strictly speaking only give the reverse probability function, i.e. the probability that the particle was seen by the detector. Here, it is needed to reverse the process by inferring a "posterior probability" by providing a probability model, antecedents and a prior probability. Here, the antecedents are used to update the statistical model. This is summarized in Bayes' rule:

$$P(\vec{\lambda}, M | \vec{x}) = \frac{P(\vec{x} | \vec{\lambda}, M) \cdot P(\vec{\lambda} | M)}{P(\vec{x})} \tag{A.5}$$

where $P(\vec{\lambda}, M | \vec{x})$ is the probability that a model M and parameters $\vec{\lambda}$ given the outcome $\vec{x}$ is true. This is a different approach to statistics, as it is giving a credibility or "degree of belief" of the tested model instead of a confidence interval for a determined value. Usually, such a value is given as a percentage of a certain effect happening in an interval given that the model is right. This model gives a degree of credibility that the value is within an interval.

Applied to the binomial distribution, the posterior probability function becomes:

$$P(p|N,n) = \frac{(N+1)!}{(N-n)!\, n!}\, p^n\, (1-p)^{N-n}. \tag{A.6}$$

This can now be used to calculate credibility intervals like in Sec. 7.1.2. A graphical representation of the probability density function can be seen in Fig. A.1. The outcome
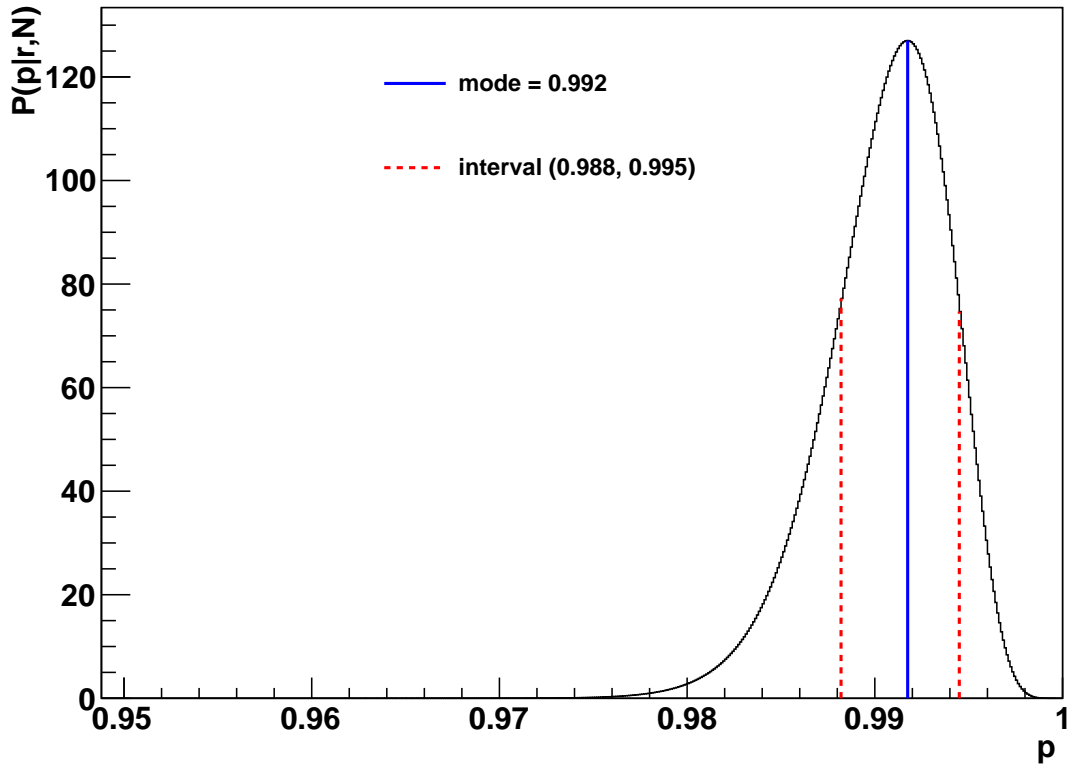
Figure A.1: *Probability density function of the muon rejection efficiency assuming a flat prior probability between 0 and 1 and assuming the values found in Sec. 7.1.2.*

of such a test is here always given as the mode (i.e. the most probable value) and the smallest interval for 68% credibility as opposed to e.g. the median of the distribution and a central interval around the median for a fixed probability. With this method, the mode and cedibility interval of in this case the MRE is:

$$\varepsilon_{\mu r} = 99.2^{+0.3}_{-0.4}\% \tag{A.7}$$

The values are the same as in the previous section, however, the statistical conclusion is different. Unless otherwise noted, values like efficiencies in this work are given with this method, i.e. mode and credibility interval.

POISSON DISTRIBUTION

In the limit of a constant process but with small count-rate or probability the binomial distribution takes the simplified form:

$$P(x) = \frac{(\bar{x})^x e^{-\bar{x}}}{x!} \tag{A.8}$$

where $\bar{x} = pn$ is the expected value of x given a probability p and n trials. This is the only parameter required, which makes it an easy function to work with. Since this is

a normalized function i.e. $\sum_{x=0}^{n} P(x) = 1$, the error is given as

$$\sigma^2 = \sum_{x=0}^{n} (x - \bar{x})^2 P(x) = \bar{x}, \qquad (A.9)$$

i.e. the standard deviation is the square root of the mean. A standard example for the Poisson distribution are the usual calibration spectra of PMTs. Here, it is common to observe the SPP of the PMT as a measure of the recorded light. However, if more photons than the SPP is recorded, the spectra become distorted. For this reason, it is common practice to trigger on the calibration light source which is so dim, that for one single photon, there are 10 events in which the PMT has seen nothing, i.e. $\bar{x} = \frac{1}{10}$. The Poisson statistics now tells that $P(0) = 0.9$, $P(1) = 0.09$ and $P(2) = 0.0045$. This means that the "contamination" of two photon events is 20 times lower than those of single photon events. This is a general guideline applied to all calibration measurements such as in Sec. 5.3.1 or Fig. 6.18.

Correlation Coefficient

When two physical properties are seemingly related, a way is needed to measure the degree of correlation [Gal88]. For the comparatively simple case of linear correlation, a method often used to describe the degree of correlation is the Pearsons correlation coefficient:

$$R = \frac{\sum_{i=0}^{n}(X_i - \bar{X})(Y_i - \bar{Y})}{\sqrt{\sum_{i=0}^{n}(X_i - \bar{X})^2}\sqrt{\sum_{i=0}^{n}(Y_i - \bar{Y})^2}} \qquad (A.10)$$

The dimensionless parameter R is $+/-1$ for a full positive/negative correlation and 0 for linearly uncorrelated values of X and Y. A value of $R = 0$ signifies only that the values are linearly uncorrelated as even simple non-linear functions like e.g. $y = \sin x$ cannot be properly described by this method. Since the value is dimensionless it is only a measure for the degree of correlation, not the slope of the linear dependence. This has to be determined separately.

DETECTOR RATES AND PERFORMANCE

As the muon veto of the GERDA muon veto consists in its current form of over 100 different detectors, here a brief performance report will be given. Rates of the detectors over time will be shown as well as calibration spectra. Malfunctioning detectors will be discussed, if not already done in the main chapters.

B.1   PMTS PERFORMANCE

In the GERDA water tank there are a total of 66 PMT operated under water over a time of more than 2.5 years. As the performance of the muon veto is dependent on the individual performance of each single PMT, here an overview over their individual performance will be given.

The malfunctioning PMTs were already mentioned in Sec. 6.1.1. The distribution in the water tank of these PMTs is shown in in Fig. B.1. It is apparent that there could be hardly any relation between especially the implosion of the two PMTs 401 and 604, as they are roughly 13 m apart. None of the PMTs inbetween have suffered any deterioration and hence the two implosions have to be considered as self-contained events. Unfortunately, another PMT stopped working after the second filling of the water tank, which is pillbox PMT 106. It has been shown in Sec. 5.6 that the MDE for muons depositing energy in the germanium detectors depends mostly on the PMT in the pillbox. However, the loss of only one of these PMT is still acceptable considering that the revised efficiency is still higher than the efficiency with the previous geometry. Nevertheless, this issue needs to be kept in mind. The other PMTs however work reliably as can be seen in Fig. B.3 and Fig. B.3 which show the rate of each single PMT over the entire duty cycle of the veto. The obvious pauses are due to pauses in the data taking during calibrations or work on the veto. It is apparent that the rates of the PMTs in a ring differ only little, an effect that is due to the predominant direction of the muons. Apart from this, even the rates of the single PMTs already show the annual modulation, which is explored in detail in Sec 6.5 and Sec 6.6. Ring 2,3,4 and 6 each contain a PMT which does not behave as expected, these are highlighted in Sec. 6.1. Ring 4 contains another PMT which shows a lower rate after the end of Phase I in Aug. 2013. This PMT showed its original behaviour after the indicated pause at a much lower voltage. This however settled back to its original value and due
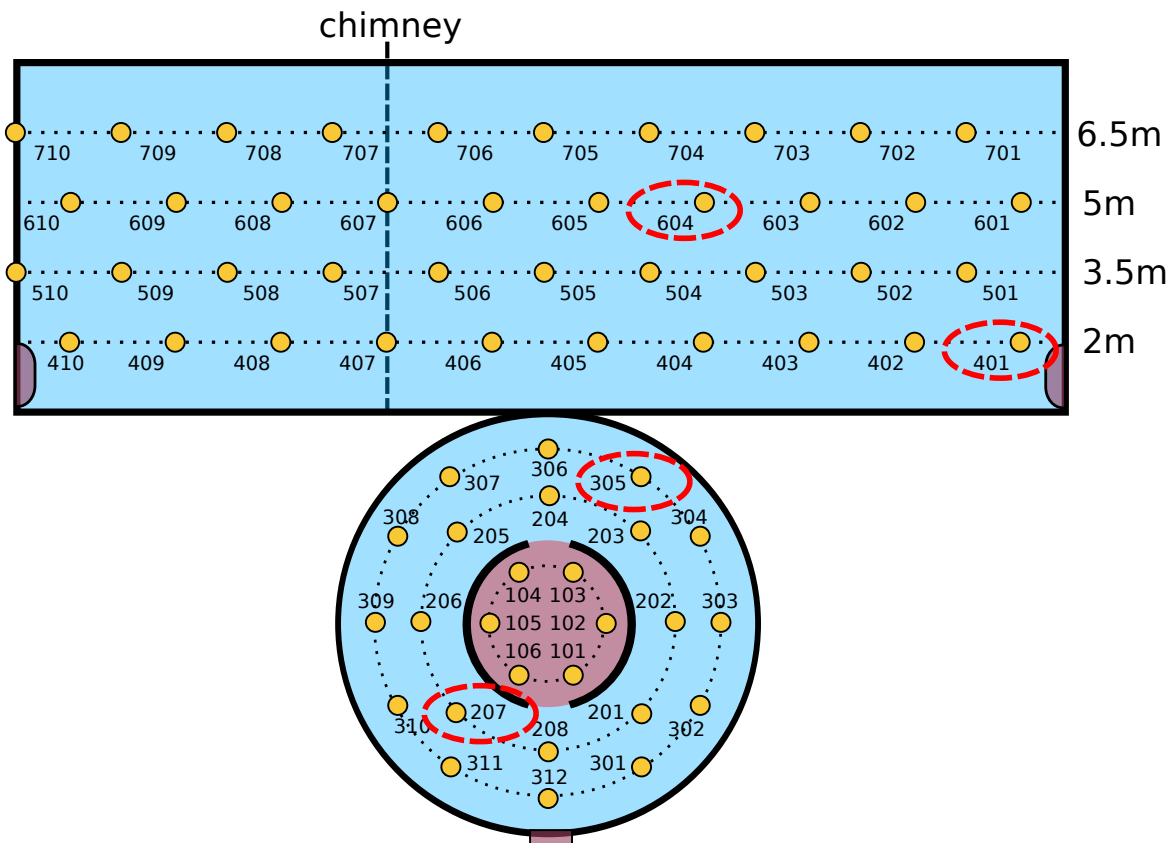
Figure B.1: *Distribution of the malfunctioning PMTs in the water tank. The problematic PMTs are marked in red. The imploded PMTs 604 and 401 are about 13 m apart.*

to the low frequency of calibrations, it was rectified only a few months later. As the overall efficiency suffers little if a single PMT is malfunctioning and as there were no germanium measurements in this time, this PMT was not listed in Sec. 6.1.

Fig. B.2 shows calibration curves of the first PMT of each respective ring of PMTs in the water tank. This data was recorded in calibration mode, i.e. with a trigger on a pulsed LED-driven light source in the tank. Each inset shows a large peak close to zero, which is random noise of the PMT when it was not recording any light when the LED was pulsed. The peak in the middle corresponds to the SPP of each single PMT. As the pedestal contains >10 times more entries as the peak, it is certain that this peak is indeed the SPP with small contaminations of the double-photon-peak. Each PMT shows a clear separation between pedestal and SPP, the ration between peak and "valley" is $1.5 - 2.5$. The mean of each PMT is very close around the desired value of 100 FADC channels, which allows a convenient common trigger condition for all PMT. Both peak position and standard deviation of the gaussian show little deviation.
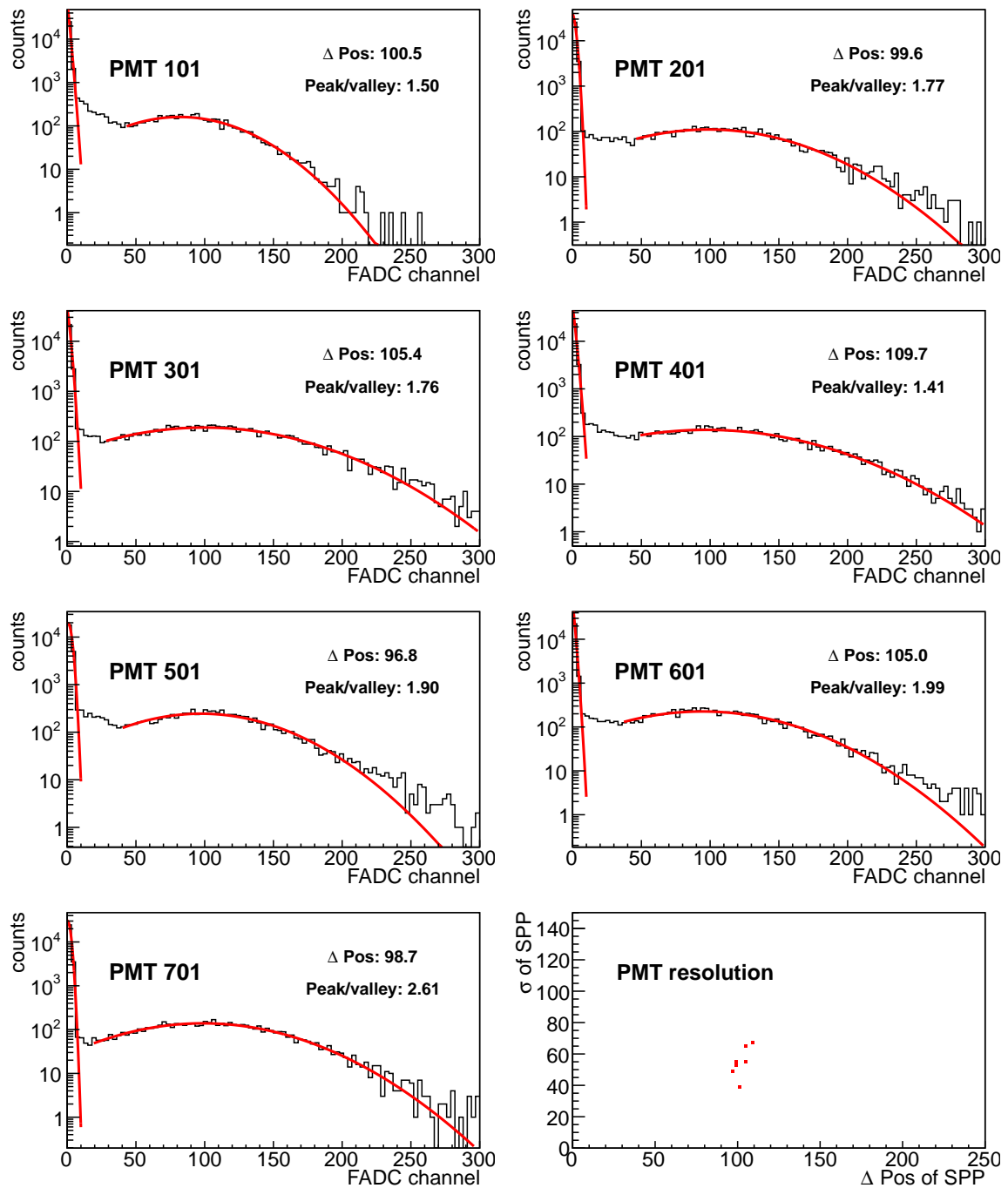
Figure B.2: *Calibration SPPs of seven PMTs with a gaussian fit to both SPP and pedestal. Each inset for the seven PMTs contains the position of the SPP in relation to the pedestal and the peak-to-valley ratio. The detector resolution in terms of the width of the SPP vs. the position of the SPP is shown in the last inset.*
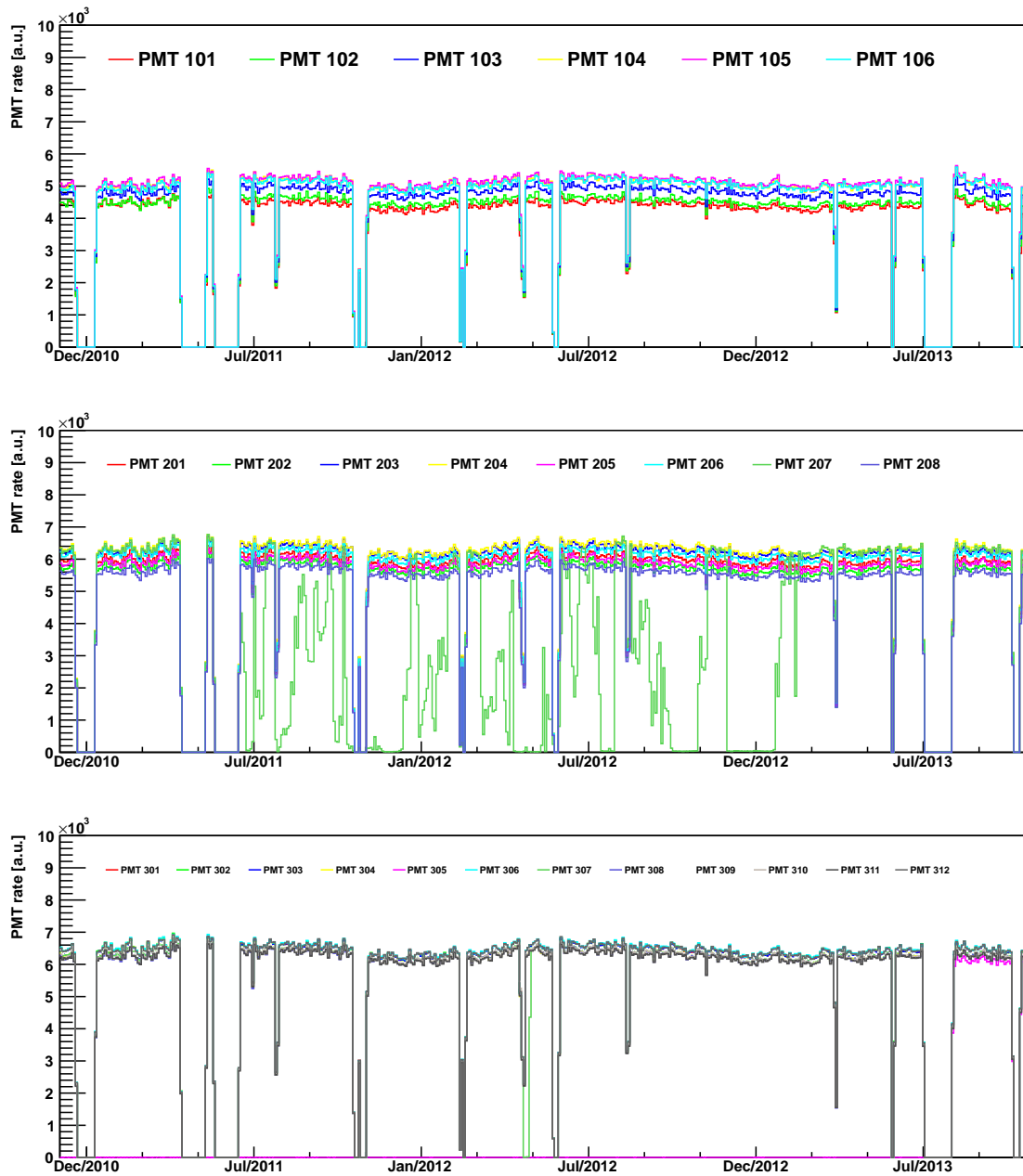
Figure B.3: *Rates of the first three rings of PMTs.*
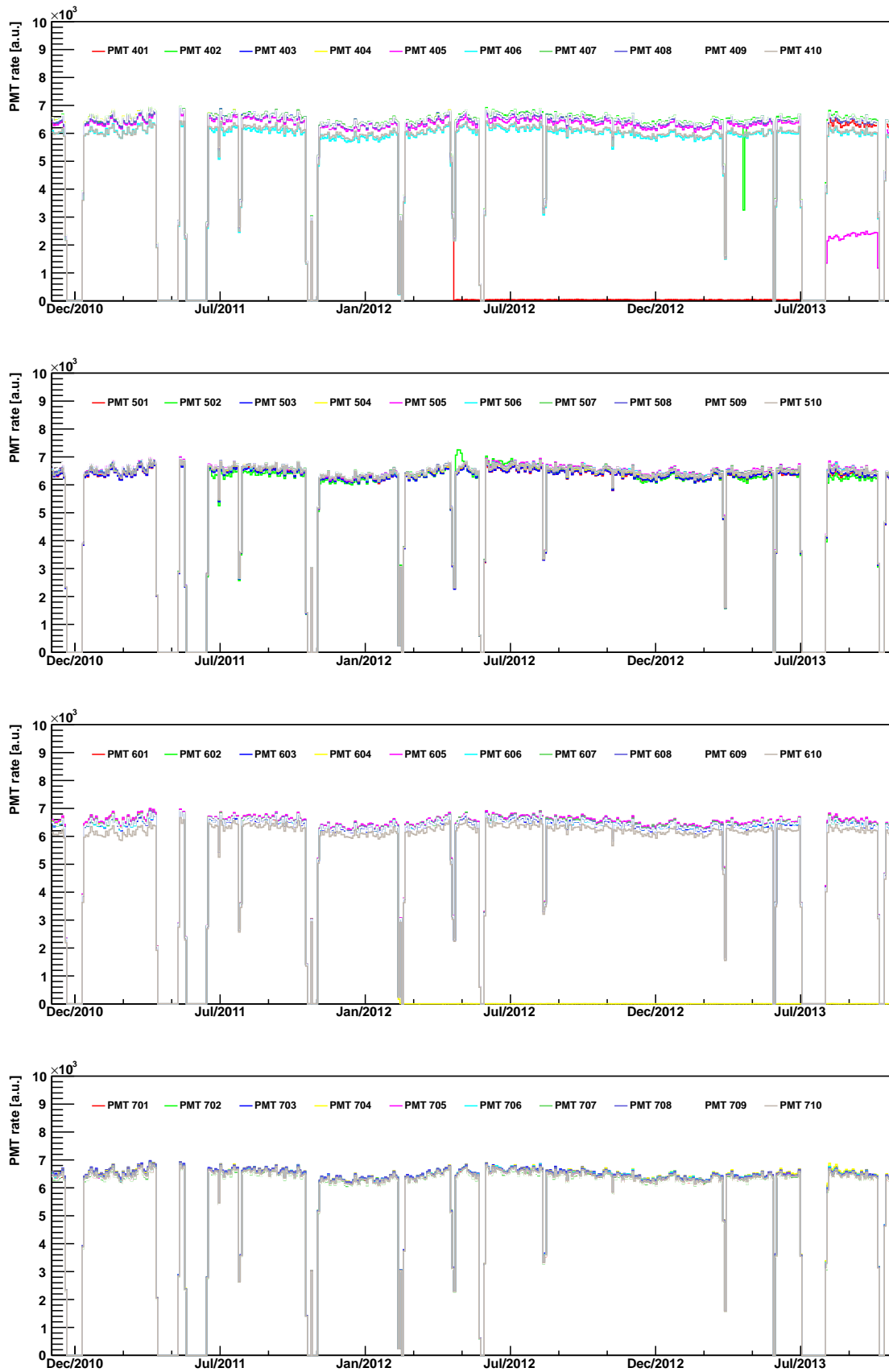
Figure B.4: *Rates of the last four rings of PMTs.*

Table B.1: *Rates of the separate pixel. Each value is given in the rate per m² for better comparison. Pixel 3-34 are 50×50 cm, the others 200×50 cm.*

pixel	rates $[1/(\mathrm{s\,m^2})]$	pixel	rates $[1/(\mathrm{s\,m^2})]$
#1	$3.32 \times 10^{-4} \pm 3 \times 10^{-6}$	#19	$3.59 \times 10^{-4} \pm 6 \times 10^{-6}$
#2	$3.29 \times 10^{-4} \pm 3 \times 10^{-6}$	#20	$3.65 \times 10^{-4} \pm 6 \times 10^{-6}$
#3	$2.80 \times 10^{-5} \pm 5 \times 10^{-6}$	#21	$3.74 \times 10^{-4} \pm 6 \times 10^{-6}$
#4	$3.21 \times 10^{-4} \pm 6 \times 10^{-6}$	#22	$3.68 \times 10^{-4} \pm 6 \times 10^{-6}$
#5	$3.31 \times 10^{-4} \pm 6 \times 10^{-6}$	#23	$3.20 \times 10^{-4} \pm 6 \times 10^{-6}$
#6	$3.23 \times 10^{-4} \pm 6 \times 10^{-6}$	#24	$3.70 \times 10^{-4} \pm 6 \times 10^{-6}$
#7	$2.89 \times 10^{-4} \pm 5 \times 10^{-6}$	#25	$2.97 \times 10^{-4} \pm 5 \times 10^{-6}$
#8	$3.37 \times 10^{-4} \pm 6 \times 10^{-6}$	#26	$3.86 \times 10^{-4} \pm 6 \times 10^{-6}$
#9	$2.55 \times 10^{-4} \pm 5 \times 10^{-6}$	#27	$2.05 \times 10^{-5} \pm 1 \times 10^{-6}$
#10	$3.41 \times 10^{-4} \pm 6 \times 10^{-6}$	#28	$3.08 \times 10^{-5} \pm 2 \times 10^{-6}$
#11	$3.24 \times 10^{-4} \pm 6 \times 10^{-6}$	#29	$2.15 \times 10^{-5} \pm 1 \times 10^{-6}$
#12	$3.49 \times 10^{-4} \pm 6 \times 10^{-6}$	#30	$2.82 \times 10^{-5} \pm 2 \times 10^{-6}$
#13	$3.55 \times 10^{-4} \pm 6 \times 10^{-6}$	#31	$2.63 \times 10^{-4} \pm 6 \times 10^{-6}$
#14	$3.54 \times 10^{-4} \pm 6 \times 10^{-6}$	#32	$3.13 \times 10^{-4} \pm 6 \times 10^{-6}$
#15	$2.43 \times 10^{-6} \pm 5 \times 10^{-7}$	#33	$3.61 \times 10^{-4} \pm 5 \times 10^{-6}$
#16	$2.86 \times 10^{-5} \pm 5 \times 10^{-6}$	#34	$2.89 \times 10^{-4} \pm 6 \times 10^{-6}$
#17	$1.95 \times 10^{-5} \pm 4 \times 10^{-6}$	#35	$3.37 \times 10^{-4} \pm 3 \times 10^{-6}$
#18	$2.93 \times 10^{-5} \pm 5 \times 10^{-6}$	#36	$2.20 \times 10^{-4} \pm 3 \times 10^{-6}$

B.2   Panel Performance

Here, the rates of the panels and the respective pixel are listed. Contrary to the PMTs, where small differences are expected, the panel and pixel rates should be uniform. For the panels, there are no shadowing effects or different volume sizes, but just a flat uniform detector, which should see the same muon flux. As already mentioned in Sec.6.2, pixels 15-18 and 27-30 exhibit a lower rate compared to the others and share FADC channel #16. However, as can be seen in Fig. B.5 and Fig. B.6, only panel 16 and 32 show lower rates and these two belong to pixels 15-18. In any case, this irregularity needs to be investigated, especially since the two panels 17 and 31 belonging to pixel 27-30 were malfunctioning in the very beginning of the data taking. This however was fixed and the panels were working sufficiently well afterwards. Apart from that, most other panel and pixel show a constant performance over time.
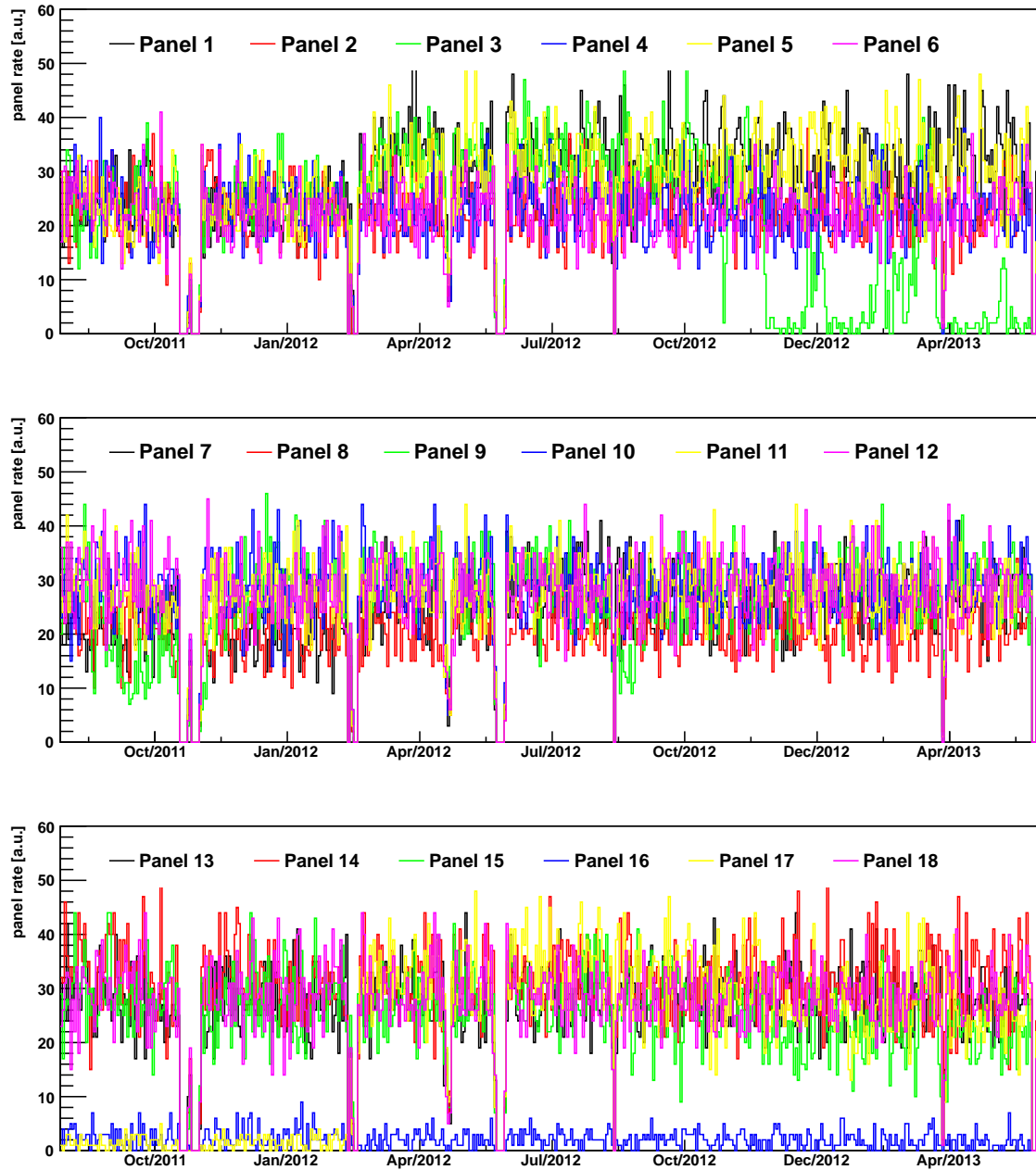
Figure B.5: *Rates of the first 18 panels.*
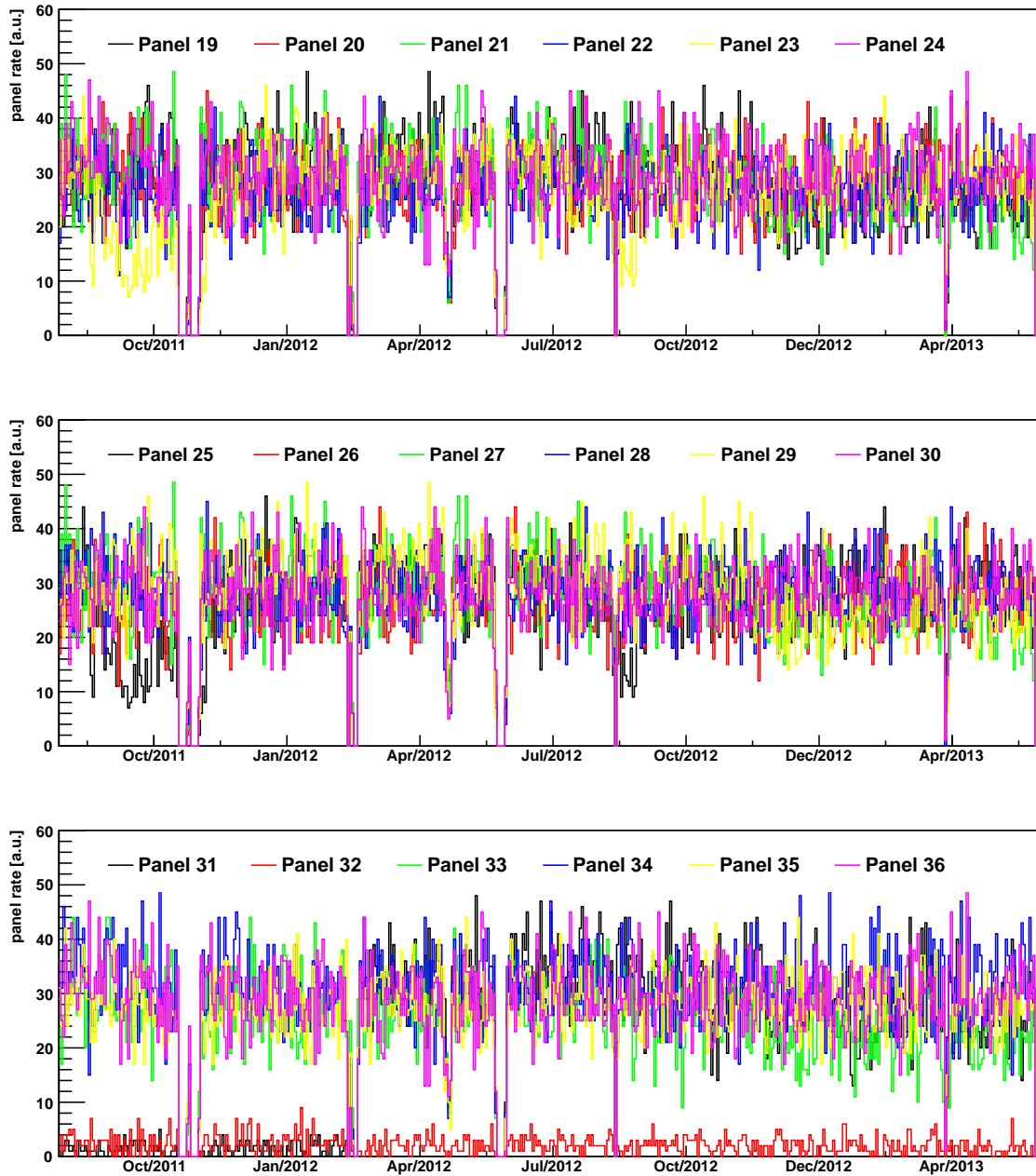
Figure B.6: *Rates of the second 18 panels.*

CNGS EVENTS IN THE CRESST EXPERIMENT

The CRESST experiment [Ang09] searches for Dark Matter with the help of cryogenic calorimeter. CRESST is searching for Weakly Interactive Massive Particles (WIMPs), a so far hypothetical particle, which could be responsible for the excess matter in the universe. The used scintillating crystals are sapphire (Al_2O_3) or calcium-tungstate ($CaWO_4$). In these scintillators, a nuclear recoil can be characterized by both the deposited temperature and the scintillation light caused in the crystal. The change in temperature is measured with a superconducting films glued to the film operated at its critical temperature. A small change in temperature causes a great change in the resistivity of the film which can be hence used as a very sensitive thermometer. The scintillation light is measured with cryogenic light absorbers close to the crystals and read out with superconducting films as well. In order to maximize the amount of light the absorber is able to see, the inside of each detector module is covered with the VM2000 foil also used in the GERDA muon veto. By measuring both of these, very faint effects like nuclear recoils which e.g. WIMPs would cause can be identified. The two read-out channels allow a powerful discrimination between the interaction caused by radioactivity (α, β and γ) or nuclear recoils caused by other particles (such as neutrons).

Much like the GERDA experiment, CRESST is subject to the same muon flux, as both experiments are neighbours in the Sala A of the LNGS. This means, that the same influence of the CNGS beam is to be expected (see Sec. 3.2.2 and Sec. 6.4). The CRESST muon veto system consists of a rectangular box of 20 plastic scintillator panels, which are read out with a PMT. The only hole in the muon veto is on top, which is needed to fit the cryostat into the veto. However, this does no concern the measurement of the CNGS muons as they come almost directly from the side. A data sample of the CRESST muon veto[†] was used to search for similar coincidences as in Sec. 6.5.

The main difference can already be seen in the time difference between the two systems, which is shown in Fig. C.1. The same time difference for GERDA (see Fig. 6.6) showed a peak on a much smaller scale, especially once the GPS clock was installed. While the resolution of GERDA allowed to reproduce the 10.5 µm beam structure, the CRESST

[†]K. Rottler, *priv. comm.*, 2014
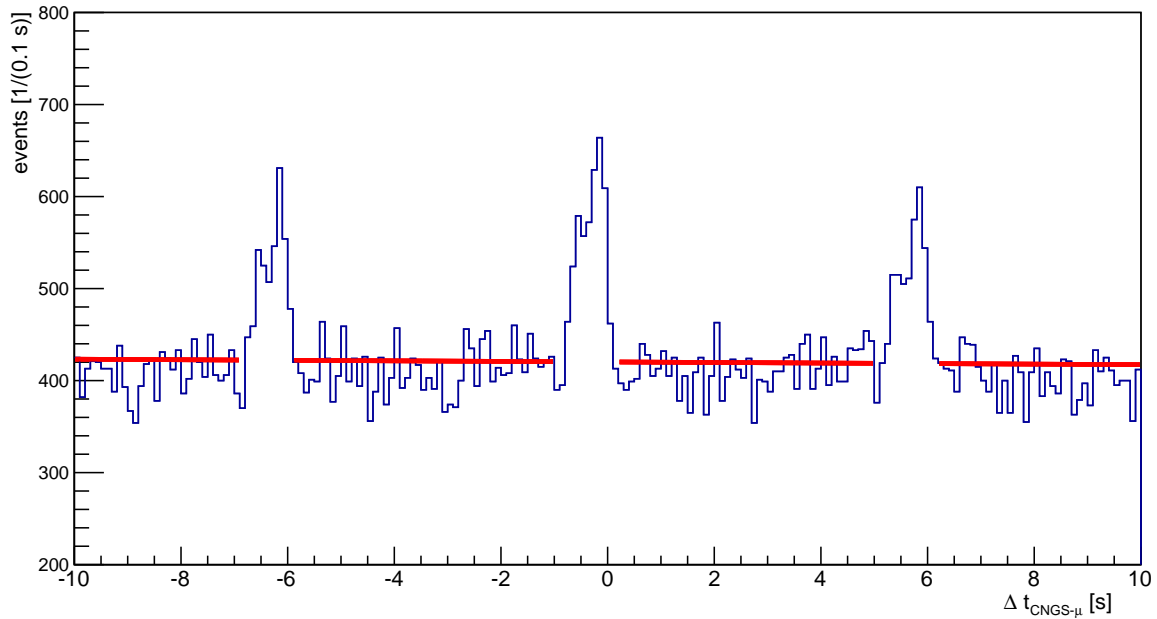
Figure C.1: *Time difference between* Cngs *beam (at t=0) and the* Cresst *muon veto. The peak is much wider in comparison to the* Gerda *result (see Fig. 6.6).*

has a resolution in the range of 2 s. However, a clear enhancement at 0 s and ±6 s can be seen, which represents the repetition time of the beam. The time resolution for an experiment as Cresst is not top priority, as e.g. for TOF experiments like Opera. Due to the clean environment and the low count rates a better time resolution would yield little as the random coincidences are negligible.

The rates of the different components can be seen in Fig. C.2. The muon veto has a rate of 0.0015/s and the Cngs beam has a mean rate of 0.12/s, the two systems have 243 days of overlapping data. Apart from this, coincident events and the corrected rate show no major deviations from a flat distribution over time. The fit in Fig. C.1 shows a background of 4200/s. Given a beam rate, veto rate of 0.0015/s and duty cycle, this yields a number of random coincidences of 3700/s, which can be considered in good agreement with the fit.

In Fig. C.3 is is shown how the time difference Δt between events from the Cngs and Cresst changes over time. While Δt stays constant at $0, \pm 6$ s respectively in 2010, it drifts by about 2 s in 2009, which is a reason for the poor time resolution. However, drifts in regular CPU clocks of 2 s/yr are not uncommon and have to be considered in an analysis like this.
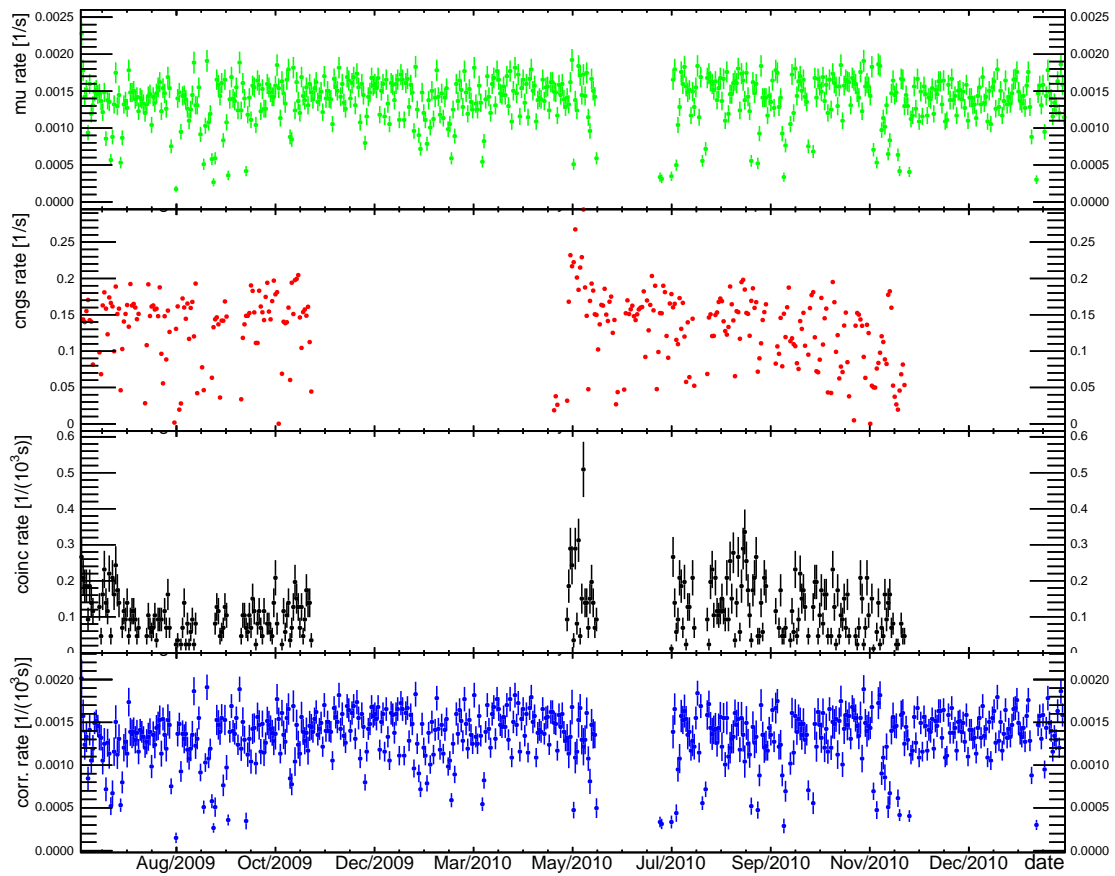
Figure C.2: *Rates of the* CRESST *veto,* CNGS *beam, coincident events and corrected muon spectrum.*
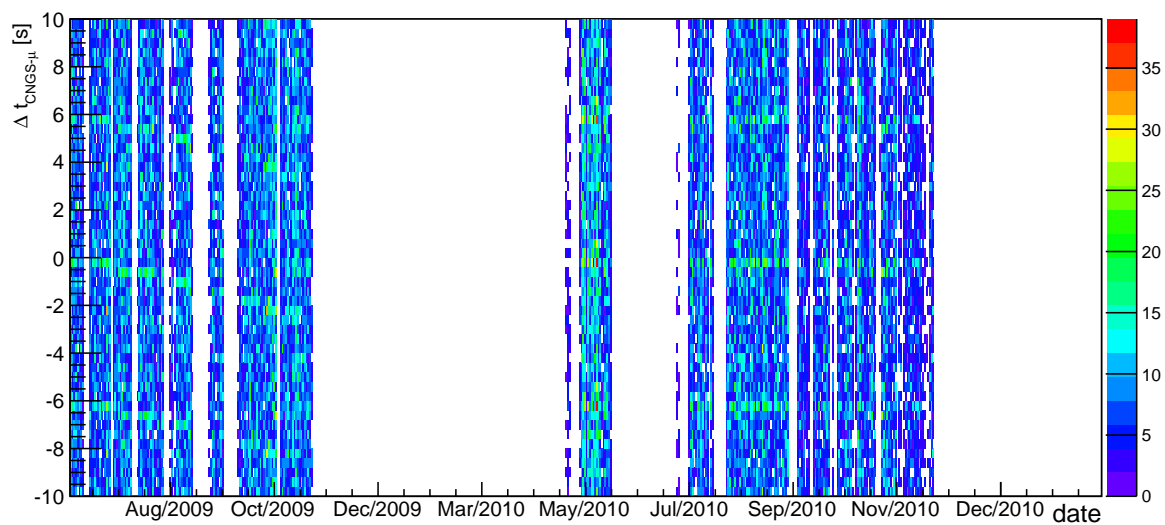
Figure C.3: *Time difference between* CRESST *and* CNGS *over time. In 2009, the coincident peak shifts by about 1 s.*

GELATIO DEVELOPMENT

The GELATIO framework is the common data analysis tool of the GERDA collaboration [Ago11]. The main goal of this software is to have a standardized analysis software, which allows a quick, modular and above all reproducible analysis chain of mostly the data from the germanium detectors.

If the system supports the necessary libraries for the operation of GELATIO (i.e. ROOT, CLHEP, TAM and MGDO), the converter can be invoked with the following command:

```
Raw2MGDO -i -c StruckMu rawfile.events -f output.root
```

This converts the muon data taken with the DAQ described in chapter 5. This converter can be used for both calibration and data files. As this is a text-line command if the necessary paths are set correctly, it can be used in an automatized shell-script.

The analysis of the muon data in GELATIO is realized in a multi-tier approach, much like the germanium data. First, the raw data from both calibration and background runs are converted to `Tier1` i.e. are "rootified" with the command given above. Now, the two data streams are treated differently. The calibration data is used to produce standard or template pulses. These pulses are mean traces for each PMT. For each event, the trigger condition is checked, then the trigger point is determined, the pulses of each PMT are shifted onto a common trigger point in the trace and afterwards all traces with a trigger are summed and divided by the number of triggered events. This functionality is provided by a new `GEMDTemplatePulse` module. These standard pulses are stored in the output `Tier2` file for use in a subsequent `ini`-file.

For the background muon data, the files are first converted into `Tier1` as the calibration files. Similar to the generation of the `Tier3` germanium data, a calibration file is needed for the `Tier2` muon files. As in the calibration file conversion, the "standard" modules `GEMDTop`, `GEMDFADC` and `GEMDBaseline` are executed. Several values in the `GEMDBaseline` modules are geared specifically towards germanium detectors, but do not seem to affect the baseline restoration for much shorter pulses as the PMT traces as in this case. Afterwards a trigger is found with the new `GEMDTriggerThr` module, which determines the trigger point by applying a fixed threshold, as the hardware trigger does. The already available trigger module `GEMDTrigger` does not offer this possibility. In the next step, i.e. the module `GEMDMuPE`, the traces of both the calibration as well the background runs are transformed into Fourier space, divided and transformed back.
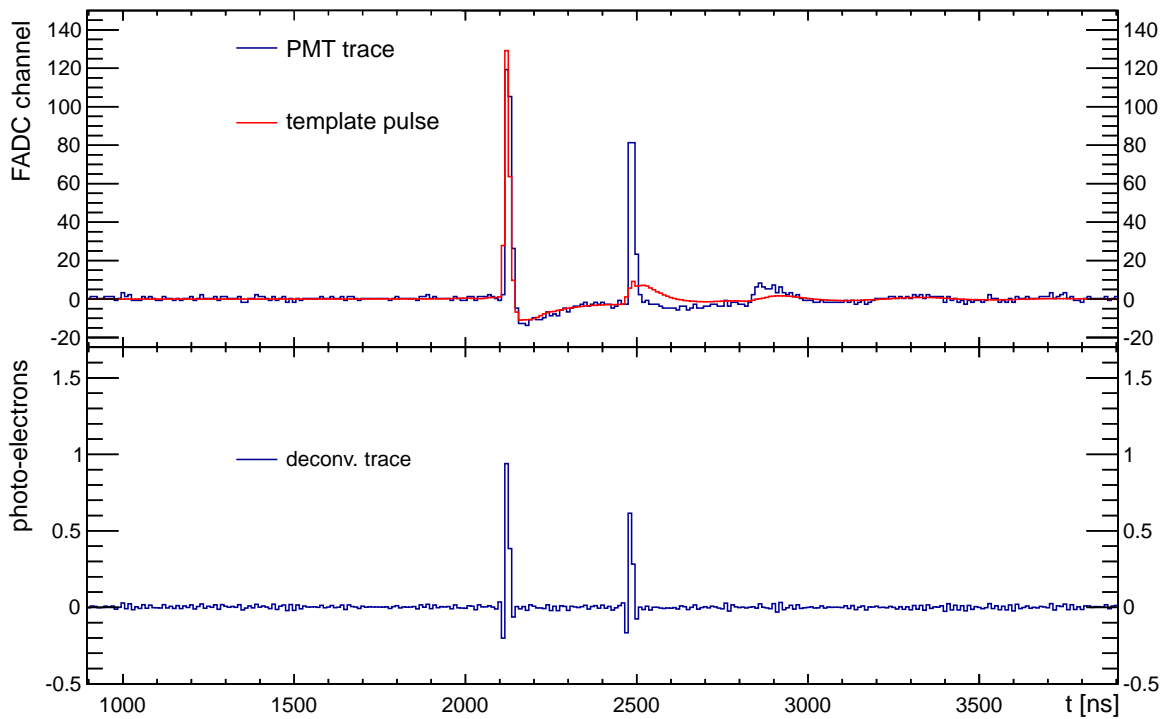
Figure D.1: *Example of a template pulse in* Gelatio*. The template is shown in red, an example trace containing two separate PMT pulses is shown in black.*

This is a deconvolution of each trace with the template pulse and leaves a single peak with the height of the amount of PE in the trace for each peak in the original trace. As the data is compared to template pulses, a calibration file has to be provided. An exemplary trace and template pulse can be seen in Fig. D.1. The trace contains two PMT responses to one of which the template pulse is fit for optical reasons. As the trace is moved to Fourier space, a deconvolution will of course affect both PMT responses. The following section show exemplary `ini`-files for the generation of `Tier2` muon files.

EXEMPLARY INI-FILE TO GENERATE TIER2 CALIBRATION FILES

```
[Parameters]
FileList=mu_run*.t1.root
RootOutputFile=mu_run*.t2.root
LogFile=mu_run*.t2.log

[TaskList]
GEMDTop_1=true
GEMDFADC_1=true
GEMDBaseline_1=true
GEMDTrigger_1=true
GEMDTemplatePulse_1=true
GEMDQuality_1=true

[GEMDTop_1]
Module=GEMDTop
VerbosityLevel=0
outputFormat=kTreeList
InvertWaveform=kAuto
InvertAuxWaveform=kAuto
OutputWaveformName=GEMDTop_wf
OutputAuxWaveformName=GEMDTop_wfHF
enableCh0=true
enableCh1=true
[...]
enableCh110=true
enableCh111=true
EventListName=
EventListPath=

[GEMDFADC_1]
Module=GEMDFADC
VerbosityLevel=0
EnegyStart=-1
EnergyStop=-1
ProcessTP=true
ProcessOvershot=false

[GEMDBaseline_1]
Module=GEMDBaseline
```

```
VerbosityLevel=0
InputWaveformName=GEMDTop_wf
OutputWaveformName=GEMDBaseline_wf
BaselineStart=0ns
BaselineStop=500ns
RestoredWfBaselineStart=0ns
RestoredWfBaselineStop=500ns
PileUpCorrection=false
TauPreamp=47us
expCoefThreshold=0
ComputeAuxBaselines=false
AuxBaseline1Start=-1ns
AuxBaseline1Stop=-1ns
AuxBaseline2Start=-1ns
AuxBaseline2Stop=-1ns

[GEMDTrigger_1]
Module=GEMDTrigger
VerbosityLevel=0
InputWaveformName=GEMDBaseline_wf
StartTime=-1ns
EndTime=-1ns
BaselineStart=0ns
BaselineStop=500ns
NumberOfSigmaThs=10
TimeAboveThs=10ns

[GEMDTemplatePulse_1]
Module=GEMDTemplatePulse
VerbosityLevel=0
InputWaveformName=GEMDBaseline_wf
OutputWaveformName=GEMDTemplatePulse_wf
FitWidth=500ns
StartAlign=1500ns
StopAlign=2500ns

[GEMDQuality_1]
Module=GEMDQuality
VerbosityLevel=0
```

Exemplary ini-file to generate Tier2 background files

```
[Parameters]
FileList=mu_run*.t1.root
RootOutputFile=mu_run*.t2.root
LogFile=mu_run*.t2.log

[TaskList]
GEMDTop_1=true
GEMDFADC_1=true
GEMDBaseline_1=true
GEMDTriggerThr_1=true
GEMDMuPE_1=true
GEMDQuality_1=true

[GEMDTop_1]
Module=GEMDTop
VerbosityLevel=0
outputFormat=kTreeList
InvertWaveform=kAuto
InvertAuxWaveform=kAuto
OutputWaveformName=GEMDTop_wf
OutputAuxWaveformName=GEMDTop_wfHF
enableCh0=true
enableCh1=true
[...]
enableCh110=true
enableCh111=true
EventListName=
EventListPath=

[GEMDFADC_1]
Module=GEMDFADC
VerbosityLevel=0
EnegyStart=-1
EnergyStop=-1
ProcessTP=true
ProcessOvershot=false

[GEMDBaseline_1]
Module=GEMDBaseline
VerbosityLevel=0
InputWaveformName=GEMDTop_wf
OutputWaveformName=GEMDBaseline_wf
BaselineStart=0ns
BaselineStop=500ns
RestoredWfBaselineStart=0ns
RestoredWfBaselineStop=500ns
PileUpCorrection=false
TauPreamp=47us
expCoefThreshold=0
ComputeAuxBaselines=false
AuxBaseline1Start=-1ns
AuxBaseline1Stop=-1ns
AuxBaseline2Start=-1ns
AuxBaseline2Stop=-1ns

[GEMDTriggerThr_1]
Module=GEMDTriggerThr
VerbosityLevel=0
InputWaveformName=GEMDBaseline_wf
StartTime=-1ns
EndTime=-1ns
Threshold=50
TimeAboveThs=10ns

[GEMDMuPE_1]
Module=GEMDMuPE
VerbosityLevel=0
InputWaveformName=GEMDBaseline_wf
CalibrationFile=calib-XXX.t2.root
Threshold for FFT [in PE]=0.2

[GEMDQuality_1]
Module=GEMDQuality
VerbosityLevel=0
```

Muon veto Tier3 files

For easier access, the output data for Phase I was transformed to pure Root-based data Tier3-files, much like the Tier3 germanium files. These files contain a Root-tree with the following entries, but will be expanded in the future with informations regarding the panels.

```
-outTree
     |-eventNumber/l
     |-channelID[ch]
     |-timestamp/l
     |-decimaltimestamp/i
     |-baseline[ch]
     |-baselineRes[ch]
     |-baselineSigma[ch]
     |-triggerNumber[ch]
     |-trigger1[ch]
     [...]
     |-trigger10[ch]
     |-integral[ch]
     |-pulseHeight[ch]
     |-PE_total/D
     |-multiplicity/I
     |-multiplicity_Pillbox/I
     |-fired[ch]
```

ATTENUATION STUDIES

In Sec. 5.6 and Sec. 6.7, PE spectra for different muons classes are shown. The peaks and their respective track-lengths could be identified and with this a model for the relation between detected light and track can be formulated. Each track class has a mean length, which suggests a linear dependency of the two values. However, the larger the volume, the further away are the PMT which detect the light. As optical photons have an attenuations length of ≈ 12 m in water, this effect should be visible as the mean distance to the PMT in the pillbox is ≈ 2 m while it is ≈ 5 m in the main water tank. Thus, the relation between track and detected light is a convolution between the attenuation of optical photons in the water and the statistical mean distance to the PMTs in the respective volume.

Fig. E.1 shows the relation of the peaks seen in the different muon classes in relation to the relative light-yield given in photons/m for both simulated and experimental data. The traversed lengths are results of toy simulations using the angular muon distribution at the LNGS and simplified geometries of the water tank. As can be seen, both sets of data appear non-linear and exhibit a slope towards longer track lengths. Since the attenuation length of optical photons can be assumed to play a major factor, an exponential $a \cdot e^{b \cdot x}$ was fit to both sets data. Both fits yield almost the same values for the simulation and experimental data of $a = (124 \pm 24)$ and $b = (-6.9 \pm 4.2) \times 10^{-2}$. As this function does not only depend on the attenuation length but of the mean distance to the PMTs as well, the attenuation length cannot be directly be determined from these values. In order to get a better handle, simulation data sets with different attenuation lengths are needed.

In an additional simulation the attenuation length for optical photons in water was halved and doubled to 6 m and 24 m respectively and simulation data for cosmic and CNGS muons were produced. The related PE spectra are shown in Fig. E.2. As can be seen, in the 6 m case there are less and in the 24 m case there are more photons detected as compared to the standard case of 12 m shown in Fig. 5.13 so an effect of the different attenuation length is clearly visible. The additional features in the CNGS PE spectra introduced in Fig. 5.13 appear in these simulations was well.

The relative light-yield for these two different cases is shown in Fig. E.3. As in the previous case, a slope towards longer track-lengths can be observed and the light-yield of the longer track is clearly higher in comparison to the lower track length.
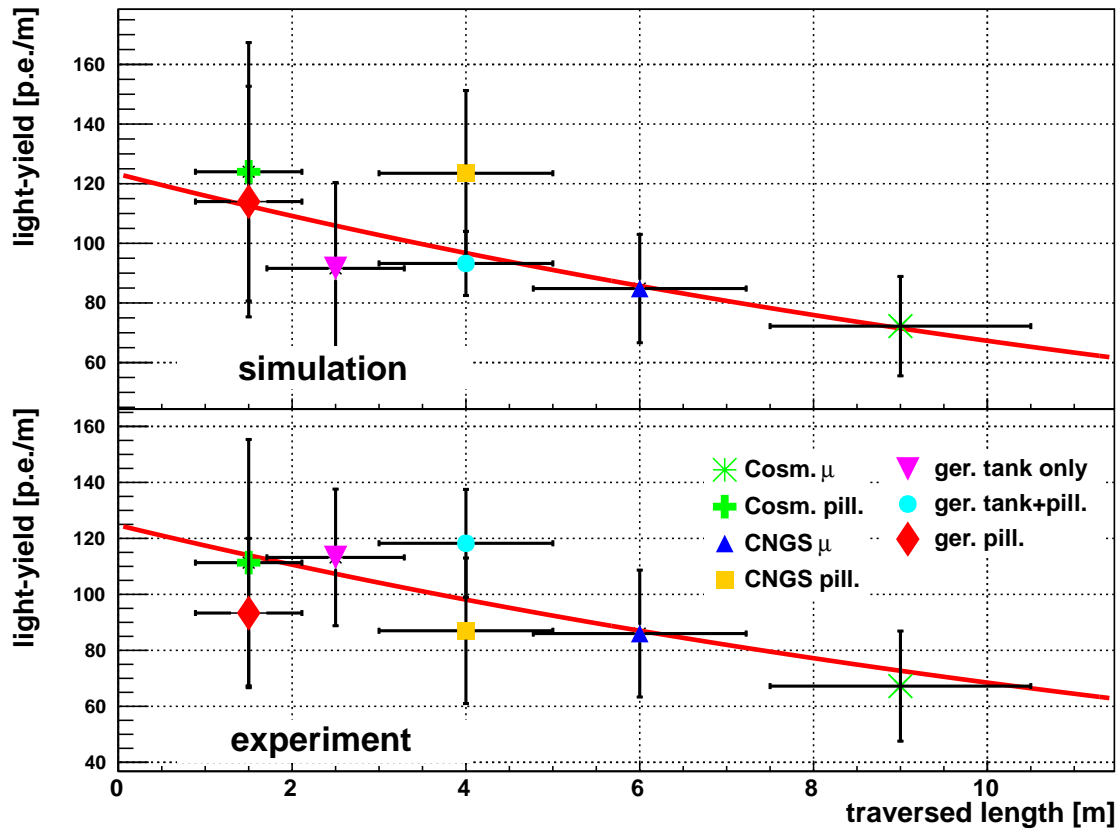
Figure E.1: *Photon yield in the water tank for different track-lengths. The two panels show the relative light-yield in PE for the different classes of muons. The considered classes are cosmogenic, Cngs and energy-depositing, for each class muons in the water tank and in the pillbox are considered separately. The muons with energy deposition show two peaks in the water tank.*

The fit values yield $a_6 = (106 \pm 41)$ and $b_6 = (-8.9 \pm 7.0) \times 10^{-2}$ for the short and $a_{24} = (169 \pm 48)$ and $b_{24} = (-5.9 \pm 4.9) \times 10^{-2}$ for the long attenuation length. While the errors on these values are high enough to make any concise assumptions regarding the effect of the attenuation inconclusive, its dependence on the light-yield can be considered proven. The values given above are hence a first-order approximation to the real amount of light deposited for a certain track length. Since the simulations and the experiment agree with small inconsistencies, a simulation of exact tracks and their respective light deposition could be a next step.
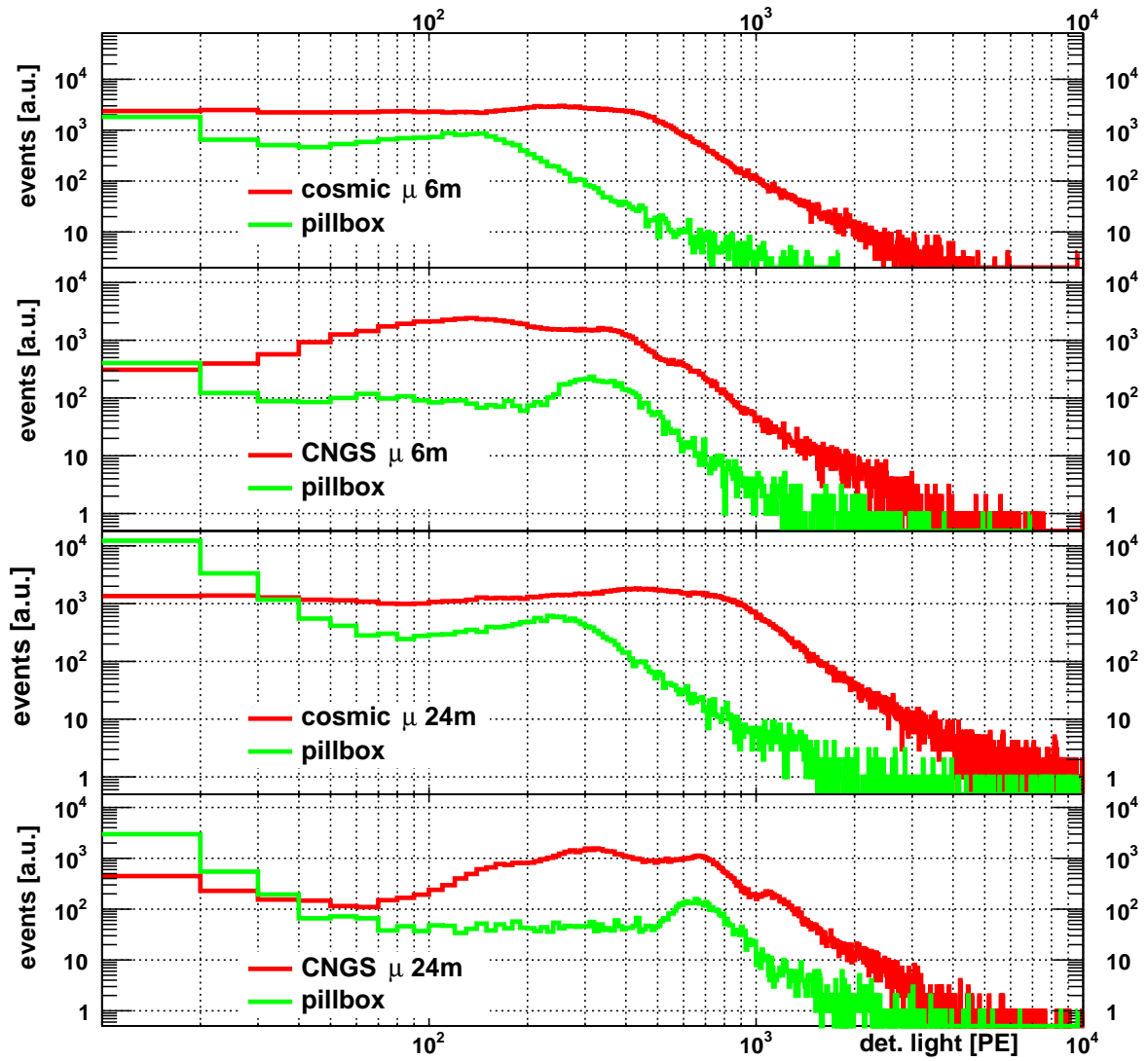
Figure E.2: *Photon spectra of the simulated muons for different attenuation lengths. The pillbox (green) and the entire water tank (red). The top panel shows the spectra for cosmogenic muons, the middle for* Cngs *muons and the bottom panel shows muons with energy deposition.*
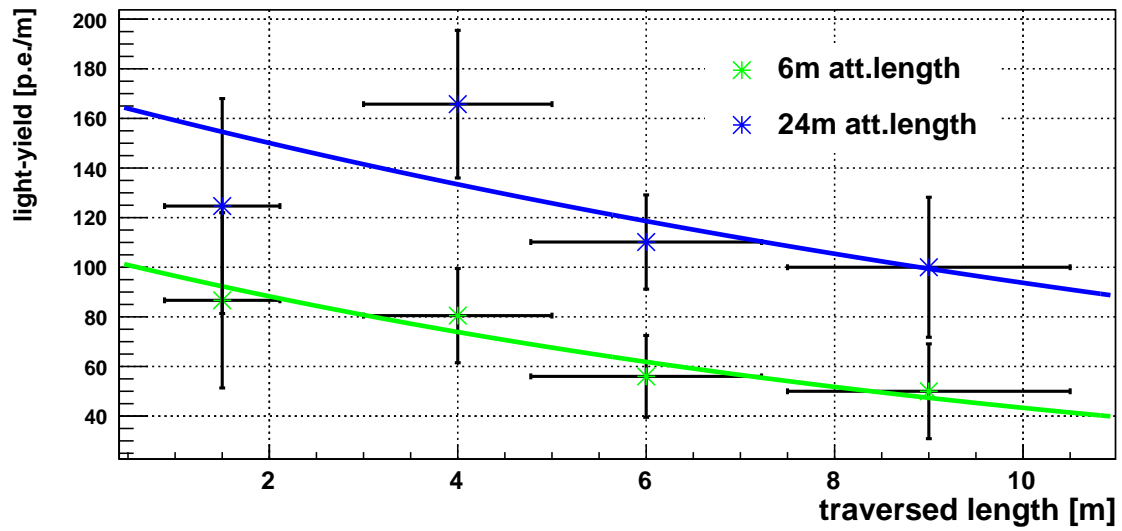
Figure E.3: *Photon attenuation for different attenuation lengths.*

APPENDIX F

POTENTIAL COSMOGENIC ISOTOPES

Here, the different cosmogenic isotopes are listed which can potentially be produced in the GERDA experiment. For this overview, the components of the tanks (water tank and cryostat) have been omitted. Since the spallation products of the argon can potentially be produced in the closest vicinity of the detectors, the resulting γ-rays would suffer less attenuation in comparison to the distance of > 2 m were they originating from the cryostat or even > 5 m from the water tank. Since no argon isotopes could be identified yet, the different metals from the tanks would contribute even less to the background.

Table F.1: *Decay properties of ^{77}Ge and ^{75}Ge. [Mei10].*

isotope	decay	$\mathrm{T}_{1/2}$	energy [MeV]	intensity [%]
^{77}Ge	β^-	11.3 h	2.70	100
^{77m}Ge	β^-	52.9 s	2.86	58
	β^-		2.65	22
^{75}Ge	β^-	82.8 m	1.16	87
	β^-		0.91	12

Table F.2: *Transitions in ^{77}As after β-decay of ^{77}Ge [Mei10].*

E_γ [keV]	per 100 dec.	E_γ[keV]	per 100 dec.
211.1	29.6	1085.3	6.8
264.4	53.8	1193.3	2.9
558.0	18.0	1573.8	0.8
631.9	7.8	2000.3	0.6
714.4	8.0	2341.8	0.5

Table F.3: *Prompt germanium transitions after neutron capture [Mei10]. The first lines are caused by neutron capture on on ^{76}Ge, the next two are combination spectra from different transitions and isotopes. The intensity is given in relation to the strongest $^{76}Ge(n,\gamma)$ transition. Two $^{74}Ge(n,\gamma)$ transitions are given for comparison.*

isotope	E_γ [keV]	per 100 dec.
^{76}Ge	2026.4	0.14
^{76}Ge	2029.6	0.37
^{76}Ge	2035.5	0.27
^{76}Ge	5911.3	25.5
^{76}Ge	861.8	13.1
^{74}Ge	253.0	32.0_{74Ge}
^{74}Ge	575.0	15.8_{74Ge}
^{74}Ge	2091.5	1.5_{74Ge}

Table F.4: *Argon spallation: possible isotopes after [Bro70] and [NND14]. The energy given for β-decays is always the endpoint energy.*

isotope	decay	$T_{1/2}$	energy [MeV]	intensity [%]
^{39}Cl	β^-	55.6 m	1.92	83
	β^-		2.18	4.5
	β^-		3.44	7.1
	γ		0.25	46.1
	γ		1.27	53.6
	γ		1.52	39.2
^{38}Cl	IT	715 ms	0.67	99.9
	β^-	37.2 m	4.92	55.6
	β^-		2.75	11.3
	γ		1.64	33.3
	γ		2.17	44.4
^{37}S	β^-	5.05 m	1.76	94.0
	β^-		4.87	5.6
	γ		3.10	93.9
^{34m}Cl	IT	32.0 m	0.14	44.6
^{29}Al	β^-	6.56 m	1.25	6.3
	β^-		2.40	89.9
	γ		1.27	91.3
	γ		2.43	5.2
^{28}Al	β^-	2.25 m	2.86	99.99
	γ		1.78	100
^{28}Mg	β^-	20.9 h	0.46	94.8
	γ		0.94	36.3
	γ		1.34	54
^{27}Mg	β^-	9.5 m	1.60	29.1
	β^-		1.77	70.9
	γ		0.84	71.8
	γ		1.01	28.2
^{24}Na	β^-	14.997 h	1.39	99.9
	γ		1.37	99.99
	γ		2.75	99.85
^{22}Na	β^+	2.6 y	0.55	90.3
	γ		1.27	99.9
^{7}B	p$^+$	350×10^{-24}	1.4	

Table F.5: *Cosmogenic activity in water after [Abe10], [Ahm02] and [NND14]. The energy given for β-decays is always the endpoint energy.*

isotope	decay	$T_{1/2}$	energy [MeV]	intensity [%]
^{18}N	β^-	624 ms	13.9	100
^{17}N	$\beta^- n$	4.17 s	3.7	95.1
^{16}N	β^-	7.13 s	10.42	28
	β^-		4.29	66.2
	γ		6.13	67.0
^{16}C	$\beta^- n$	0.77 s	4.6	99.0
^{15}C	β^-	2.45 s	9.77	38.8
	β^-		4.47	63.2
	γ		5.30	63.2
^{15}B	β^-	9.93 ms	19.09	100
^{14}O	β^+	70.6 s	1.81	99.2
	γ		2.39	99.3
^{13}O	$\beta^+ p$	8.58 ms	17.8	89.2
	β^+		14.3	9.8
^{13}B	β^-	17.4 ms	13.4	92.1
	β^-		9.75	7.6
	γ		3.68	7.6
^{12}N	β^+	11.0 ms	16.3	94.6
^{12}B	β^-	20.2 ms	13.3	97.2
^{12}Be	β^-	21.3 ms	11.7	100
^{11}Be	β^-	13.6 s	11.5	55
	β^-		9.4	42
	γ		8.18	42
^{11}Li	β^-	8.75 ms	20.6	17
	$\beta^- n(n)$		16	83
^{9}C	β^-	127 ms	16.5	100
^{9}Li	β^-	178 ms	13.6	49.2
	$\beta^- n$		11.2	50.8
^{8}Li	β^-	840 ms	16.0	100
^{8}B	β^-	770 ms	12.1	100
^{8}He	β^-	119 ms	9.76	84.0
	β^-		7.57	8
	β^-		5.50	8
	γ		0.98	84
^{6}He	β^-	807 ms	3.51	100

List of Figures

LIST OF TABLES

Glossary

$0\nu\beta\beta$ . . . . . Neutrinoless Double-Beta Decay

$2\nu\beta\beta$ . . . . . Two-Neutrino Double-Beta Decay

AIRS . . . . . Atmospheric Infrared Sounder

BEGe . . . . . Broad-Energy Germanium detector

BI . . . . Background Index

CC . . . . . . Charged-Current

Cern . . . . . Conseil Européen pour la Recherche Nucléaire

Cngs . . . . . Cern Neutrinos to Gran Sasso

Cresst . . . Cryogenic Rare Event Search with Superconducting Thermometers

DAC . . . . . Digital-to-Analog Converter

DAQ . . . . . Data Acquisition system

ECMWF . . . European Centre for Medium-Range Weather Forecast

FADC . . . . . Flash Analog-to-Digital Converter

FWHM . . . . Full Width at Half-Maximum

Geant4 . . . Geometry and Tracking Toolkit

Gelatio . . . Gerda Layout for Input/Output

Gerda . . . . Germanium Detector Array

GPS . . . . . . Global Positioning System

HdM . . . . . Heidelberg-Moscow

HPGe . . . . . High-Purity Germanium detector

HV . . . . . . High-Voltage supply

Igex . . . . . International Germanium Experiment

LAr . . . . . . Liquid Argon

LED . . . . . . Light-Emitting Diode

LHC . . . . . . Large Hadron Collider

LN2 . . . . . . Liquid Nitrogen

LNGS . . . . . Laboratori Nazionali del Gran Sasso

Lvd . . . . . . Large Volume Detector

Macro . . . . Monopole, Astrophysics and Cosmic Ray Observatory

MaGe . . . . Majorana and Gerda Simulation Framework

MDE . . . . . Muon Detection Efficiency

MGDO . . . . Majorana-Gerda Data Objects

MRE . . . . . Muon Rejection Efficiency

MSE . . . . . Multi-Site Event

NC . . . . . . Neutral-Current

NIM . . . . . . Nuclear Instrumentation Module

NME . . . . . Nuclear Matrix Elements

Opera . . . . Oscillation Project with Emulsion-tRacking Apparatus

PE . . . . Photo-Electron

PET . . . . . . Polyethylene

PMT . . . . . Photo-Multiplier Tube

POT . . . . . Protons-On-Target

PSD . . . . . . Pulse-Shape Discrimination

ROI . . . . . . Region of Interest

SHV . . . . . . Safe High-Voltage

SPP . . . . . . Single-Photon Peak

SPS . . . . . . Super Proton Synchrotron

SSE . . . . . . Single-Site Event

TOF . . . . . Time-of-Flight

VME . . . . . Versa Module Eurocard

WIMP . . . . Weakly Interactive Massive Particle

Gerda Scientific / Technical Reports

[-]   The GSTRs cited in this work are internal, unpublished notes of the
             Gerda collaboration. They are available on demand from the Editorial
             Board of the experiment at http://www.mpi-hd.mpg.de/gerda/.

[GSTR06-10] I. Abt, K. Kröninger, X. Liu and B. Majorovits, *Background contribu-
             tions by cosmogenically produced isotopes in argon*, 2006.

[GSTR06-16] A. Denisov and S. Belogurov, *Cosmogenic Background in the Phase I of
             the GERDA Experiment*, 2006.

[GSTR06-02] L. Pandola, *Muon-induced background in the liquid nitrogen and liquid
             argon options*, 2006.

[GSTR10-03] K. Freund, F. Ritter, B. Shaybonov and P. Grabmayr, *Update on the
             Muon Veto — installation of the DAQ*, 2008.

[GSTR08-16] M. Shirchenko, F. Ritter, V. Egorov, D. Zinatulina, J. Jochum, P. Grab-
             mayr, M. Knapp, G. Meierhofer, K.-T. Knöpfle and M. Junker, *Testing
             and transportation of muon-veto panels to LNGS*, 2008.

[GSTR11-02] D. Budjas, L. Pandola and P. Zavarise, *Rejection efficiency of muon-
             induced events in the commissiong GERDA array*, 2011.

[GSTR11-11] K. Freund, P. Grabmayr, T. Kihm, F. Ritter, E. Shevchik,
             M. Shirichenko, K. von Sturm, D. Zinatulina and I. Zhitnikov, *The Muon
             Panels II: Installation, DAQ-Integration and "First Light"*, 2011.

[GSTR11-10] E. Shevchik, M. Shirchenko, I. Zhitnikov, D. Zinatulina, K. Freund,
             P. Grabmayr, F. Ritter and K. von Sturm, *The Muon Panels I: Panel
             Tests and Efficiency Estimations*, 2011.

[GSTR11-05] M. Shirchenko, D. Zinatulina, E. Shevchik, F. Ritter, K. Freund and
             P. Grabmayr, *Muon veto tests and installation*, 2011.

[GSTR12-04] R. Brugnera, A. Caldwell, A. Garfagnini, S. Hemmer, L. Pandola and
             P. Zavarise, *Measurement of the ^{42}Ar contamination in natural argon
             with Gerda*, 2012.

[GSTR13-19] K. Freund, P. Grabmayr, N. Lubsandorzhiev and C. Schmitt, *Inspecton
             of the muon veto, exchange of the PMTs*, 2013.

[GSTR14-02] T. Kihm and B. Schwingenheuer, *List of DAQ tags*, 2014.

Bibliography

[3M07]   3M, *Daylighting Film DF2000MA*, 2007.

[Aad12]   G. Aad et al. (ATLAS Collaboration), *Observation of a new particle in the search for the Standard Model Higgs boson with the ATLAS detector at the LHC*, Phys. Lett. **B**, 716(1):1 – 29, doi:10.1016/j.physletb.2012.08.020, 2012.

[Aal99]   C. E. Aalseth et al. (IGEX Collaboration), *Neutrinoless double-β decay of ^{76}Ge: First results from the International Germanium Experiment (IGEX) with six isotopically enriched detectors*, Phys. Rev. C, 59:2108–2113, doi:10.1103/PhysRevC.59.2108, 1999.

[Abe10]   S. Abe et al. (KamLAND Collaboration), *Production of radioactive isotopes through cosmic muon spallation in KamLAND*, Phys. Rev. C, 81:025807, doi:10.1103/PhysRevC.81.025807, 2010.

[Abg14]   N. Abgrall et al. (MAJORANA Collaboration), *The MAJORANA DEMONSTRATOR Neutrinoless Double-Beta Decay Experiment*, Advances in High Energy Physics, 2014, doi:10.1155/2014/365432, 2014.

[Abt04]   I. Abt et al. (GERDA Collaboration), *A New 76Ge Double Beta Decay Experiment at LNGS*, ArXiv e-prints, hep-ex/0404039, 2004.

[Ack13]   K.-H. Ackermann et al. (GERDA Collaboration), *The Gerda experiment for the search of $0\nu\beta\beta$ decay in ^{76}Ge*, Eur. Phys. J. **C**, 73(3):1–29, doi:10.1140/epjc/s10052-013-2330-0, 2013.

[Ada10]   P. Adamson et al. (MINOS Collaboration), *Observation of muon intensity variations by season with the MINOS far detector*, Phys. Rev. D, 81:012001, doi:10.1103/PhysRevD.81.012001, 2010.

[Ada11]   T. Adam et al. (OPERA Collaboration), *Measurement of the neutrino velocity with the OPERA detector in the CNGS beam*, ArXiv e-prints, hep-ex/1109.4897, 2011.

[Ada12]   T. Adam et al. (OPERA Collaboration), *Measurement of the neutrino velocity with the OPERA detector in the CNGS beam*, J. of High Energy Phys., 2012(10):1–37, doi:10.1007/JHEP10(2012)093, 2012.

[Ade13a] P. Ade et al. (Planck Collaboration), *Planck 2013 results. I. Overview of products and scientific results*, ArXiv e-prints, 1303.5062, 2013.

[Ade13b] P. Ade et al. (Planck Collaboration), *Planck 2013 results. XVI. Cosmological parameters*, ArXiv e-prints, 1303.5076, 2013.

[Aga13a] N. Agafonova et al. (OPERA Collaboration), *New results on ν_μ to ν_τ appearance with the OPERA experiment in the CNGS beam*, ArXiv e-prints, hep-ex/1308.2553, 2013.

[Aga13b] N. Y. Agafonova and A. S. Malgin, *Universal formula for the muon-induced neutron yield*, Phys. Rev. D, 87:113013, doi:10.1103/PhysRevD.87.113013, 2013.

[Agl04] M. Aglietta et al. (LVD Collaboration), *CNGS beam monitor with the LVD detector*, Nucl. Instr. Methods **A**, 516(1):96 – 103, doi:10.1016/j.nima.2003.07.068, 2004.

[Ago03] S. Agostinelli et al. (Geant4 Collaboration), *Geant4—a simulation toolkit*, Nucl. Instr. Methods **A**, 506(3):250 – 303, doi:10.1016/S0168-9002(03)01368-8, 2003.

[Ago11] M. Agostini et al., *GELATIO: a general framework for modular digital analysis of high-purity Ge detector signals*, J. of Instrumentation, 6(08):P08013, doi:10.1088/1748-0221/6/08/P08013, 2011.

[Ago12] M. Agostini, L. Pandola and P. Zavarise, *Off-line data processing and analysis for the GERDA experiment*, J. Phys.: Conf. Ser., 368(1):012047, doi:10.1088/1742-6596/368/1/012047, 2012.

[Ago13a] M. Agostini et al. (GERDA Collaboration), *Measurement of the half-life of the two-neutrino double beta decay of 76 Ge with the GERDA experiment*, J. Phys. G: Nucl. Part. Phys., 40(3):035110, doi:10.1088/0954-3899/40/3/035110, 2013.

[Ago13b] M. Agostini et al., *Pulse shape discrimination for Gerda Phase I data*, Eur. Phys. J. **C**, 73(10):1–17, doi:10.1140/epjc/s10052-013-2583-7, 2013.

[Ago13c] M. Agostini et al. (GERDA Collaboration), *Results on Neutrinoless Double-β Decay of ^{76}Ge from Phase I of the GERDA Experiment*, Phys. Rev. Lett., 111:122503, doi:10.1103/PhysRevLett.111.122503, 2013.

[Ago14] M. Agostini et al., *The background in the $0\nu\beta\beta$ experiment Gerda*, Eur. Phys. J. **C**, 74(4):2764, doi:10.1140/epjc/s10052-014-2764-z, 2014.

[Ahl93] S. Ahlen et al. (MACRO Collaboration), *Muon astronomy with the MACRO detector*, Astrophysical Journal, 412:301–311, doi:10.1086/172921, 1993.

[Ahm01] Q. R. Ahmad et al. (SNO Collaboration), *Measurement of the Rate of $\nu e + d \rightarrow p + p + e$- Interactions Produced by B8 Solar Neutrinos at the Sudbury Neutrino Observatory*, Phys. Rev. Lett., 87:071301, doi:10.1103/PhysRevLett.87.071301, 2001.

[Ahm02] Q. R. Ahmad, *Muon Correlated Background at The Sudbury Neutrino Observatory*, Ph.D. thesis, Brown University, 2002.

[Amb95] M. Ambrosio et al., *Vertical muon intensity measured with MACRO at the Gran Sasso laboratory*, Phys. Rev. D, 52:3793–3802, doi:10.1103/PhysRevD.52.3793, 1995.

[Amb97] M. Ambrosio et al. (MACRO Collaboration), *Seasonal variations in the underground muon intensity as seen by MACRO*, Astroparticle Physics, 7(1-2):109–124, doi:10.1016/S0927-6505(97)00011-X, 1997.

[Amb03] M. Ambrosio et al. (MACRO Collaboration), *Search for the sidereal and solar diurnal modulations in the total MACRO muon data set*, Phys. Rev. D, 67:042002, doi:10.1103/PhysRevD.67.042002, 2003.

[An12] F. P. An et al., *Observation of Electron-Antineutrino Disappearance at Daya Bay*, Phys. Rev. Lett., 108:171803, doi:10.1103/PhysRevLett.108.171803, 2012.

[Ang09] G. Angloher et al. (CRESST Collaboration), *Commissioning run of the CRESST-II dark matter search*, Astroparticle Physics, 31(4):270 – 276, doi:10.1016/j.astropartphys.2009.02.007, 2009.

[Ang12] G. Angloher et al. (CRESST collaboration), *Results from 730 kg days of the CRESST-II Dark Matter search*, Eur. Phys. J. **C**, 72:1–22, doi:10.1140/epjc/s10052-012-1971-8, 2012.

[Arn10] R. Arnold et al., *Probing new physics models of neutrinoless double beta decay with SuperNEMO*, Eur. Phys. J. **C**, 70(4):927–943, doi:10.1140/epjc/s10052-010-1481-5, 2010.

[Aug12] M. Auger et al. (EXO Collaboration), *Search for Neutrinoless Double-Beta Decay in ^{136}Xe with EXO-200*, Phys. Rev. Lett., 109:032505, doi:10.1103/PhysRevLett.109.032505, 2012.

[Bal01] A. E. Ball et al., *CNGS: Update on secondary beam layout.*, Tech. Rep. SL-Note-2000-063-DI, CERN, Geneva, 2001.

[Bar52] P. H. Barrett et al., *Interpretation of Cosmic-Ray Measurements Far Underground*, Rev. Mod. Phys., 24:133–178, doi:10.1103/RevModPhys.24.133, 1952.

[Bar89] R. J. Barlow, *A Guide to the Use of Statistical Methods in the Physical Sciences*, Wiley, 1989.

[Bar06] G. D. Barr et al., *Uncertainties in atmospheric neutrino fluxes*, Phys. Rev. D, 74:094009, doi:10.1103/PhysRevD.74.094009, 2006.

[Bar10] M. Barnabé Heider et al., *Operation and performance of a bare broad-energy germanium detector in liquid argon*, J. of Instrumentation, 5(10):P10007, doi:10.1088/1748-0221/5/10/P10007, 2010.

[Bar11] A. Barabash, *Experiment double beta decay: Historical review of 75 years of research*, Physics of Atomic Nuclei, 74(4):603–613, doi:10.1134/S1063778811030070, 2011.

[Bar13] A. S. Barabash, *Average and recommended half-life values for two neutrino double beta decay: Upgrade-2013*, AIP Conference Proceedings, 1572(1):11–15, 2013.

[Bau06] M. Bauer et al., *MaGe: a Monte Carlo framework for the Gerda and Majorana double beta decay experiments*, J. Phys.: Conf. Ser., 39(1):362, doi:10.1088/1742-6596/39/1/097, 2006.

[Bel12] G. Bellini et al. (BOREXINO Collaboration), *Cosmic-muon flux and annual modulation in Borexino at 3800 m water-equivalent depth*, J. of Cosmol. and Astropart. Phys., 2012(05):015, doi:10.1088/1475-7516/2012/05/015, 2012.

[Bel13]   G. Bellini et al., *Cosmogenic Backgrounds in Borexino at 3800 m water-equivalent depth*, J. of Cosmol. and Astropart. Phys., 8:049, doi:10.1088/1475-7516/2013/08/049, 2013.

[Ber12]   J. Beringer et al. (Particle Data Group), *Review of Particle Physics*, Phys. Rev. D, 86:010001, doi:10.1103/PhysRevD.86.010001, 2012.

[Bil10]   S. Bilenky, *Introduction to the Physics of Massive and Mixed Neutrinos*, Lecture Notes in Physics, Springer, 2010.

[Bir95]   D. J. Bird et al., *Detection of a cosmic ray with measured energy well beyond the expected spectral cutoff due to cosmic microwave radiation*, Astrophysical Journal, 441:144–150, doi:10.1086/175344, 1995.

[Bou99]   A. Bouchta (Amanda Collaboration), *Seasonal variation of the muon flux seen by AMANDA*, Int. Cosmic Ray Conf., 2:108, 1999.

[Bro70]   R. L. Brodzinski and N. A. Wogman, *High-Energy Proton Spallation of Argon*, Phys. Rev. C, 1:1955–1959, doi:10.1103/PhysRevC.1.1955, 1970.

[Bug98]   E. V. Bugaev et al., *Atmospheric muon flux at sea level, underground, and underwater*, Phys. Rev. D, 58:054001, doi:10.1103/PhysRevD.58.054001, 1998.

[Cas67]   G. Castagnoli and M. Dodero, *Temperature effect of the muon component underground and pion attenuation length*, Il Nuovo Cimento B Series 10, 51(2):525–534, doi:10.1007/BF02712070, 1967.

[Cha12]   S. Chatrchyan et al. (CMS Collaboration), *Observation of a new boson at a mass of 125 GeV with the CMS experiment at the LHC*, Phys. Lett. **B**, 716(1):30 – 61, doi:10.1016/j.physletb.2012.08.021, 2012.

[Che08]   E. P. Cherenkova, *The discovery of the Cherenkov radiation*, Nucl. Instr. Methods **A**, 595(1):8 – 11, doi:10.1016/j.nima.2008.07.006, 2008.

[Clo34]   C. Clopper and E. S. Pearson, *The use of confidence or fiducial limits illustrated in the case of the binomial*, Biometrika, pages 404–413, 1934.

[CNG13]   CNGS Collaboration, *CERN Neutrinos to Gran Sasso*, 2013, URL http://proj-cngs.web.cern.ch/proj-cngs/, visited: 2013-12-16.

[Cow56]   C. L. Cowan et al., *Detection of the Free Neutrino: a Confirmation*, Science, 124(3212):103–104, doi:10.1126/science.124.3212.103, 1956.

[Dan62]   G. Danby et al., *Observation of High-Energy Neutrino Reactions and the Existence of Two Kinds of Neutrinos*, Phys. Rev. Lett., 9:36–44, doi:10.1103/PhysRevLett.9.36, 1962.

[Dav68]   R. Davis, D. S. Harmer and K. C. Hoffman, *Search for Neutrinos from the Sun*, Phys. Rev. Lett., 20:1205–1209, doi:10.1103/PhysRevLett.20.1205, 1968.

[Des11]   P. Desiati et al. (IceCube Collaboration), *Seasonal Variations of High Energy Cosmic Ray Muons Observed by the IceCube Observatory as a Probe of Kaon/Pion Ratio*, Proc. 32nd Int. Cosmic Ray Conf., 1, doi:10.7529/ICRC2011/V01/0662, 2011.

[Die09]   D. Dietrich, *Aufbau, Inbetriebnahme und Messungen mit einer Myonveto-Testversion der Experimente* GERDA *und DoubleChooz*, Master's thesis, Universität Tübingen, 2009.

[Die13]   D. Dietrich, *Studying the muon background component in the Double Chooz experiment*, Ph.D. thesis, Universität Tübingen, 2013.

[Due11]   A. Dueck, W. Rodejohann and K. Zuber, *Neutrinoless double beta decay, the inverted hierarchy, and precision determination of* θ_{12}, Phys. Rev. D, 83:113010, doi:10.1103/PhysRevD.83.113010, 2011.

[Ebe13]   J. Ebert et al. (COBRA Collaboration), *Current Status and Future Perspectives of the COBRA Experiment*, Advances in High Energy Physics, 2013, doi:10.1155/2013/703572, 2013.

[ECM13]   ECMWF, *European Centre for Medium-Range Weather Forecasts*, 2013, URL http://www.ecmwf.int/, visited: 2013-05-30.

[Els98]   K. Elsener et al., *The CERN neutrino beam to Gran Sasso (NGS): conceptual technical design*, CERN, Geneva, 1998.

[Ent12]   E. T. Enterprises, *9354KB series data sheet*, 2012, URL http://my.et-enterprises.com/pdf/9354KB.pdf, visited: 2012-08-10.

[Fey58]   R. P. Feynman and M. Gell-Mann, *Theory of the Fermi Interaction*, Phys. Rev., 109:193–198, doi:10.1103/PhysRev.109.193, 1958.

[Fry75]   W. F. Fry and D. Haidt, *Calculation of the neutron-induced background in the Gargamelle neutral current search*, CERN Yellow Report 75-01, 1975.

[Gai90]   T. Gaisser, *Cosmic Rays and Particle Physics*, Cambridge University Press, 1990.

[Gal88]   F. Galton, *Co-relations and their measurement, chiefly from anthropometric data*, Proc. Royal Soc., 45(273-279):135–145, 1888.

[Gan12]   A. Gando et al. (KamLAND-Zen Collaboration), *Measurement of the double-β decay half-life of* ^{136}Xe *with the KamLAND-Zen experiment*, Phys. Rev. C, 85:045504, doi:10.1103/PhysRevC.85.045504, 2012.

[Gan13]   A. Gando et al. (KamLAND-Zen Collaboration), *Limit on Neutrinoless $\beta\beta$ Decay of* ^{136}Xe *from the First Phase of KamLAND-Zen and Comparison with the Positive Claim in* ^{76}Ge, Phys. Rev. Lett., 110:062502, 2013.

[GG12]   M. Gonzalez-Garcia et al., *Global fit to three neutrino mixing: critical look at present precision*, J. of High Energy Phys., 2012(12):1–24, doi:10.1007/JHEP12(2012)123, 2012.

[Giu07]   C. Giunti and C. Kim, *Fundamentals of Neutrino Physics and Astrophysics*, OUP Oxford, 2007.

[Gol58]   M. Goldhaber, L. Grodzins and A. W. Sunyar, *Helicity of Neutrinos*, Phys. Rev., 109:1015–1017, doi:10.1103/PhysRev.109.1015, 1958.

[Gra08]   E. W. Grashorn, *Astroparticle physics with the MINOS Far Detector*, Ph.D. thesis, Fermilab, 2008.

[Gra10] E. Grashorn et al., *The atmospheric charged kaon/pion ratio using seasonal variation methods*, Astroparticle Physics, 33(3):140 – 145, doi:10.1016/j.astropartphys.2009.12.006, 2010.

[Gsc13] E. Gschwendtner et al., *CNGS, CERN Neutrinos to Gran Sasso, Five Years of Running a 500 Kilowatt Neutrino Beam Facility at CERN*, (CERN-ACC-2013-0266):4 p, 2013.

[Ham99] W. Hampel et al. (Gallex collboration), *GALLEX solar neutrino observations: results for GALLEX IV*, Phys. Lett. **B**, 447(1-2):127–133, doi:http://dx.doi.org/10.1016/S0370-2693(98)01579-2, 1999.

[Hel97] J. Hellmig and H. V. Klapdor-Kleingrothaus, *A large scale double beta and dark matter experiment: GENIUS.*, Zeitschrift fur Physik A Hadrons and Nuclei, 359:351–359, nucl-ex/9801004, 1997.

[Heu95] G. Heusser, *Low-Radioactivity Background Techniques*, Annual Review of Nuclear and Particle Science, 45(1):543–590, doi:10.1146/annurev.ns.45.120195.002551, 1995.

[Jel58] J. V. Jelley, *Cerenkov radiation and its applications*, Pergamon Press, 1958.

[KK01] H. Klapdor-Kleingrothaus et al., *Latest results from the Heidelberg-Moscow double beta decay experiment*, Eur.Phys.J., A12:147–154, doi:10.1007/s100500170022, 2001.

[KK04] H. Klapdor-Kleingrothaus et al., *Search for neutrinoless double beta decay with enriched 76Ge in Gran Sasso 1990-2003*, Phys. Rev. B, 586(3-4):198 – 212, doi:10.1016/j.physletb.2004.02.025, 2004.

[KK06] H. V. Klapdor-Kleingrothaus and I. V. Krivosheina, *The evidence for the observation of $0\nu\beta\beta$ decay: the identification of $0\nu\beta\beta$ events from the full spectra*, Mod. Phys. Lett. **A**, 21(20):1547–1566, doi:10.1142/S0217732306020937, 2006.

[Kna09] M. A. Knapp, *Design, Simulation und Aufbau des GERDA-Myonvetos*, Ph.D. thesis, Universität Tübingen, 2009.

[Kno00] G. Knoll, *Radiation detection and measurement*, Wiley, 2000.

[Kod01] K. Kodama et al. (DONUT Collaboration), *Observation of tau neutrino interactions*, Phys. Rev. B, 504(3):218 – 224, doi:10.1016/S0370-2693(01)00307-0, 2001.

[Kra10] H. Kraus and V. Mikhailik, *First test of a cryogenic scintillation module with a CaWO4 scintillator and a low-temperature photomultiplier down to 6K*, Nucl. Instr. Methods **A**, 621(1 - 3):395 – 400, doi:10.1016/j.nima.2010.05.008, 2010.

[Krá10] A. Krása, *Spallation Reaction Physics*, 2010.

[Kud03] V. A. Kudryavtsev, N. J. C. Spooner and J. E. McMillan, *Simulations of muon-induced neutron flux at large depths underground*, Nucl. Instr. Methods **A**, 505:688–698, doi:10.1016/S0168-9002(03)00983-5, 2003.

[Leo94] W. Leo, *Techniques for Nuclear and Particle Physics Experiments*, Springer, 1994.

[Loh85] W. Lohmann, R. Kopp and R. Voss, *Energy loss of muons in the energy range 1-10000 GeV*, CERN, Geneva, 1985.

[Maj37] E. Majorana, *Teoria simmetrica dell' elettrone e del positrone*, Il Nuovo Cimento, 14:171–184, doi:10.1007/BF02961314, 1937.

[Mak62] Z. Maki, M. Nakagawa and S. Sakata, *Remarks on the Unified Model of Elementary Particles*, 28(5):870–880, doi:10.1143/PTP.28.870, 1962.

[Man08] W. Maneschg et al., *Measurements of extremely low radioactivity levels in stainless steel for GERDA*, Nucl. Instr. Methods **A**, 593(3):448 – 453, doi:10.1016/j.nima.2008.05.036, 2008.

[Mei10] G. Meierhofer, *Neutron capture on ^{76}Ge*, Ph.D. thesis, Universität Tübingen, 2010.

[Moh04] R. Mohapatra and P. Pal, *Massive Neutrinos in Physics and Astrophysics*, Lecture Notes in Physics Series, World Scientific, 2004.

[Mos05] M. Moszyński et al., *Characterization of CaWO4 scintillator at room and liquid nitrogen temperatures*, Nucl. Instr. Methods **A**, 553(3):578 – 591, doi:10.1016/j.nima.2005.07.052, 2005.

[NAS13] NASA, *Atmospheric Infrared Sounder (AIRS)*, 2013, URL http://airs.jpl.nasa.gov/, visited: 2013-05-30.

[NIS14] NIST: National Institute of Standards and Technology, *Stopping-Power and Range Tables for Electrons, Protons, and Helium Ions*, 2014, URL http://www.nist.gov/pml/data/star/, visited: 2014-02-21.

[NND14] NNDC: National Nuclear Data Center, Brookhaven National Laboratory, *Nuclear Database, NuDat 2.6*, 2014, URL http://www.nndc.bnl.gov/nudat2/, visited: 2014-02-21.

[Oor32] J. H. Oort, *The force exerted by the stellar system in the direction perpendicular to the galactic plane and some related problems*, Bull. Astr. Inst. Netherlands, 6:249, 1932.

[OPE13] OPERA, *New neutrino oscillation event discovered at OPERA*, 2013, URL http://operaweb.lngs.infn.it/spip.php?article58, visited: 2014-02-11.

[Pan07] L. Pandola et al., *Monte Carlo evaluation of the muon-induced background in the GERDA double beta decay experiment*, Nucl. Instr. Methods **A**, 570(1):149 – 158, doi:10.1016/j.nima.2006.10.103, 2007.

[Par03] C. Parkinson, *Aqua: an Earth-Observing Satellite mission to examine water and other climate variables*, IEEE Trans. on Geo. and Rem. Sensing, 41(2):173 – 183, doi:10.1109/TGRS.2002.808319, 2003.

[Pat13] L. Pattavina (CUORE Collaboration), *Status of the CUORE experiment*, J. Phys.: Conf. Ser., 447(1):012066, doi:10.1088/1742-6596/337/1/012066, 2013.

[Pau30] W. Pauli, *Offener Brief an die Gruppe der Radioaktiven bei der Gauvereinstagung zu Tübingen*, 1930, URL http://cds.cern.ch/record/83282/files/meitner_0393.pdf, visited: 2013-11-15.

[Phi12] D. G. Phillips, II et al. (MAJORANA Collaboration), *The MAJORANA experiment: an ultra-low background search for neutrinoless double-beta decay*, J. Phys.: Conf. Ser., 381(1):012044, doi:10.1088/1742-6596/381/1/012044, 1111.5578, 2012.

[Rit10] F. Ritter et al., *The calibration system of the GERDA muon veto Cherenkov detector*, Nucl. Instr. Methods **A**, 617(1-3):420 – 421, doi:10.1016/j.nima.2009.08.080, 2010.

[Rit12] F. Ritter, *Analysis of the GERDA muon veto - first light*, Ph.D. thesis, Universität Tübingen, 2012.

[SA14] Sigma-Aldrich, *161403 IR Spectroscopy Oil*, 2014, URL http://www.sigmaaldrich.com/catalog/product/sial/161403, visited: 2014-02-18.

[Sch97] N. Schmitz, *Neutrinophysik*, Teubner-Studienbücher : Physik, Teubner, 1997.

[Sch13] B. Schwingenheuer, *Status and prospects of searches for neutrinoless double beta decay*, Annalen d. Phys., 525(4):269–280, doi:10.1002/andp.201200222, 2013.

[Smo10] A. Smolnikov and P. Grabmayr, *Conversion of experimental half-life to effective electron neutrino mass in $0\nu\beta\beta$ decay*, Phys. Rev. C, 81:028502, doi:10.1103/PhysRevC.81.028502, 2010.

[Spi05] H. Spieler, *Semiconductor Detector Systems*, Oxford Science Publications, 2005.

[Sud58] E. Sudarshan and R. Marshak, *Chirality Invariance and the Universal Fermi Interaction*, Phys. Rev., 109:1860–1862, doi:10.1103/PhysRev.109.1860.2, 1958.

[Tho10] S. A. Thomas, F. B. Abdalla and O. Lahav, *Upper Bound of 0.28 eV on Neutrino Masses from the Largest Photometric Redshift Survey*, Phys. Rev. Lett., 105:031301, doi:10.1103/PhysRevLett.105.031301, 2010.

[Wei67] S. Weinberg, *A Model of Leptons*, Phys. Rev. Lett., 19:1264–1266, doi:10.1103/PhysRevLett.19.1264, 1967.

[Wu57] C. S. Wu et al., *Experimental Test of Parity Conservation in Beta Decay*, Phys. Rev., 105:1413–1415, doi:10.1103/PhysRev.105.1413, 1957.

[Zwi33] F. Zwicky, *Die Rotverschiebung von extragalaktischen Nebeln*, Helvetica Physica Acta, 6:110–127, 1933.

Acknowledgement / Danksagung

utes later. I would specifically like to thank Mathias Junker for being the ever helpful "local organizing committee" at the LNGS, Karl-Tasso Knöpfle and Bernhard Schwingenheuer for their many good advices, helpful comments and especially helpful actions regarding the hardware. And a big thanks goes to the analysis and simulation team Luciano Pandola, Matteo Agostini and Paolo Zavarise for lots of input, many needed reminders and exchanges of ideas. Many thanks to Egor Shevchik, Mark Shirichenko, Daniya Zinatulina and Igor Zhitnikov for the construction and help with the installation of the scintillator panels. Thanks to Riccardo Brugnera and Alfredo Garfagnini for the set-up, management and help with the slow control. At this point I would also like to thank Chris Roderick and Edda Gschwendtner of the CNGS for providing the beam data sets.

Es gibt eine Anzahl von Menschen, von denen man im Leben mehr lernt, als einem im Augenblick eigentlich klar ist. Zu denen gehören bei mir auf jeden Fall meine ehemaligne Lehrer Michael Rode, Ulrich Prinz und Dörte Haftendorn. Sie alle konnten mich begeistern zu lernen, unabhängig von Fach oder "Lehrmode". Ein grosser Dank gebührt auch meinen ehemaligen Kollegen Chris Tenzer, Siegfried Vetter, Thorsten Nagel und insbesondere Thomas Schanz vom AIT für die schönen und lehrreichen Stunden mit Elektronik, Politik, Astronomie, FPGAs und Schokolade.

Insbesondere dankbar bin ich ich all meinen Freunden, die mich in der Zeit der Doktorarbeit und davor begleitet und unterstützt haben und dies hoffentlich auch danach noch tun. Dazu gehören auf jeden Fall Stefan Arbeiter, Christin Gumbinger, Andrea Staffler, Jakob Hasselmann, Anika Rudolf, Georg Rudolf, Laura Mega, Nicole Frank, Daniel Lede Abal und Katharina Schäfer. Danke für die vielen Stunden, die wir gemeinsam in der Fachschaft, dem Clubhaus, in den Sitzungen, auf den Festivals, beim diskutieren, bei den spontanen Weinseminaren, beim Rätetä-Editieren, beim kochen und bei so vielem mehr verbracht haben. Ein ganz besonderer Dank geht an Antje Ludewig fürs helfen, klönen, die schöne Zeit im Studium (und danach) und diese hervorragende LaTeX-Vorlage. Ebenfalls sehr vielen Dank an Hannah Tomczyk und David Auwärter für die vielen schönen Koch-, Klampf-, Wander-, Summer Breeze- und sonstigen Aktionen, die immer sehr entspannt waren und mir viel Spass gemacht haben. Ich hoffe, daß wir das alles beibehalten, selbst wenn uns das Schicksal an andere Orte verschlägt.

Vielen Dank auch an meine beiden reizenden Tanzpartnerinnen Irina Tolokonnikowa und Gabriele Warth, für die kessen Sohlen auf dem Parkett und überraschend wenig blauen Flecken, die wir uns geholt haben. Die schwarz-bunten Sendungsmitschnitte von W.o.11 von den Ultimas Lagrimas habe ich immer mal wieder sehr gerne gehört, sei bedankt! Ein aufmunternder Ruf geht an die ehemalige Besatzung (und natuerlich den omniscienten Bordcomputer) der "King-Liam II"! Ein grosser Dank an Felicia Rappe für die (viel zu wenigen) lehrreichen Gespräche über Kunst, Kultur und Küchenpsychiologie. Vielen Dank an Katja Ostermeir fürs mitleiden und die vielen schönen Abende in München. You are next! Vielen Dank auch an Katharina von Sturm, Simon Bell, Rainer Schmidt, Christian Pflüger, Tina Oexl, Markus Pak und alle anderen für nette Abende, Raucherpausen, Gran-Sasso Fahrten und vieles mehr.

Zuguterletzt möchte ich mich noch bei meiner Familie für deren konstante Unterstützung, die zwei Heimathäfen und den andauernden Zuspruch bedanken.

Vielen Dank!

LIST OF PUBLICATIONS

- F. Ritter, B. Lubsandorshiev, K. Freund *et al.*
  The calibration system of the GERDA *muon veto Cherenkov detector*
  Nucl. Instr. A, vol 617, pg. 420, 2010

- R. Falkenstein, L. Bezrukov, K. Freund *et al.*
  Extensive studies of MRS APDs for plastic scintillator muon veto detectors of cryogenic experiments
  Nucl. Instr. A, vol. 695, pp. 330-333, 2012

- M. Agostini, M. Allardt, E. Andreotti *et al.* (GERDA Collaboration)
  Measurement of the half-life of the two-neutrino double beta decay of ^{76}Ge with the GERDA *experiment*
  J. Phys. G: Nucl. Part.Phys., vol 40(3), pg. 035110, 2013

- K.-H. Ackermann, M. Agostini, M. Allardt *et al.* (GERDA Collaboration)
  The Gerda experiment for the search of $0\nu\beta\beta$ decay in ^{76}Ge
  Eur. Phys. J C, vol. 73(3), pp. 1-29, 2013

- M. Agostini, M. Allardt, E. Andreotti *et al.* (GERDA Collaboration)
  Pulse shape discrimination for GERDA *Phase I data*
  Eur. Phys. J. C, vol. 73(10), pp. 1-17, 2013

- M. Agostini, M. Allardt, E. Andreotti *et al.* (GERDA Collaboration)
  The background in the $0\nu\beta\beta$ experiment GERDA
  Eur. Phys. J. C, vol. 74(4):2764, 2014

- M. Agostini, M. Allardt, E. Andreotti *et al.* (GERDA Collaboration)
  Results on Neutrinoless Double-β Decay of ^{76}Ge from Phase I of the GERDA *Experiment*
  Phys. Rev. Lett., vol. 111(12), pg. 122503, 2013

- K. Freund, P. Grabmayr, J. Jochum *et al.*
  Performance of the Muon Veto of the GERDA $0\nu\beta\beta$ *Experiment*
  in preparation